Politecnico di Torino

Master's degree course in Aerospace Engineering

Master's thesis

Analysis of numerical methods based on modal shapes for the dynamic response analysis of aircraft structures

STUDENT
S303611 ANDREA MACAR

Academic year 23/24

Supervisor: Marco Gherlone

[This page was intentionally left blank]

Acknowledgments

As I conclude this essay, it is essential for me to express my deep gratitude to the individuals who have supported me throughout my university years, furthering my knowledge.

I am particularly thankful to my family for their unwavering moral support during my moments of dejection, to my girlfriend, Martina, for her steadfast presence during my moments of greatest need, and to my supervisor, Professor Marco Gherlone, for his dedicated guidance during the writing of this master's thesis and throughout his courses I have attended. His passion and the clarity he explained the subjects covered in the thesis have inspired me greatly.

Index

Introduction

The thesis compares different methods used to obtain structural dynamic responses: Mode Displacement, Modal Truncation Augmentation, and Mode Acceleration. There is limited existing literature on these methods, with only a few recent scientific articles providing further insights into their differences and capabilities [1].

The thesis conducts detailed analyses of the mentioned methods and also compares the "Inertia Relief-based" method to the Modal Truncation Augmentation method. Both methods are implemented by default in MSC Nastran's RESVEC function, which calculates residual vectors to obtain improved structural dynamic responses.

Chapter 1 discusses the first methods, while Chapter 2 focuses on their implementation, code validation using reference literature data, and application to the Euler-Bernoulli beam finite element model. This section also aims to numerically and analytically compare the methods using different defined performance coefficients. Analyses show that the methods exhibit different behaviours depending on the frequency content, spatial distribution of the applied loads, and the system's modal shapes and associated natural frequencies. Therefore, enhancement approaches are designed to optimize the solution at each applied load’s frequency.

Finally, in Chapter 3, it is provided an analytical comparison of the methods already implemented in MSC Nastran. This is achieved through the definition of other performance coefficients, conceptually similar to those used in the previous chapter. The effectiveness of the methods is evaluated by their adherence to the ideal solution and their computational cost, the latter is directly related to the total number of solved 1-DOF differential equations, which is equal to the combined number of retained and residual modal shapes.

The results obtained in Chapter 2 indicate possible reasons why MSC Nastran's algorithm progressively adopted the Modal Truncation method over the Mode Acceleration method, whereas results from Chapter 3 suggest on which occasions it is more convenient to use the residual vector methods adopted by MSC Nastran's RESVEC function. It is anticipated that the Modal Truncation method is more effective than the Inertia Relief-based method at higher numbers of retained modes, providing the best approximation of the ideal solution at a reasonable computational cost. However, their simultaneous use could provide the best solution approximation in cases where the retained modes have frequencies far below the load’s frequencies, especially in presence of complex spatial components of the considered dynamic loads.

1. Analysis of numerical methodologies based on modal shapes for determining the dynamic response of N-DOF systems.

1.1. Theoretical foundations

1.1.1. The Mode-Displacement Method and Modal Shapes

The Mode-Displacement (MD) method is widely used to obtain structural system's complete dynamic responses. This chapter will study the mentioned method, along with the Modal Truncation Augmentation and Mode Acceleration methods, in the first section of the next chapter they will be used to analyse an N Degree of Freedom (NDOF) system extracted from reference [2], then, they will be applied to an Euler-Bernoulli beam model discretized with the Finite Elements Method.

To obtain the MD equations, let's start with the differential motion equation for a generic NDOF system, which is:

$$[M]\{\ddot{y}(t)\} + [C]\{\dot{y}(t)\} + [K]\{y(t)\} = \{F(t)\} = \{F_0\}r(t) \quad (1)$$

$\{F(t)\}$ was decomposed in its spatial and temporal components, $\{F_0\}$ and $r(t)$, respectively.

Typically, the physical coordinates are transformed to modal coordinates $v(t)$. This is done using the associated set of eigenvectors. They represent the way in which a structural system can be deformed under a generic dynamic set of forces and are obtained by the solution of the general eigenvalue problem, given by:

$$\left([K] - \omega_i^2[M]\right)\{\phi\}_i = 0$$

The number of existing modal shapes is equal to the number of DOFs. The MD method considers all of them for the dynamic response calculation, differently from the methods analysed later. Across this and the next chapters, the eigenvectors matrix will be normalized with respect to the mass matrix. Considering the eigenvectors' orthogonality respect to the mass matrix and the normalization chosen, the generalized mass and stiffness matrices must satisfy the conditions:

$$[D_M] = [\phi]^T[M][\phi] = I; \quad [D_K] = [\phi]^T[K][\phi] = \Omega^2 \quad (2)$$

Where: $\Omega^2 = \begin{bmatrix} \omega_1^2 & 0 & 0 & 0 & 0 \\ 0 & \ddots & 0 & 0 & 0 \\ 0 & 0 & \omega_i^2 & 0 & 0 \\ 0 & 0 & 0 & \ddots & 0 \\ 0 & 0 & 0 & 0 & \omega_N^2 \end{bmatrix}$ and ω_i is the modal pulsation associated to the i-th modal shape.

This way, the complex N by N differential equation system can be rearranged in a more practical set of N 1-DOF differential equations, where N is the number of retained modes. Each of the N equations is given by the general formulation:

$$\ddot{v}_i(t) + 2\xi_i\omega_i\dot{v}_i(t) + \omega_i^2 v_i(t) = \hat{F}_{0,i}\, r_i(t) \qquad (3)$$

Where $v_i(t)$ represents the participation of the $i-th$ modal shape to the total dynamic response as a time-function. The modal damping term ξ_i is obtained experimentally or rather hypothesized, a model largely in use today provides $[C]$ (eq. *(1)*) as a linear combination of mass and stiffness matrices. The force term was rearranged using the eigenvectors matrix, as follows:

$$\{\hat{F}_0\} = [\phi]^T\{F_0\}$$

$\{F_0\}$ has the same dimension of the DOFs, while $\{\hat{F}_0\}$ has the dimension of the number of modes considered. The transformation from physical coordinates to modal coordinates and vice versa is obtained through the relations:

$$\{y(t)\} = [\phi]\,\{v(t)\}$$

$$\{v(t)\} = [D_M]^{-1}[\phi]^T[M]\{y(t)\} = [\phi]^T[M]\{y(t)\} \qquad (4)$$

Because of the eigenvector's normalization used, the inverse of the matrix $[D_M]$ is: $[D_M]^{-1} = I$. The relation (*4*), used in the next paragraph to determine the modal coordinates relative to the initial conditions, is more efficient than inverting the eigenvectors matrix, especially if the system is large.

To determine the importance of modal shapes let's consider a generic NDOF non-labile system in which the force applied on each DOF has in common the same $\mathrm{r}(t)$. Let's furthermore suppose that each force $F_i(t)$ and so $\hat{F}_i(t)$ are a linear combination of harmonic oscillators. This means that:

$$\{F_0\}r(t) = \sum_{j=1}^{M}\{F_1\}\cdot osc_j\,(t) \rightarrow \{\hat{F}_0\}r(t) = [\phi]^T\{F_0\}r(t) = [\phi]^T\{F_1\}\sum_{j=1}^{M} osc_j\,(t)$$

Where $\{F_1\}$ is a generic set of forces applied to the DOFs and $osc_j(t)$ represents the j-th harmonic oscillator:

$$osc_j(t) = A_j e^{i\omega_j t-\varphi_j}$$

Therefore, the components of the modal force can be written as:

$$\hat{F}_i = \sum_{j=1}^{M} C_{ij}e^{i\omega_j t-\varphi_{ij}} = C_{i1}e^{i\boldsymbol{\omega_1} t-\varphi_1} + \cdots + C_{ij}e^{i\boldsymbol{\omega_j} t-\varphi_j} + \cdots + C_{iM}e^{i\boldsymbol{\omega_M} t-\varphi_M}$$

This approach can be extended to the generic case in which $M \rightarrow \infty$. Each modal coordinate v_i will be the sum of a general and particular solution for the respective 1-DOF system: $v_i(t) = v_{g,i}(t) + v_{p,i}(t)$.

Considering the realistic case in which ξ_i<1, the general solution for the generic DOF *'i'* can be written as:

$$v_{g,i}(t) = e^{-\xi_i\omega_{Ni}t}(A_1\cos(\boldsymbol{\omega_{Di}}t) + A_2\sin(\boldsymbol{\omega_{Di}}t))$$

Where $\omega_D = \omega_N\sqrt{1-\xi_i^2}$ and $f_D = \frac{\omega_D}{2\pi}$ is the damped modal frequency. The particular solution, instead, is for superposition:

$$v_{p,i}(t) = \sum_{j=1}^{M} B_{ij}e^{i\omega_j t-\varphi'_{ij}} = B_{i1}e^{i\boldsymbol{\omega_1} t-\varphi'_{i1}} + \cdots + B_{ij}e^{i\boldsymbol{\omega_j} t-\varphi'_{ij}} + \cdots + B_{iM}e^{i\boldsymbol{\omega_M} t-\varphi'_{iM}}$$

Finally, physical displacements are given by:

$$\{y(t)\} = [\phi]\,\{v(t)\}$$

$$\begin{Bmatrix} y_1(t) \\ \vdots \\ y_i(t) \\ \vdots \\ y_N(t) \end{Bmatrix} =$$

$$\left[\begin{Bmatrix} \phi_1 \\ \vdots \\ \phi_j \\ \vdots \\ \phi_M \end{Bmatrix}_1 \cdots \begin{Bmatrix} \phi_1 \\ \vdots \\ \phi_j \\ \vdots \\ \phi_M \end{Bmatrix}_i \cdots \begin{Bmatrix} \phi_1 \\ \vdots \\ \phi_j \\ \vdots \\ \phi_M \end{Bmatrix}_N\right] \begin{Bmatrix} v_{g,1}(t) + B_{11}e^{i\boldsymbol{\omega_1} t-\varphi'_{11}} + \cdots + B_{1j}e^{i\boldsymbol{\omega_j} t-\varphi'_{1j}} + \cdots + B_{1M}e^{i\boldsymbol{\omega_M} t-\varphi'_{1M}} \\ \vdots \\ v_{g,i}(t) + B_{i1}e^{i\boldsymbol{\omega_1} t-\varphi'_{i1}} + \cdots + B_{ij}e^{i\boldsymbol{\omega_j} t-\varphi'_{ij}} + \cdots + B_{iM}e^{i\boldsymbol{\omega_M} t-\varphi'_{iM}} \\ \vdots \\ v_{g,N}(t) + B_{N1}e^{i\boldsymbol{\omega_1} t-\varphi'_{N1}} + \cdots + B_{Nj}e^{i\boldsymbol{\omega_j} t-\varphi'_{Nj}} + \cdots + B_{NM}e^{i\boldsymbol{\omega_M} t-\varphi'_{NM}} \end{Bmatrix}$$

Each modal shape oscillates both at its damped modal frequency and at the force's frequencies. Not including some of the modal shapes, especially when the force has frequencies in the range of the not-included mode, can determine important displacement mispredictions.

1.1.2. 1-DOF equation and solution

To solve the N equations in the form shown in eq. (*3*), it can be used the Laplace Transform. The complete solution includes the Duhamel's integral and a series of terms relative to the initial conditions. Therefore, being the eq. (*3*):

$$\ddot{v}_i(t) + 2\xi_i\omega_i\dot{v}_i(t) + \omega_i^2 v_i(t) = \hat{F}_i\, r_i(t)$$

The solution obtained by applying the Laplace Transform is:

$$v_i(t) = \int_0^t F(\tau)h(t-\tau)\,d\tau + M_i\left[v_{0,i}\left(\dot{h}(t) + h_0\right) + \left(\dot{v}_{0,i} + 2\xi_i\omega_i v_{0,i}\right)h(t)\right]$$

Where $v_{0,i}$ and $\dot{v}_{0,i}$ are the initial conditions expressed in modal coordinates, easily obtainable using eq. (4); while the response to the unitary impulse $h(t)$ and its derivative $\dot{h}(t)$ (both obtained considering $\xi_i < 1$) are given by:

$$h(t) = \frac{1}{M_i\omega_i}e^{-\xi_i\omega_i t}\sin\left(\omega_i\sqrt{1-\xi_i^2}t\right)$$

$$\dot{h}(t) = \frac{1}{M_i\omega_i\sqrt{1-\xi_i^2}}e^{-\xi_i\omega_i t}\left(\omega_i\sqrt{1-\xi_i^2}\cdot\cos\left(\omega_i\sqrt{1-\xi_i^2}t\right) - \xi_i\omega_i\cdot\sin\left(\omega_i\sqrt{1-\xi_i^2}t\right)\right)$$

1.1.3. The Mode-Displacement Method: limits and alternatives

Considering modal shapes in an adequate range of frequencies can represent almost completely the solution searched. Commercial software can determine a priori the number of modal shapes to retain. The decision of how many modes to keep is based on the relevant frequency content of the applied force. It is also advised that the highest mode retained should have a frequency well above the applied time history loading frequency by a certain margin ([2], [3]). However, some problems may require the calculation of many modal shapes for the solution to converge, this is because some forces cannot be modally represented easily, as a result, in certain cases, adding each modal shape to the modal eigenvectors matrix may gradually reduce its overall benefit. In other words, for a linear increase in computational cost, the overall solution enhancements will experience an increase similar to a logarithmic-like curve with a horizontal asymptote. An example of different types of convergences is reported in the final section of paragraph 2.2. This is also related to the fact some spatial forces can in part excite modal shapes having much higher frequencies, leading to the retention of many modal shapes before the excited one, therefore, increasing the overall computational cost for the full solution convergence. This will be one of the main topics of this thesis.

There are different alternatives to the Mode-Displacement method which do not need to calculate integrally all the modal shapes. Instead, these alternatives typically rely on Residual Vectors (Res-Vec) for computation. Residual Vectors can enhance the solution accuracy in certain scenarios while using fewer modal shapes. Essentially, they function as pseudo-modes, aiding in the representation of more accurate deformations and ultimately decreasing the number of retained modes necessary to correctly calculate the system's displacements [*4*].

At first glance, it may seem that the retained modes could adequately represent the full displacements of the DOFs. However, the criterion mentioned earlier - which only considers modes that accurately span the frequencies of interest - applies to $\boldsymbol{r(t)}$ but fails to consider the spatial component of the load for the reasons discussed before. By not accounting for modal truncation on the spatial portion of the applied load, inaccuracies can arise. The force truncation vector $\boldsymbol{R_t}$ addresses this issue by representing the portion of the load that is not accounted for. The rationale behind this approach is that the main dynamic response has already been enveloped by the retained modes, leaving the neglected modes with a quasi-static response. In other words, since the frequencies of the non-retained modes should be widely higher than those of the applied forces, they should perceive the applied forces as quasi-static ([2], [3], [*4*]).

The physical force represented by each mode is given by:

$$\{R_n(t)\} = [K]\{\phi_n\}v_n(t) = [M]\{\phi_n\}\omega_n^2 v_n(t) = [M]\{\phi_n\}\omega_n^2 \frac{\hat{F}_n}{\omega_n^2} r(t) = [M]\{\phi_n\}\hat{F}_n r(t)$$

$$\rightarrow R_s = [M][\phi]_R\{\hat{F}\} \rightarrow \boldsymbol{R_t} = F_0 - R_s$$

Where $[\phi]_R$ addresses to all the modal shapes retained, R_s is the modally represented force and R_t the modally non represented force. $\{\hat{F}\} = [\phi]_R^T\{F_0\}$, and the relation $\hat{F}_n r(t) = \omega_n^2 v_n(t)$ is valid since the normalization reported in the eq. (*2*). The equation $R_s = [M][\phi]_R\{\hat{F}\}$ determines how well the retained modal shapes can describe the statical response to the spatial portion of the applied dynamic load, or in other words, their capability of representing it.

1.1.4. The Modal Truncation Augmentation Method

The main difference between some of the methods that emerged to deal with the problems mentioned in paragraph 1.1.3 is the way they use the force truncation vector R_t.

A key method is the Modal Truncation Augmentation (MT method) which creates a pseudo eigen known as MT vector for each differentiated dynamic force applied. Each MT vector is orthogonal to the other MT vectors in relation to the mass and stiffness matrices. Furthermore, the MT vectors are also orthogonal to the retained eigenvectors since the force truncation vectors do not contain any components of the retained eigenvectors. However, they do not fulfil the original eigenvalue problem. The method consists of adding the MT vectors calculated to the real retained eigenvectors, allowing the analysis of modal response to proceed as if the augmented vector set was the complete set of original eigenvectors, or in other words, the procedure from this point is analogous to the MD method except for the augmented eigenvectors matrix ([2],[5]), which is:

$$[\phi]_{TOT,MT} = [\,[\phi]_R\,, [\phi]_{MT}].$$

As stated by the hypothesis cited before, the non-retained modes react quasi-statically to the virtually applied load, which is the force truncation vector $\{R_t\}$, therefore, the solution associated to $\{R_t\}$ does not necessitate the calculation of the non-retained eigenvectors and it is initially set as:

$$[K]\{X\} = \{R_t\} \qquad (5)$$

The next step, to calculate the MT pseudo eigenvectors is to calculate:

$$[D_K] = [X]^T[K][X];\ [D_M] = [X]^T[M][X]$$

Where:

$$[X] = [\{X\}_1 \dots \{X\}_i \dots \{X\}_N]$$

Where N is the number of the applied differentiated forces and $\{X\}_i$ is associated to the respective $\{R_t\}_i$. The Mode Acceleration method, reviewed hereafter, spatially solves the non-represented loads as reported in eq. (*5*) ([2],[5]).

$[D_K]$ and $[D_M]$ are scalars if it is applied a single differentiated dynamic force:

$$[D_K] = \{X\}^T[K]\{X\} = \bar{\boldsymbol{K}};\ [D_M] = \{X\}^T[M]\{X\} = \bar{\boldsymbol{M}}$$

Now, the approximation the method makes is to consider the vector $\{X\}$ as a modal shape, as if the only way the system could dynamically respond to R_t was represented by $\{X\}$, which is a static response indeed but it is considered as the dynamic response of a modal shape excited at frequencies much lower than its frequency.

Therefore, the reduced eigenvalue problem can be solved, and the MT vector $\boldsymbol{P}$ is appended to the retained eigenvectors matrix $[\phi]_R$ to construct the augmented eigenvectors matrix $[\phi]_{TOT,MT}$:

$$[D_K]Q = [D_M]Q\bar{\omega}_P^2$$

For a single MT vector, the equation above becomes:

$$\bar{K}Q = \bar{M}Q\bar{\omega}_P^2 \rightarrow \{P\} = \{X\}Q \rightarrow [\phi]_{TOT} = [[\phi]_{RM}\ \ P]$$

Q normalizes the eigenvector $\{X\}$ respect to mass matrix (the Matlab algorithm for the eigenvalue problem does that by default), so the normalization is in line with that of the other eigenvectors:

$$\{X\}^T[M]\{X\} \neq 1\ \rightarrow \{P\}^T[M]\{P\} = 1;\ \ \{P\}^T[K]\{P\} = \bar{\omega}_P^2$$

The calculated pseudo-modal shape $\{P\}$ oscillates at its pseudo-modal frequency $\bar{f}_P = \frac{\sqrt{\bar{\omega}_P^2}}{2\pi}$.

1.1.5. Other alternative methods

As was hinted in the previous paragraph, the Mode Acceleration method (MA) is a particular case of the Modal Truncation Augmentation method. If the generalized mass and modal damping terms are set to 0 while using the MT vectors in the equation:

$$\ddot{v}_i(t) + \xi_{P,i}\dot{v}_i(t) + \omega_{P,i}v_i(t) = \hat{F}_{P,i}\, r_i(t)$$

The MT vectors will be forced to respond quasi-statically and the mode acceleration result will be exactly reproduced in the time domain, while in the frequency domain would exactly reproduce the "residual stiffness" method result. If the generalized mass is set to 0 the result will exactly match the missing mass method result. If no eigenvectors are retained and MT vectors are calculated from vectors of unitary forces at selected degrees of freedom, a Guyan reduction will be produced ([2], [3]). An algorithm that does not use eigenvectors but instead uses a series of specially constructed Ritz vectors for the dynamic response calculation is given by Wilson et al. [*6*].

1.1.6. The Mode Acceleration Method

The logic of the MA method is that since the modes retained already span the frequency range of interest, any loading not represented by the retained modes will produce a complete quasi-static response. In other words, the response due to the non-retained modes will have no dynamic amplification and the modes not retained will cause no appreciable velocity or acceleration response.

To introduce the MA algorithm, the eq. (*1*), reported below, is rewritten as follows:

$$[M]\{\ddot{y}(t)\} + [C]\{\dot{y}(t)\} + [K]\{y(t)\} = \{F_0\}r(t) \rightarrow \{F_{elast}\} = \{F_0\}r(t) - \{F_{inert}\} - \{F_{damp}\}$$

$$\{y_u(t)\}_{MA} = [K]^{-1}\{F_0\}r(t) - [K]^{-1}[M][\phi]_R\{\ddot{v}(t)\} - [K]^{-1}[C][\phi]_R\{\dot{v}(t)\} = \begin{bmatrix} F_0^{\psi} & \ddot{v}^{\psi} & \dot{v}^{\psi} \end{bmatrix} \begin{Bmatrix} r(t) \\ \ddot{v}(t) \\ \dot{v}(t) \end{Bmatrix}$$

Given N as the system size and n as the number of retained modes, for each set of applied loads the dimension of F_0^{ψ} is Nx1, while $\ddot{v}^{\psi}$ and $\dot{v}^{\psi}$ are Nxn. $r(t)$ is 1x1 and $\ddot{v}(t)$, $\dot{v}(t)$ are nx1.

Another way to write the total displacement term is:

$$\{y_u(t)\}_{MA} = [K]^{-1}\{F_0\}r(t) - [K]^{-1}[M][\phi]\{\ddot{v}(t)\} - [K]^{-1}[C][\phi]\{\dot{v}(t)\}$$

$$= [K]^{-1}(\{R_s\} + \{R_t\})r(t) - [K]^{-1}[M][[\phi]_R \;\; [\phi]_{NR}] \begin{Bmatrix} \ddot{v}_R(t) \\ \ddot{v}_{NR}(t) \end{Bmatrix} - [K]^{-1}[C][[\phi]_R \;\; [\phi]_{NR}] \begin{Bmatrix} \dot{v}_R(t) \\ \dot{v}_{NR}(t) \end{Bmatrix}$$

$$= [K]^{-1}(\{R_s\})r(t) - [K]^{-1}[M][\phi]_R\{\ddot{v}_R(t)\} - [K]^{-1}[C][\phi]_R\{\dot{v}_R(t)\} +$$

$$[K]^{-1}(\{R_t\})r(t) - [K]^{-1}[M][\phi]_{NR}\{\ddot{v}_{NR}(t) = \{0\}\} - [K]^{-1}[C][\phi]_R\{\dot{v}_{NR}(t) = \{0\}\}$$

The Mode Acceleration method formulation becomes:

$$\{y(t)\}_{MA} = \{y_s(t)\}_{MA} + \{y_t(t)\}_{MA}$$

Where $\{y_s(t)\}_{MA}$ is the part of the solution relative to the retained modes and $\{y_t(t)\}_{MA}$ refers to the part of it calculated considering the system's quasi-statical response to $\{R_t\}r(t)$.

1.1.7. MD, MT, and MA methods comparison

To compare the 3 methods, the global solution can be decomposed into the part relative to the retained modes (pedicle 's') and the part relative to the modal truncation (pedicle 't'), or in other words the common and the different parts of the solutions offered by the presented methods:

$$\{y(t)\} = \{y_s(t)\} + \{y_t(t)\}$$

$$[M]\{\ddot{y}_s(t)\} + [C]\{\dot{y}_s(t)\} + [K]\{y_s(t)\} + [M]\{\ddot{y}_t(t)\} + [C]\{\dot{y}_t(t)\} + [K]\{y_t(t)\} = \{R_s + R_t\}r(t)$$

Let's focus on the part relative to the non-represented force; the solutions calculated by MD, MA and MT methods are shown below.

$$[M]\{\ddot{y}_t(t)\} + [C]\{\dot{y}_t(t)\} + [K]\{y_t(t)\} = R_t r(t)$$

MD method: $\{y_t(t)\}_{MD} = [\phi]_{NR}\,\{v(t)\}_{NR}$

MA method: $[K]\{y_t(t)\}_{MA} = R_t r(t)$

MT method: $\{y_t(t)\}_{MT} = [P]\{v_P(t)\} \rightarrow$

$$[P]^T[M][P]\{\ddot{v}_P(t)\} + [P]^T[C][P]\{\dot{v}_P(t)\} + [P]^T[K][P]\{v_P\}(t) = [P]^T\{R_t\}r(t)$$

Obviously, the MD method calculates $\{y_t(t)\}_{MD}$ using all the modes not retained ($[\phi]_{NR}$).

2. Code validation and beam finite element model study case

2.1. Code validation

2.1.1. Problem description

The problem analysed deals with a 4-DOF system taken from [2], the model and the forces applied to its DOF are reported below. They are split into their spatial and their time/frequency domain components:

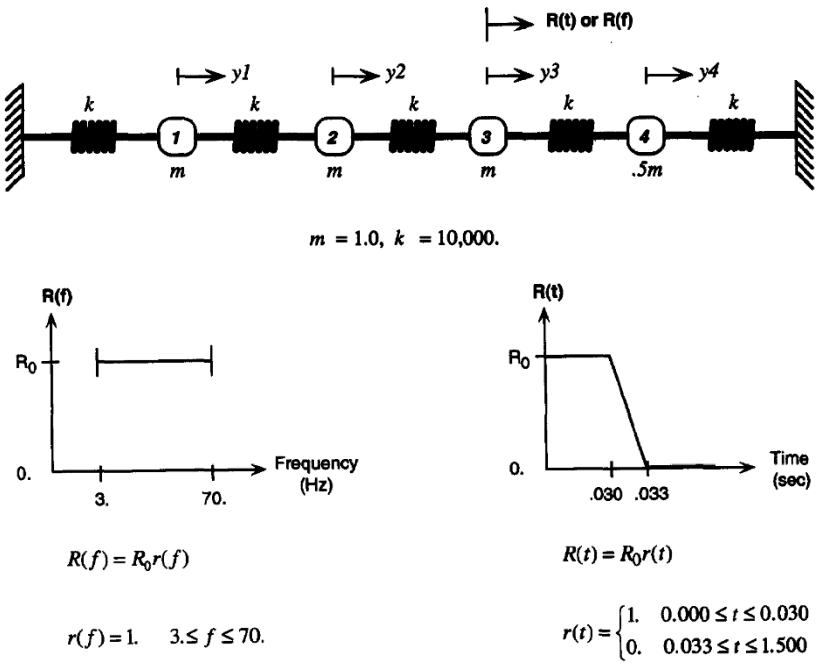

Figure 2.1: System representation and temporal/frequency components of the forces analysed.

The spatial components of the forces applied to each DOF are defined, for both cases, as:

$$F_0 = \begin{Bmatrix} 0 \\ 0 \\ 1 \\ 0 \end{Bmatrix} \tag{6}$$

The assembled mass and stiffness matrices of the system considered are shown below, the modal damping is set to 2% of the critical modal damping coefficient for all the modes and also for the MT vector. The number of eigenvectors retained is always 1 in this application.

To summarize, the physical properties of the system are:

$$[M] = \begin{bmatrix} 1 & & & \\ & 1 & & \\ & & 1 & \\ & & & 0.5 \end{bmatrix}; \ [K] = 10^4 \begin{bmatrix} 2 & -1 & & \\ -1 & 2 & -1 & \\ & -1 & 2 & -1 \\ & & -1 & 2 \end{bmatrix}; \ \xi_i = 0.02$$

The spatial forces represented by the first mode and the MT vector are:

$$R_s \cong \begin{Bmatrix} 0.25 \\ 0.39 \\ 0.38 \\ 0.1 \end{Bmatrix}; \ P \cong \begin{Bmatrix} -0.53 \\ -0.42 \\ 0.72 \\ 0.22 \end{Bmatrix}; \bar{f}_P \cong 22Hz.$$

Both time and frequency domain results obtained by the created framework are consistent with those reported in the reference [2]. Both results are presented in the paragraphs 2.1.2 and 2.1.3.

2.1.2. Frequency domain results

The results for the frequency domain case were obtained by applying the load shown in Figure 2.1 ($r(f)$) and in the eq. ((*6*), F_0). The displacements in the frequency domain can be obtained by:

$$\{U(\omega)\} = [H(\omega)]\{F(\omega)\}$$

This means that:

$$U_\alpha(\omega) = \sum_{\beta=1}^{N} H_{\alpha\beta}(\omega) F_\beta(\omega)$$

Where $H_{\alpha\beta}(\omega)$ is an element of the matrix $[H(\omega)]$ containing the Frequency Response Function (FRF), which associates the dynamic response of the node α to the solicitation applied on the node β and vice versa, considering all the calculated modes and pseudo-modes. It is given by:

$$H_{\alpha\beta}(\omega) = \sum_{k=1}^{N} \frac{\phi_{k\alpha}\phi_{k\beta}}{M_k(\omega_k^2 + 2\xi\omega\omega_k i - \omega^2)}$$

$\phi_{k\alpha}\phi_{k\beta}$ is the modal partecipation factor and $\phi_{k\alpha}$ or $\phi_{k\beta}$ represents the α-th or β-th element of the eigenvector k. ω_k is the modal pulsation associated to the respective modal shape k. In Figure 2.2 and in Figure 2.3 are reported all the elements of the FRF matrix, it is evident that the number of resonance frequencies depend on the method chosen and the number of retained eigenvectors. Furthermore, for the MT method the number of resonance frequencies depends also on the number of separated dynamic forces applied to the system, because for each of them it is calculated the respective pseudo eigenvector and its frequency $f_{P,i}$.

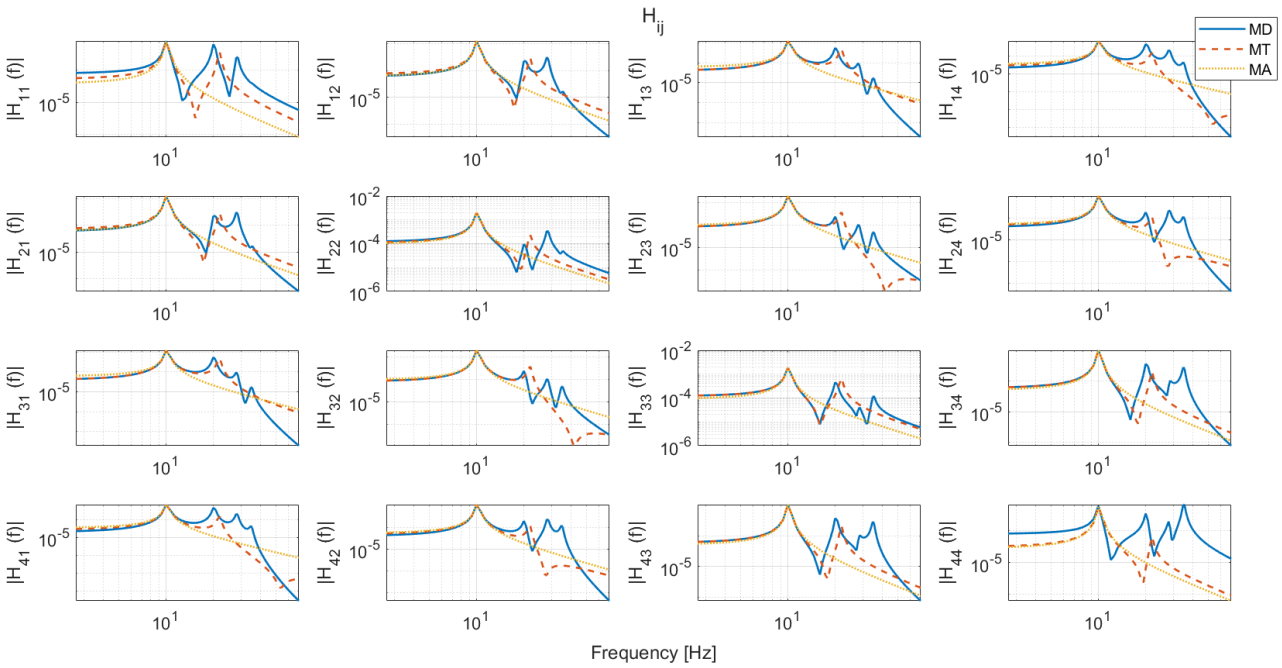

Figure 2.2: Full FRF matrix representation as a function of frequency.

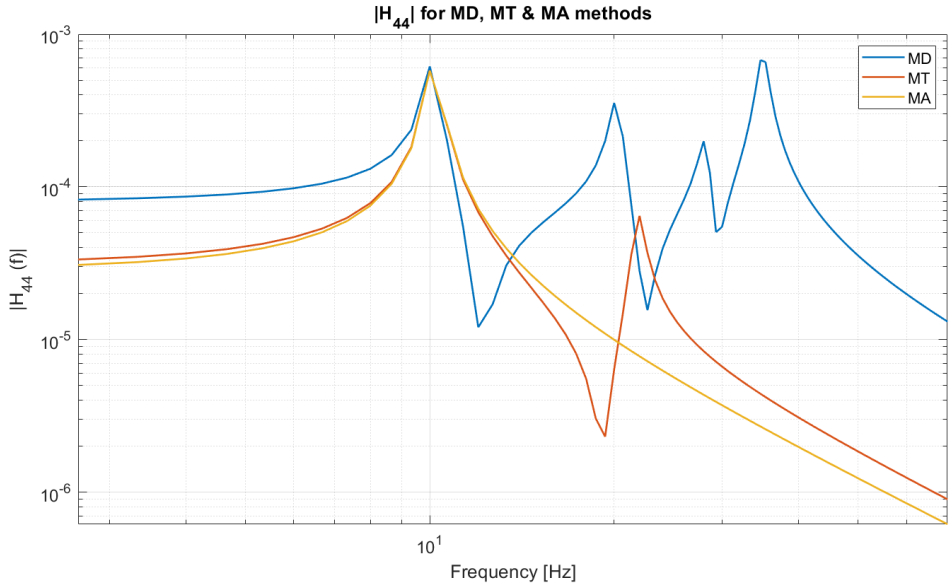

Figure 2.3: FRF element $|H_{44}|$ for all the methods presented. The FRF function obtained by the MD method has 4 peaks, while the MT and MA methods have respectively 2 and 1 peaks. The number of peaks is related to the number of retained modes and it is equal to the sum of real and residual eigenvectors.

Note: for the Mode Acceleration method were used 2 equations: one for the forces represented by the single retained mode (R_s) and the second for the forces not represented by it (R_t).

$$\{U_R(\omega)\}_{MA} = [H(\omega)]\{R_s\}r(\omega);$$

$$\{U_{NR}(\omega)\}_{MA} = [K]^{-1}\{R_t\}r(\omega)$$

The total displacements response is obtained by the sum of $\{U_R(\omega)\}_{MA}$ and $\{U_{NR}(\omega)\}_{MA}$.

In the following pages, both my results and the reference's results are reported. Overall, the comparison of the results is more than acceptable.

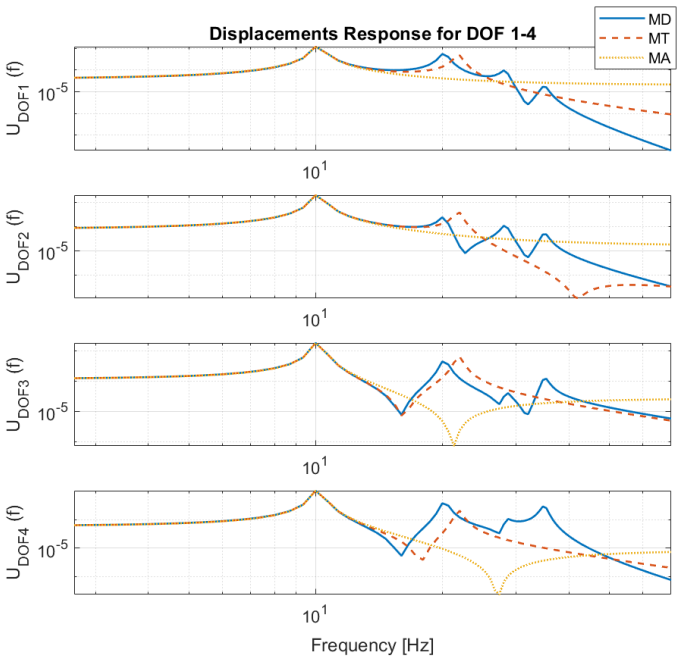

Figure 2.4: Displacement response in the frequency domain for all the DOFs.

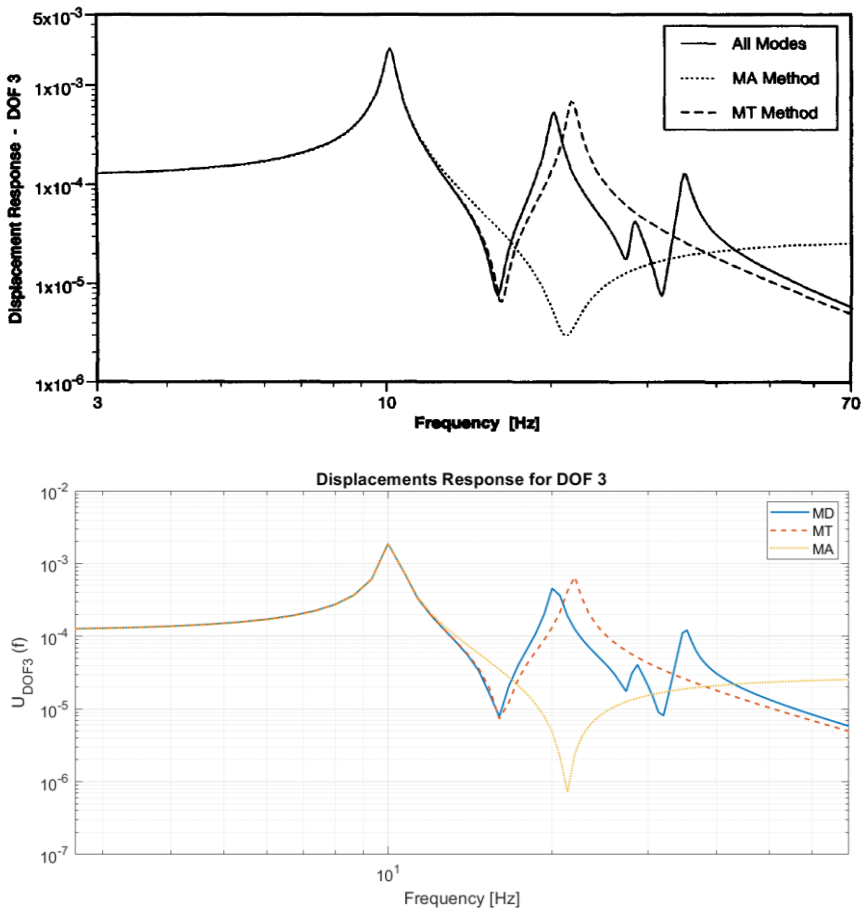

Figure 2.5: Comparison of the results presented in the paper [2] and those obtained by the created framework for the DOF 3 response in the frequency domain.

Any difference may be addressed to the different Fourier Transform algorithms used (in the created framework it was used the Fast Fourier Transform (FFT) algorithm already implemented in Matlab). Two comparative tables for the displacements of $U_{iDOF}(\omega)$ obtained at 3Hz are presented in Table 2.1.

$(\cdot 10^{-5})$	DOF 1	DOF 2	DOF 3	DOF 4
MD	4.52	8.89	12.90	6.53
MA	4.58	8.92	12.90	6.49
MT	4.54	8.89	12.90	6.51

$(\cdot 10^{-5})$	DOF 1	DOF 2	DOF 3	DOF 4
MD	4.53	8.91	12.95	6.54
MA	4.59	8.93	12.90	6.50
MT	4.55	8.90	12.95	6.52

Table 2.1: Displacements response of $U_{iDOF}(\omega)$ at 3Hz. The first table is taken from the reference [2], while the second reports the results obtained.

2.1.3. Time domain results

Overall, the results were in good agreement for the time domain loading too. Table 2.2 reports the maximum and minimum displacements obtained by Reference [2] and from the created framework for the time domain loading at each DOF. While Figure 2.6 refers to the displacements obtained for DOF 1.

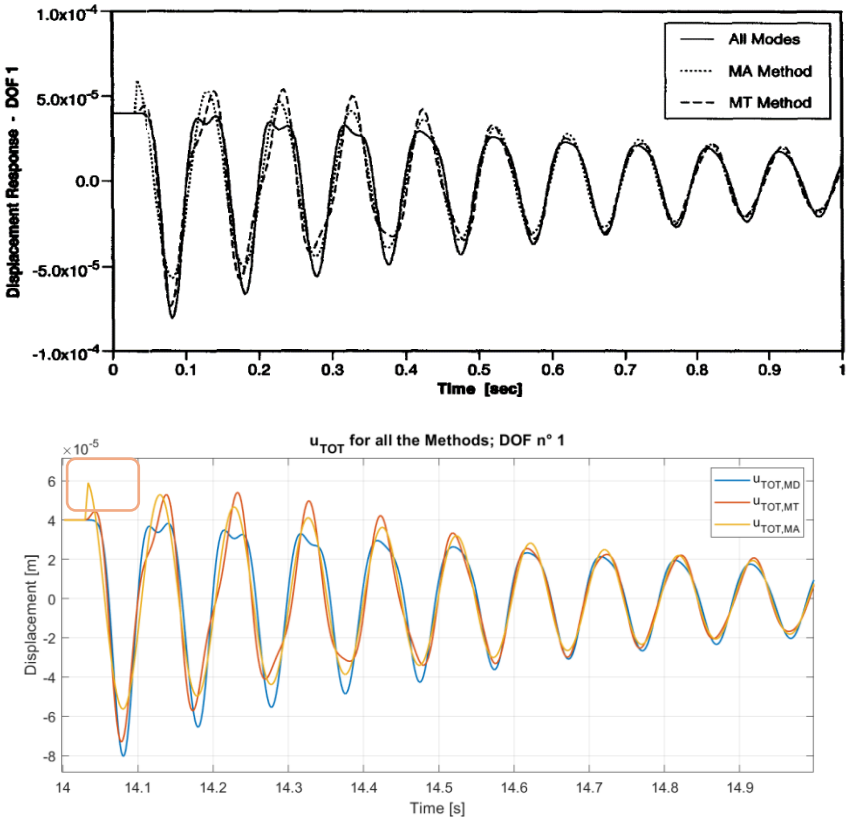

Figure 2.6: Comparison of the time domain responses for each method analysed at DOF 1. The first image is taken from reference [2] while the displacements reported in the second image are those obtained by the created framework. The two results are in good agreement, minor differences are addressed to MA's first peaks.

$(\cdot 10^{-5}\ m)$	DOF 1	DOF 2	DOF 3	DOF 4
Max MD	3.84	7.81	9.48	6.72
Max MA	5.97	9.50	8.16	4.54
Max MT	5.42	8.10	9.83	4.99
Min MD	-8.08	-9.52	-7.16	-4.42
Min MA	-5.65	-8.99	-8.68	-4.83
Min MT	-7.33	-10.30	-8.21	-4.34

$(\cdot 10^{-5}\ m)$	DOF 1	DOF 2	DOF 3	DOF 4
Max MD	3.83	7.81	9.48	6.67
Max MA	5.90	9.41	8.14	4.53
Max MT	5.41	8.09	9.81	4.99
Min MD	-8.03	-9.51	-7.18	-4.45
Min MA	-5.64	-8.98	-8.67	-4.82
Min MT	-7.31	-10.26	-8.18	-4.33

Table 2.2: Comparative tables for the maximum and minimum displacements of $u_{i,DOF}(t)$. The first table is taken from the reference [2], the second reports the results obtained from the created framework. Small differences are observable for maximum MA displacements at DOF 1 and DOF 2, these are associated with differences in the first peaks, as highlighted in Figure 2.6.

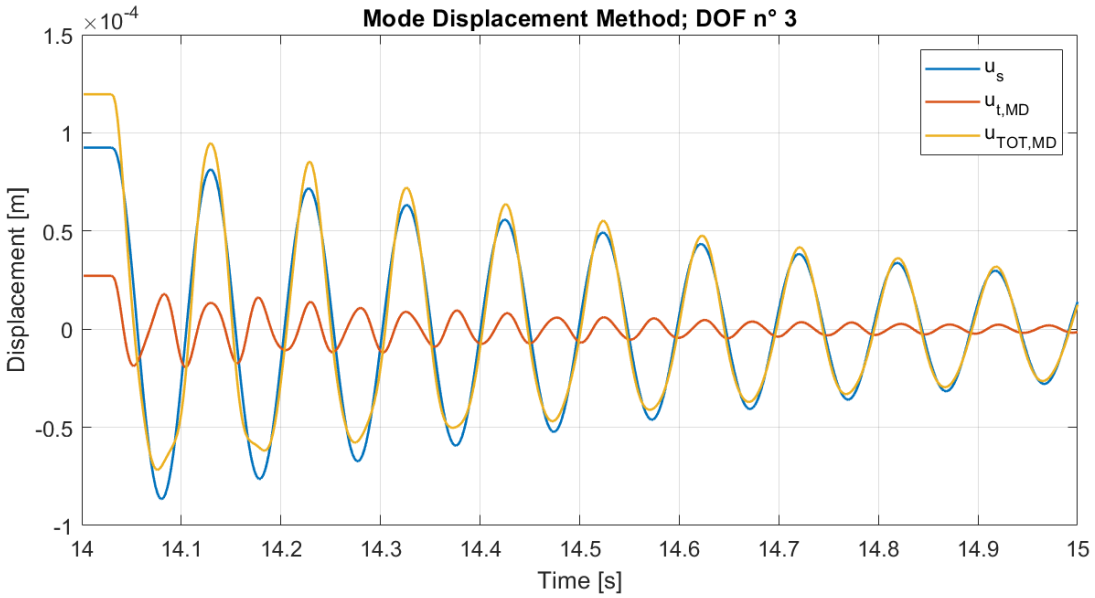

Figure 2.7: Comparison of the part of the solution obtained using the retained modes (u_s), the part obtained using the non retained modes (u_t) and the total solution ($u_{TOT} = u_s + u_t$) for the Mode Displacement Method at DOF n° 3.

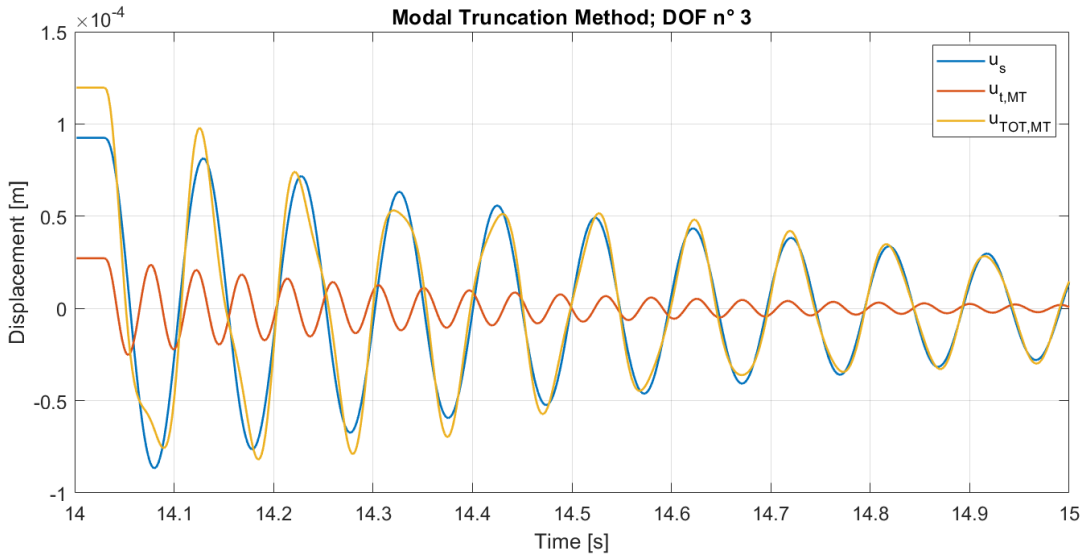

Figure 2.8: Comparison of the part of the solution obtained using the retained modes (u_s), the part obtained using the residual vector (u_t) and the total solution (u_{TOT}) for the Modal Truncation Augmentation Method at DOF n° 3.

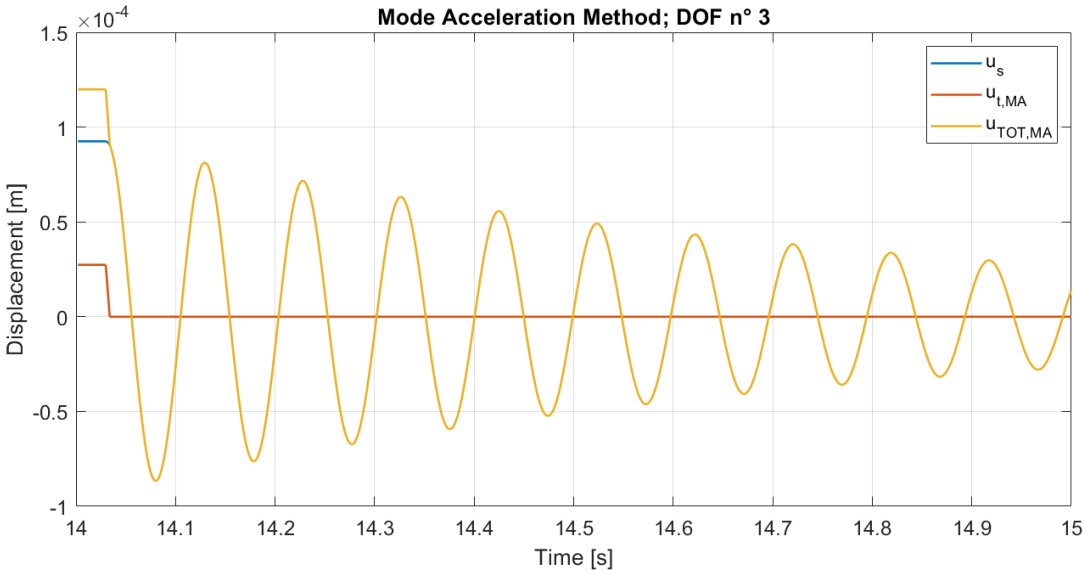

Figure 2.9: Comparison of the part of the solution obtained using the retained modes (u_s), the part obtained from the modally non-represented part of the load (u_t) and the total solution (u_{TOT}) for the Mode Acceleration Method at DOF n° 3.

It is clear from the comparison of Figures 2.7, 2.8, 2.9, and 2.10 the absence of dynamic amplification of $\{u_t\}_{MA}$, differently from the results obtained by MT and MD methods. Are now clear the possible advantages of the MT method over the MA method. Starting from paragraph 2.3 will be further investigated the differences between these 2 methodologies.

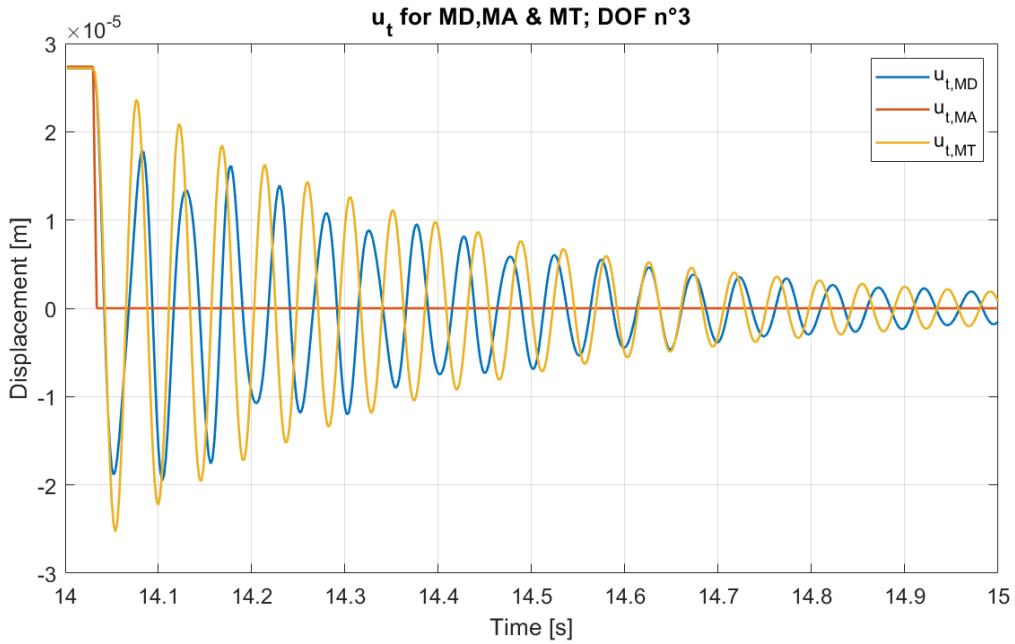

Figure 2.10: Results obtained from the time domain loading: u_t comparison for all the methods.

2.1.4. Observations

In reference [2], from which the analysed system was extracted, some informations regarding the force inputs and the displacement outputs were not reported. Specifically, at the time $t = 0\ s$ in Figure 2.6, the system already experiences some displacements as if the force was acting on node 3 for an indefinite amount of time. Therefore, in the created framework, the force applied to DOF 3 was applied for 14.033 seconds as shown in Figure 2.11, instead of 0.033 seconds as reported in Figure 2.1. However, the dynamic response of the system was collected in the time window of interest: $t_{Output} = 14 - 15\ s$.

Figure 2.12 demonstrates that at the initial time of observation ($14\ s$), the displacements were steady, similarly to the results extracted from Reference [2]. Furthermore, in Table 2.2, the maximum displacements refer not to the absolute maximums but instead to the maximums after the first oscillation, as reported in Figure 2.13.

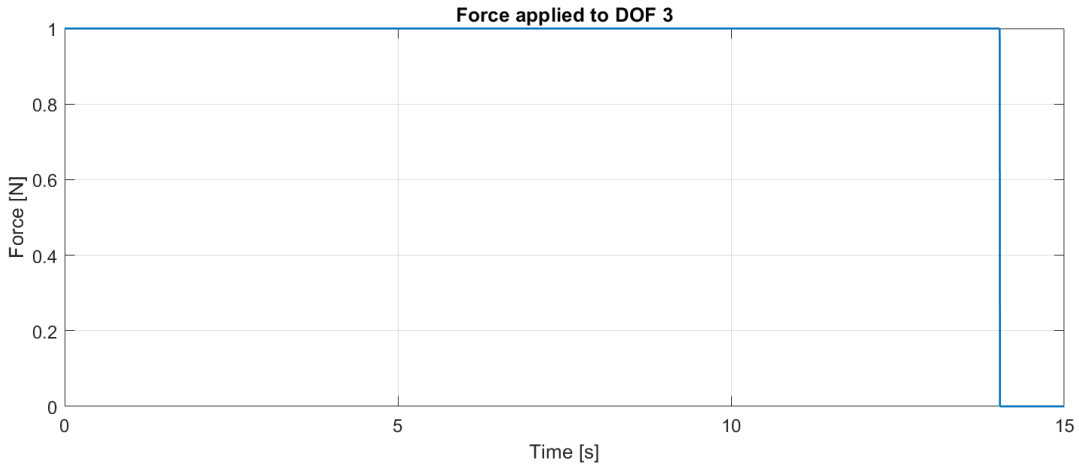

Figure 2.11: Force applied to DOF 3. The solution is extracted at $t = 14 - 15\ s$.

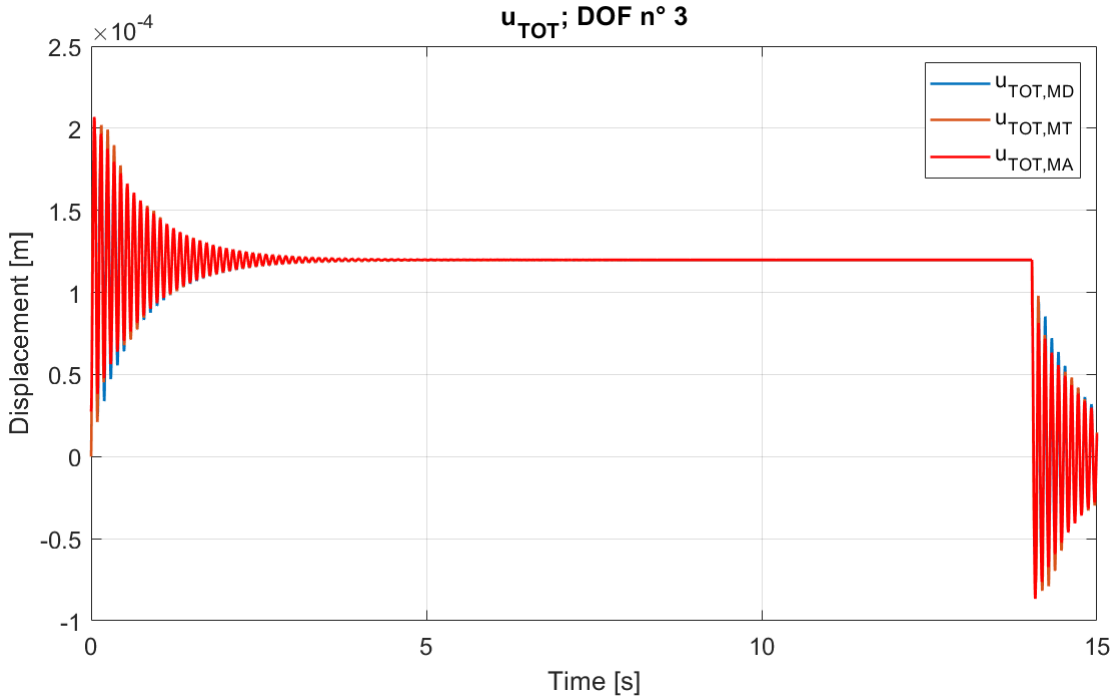

Figure 2.12: Results obtained in the full time domain. The solution is extracted at $t = 14 - 15\ s$.

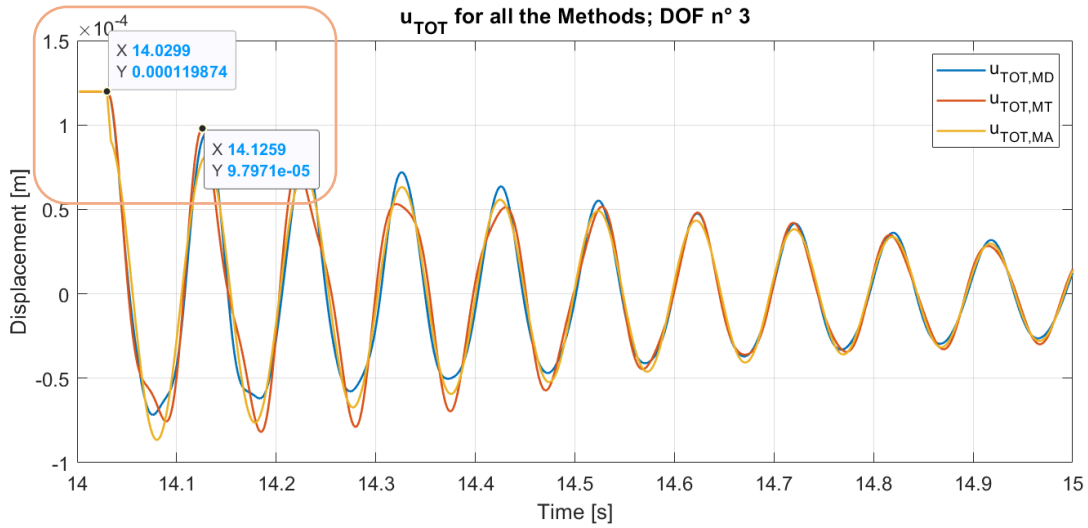

Figure 2.13: In Reference [2], maximum values were extracted after the first oscillation of the solution.

2.2. Euler-Bernoulli beam: theoretical foundations

2.2.1. Euler-Bernoulli beam equations

In this paragraph are reported the constitutive equations for the Euler-Bernoulli's (EB) beam model. The model hypothesizes that the only deformation occurring is ε_{xx}, the one relative to the axis of the beam. The displacement equations can be written as:

$$\begin{cases} u = u^{(0)} - z w_{,x}^{(0)} \\ w = w^{(0)} \end{cases} \rightarrow \{s(x,z,t)\} = [Z_u(z)]\{g_u(x,t)\} \rightarrow \begin{Bmatrix} u \\ w \end{Bmatrix} = \begin{bmatrix} 1 & 0 & z \\ 0 & 1 & 0 \end{bmatrix} \begin{Bmatrix} u^{(0)} \\ w^{(0)} \\ -w_{,x}^{(0)} \end{Bmatrix}$$

Stress and strain, for their definition, are:

$$\{\varepsilon_{xx} = u_{,x}^{(0)} - z w_{,xx}^{(0)} \rightarrow \{\varepsilon(x,z,t)\} = [Z_\varepsilon(z)]\{g_\varepsilon(x,t)\} \rightarrow \{\varepsilon_{xx}\} = [1 \quad +z] \begin{Bmatrix} u_{,x}^{(0)} \\ -w_{,xx}^{(0)} \end{Bmatrix}; \; \sigma_{xx}^{(k)} = E_x^{(k)} \cdot \varepsilon_{xx}$$

The D'Alembert principle can be expressed as follows:

$$\delta E_p = \delta L_e + \delta L_{in} \tag{7}$$

The equation (*7*) generalizes the principle of virtual work from static to dynamical systems by introducing forces of inertia which, when added to the applied forces in a system, result in dynamic equilibrium. δE_p, δL_e, δL_{in} are respectively the variations of internal or virtual work, variation of external work due to the applied forces on the system, and the variation of inertial work. They are definable as:

$$\delta E_p = \int_0^L \left(\int_S \delta \varepsilon_{xx}^T \sigma_{xx}^{(k)} \, dS \right) dx$$

$$\delta L_{in} = \int_V \delta\{s\}^T \left(-\rho^{(k)} \{\ddot{s}\} \right) dV$$

$$\delta L_e = \int_l \delta\{s\}^T \cdot f(x,z) \, dl$$

For the EB model, the components of the equation (7) become:

$$\delta E_p = \int_0^L \delta\{g_\varepsilon\}^T \left(\int_S [z_\varepsilon]^T E_x [z_\varepsilon] \, dS \right) \{g_\varepsilon\} \, dx = \int_0^L \delta\{g_\varepsilon\}^T \cdot [KZI] \cdot \{g_\varepsilon\} \, dx$$

Where: $[KZI] = \int_S E_x^{(k)} \begin{bmatrix} 1 & z \\ z & z^2 \end{bmatrix} dS = \begin{bmatrix} A & B \\ B & D \end{bmatrix}$; It is important to note that: $[KZI] \cdot \{g_\varepsilon\} = \begin{Bmatrix} N \\ M \end{Bmatrix}$

$$\delta L_{in} = \int_V \delta\{s\}^T \left(-\rho^{(k)} \{\ddot{s}\} \right) dV = -\int_0^L \delta\{g_u\}^T \left(\int_S [z_u] \rho^{(k)} [z_u] \, dS \right) \{\ddot{g}_u\} \, dx =$$

$$-\int_0^L \delta\{g_u\}^T [MZI] \{\ddot{g}_u\} \, dx; \quad [MZI] = \int_S \rho^{(k)} \begin{bmatrix} 1 & 0 & z \\ 0 & 1 & 0 \\ z & 0 & z^2 \end{bmatrix} dS = \begin{bmatrix} \mu & 0 & m_1 \\ 0 & \mu & 0 \\ m_1 & 0 & m_2 \end{bmatrix}$$

To calculate the contribution of δL_e, it must be considered all the distributed loads applied on the beam (integrated on the beam's depth) as reported in Figure 2.14.

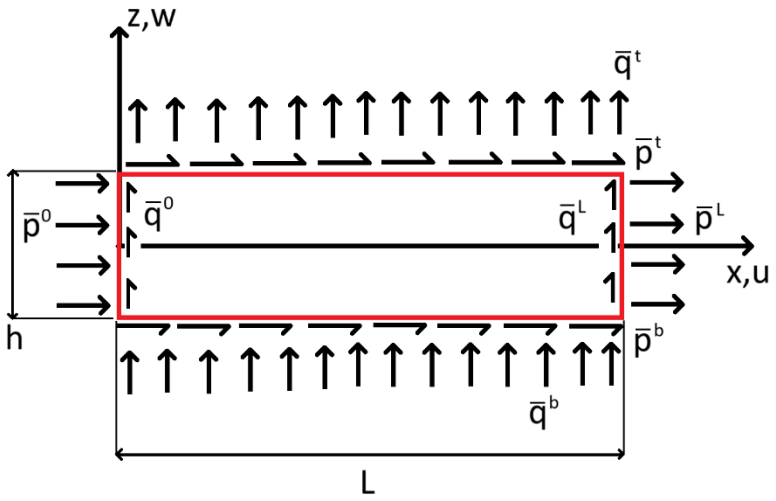

Figure 2.14: Representation of distributed loads along the elementary beam element

The total equation obtained by using the D'Alembert principle is:

$$\int_0^L \left[N_{,x} - \mu\ddot{u}^{(0)} + m_1\ddot{w}_{,x}^{(0)} + \bar{p}\right]\delta u^{(0)}\,dx + \int_0^L \left[M_{,xx} - \mu\ddot{w}^{(0)} - \left(m_1\ddot{u}^{(0)}\right)_{,x} + \left(m_2\ddot{w}_{,x}^{(0)}\right)_{,x} + \bar{q} + \bar{m}_{,x}\right]\delta w^{(0)}\,dx$$
$$+ \delta u^{(0)}(0)[N(0) + \bar{N}_0] + \delta u^{(0)}(L)[-N(L) + \bar{N}_L]$$
$$+ \delta w^{(0)}(0)\left[M_{,x}(0) - m_1\ddot{u}^{(0)}(0) + m_2\ddot{w}_{,x}^{(0)}(0) + \bar{T}_0 + \bar{m}\right]$$
$$+ \delta w^{(0)}(L)\left[-M_{,x}(L) + m_1\ddot{u}^{(0)}(L) - m_2\ddot{w}_{,x}^{(0)}(L) + \bar{T}_L - \bar{m}\right] + \delta w_{,x}^{(0)}(0)[-M(0) - \bar{M}_0]$$
$$+ \delta w_{,x}^{(0)}(L)[M(L) - \bar{M}_L] = 0$$

The first member of the equation must be 0 for any given set of displacements $\{s(x,z,t)\} = \begin{Bmatrix} u \\ w \end{Bmatrix}$. The only logic solution is that each term inside the brackets [ ] must be independently set to 0. In the equation above are underlined the motion and the boundary conditions equations.

The motion equations can be rewritten in case of constant parameters A, B, D, m_1, m_2 and symmetric lamination. Symmetric lamination also implies that $m_1 = 0$, therefore, axial and transversal displacements are now fully decoupled:

$$N_{,x} = \mu(x)\ddot{u}^{(0)} - m_1(x)\ddot{w}_{,x}^{(0)} - \bar{p}(x) \rightarrow Au_{,xx}^{(0)} = -\bar{p}(x) + \mu(x)\ddot{u}^{(0)}$$

$$M_{,xx} = \mu(x)\ddot{w}^{(0)} + \left(m_1(x)\ddot{u}^{(0)}\right)_{,x} - \left(m_2(x)\ddot{w}_{,x}^{(0)}\right)_{,x} - \bar{q}(x) - \bar{m}_{,x}(x) \rightarrow$$

$$-Dw_{,xxxx}^{(0)} = -\bar{q}(x) - \bar{m}_{,x}(x) + \mu(x)\ddot{w}^{(0)} - m_2\ddot{w}_{,xx}^{(0)}$$

Neglecting the rotary inertia term $\left(m_2\ddot{w}_{,xx}^{(0)}\right)$, considering $\mu(x)$ as constant along the beam and considering only transversal loadings, the last equation can be reformulated as:

$$-Dw_{,xxxx}^{(0)} = -\bar{q}(x) - \bar{m}_{,x}(x) + \mu(x)\ddot{w}^{(0)} - m_2\ddot{w}_{,xx}^{(0)} \rightarrow$$

$$Dw_{,xxxx}^{(0)} + \mu\ddot{w}^{(0)} = \bar{q}(x) \qquad (8)$$

The modal shapes of the problem can be calculated, starting from the homogeneous equation associated to eq. (8), as a function of the beam's boundary conditions. The modal shapes can then be used to replace physical coordinates with modal coordinates in the D'Alembert, Hamilton, or Lagrange equations.

The discussion relative to continuous systems is beyond the scope of this thesis, an analogous procedure will be better detailed for the Finite Element Method (FEM). However, in paragraph 2.2.4 are reported the modally represented loads as a function of the number of retained modes ($n°_{RM}$) of a stuck beam, which will be treated as a continuous system.

2.2.2. The Beam finite element

In the beam equation (*8*), it is present up to the fourth derivative ($r = 4$) of the transversal displacement, which is the unknown term. The compatibility and compliance condition dictates that the shape functions must be internally continuous up to the $\mathrm{r}/2 - 1$ derivative of the differential equation's variables, this is necessary for the solution convergence at the finite elements increase. Furthermore, in the FEM, the single DOFs must satisfy the geometrical boundary conditions independently, differently from the method described for continuous systems or the Rayleigh-Ritz approach in which all the modal shapes/shape functions had to satisfy them independently.

For this reason, for each node of the beam element the DOFs that must be represented are $w(t)$ and $w_x(t)$. Being that each element is composed of 2 nodes, there are 4 total local DOFs for each beam element: 2 relative to the transversal displacement and 2 for the angular orientation. Typically, the chosen shape functions for the beam element are based upon the Hermitte cubical polynomials.

The 4 shape functions are reported in the equations below:

$$w^{(e)}\left(x^{(e)},t\right) \approx H_1^{(e)}\left(x^{(e)}\right)q_{w1}^{L(e)}(t) + L^{(e)}H_2^{(e)}\left(x^{(e)}\right)q_{\varphi 1}^{L(e)}(t) + H_3^{(e)}\left(x^{(e)}\right)q_{w2}^{L(e)}(t) + L^{(e)}H_4^{(e)}\left(x^{(e)}\right)q_{\varphi 2}^{L(e)}(t)$$

$$= \left[N_w^{(e)}(x^{(e)})\right]\left\{q_w^{L(e)}(t)\right\}$$

The terms $H_i^{(e)}$, are the Hermitte cubical polynomials:

$$\left.\begin{array}{l} H_1^{(e)}\left(x^{(e)}\right) = 2\xi^3 - 3\xi^2 + 1; \quad H_2^{(e)}\left(x^{(e)}\right) = \xi^3 - 2\xi^2 + \xi; \\ H_3^{(e)}\left(x^{(e)}\right) = -2\xi^3 + 3\xi^2; \quad H_4^{(e)}\left(x^{(e)}\right) = \xi^3 - \xi^2; \end{array}\right\}$$

Where $\xi = \frac{x^{(e)}}{L^{(e)}}$, $x^{(e)}$ is the local axial coordinate of the beam element and $L^{(e)}$ is the length of the element.

The shape functions are designed to assume the value '1' on their associated DOF and the value '0' relatively to their non-associated DOFs, as reported in Figure 2.15.

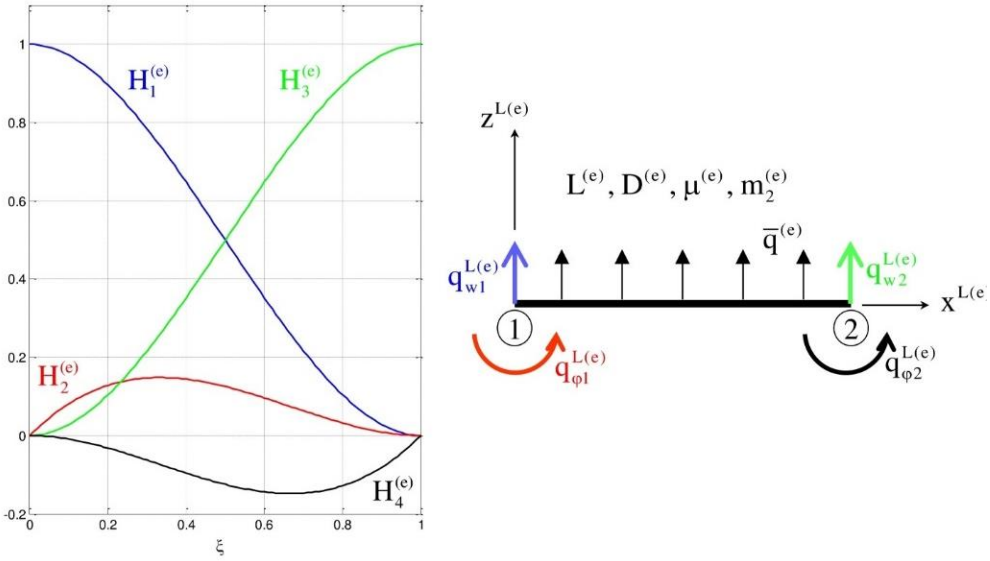

Figure 2.15: Shape functions for the beam element (Ref. [7]).

The defined transversal displacements of the beam finite element can be replaced in the D'Alembert equation to find the mass and the stiffness matrices of the element. Since the axial and transversal displacements are decoupled, the D'Alembert principle can be expressed as:

$$\delta E_p = \int_0^L \delta(-w_{,xx})^T D(x)(-w_{,xx})\,dx$$

$$\delta L_{in} = -\int_0^L \delta \begin{Bmatrix} w \\ -w_{,x} \end{Bmatrix}^T \begin{bmatrix} \mu(x) & 0 \\ 0 & m_2(x) \end{bmatrix} \begin{Bmatrix} \ddot{w} \\ -\ddot{w}_{,x} \end{Bmatrix} dx$$

$$\delta L_e = \int_0^L (\delta w)^T \bar{q}(x)\,dx$$

The equation obtained by using all the terms of the D'Alembert principle, for the local element (e), is:

$$\left[M_w^{(e)}\right]\left\{\ddot{q}_w^{L(e)}(t)\right\} + \left[K_w^{(e)}\right]\left\{q_w^{L(e)}(t)\right\} = \left\{F_w^{(e)}\right\}$$

Below are separately presented the formulations of the matrices $\left[M_w^{(e)}\right]$, $\left[K_w^{(e)}\right]$ and $\left\{F_w^{(e)}\right\}$ for the same hypothesis stated in paragraph 2.2.1 and in paragraph 2.2.3 will be presented the assembly of the global matrices.

The mass matrix for the local finite element 'beam' is:

$$\left[M_w^{(e)}\right] = \int_0^{L^{(e)}} \left(\left[N_w^{(e)}(x^{(e)})\right]^T \mu^{(e)}(x^{(e)}) \left[N_w^{(e)}(x^{(e)})\right] + \left[N_{w,x^{(e)}}^{(e)}(x^{(e)})\right]^T m_2^{(e)}(x^{(e)}) \left[N_{w,x^{(e)}}^{(e)}(x^{(e)})\right]\right) dx^{(e)}$$

$$= \mu^{(e)} \int_0^{L^{(e)}} \left(\left[N_w^{(e)}(x^{(e)})\right]^T \left[N_w^{(e)}(x^{(e)})\right]\right) dx^{(e)} + m_2^{(e)} \int_0^{L^{(e)}} \left(\left[N_{w,x^{(e)}}^{(e)}(x^{(e)})\right]^T \left[N_{w,x^{(e)}}^{(e)}(x^{(e)})\right]\right) dx^{(e)}$$

$$= \frac{\mu^{(e)} L^{(e)}}{420} \begin{bmatrix} 156 & 22L^{(e)} & 54 & -13L^{(e)} \\ 22L^{(e)} & 4(L^{(e)})^2 & 13L^{(e)} & -3(L^{(e)})^2 \\ 54 & 13L^{(e)} & 156 & -22L^{(e)} \\ -13L^{(e)} & -3(L^{(e)})^2 & -22L^{(e)} & 4(L^{(e)})^2 \end{bmatrix} + \frac{m_2^{(e)}}{210L^{(e)}} \begin{bmatrix} 252 & 21L^{(e)} & -252 & 21L^{(e)} \\ 21L^{(e)} & 28(L^{(e)})^2 & -21L^{(e)} & -7(L^{(e)})^2 \\ -252 & -21L^{(e)} & 252 & -21L^{(e)} \\ 21L^{(e)} & -7(L^{(e)})^2 & -21L^{(e)} & 28(L^{(e)})^2 \end{bmatrix}$$

In many commercial codes, the mass matrix is often implemented without accounting for the rotary inertia term (neglected term in the equation above).

The stiffness matrix for the local finite element 'beam' is:

$$\left[K_w^{(e)}\right] = \int_0^{L^{(e)}} \left[N^{(e)}_{w,x^{(e)}x^{(e)}}\left(x^{(e)}\right)\right]^T D^{(e)}\left(x^{(e)}\right)\left[N^{(e)}_{w,x^{(e)}x^{(e)}}\left(x^{(e)}\right)\right] dx^{(e)}$$

$$= D^{(e)} \int_0^{L^{(e)}} \left(\left[N^{(e)}_{w,x^{(e)}x^{(e)}}\left(x^{(e)}\right)\right]^T \left[N^{(e)}_{w,x^{(e)}x^{(e)}}\left(x^{(e)}\right)\right]\right) dx^{(e)}$$

$$= \frac{2D^{(e)}}{(L^{(e)})^3}\begin{bmatrix} 6 & 3L^{(e)} & -6 & 3L^{(e)} \\ 3L^{(e)} & 2\left(L^{(e)}\right)^2 & -3L^{(e)} & \left(L^{(e)}\right)^2 \\ -6 & -3L^{(e)} & 6 & -3L^{(e)} \\ 3L^{(e)} & \left(L^{(e)}\right)^2 & -3L^{(e)} & 2\left(L^{(e)}\right)^2 \end{bmatrix}$$

Finally, the nodal forces for the local finite element 'beam' can be expressed as:

$$\{F_w^{(e)}\} = \int_0^{L^{(e)}} \left[N_w^{(e)}\left(x^{(e)}\right)\right]^T \bar{q}^{(e)}\left(x^{(e)}\right) dx^{(e)}$$

$$= \bar{q}^{(e)} \int_0^{L^{(e)}} \left[N_w^{(e)}\left(x^{(e)}\right)\right]^T dx^{(e)}$$

$$= \frac{\bar{q}^{(e)}L^{(e)}}{12}\begin{Bmatrix} 6 \\ L^{(e)} \\ 6 \\ -L^{(e)} \end{Bmatrix}$$

Where $\bar{q}^{(e)}$ is assumed to be locally constant along the element (e).

2.2.3. Final N-DOF system

To effectively solve the discrete system as a whole, the global matrices must be accurately assembled. Each local DOF has a designated position within the global DOFs vector. To properly expand and sum the local mass and stiffness matrices, we must refer to their corresponding DOF indexes within the global vector. For the purposes of this thesis, elements with a different orientation from the system's global orientation will not be considered (no ramified structures).

The expansion and sum of each local matrix, for the defined hypothesis, can be summarized as follows:

$$\left[K_w^{(i)}\right] \cdot \left\{q_w^{L(i)}(t)\right\} = \begin{bmatrix} k_{11} & k_{12} & k_{13} & k_{14} \\ k_{21} & k_{22} & k_{23} & k_{24} \\ k_{31} & k_{32} & k_{33} & k_{34} \\ k_{41} & k_{42} & k_{43} & k_{44} \end{bmatrix}_{L(i)} \begin{Bmatrix} q_{w1}^{L(i)} \\ q_{\varphi 1}^{L(i)} \\ q_{w2}^{L(i)} \\ q_{\varphi 2}^{L(i)} \end{Bmatrix} \rightarrow$$

$$\rightarrow \left[K_w^{G(i)}\right]\{q_w^G(t)\} = \begin{bmatrix} 0 & & & & 0 \\ & \ddots & & & \\ & & k_{2i-1,2i-1} \; k_{2i-1,2i} \; k_{2i-1,2i+1} \; k_{2i-1,2i+2} & & \\ & & k_{2i,2i-1} \quad k_{2i,2i} \quad k_{2i,2i+1} \quad k_{2i,2i+2} & & \\ & & k_{2i+1,2i-1} \; k_{2i+1,2i} \; k_{2i+1,2i+1} \; k_{2i+1,2i+2} & & \\ & & k_{2i+2,2i-1} \; k_{2i+2,2i} \; k_{2i+1,2i+1} \; k_{2i+2,2i+2} & & \\ & & & \ddots & \\ 0 & & & & 0 \end{bmatrix} \begin{Bmatrix} q_{w1}^G \\ \vdots \\ q_{w(2i-1)}^G \\ q_{\varphi(2i)}^G \\ q_{w(2i+1)}^G \\ q_{\varphi(2i+2)}^G \\ \vdots \\ q_{\varphi(2N+2)}^G \end{Bmatrix}$$

Where:

$$\begin{bmatrix} k_{11} \; k_{12} \; k_{13} \; k_{14} \\ k_{21} \; k_{22} \; k_{23} \; k_{24} \\ k_{31} \; k_{32} \; k_{33} \; k_{34} \\ k_{41} \; k_{42} \; k_{43} \; k_{44} \end{bmatrix}_{L(i)} = \begin{bmatrix} k_{2i-1,2i-1} \; k_{2i-1,2i} \; k_{2i-1,2i+1} \; k_{2i-1,2i+2} \\ k_{2i,2i-1} \quad k_{2i,2i} \quad k_{2i,2i+1} \quad k_{2i,2i+2} \\ k_{2i+1,2i-1} \; k_{2i+1,2i} \; k_{2i+1,2i+1} \; k_{2i+1,2i+2} \\ k_{2i+2,2i-1} \; k_{2i+2,2i} \; k_{2i+1,2i+1} \; k_{2i+2,2i+2} \end{bmatrix}_{G(i)}$$

After their expansion, global force vector, global stiffness and global mass matrices can be assembled:

$$[K_w^G] = \sum_{i=1}^{N} \left[K_w^{G(i)}\right]; \quad [M_w^G] = \sum_{i=1}^{N} \left[M_w^{G(i)}\right]; \quad \{F_w^G(t)\} = \sum_{i=1}^{N} \left\{F_w^{G(i)}(t)\right\}$$

The final equation, using the global matrices found in precedence, is given by:

$$[M_w^G]\,\{\ddot{q}_w^G(t)\} + [K_w^G]\{q_w^G(t)\} = \{F_w^G(t)\}$$

The matrices and vectors of the previous equation must be split into the components associated with their free and constrained DOFs, as follows:

$$\begin{bmatrix} M_{FF} & M_{FV} \\ M_{VF} & M_{VV} \end{bmatrix} \begin{Bmatrix} \ddot{q}_F \\ \ddot{q}_V = 0 \end{Bmatrix} + \begin{bmatrix} K_{FF} & K_{FV} \\ K_{VF} & K_{VV} \end{bmatrix} \begin{Bmatrix} q_F \\ q_V = 0 \end{Bmatrix} = \begin{Bmatrix} F_F \\ F_V \end{Bmatrix} \rightarrow$$

$$[\boldsymbol{M_{FF}}]\{\ddot{\boldsymbol{q}}_{\boldsymbol{F}}\} + [\boldsymbol{K_{FF}}]\{\boldsymbol{q_F}\} = \{\boldsymbol{F_F}\}$$

The preceding equation is now suitable for further implementation, mirroring the approach outlined in chapter 1, given that it represents an NDOF system as well. The methods MD, MT, and MA can be seamlessly applied to the discretized beam model, exhibiting practically no substantial difference from their first application shown in paragraph 2.1.

2.2.4. Modal representation of spatial loadings

The convergence of the modally represented load to the effectively applied load is affected by various factors, such as the complexity of the applied load, the number of retained modes, and the load values near the constraints. Using a residual vector solution method instead of the Mode-Displacement method is recommended to determine the transversal displacements accurately. One of the main differences between the continuous and the discrete systems is that the FEM model can always match the discretized applied forces using all the existing modal shapes (which exist in finite numbers and are purely calculated considering the free DOFs), so methods like Modal Truncation Augmentation (MT) and Mode Acceleration (MA) are often convenient and not strictly necessary. However, for large models, the full MD method could be excessively expensive in computational terms.

To find the modally represented and non-represented loads were calculated n modal shapes and then, they were discretized along the x-axis of the beam. To calculate the modally represented and non-represented portions of the applied spatial loads were used the formulations reported below:

$$R_{\boldsymbol{s},discr}(x_{discr}) = \phi_{discr}(x_{discr}) \int_0^L \left(\phi_{discr}^T(x_{discr}) \cdot R_{discr}(x_{discr})\right) dx_{discr}$$

$$R_{\boldsymbol{t},discr}(x_{discr}) = R_{discr}(x_{discr}) - R_{\boldsymbol{s},discr}(x_{discr})$$

Where $\phi_{discr}^T(x_{discr})$ contains the n modal shapes, numerically discretized along the beam's axis.

Generally, if R_s can converge to R, then at higher n values it would be almost equal to R and the residual non-represented load R_t would tend to 0, as shown for the first load reported in Figures 2.16-2.19. Otherwise, if n is kept finite and if the applied load is not a linear combination of any set of loadings associated to the retained modal shapes, R_t will always have at least one value different from 0.
For a system discretized with FEM, unlike the presented case, only the non-constrained DOFs are considered, and the discretized applied loads can always be fully represented. Therefore, the discretized spatial forces applied to the free DOFs are always a linear combination of the forces associated to the finite modal shapes, at most if all of them are included

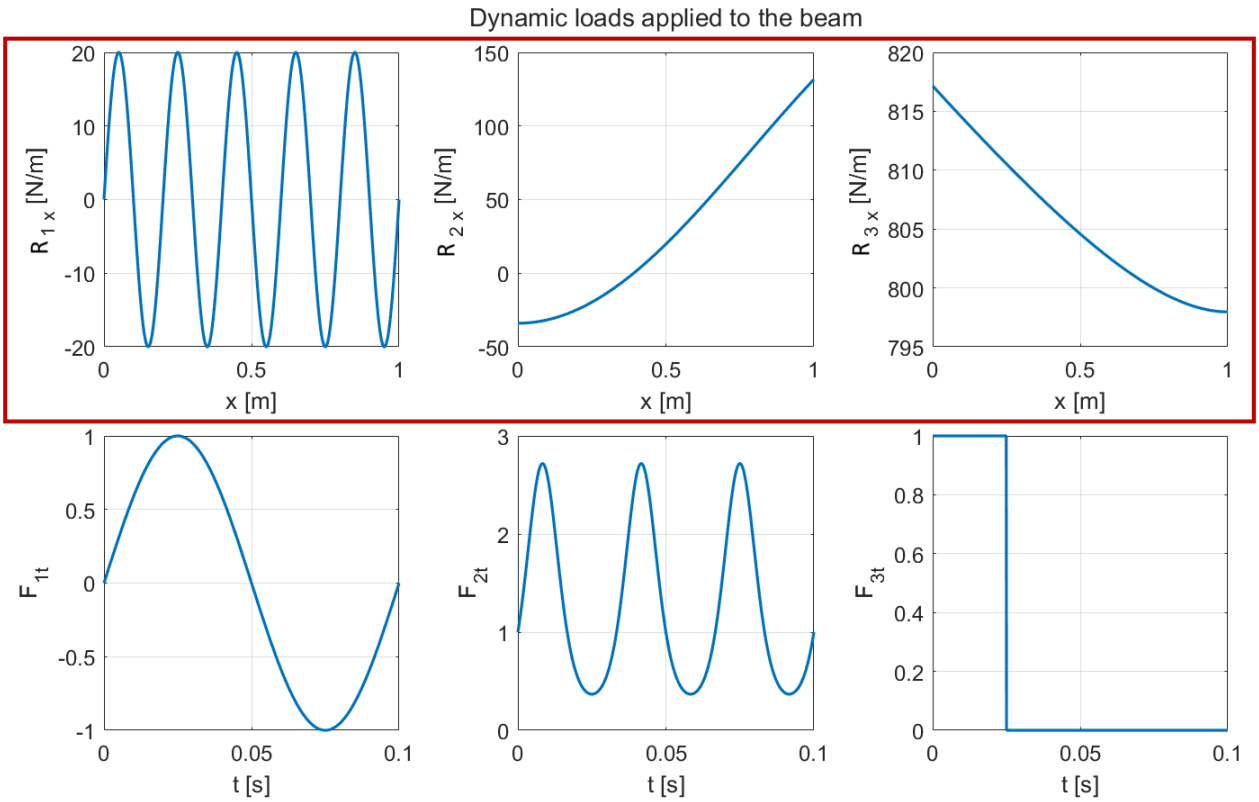

Figure 2.16: Spatial and temporal components of the dynamic loads applied to the beam.

This section focuses on the spatial components of the loads (boxed in red).

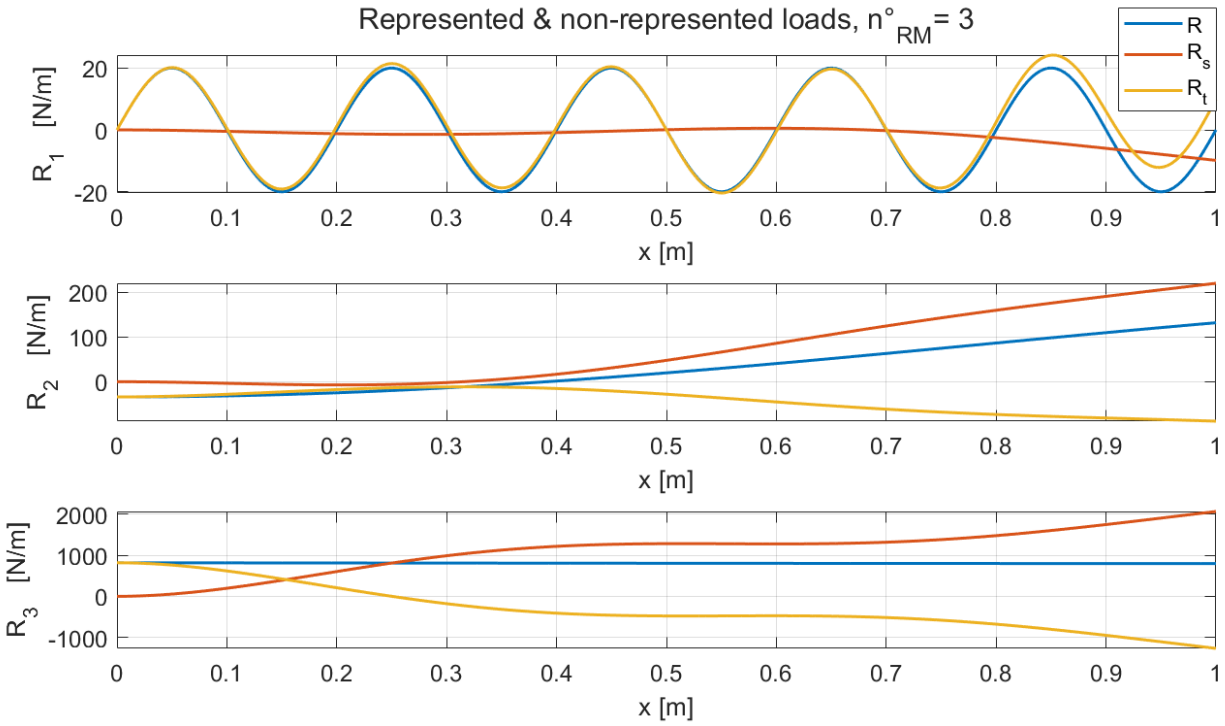

Figure 2.17: Loads (R), modally represented loads (R_s) and residual loads (R_t) for 3 retained modes.

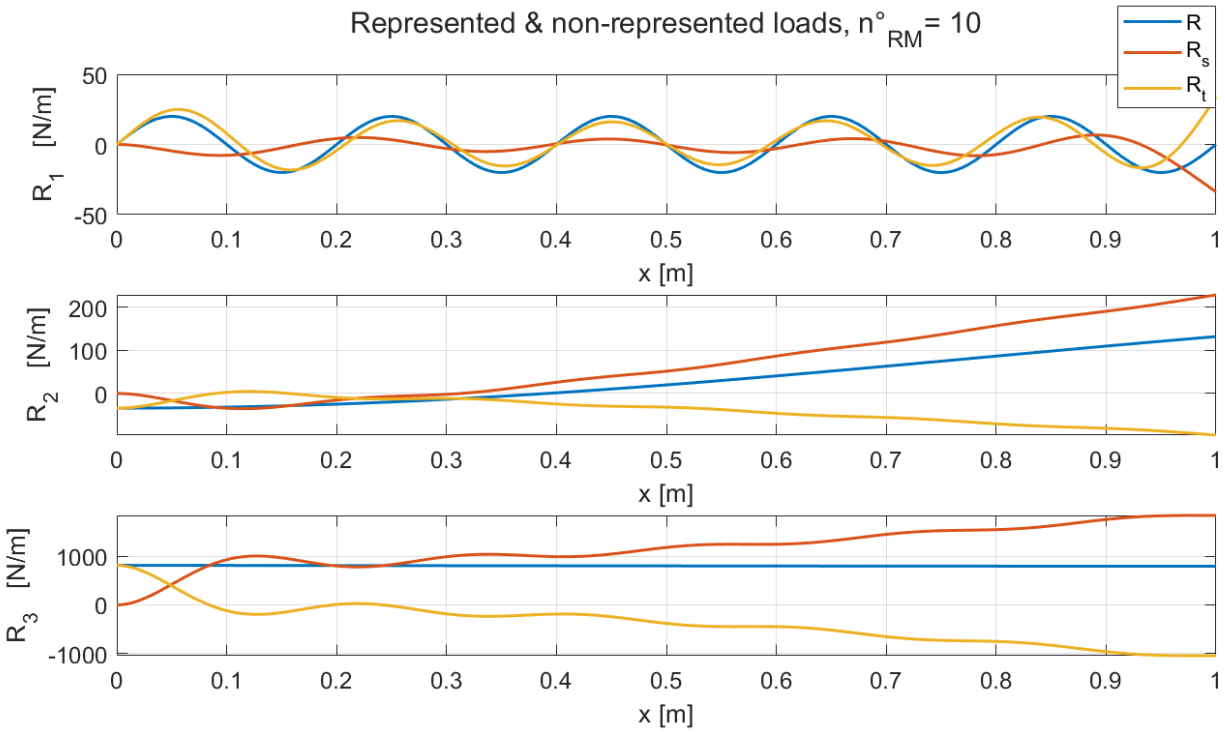

Figure 2.18: Loads (R), modally represented loads (R_s) and residual loads (R_t) for 10 retained modes.

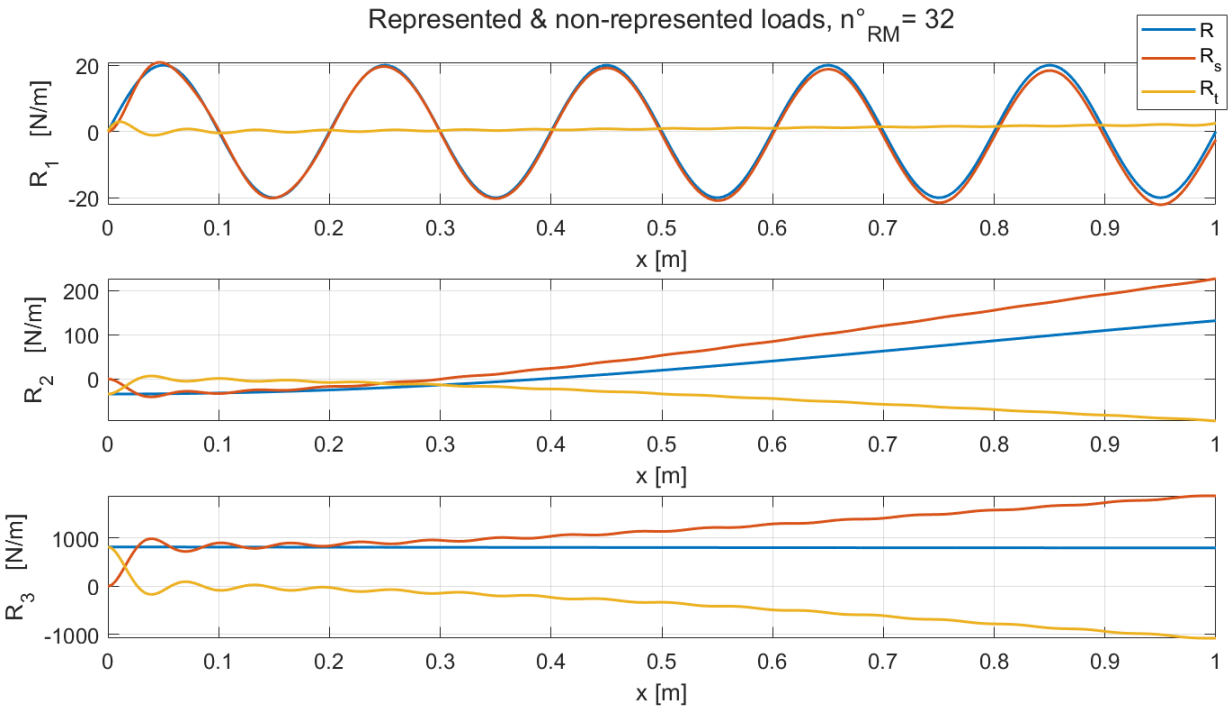

Figure 2.19: Loads (R), modally represented loads (R_s) and residual loads (R_t) for 32 retained modes. Here $\{R_1\}$ is well represented by the retained modal shapes and $\{R_t\}_1$ tends to $\{0\}$.

2.3. MD, MT, and MA methods applied to the beam finite element model

2.3.1. Problem description

The analysed beam is stuck at its left side; the geometric parameters of the model and its mechanical properties are:

$$nodes\ n° = 11;\ retained\ modal\ shapes = variable;\ length = 1m;\ height = 0.01m;\ base = 0.01m;$$

$$E = 210 \cdot 10^9\ Pa;\ \rho = 7900\ kg/m^3;\ \xi_i = 0.2$$

3 cases of single dynamic loads applied to the beam were considered, in addition, different frequencies (**3/30/100 Hz**) were used for the time components of the loads, which consist of a single sinusoidal function as reported in paragraph 2.3.2.

The used spatial forces are:

- A concentrated force applied at the tip of the beam. (Figure 2.20a)
- A constant load distributed along the length of the beam. (Figure 2.20b)
- A 'triangular' load distributed along the length of the beam. (Figure 2.20c)

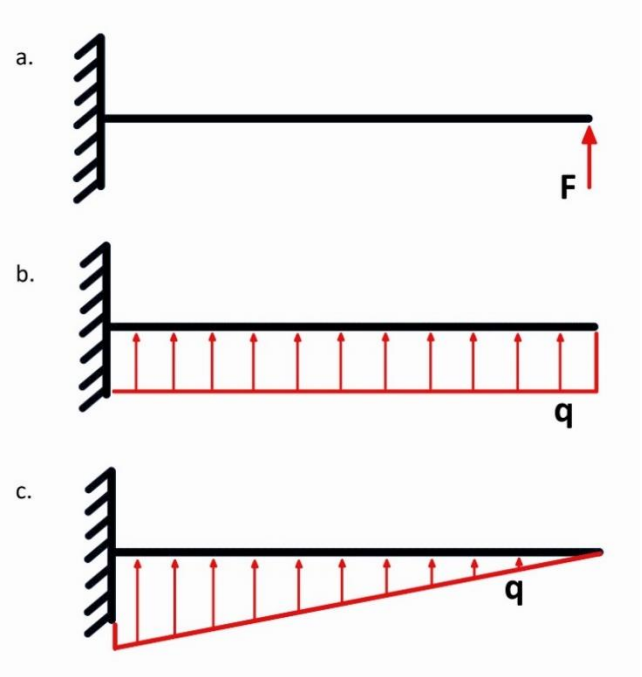

Figure 2.20: Defined spatial forces/loads: a) Concentrated force; b) Constant distributed load; c) triangular distributed load.

The number of retained modes varies according to the natural frequencies of the discretized beam system considered. In the proposed examples, are retained all the modes having a frequency inferior to the load's frequency. The natural frequencies obtained for the beam finite element model are approximately:

$$\boldsymbol{f_{N,1} = 8.33Hz;\ f_{N,2} = 52.20Hz;\ f_{N,3} = 146.18Hz;}$$

2.3.2. Concentrated force results

For the concentrated force, the component of the discretized force is 1 on the last DOF concerning the transversal displacement:

$$F_x = \{0,0,\dots,1,0\} \tag{9}$$

The temporal components of the applied dynamic force are in order:

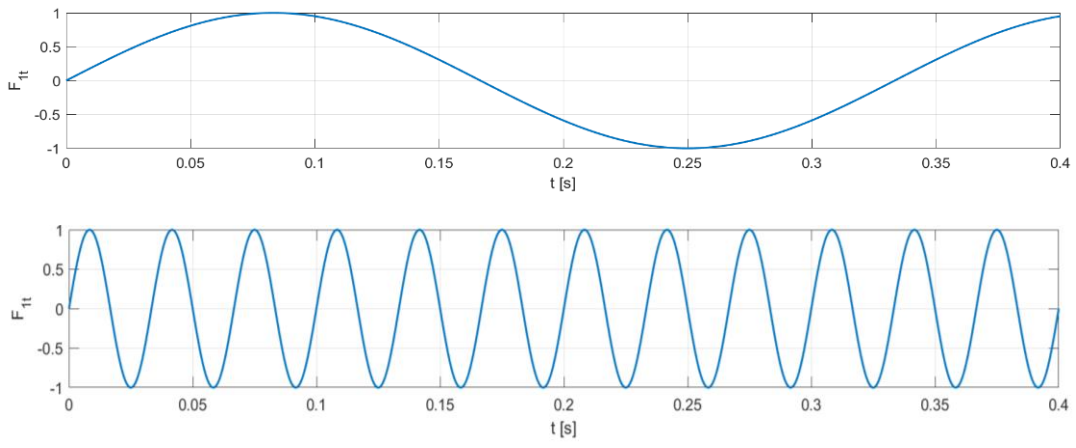

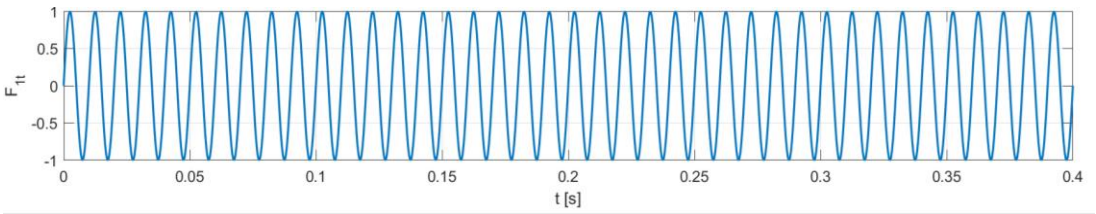

Figure 2.21: Temporal components of the force oscillating at 3 Hz, 30 Hz, and 100 Hz, respectively.

As said before, for the first two temporal components of the force the number of retained modes ($n°_{RM}$) is 1, while, for the last one $n°_{RM} = 2$.

The displacements obtained for the specified frequencies and the concentrated force are reported below:

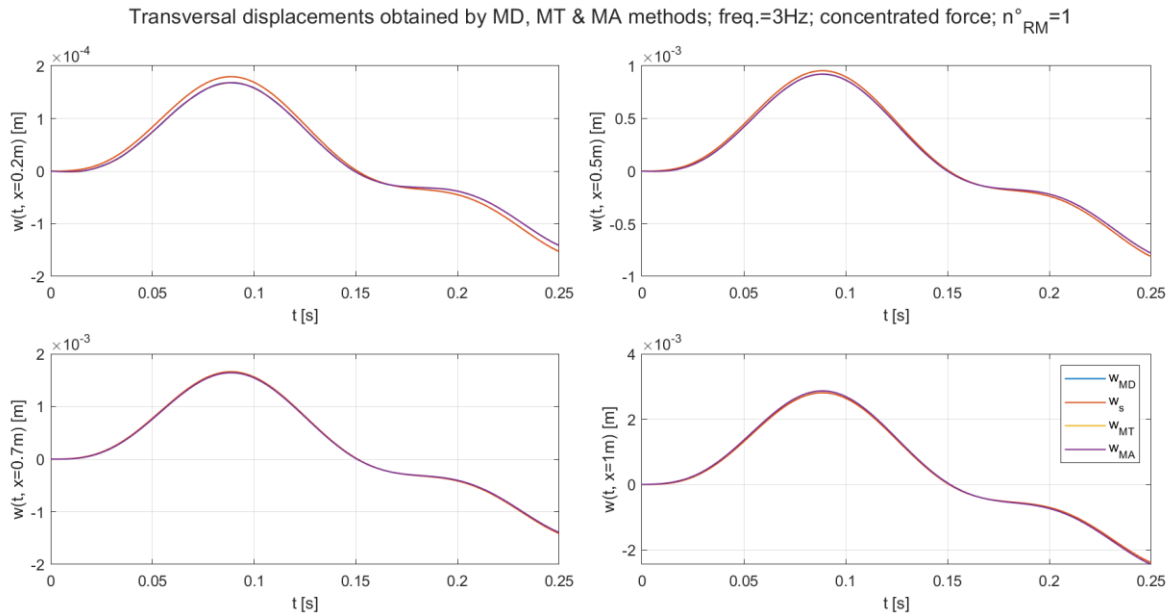

*Figure 2.22: Displacements at different distances from the beam's constraint ($x = 0\ m$) for the **concentrated force** oscillating at **3 Hz**.*

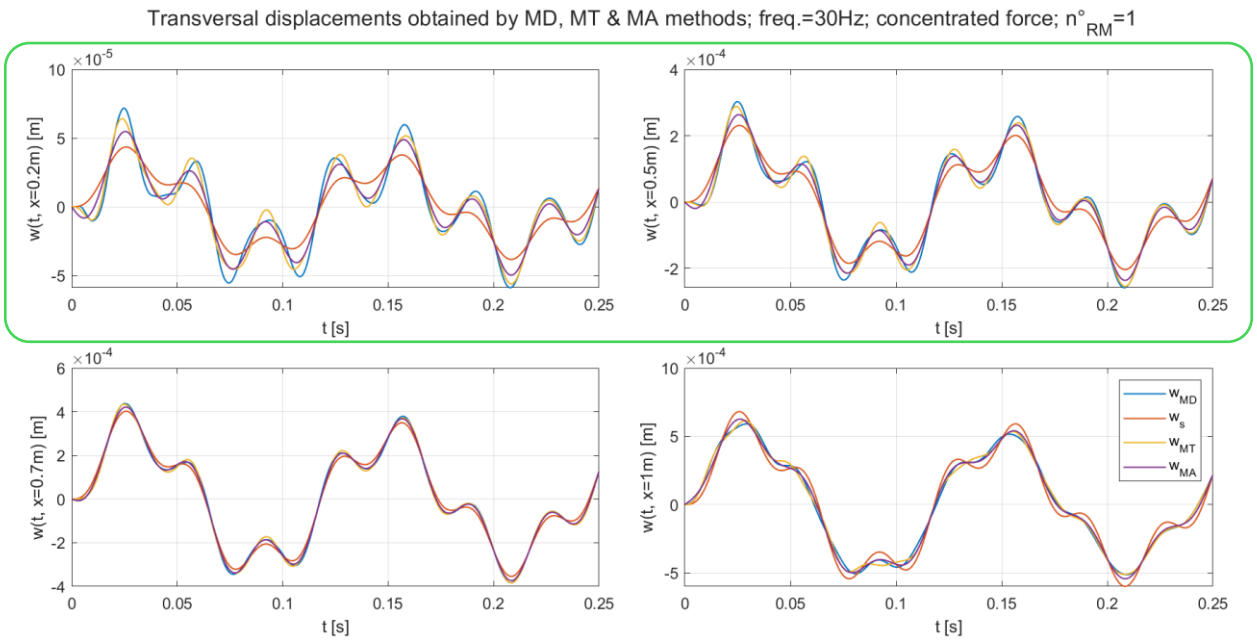

*Figure 2.23: Displacements at different distances from the beam's constraint ($x = 0\ m$) for the **concentrated force** oscillating at **30 Hz**.*

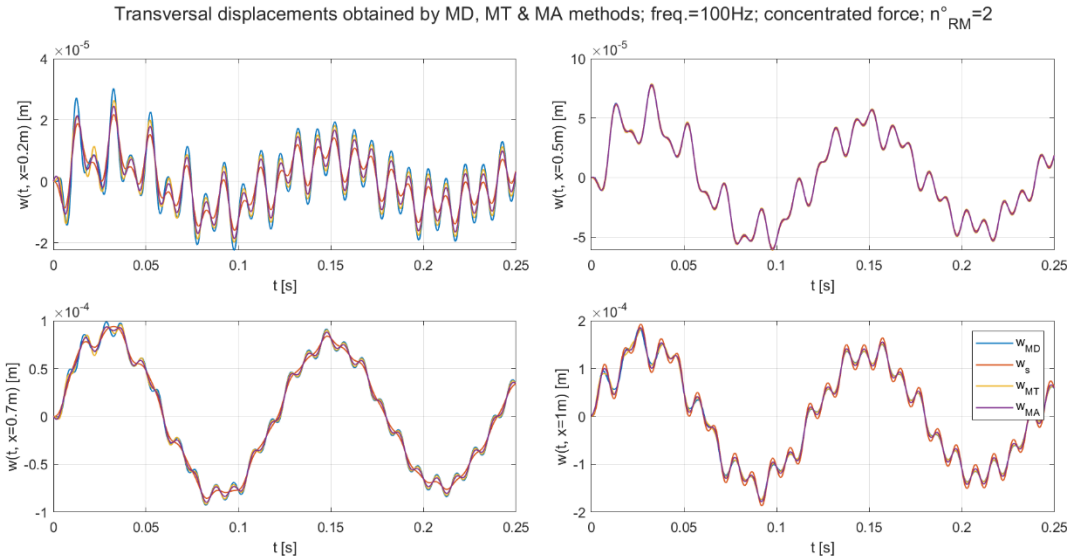

*Figure 2.24: Displacements at different distances from the beam's constraint ($x = 0\ m$) for the **concentrated force** oscillating at **100 Hz**.*

2.3.3. Constant load results

Similarly to the case presented in the paragraph 2.3.2:

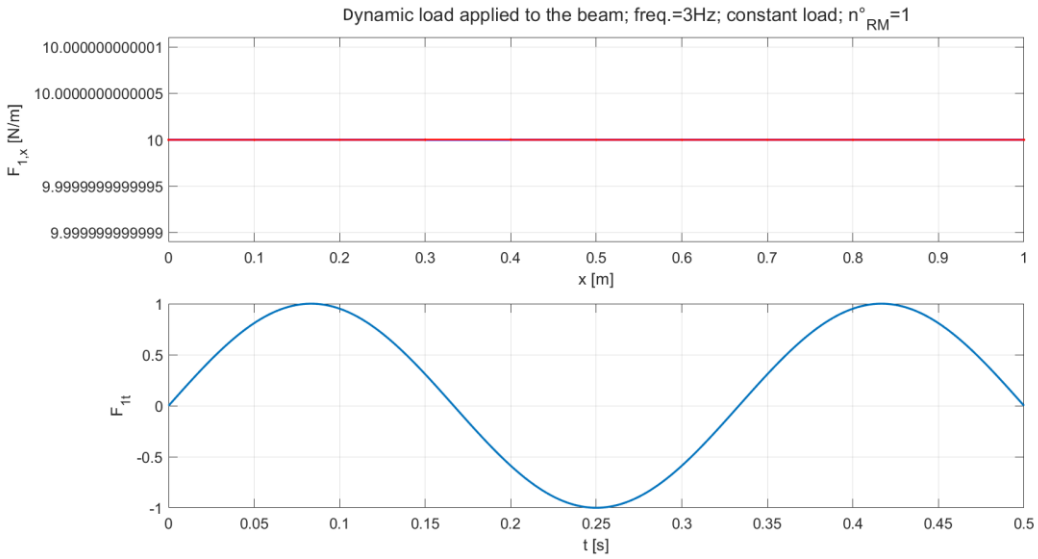

The other analysed temporal components of the force oscillate at 30 and 100 Hz, respectively:

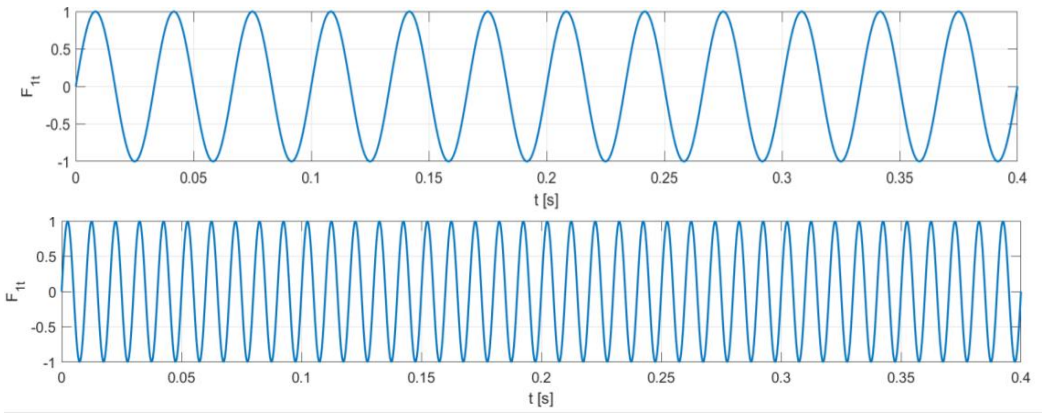

Figure 2.25: Constant spatial load and temporal components associated.

The results obtained for the constant load oscillating at the specified frequencies are reported below:

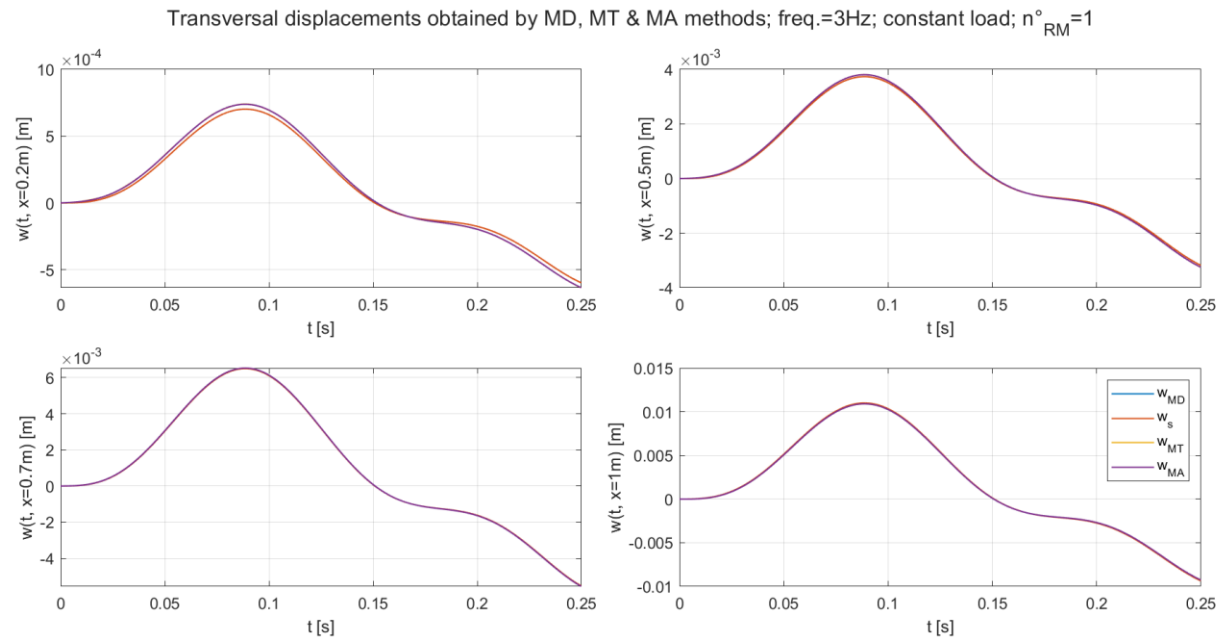

*Figure 2.26: Displacements at different distances from the beam's constraint ($x = 0\ m$) for the **constant load** oscillating at **3 Hz**.*

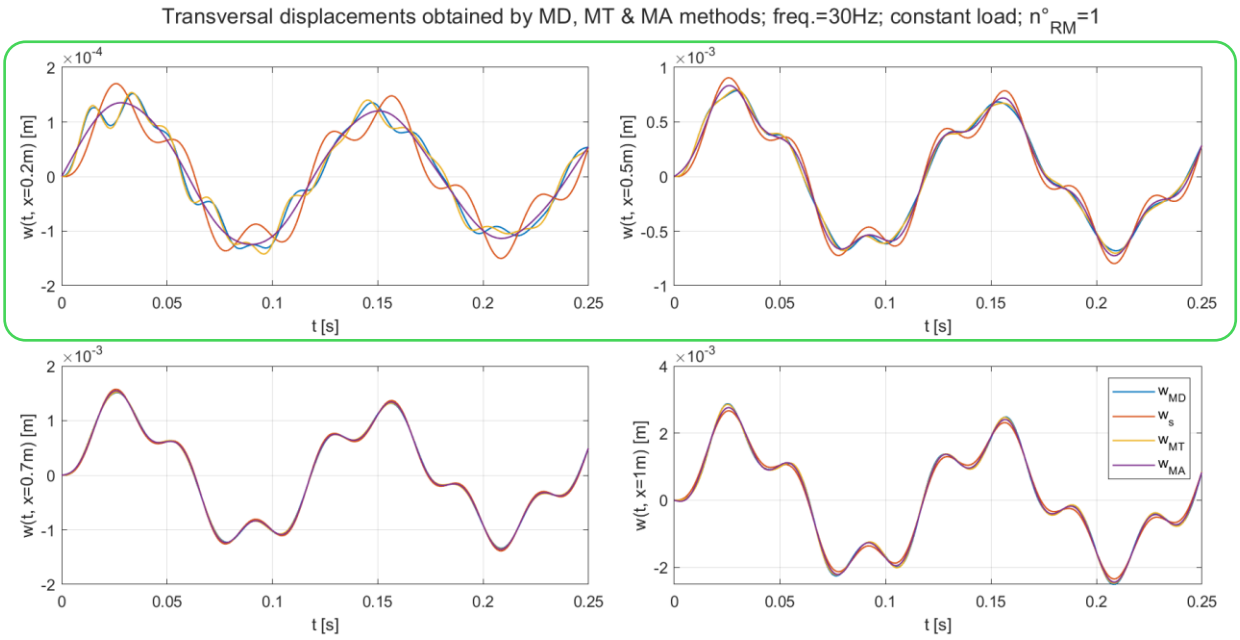

*Figure 2.27: Displacements at different distances from the beam's constraint ($x = 0\ m$) for the **constant load** oscillating at **30 Hz**.*

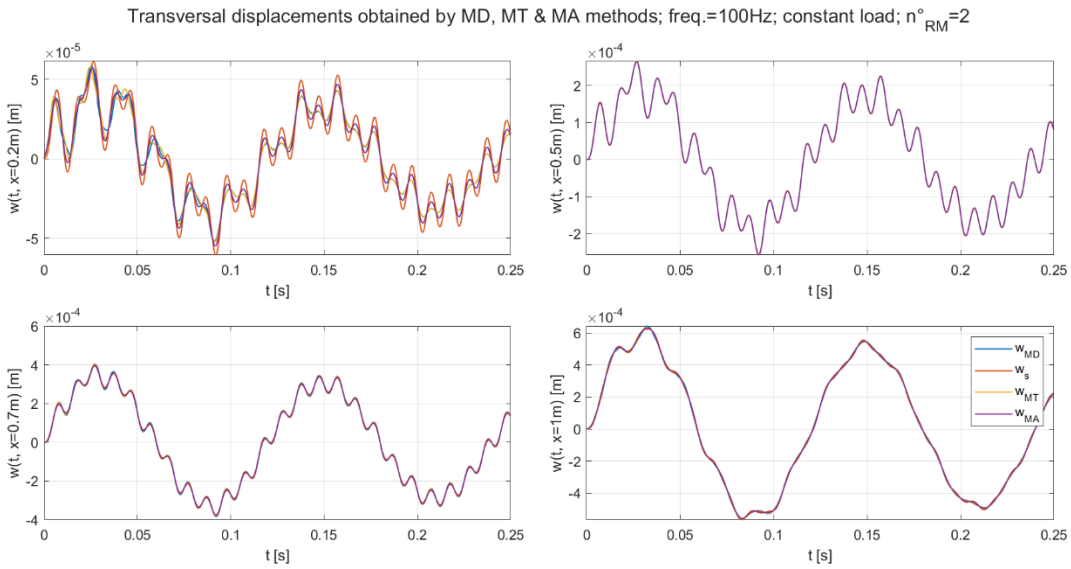

*Figure 2.28: Displacements at different distances from the beam's constraint ($x = 0\ m$) for the **constant load** oscillating at **100 Hz**.*

2.3.4. Triangular load results

Similarly to the case reported in paragraph 2.3.2:

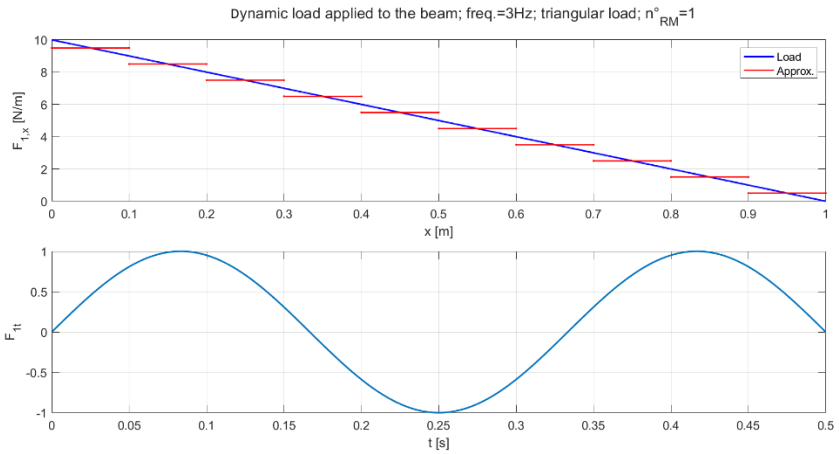

The other analysed temporal components of the load are characterized by frequencies of 30 and 100 Hz, respectively:

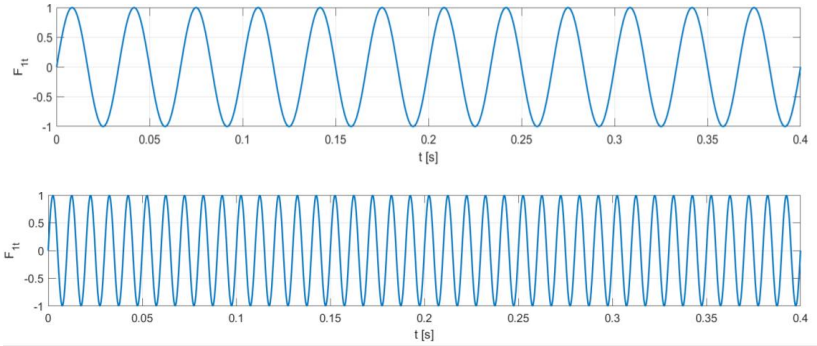

Figure 2.29: Triangular spatial load and temporal components associated.

The results obtained for the triangular load, at the specified frequencies, are reported below:

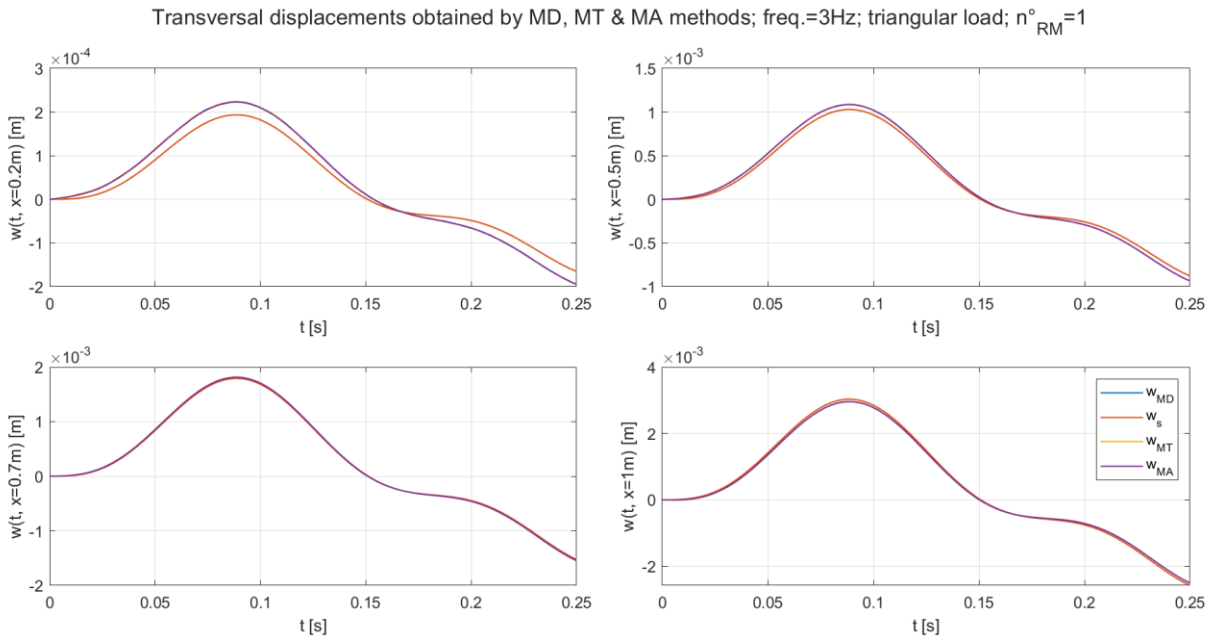

*Figure 2.30: Displacements at different distances from the beam's constraint ($x = 0\ m$) for the **triangular load** oscillating at **3 Hz**.*

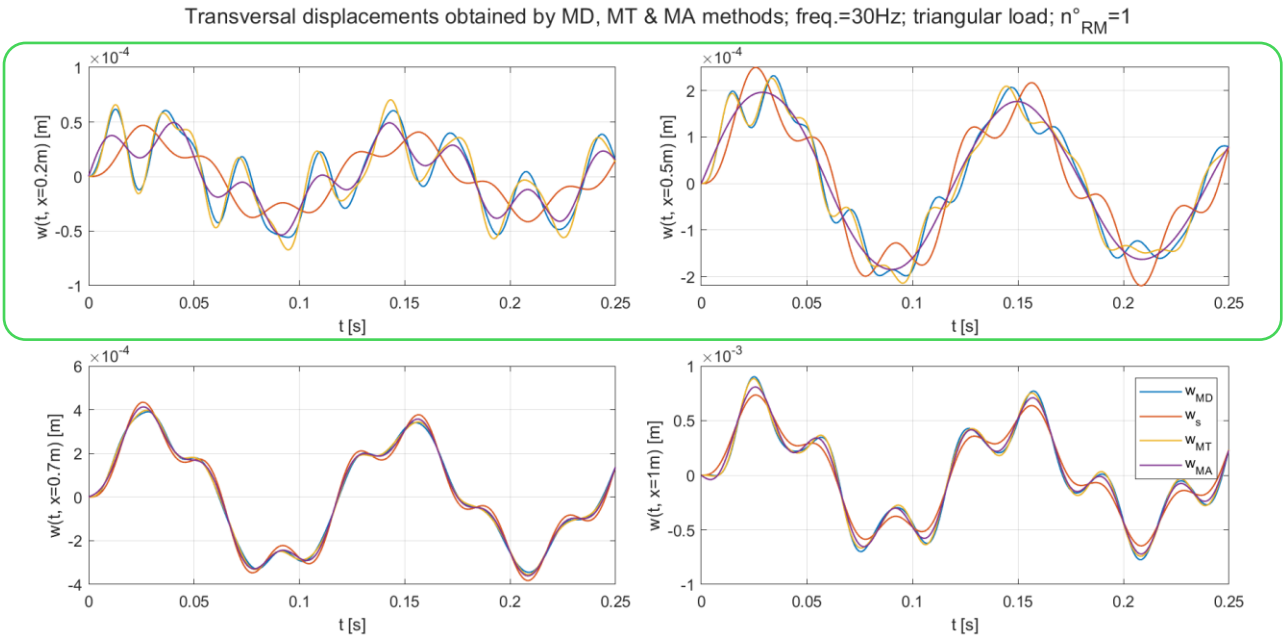

*Figure 2.31: Displacements at different distances from the beam's constraint ($x = 0\ m$) for the **triangular load** oscillating at **30 Hz**.*

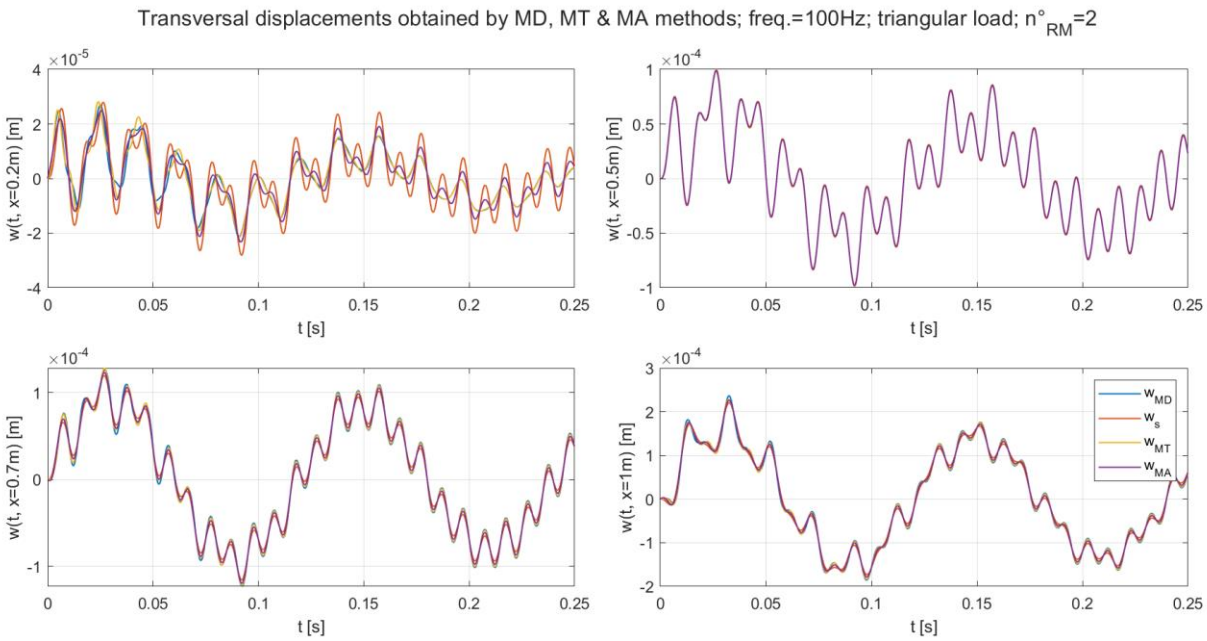

*Figure 2.32: Displacements at different distances from the beam's constraint ($x = 0\ m$) for the **triangular load** oscillating at **100 Hz**.*

The results show that the MT method generally outperforms the MA method in almost every scenario, better converging to the solution obtained using the MD method. The approach of only retaining some modes without adding any residual vectors (w_s) tends to perform the worst.

This could explain why commercial software such as MSC Nastran had started replacing the MA method with the more accurate MT method [*8*]. In particular, focusing on the figures relative to the load's frequency of 30 Hz, near the constraint (the results in question are boxed), is easy to further compare the MT and MA methods: the former seems to be closer to the MD solution, except for Figure 2.23 where it cannot be determined uniquely which method performs better.

2.3.5. Considering multiple applied forces

In considering multiple applied loads on the system described in paragraph 2.3.1, the MT vectors (matrix $[P]$) must be calculated as follows:

$$[K][\{X_1\} \dots \{X_i\} \dots \{X_N\}] = \left[\{R_{t,1}\} \dots \{R_{t,i}\} \dots \{R_{t,N}\}\right] \rightarrow [D_K] = [X]^T[K][X];\ [D_M] = [X]^T[M][X]$$

Therefore:

$$[D_K][Q] = [D_M][Q]\{\bar{\omega}_P^2\} \rightarrow [P] = [X][Q] \rightarrow \left[\tilde{\phi}\right] = \left[[\phi]_R\ [P]\right]$$

However, this approach is less suitable for the direct comparison of the methods, contrarily to applying only a single load, because it is hard to define which variations are related to which applied loads.

However, the results show again the MT method's superiority over the MA method. For instance, Figure 2.35 shows that the MT displacements obtained near the constraint at $n°_{RM} = 1$ better represent those

obtained by the MD solution, differently from the MA solution, which performs worse. However, the MA method seems capable of improving the solution offered by only considering the retained modes (solution w_s). It is worth noting that the MT method, in this case, is 4 times more expensive than the MA method.

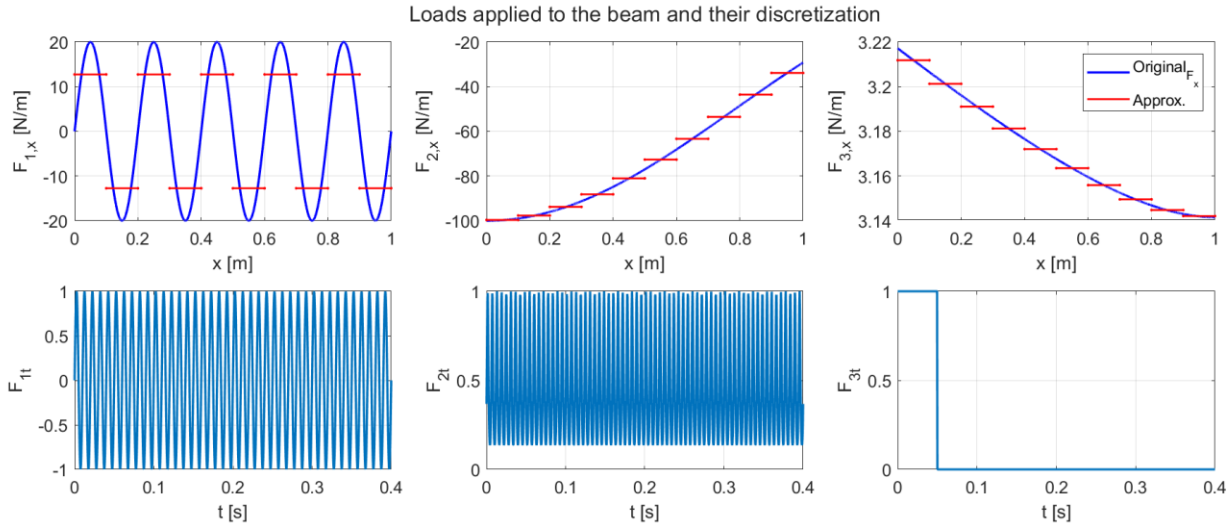

Figure 2.33: Representation of 3 dynamic forces applied simultaneously to the beam.

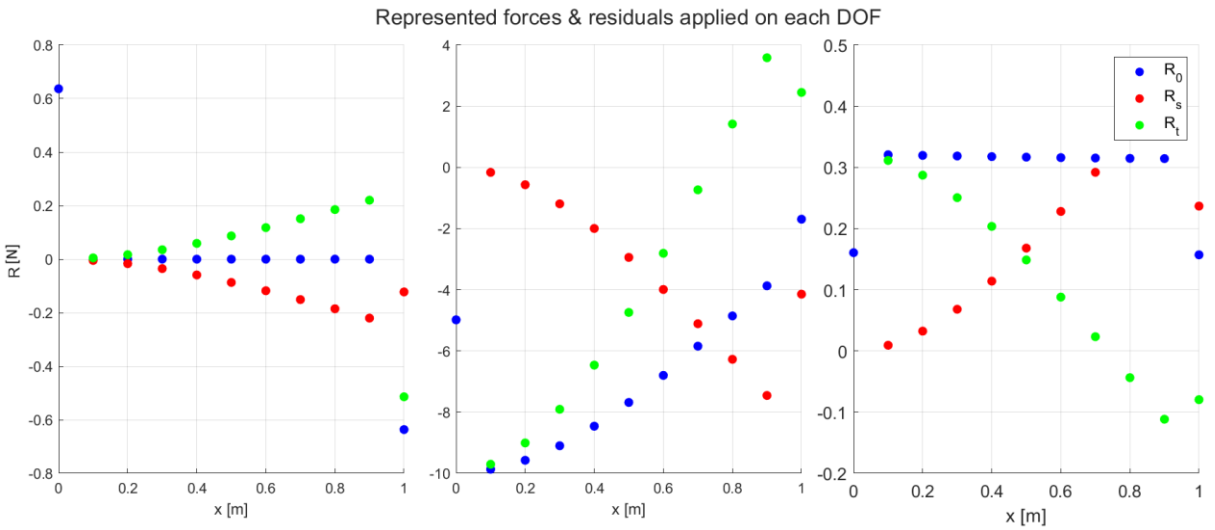

Figure 2.34: Representation of the discretized forces applied to each DOF (R_0), the modally represented forces (R_s) and the residual forces (R_t). The force applied on the constrained DOF ($x = 0\ m$) is not considered in the modal representation of the forces as stated at the end of paragraph 2.2.3.

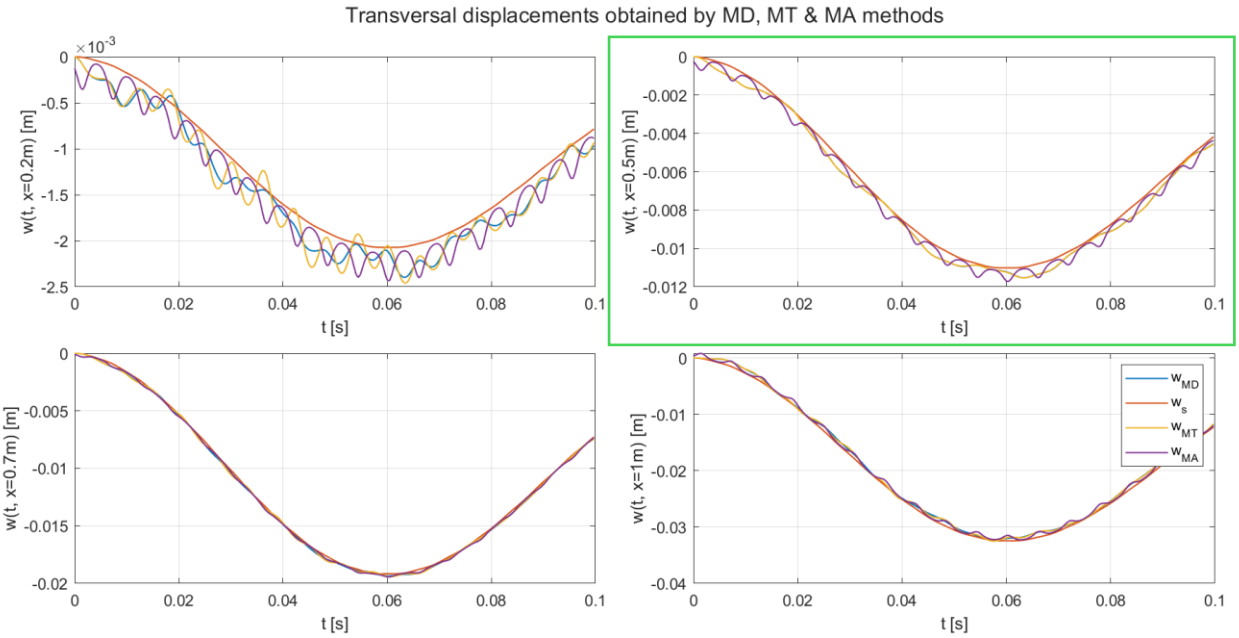

Figure 2.35: Displacements at different distances from the beam's constraint for 3 dynamic loads applied to the beam simultaneously. In the boxed figure the displacements obtained by MD and MT methods completely overlap.

2.4. Performance coefficients and results enhancement

2.4.1. Performance coefficients

At this point, it was worth finding a way to compare the methods analytically for a single applied load/force. The solution adopted consists of subtracting from the MD solution the MA and MT solutions to compare the method's differences from the complete solution. All the solutions were matrices of 22x1000, where the former is the number of global DOFs and the latter is the number of time steps.

The comparisons were performed only on the transversal displacements. Once obtained the difference results, which, were matrices of 11x1000, were calculated:

- The maximum displacement difference, normalized with $w_{MD,max}$ ($\boldsymbol{c_{MAX}}$).
- The maximum mean timed value on all the considered DOFs, normalized with $w_{MD,max}$.
- The global mean value, normalized with $w_{MD,max}$ ($\boldsymbol{c_{Mean}}$).
- Norm 1, not normalized, but the value was averaged on all the load's oscillations ($\boldsymbol{c_{Norm\ 1}}$).
- Norm ∞, not normalized, but the value was averaged on all the load's oscillations ($\boldsymbol{c_{Norm\ \infty}}$).

The overall framework was applied to each single spatial force/load shown in Figure 2.20 at several frequencies of the forces and loads' temporal components. The chosen analysis frequency range was: $f = 1 - 300\ Hz$. The coefficients described were applied after considering the absolute value of the overall transversal displacement differences. In the next paragraph are reported all the obtained results except for

the second coefficient introduced in the list above (*maximum mean timed value*), which was not reported as would not give any additional insight into the methods analysed.

2.4.2. Analytical results

In this paragraph are presented the performances of the methods analysed. The red vertical lines in each figure represent the first 4 modal frequencies of the beam in the range 0-300 Hz.

The used approach will be named '**Approach 0**' in further sections. It consists of retaining 1 mode until the dynamic load's frequency reaches the second modal shape, then, the approach retains 2 modes until the load's frequency reaches again the third, and so on. In other words, are retained all the modes having a frequency inferior to the one associated with the temporal component of the load/force.

From Figures 2.36-2.47 it is clear that after adding an ulterior mode the solutions improve instantly in the frequency domain since the methods have all the modal instruments to correctly represent the solution at the soliciting frequency, which is close to the just retained mode. However, as the force's frequency approaches the next modal frequency, the retained modes are no longer sufficient to well describe the solution, being necessary to include the next mode to represent it correctly. Different and more efficient approaches will be characterized in the next paragraphs since the retention of the next mode could be anticipated just when the error starts to increase with an exponential-like behaviour.

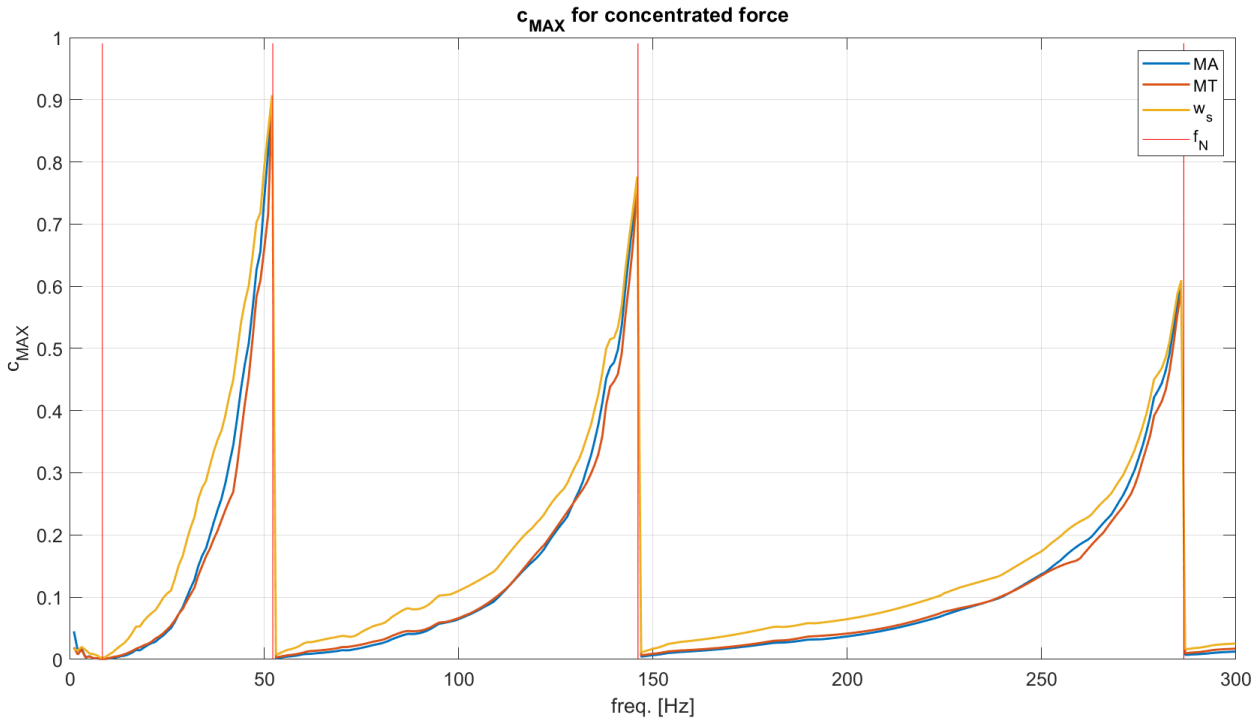

*Figure 2.36: c_{MAX} as a function of force's frequency for the **concentrated force**.*

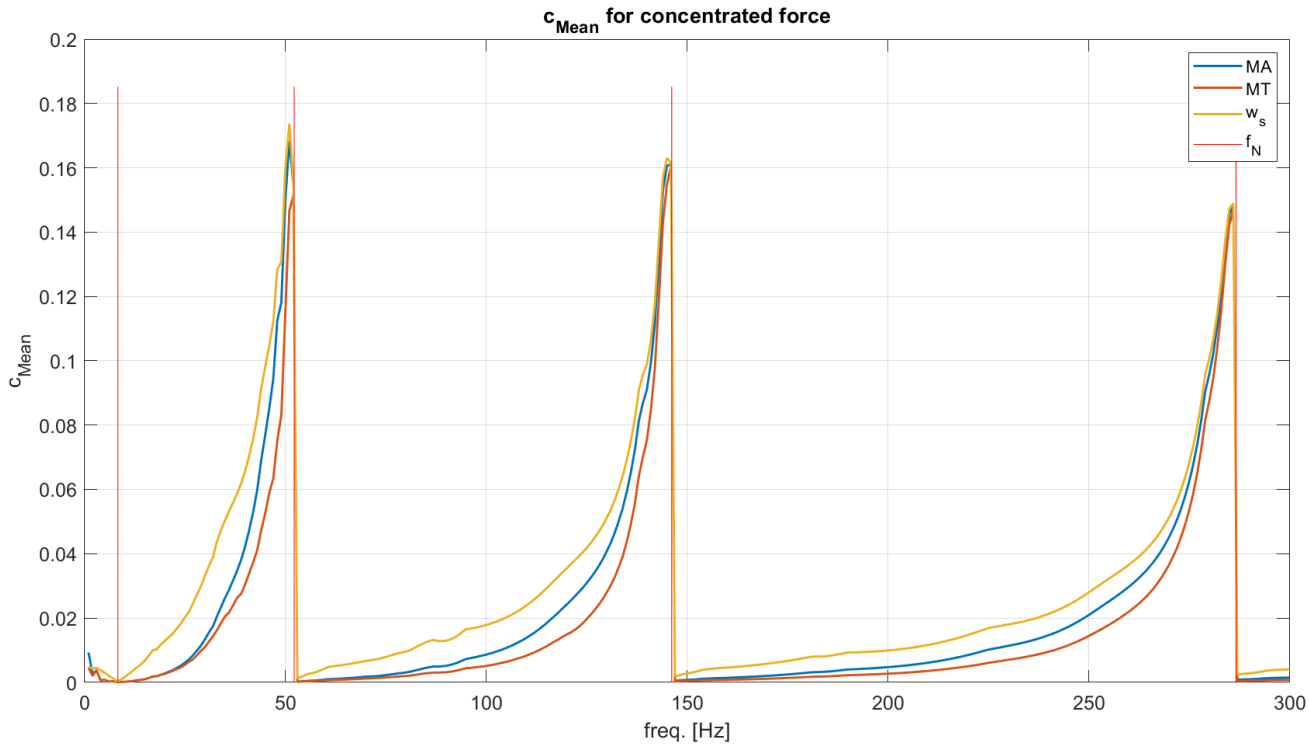

*Figure 2.37: c_{Mean} as a function of force's frequency for the **concentrated force**.*

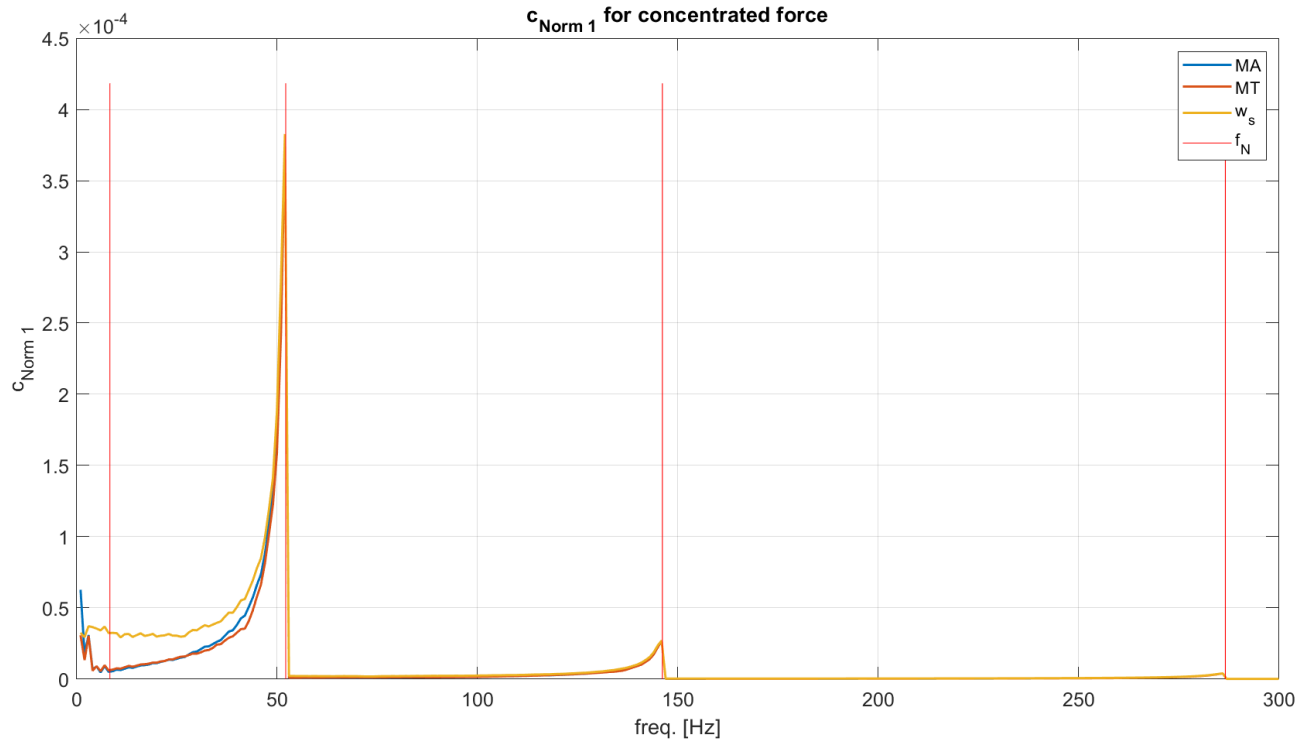

*Figure 2.38: $c_{Norm\ 1}$ as a function of force's frequency for the **concentrated force**.*

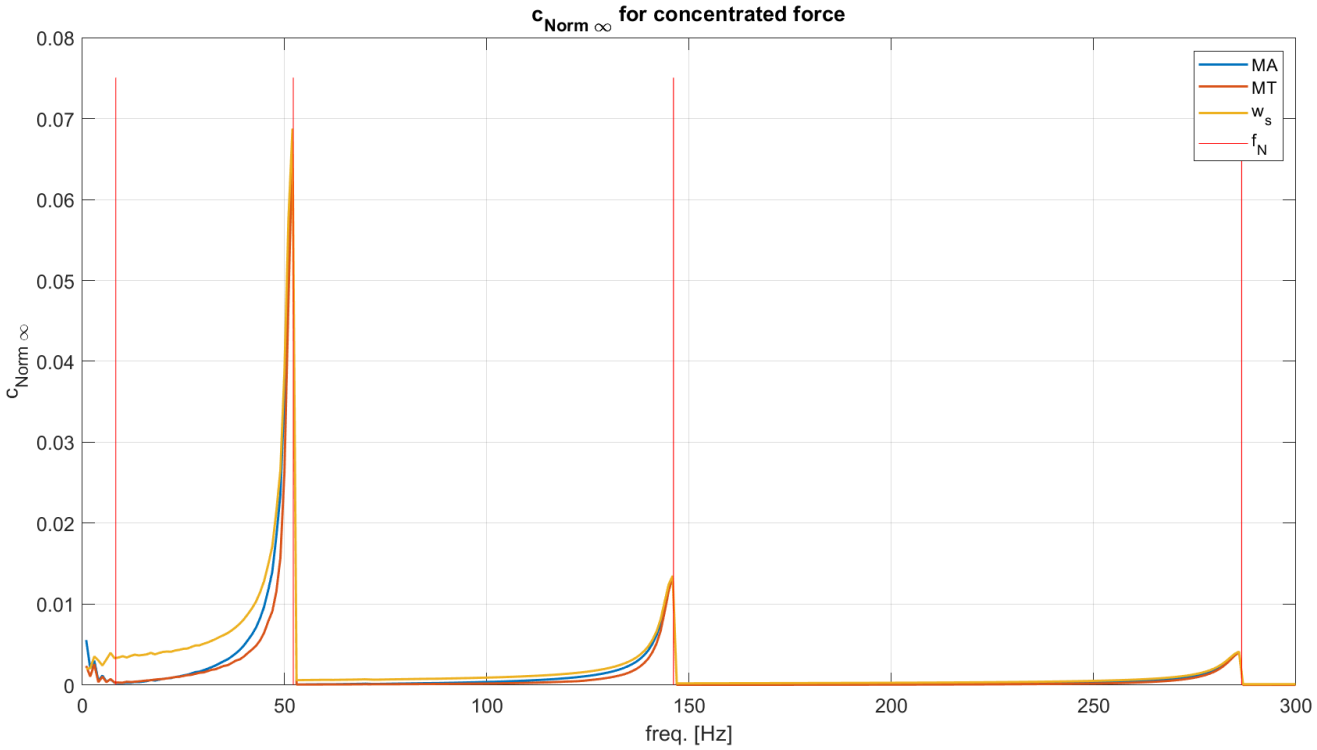

*Figures 2.39: $c_{Norm\ \infty}$ as a function of force's frequency for the **concentrated force**.*

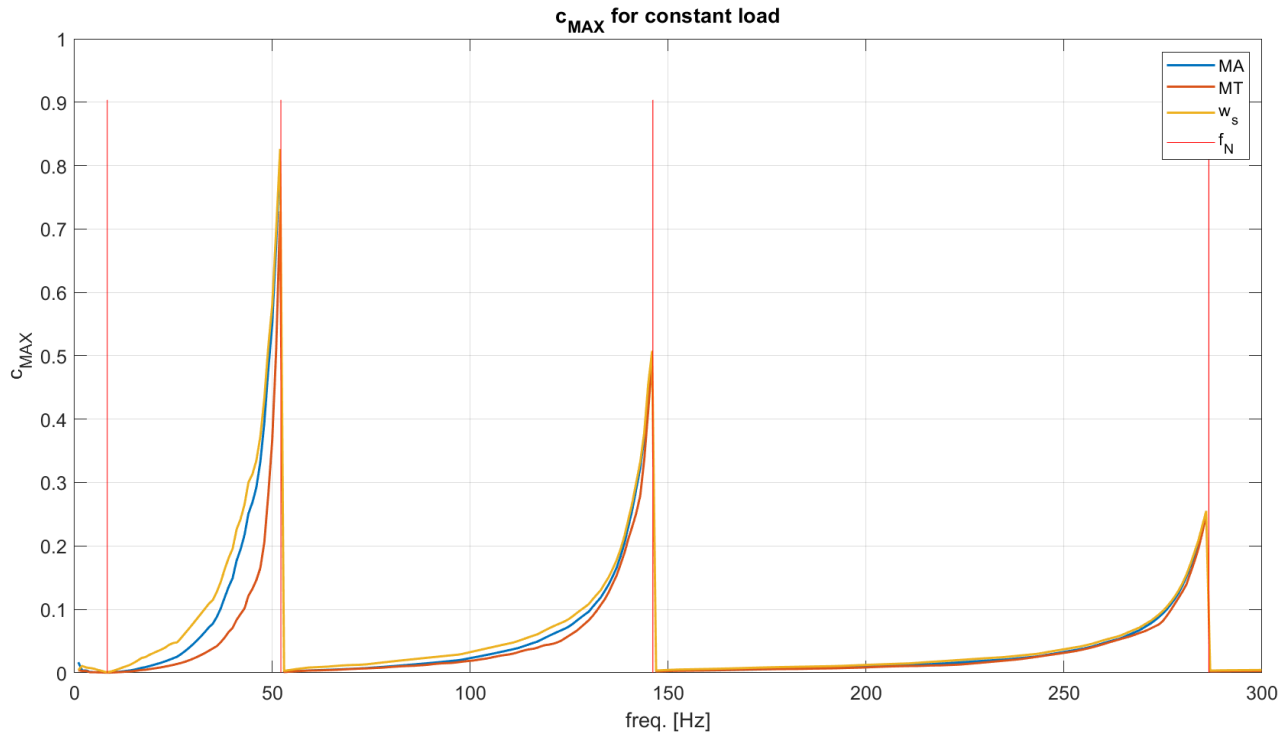

*Figure 2.40: c_{MAX} as a function of load's frequency for the **constant load**.*

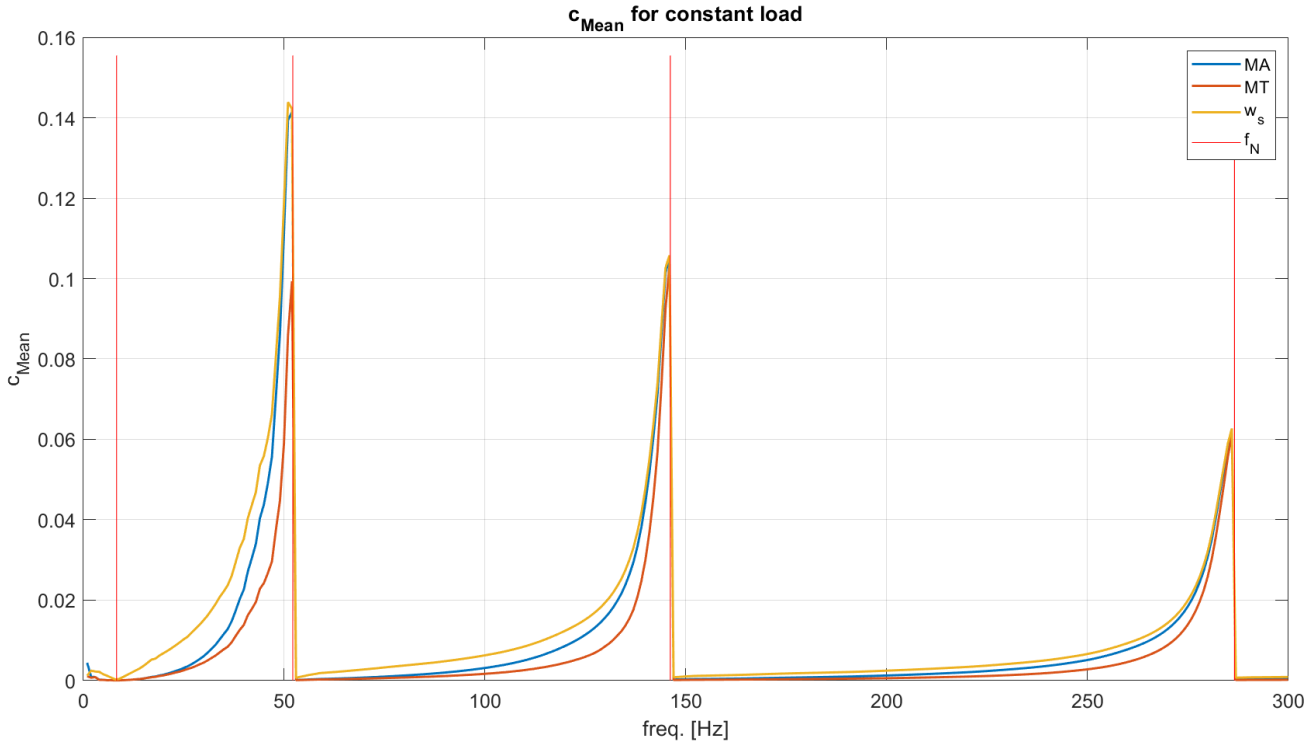

*Figure 2.41: c_{Mean} as a function of load's frequency for the **constant load**.*

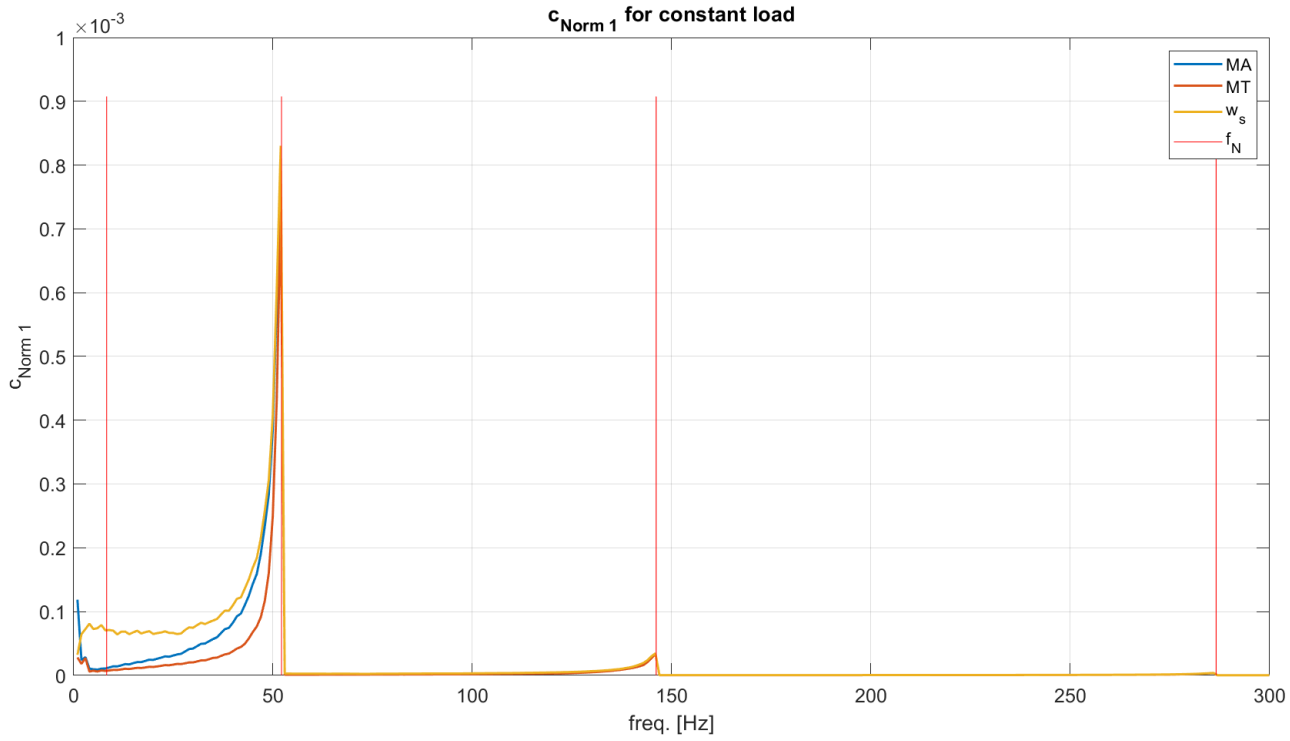

*Figure 2.42: $c_{Norm\ 1}$ as a function of load's frequency for the **constant load**.*

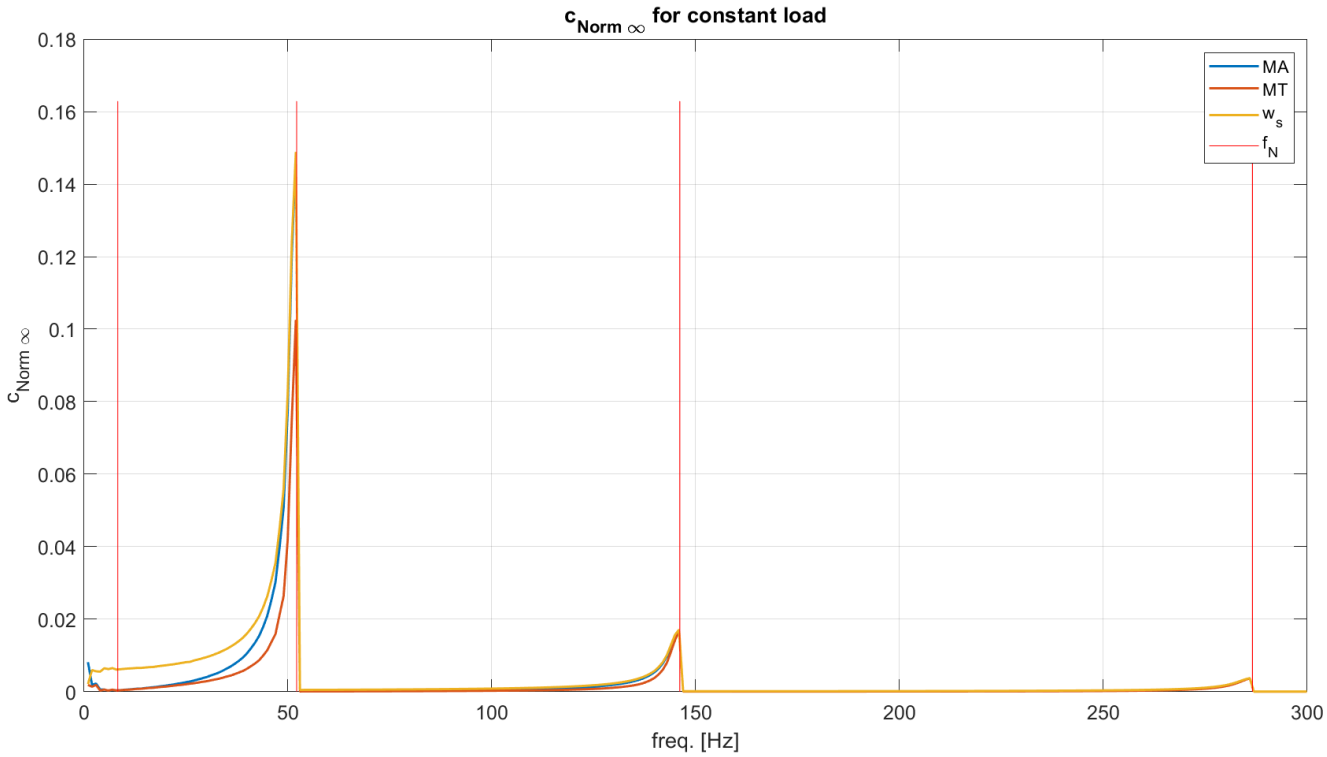

*Figures 2.43: $c_{Norm\,\infty}$ as a function of load's frequency for the **constant load**.*

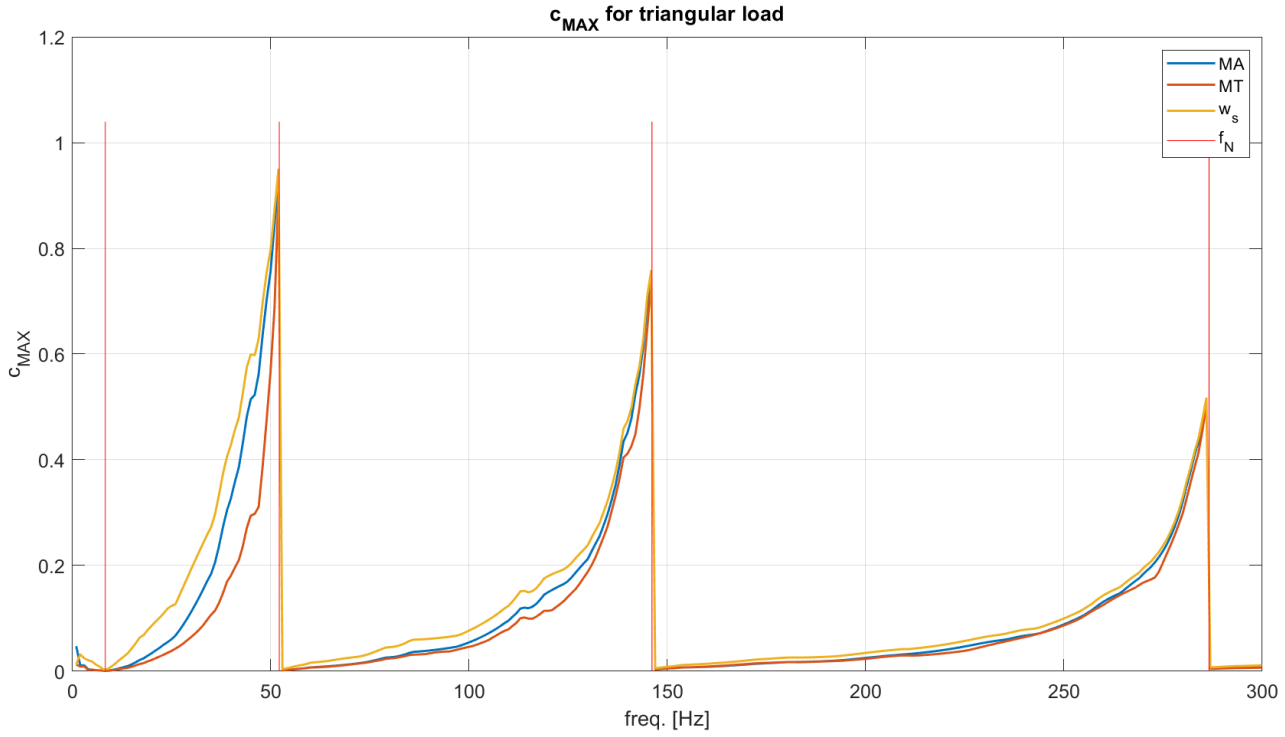

*Figure 2.44: c_{MAX} as a function of load's frequency for the **triangular load**.*

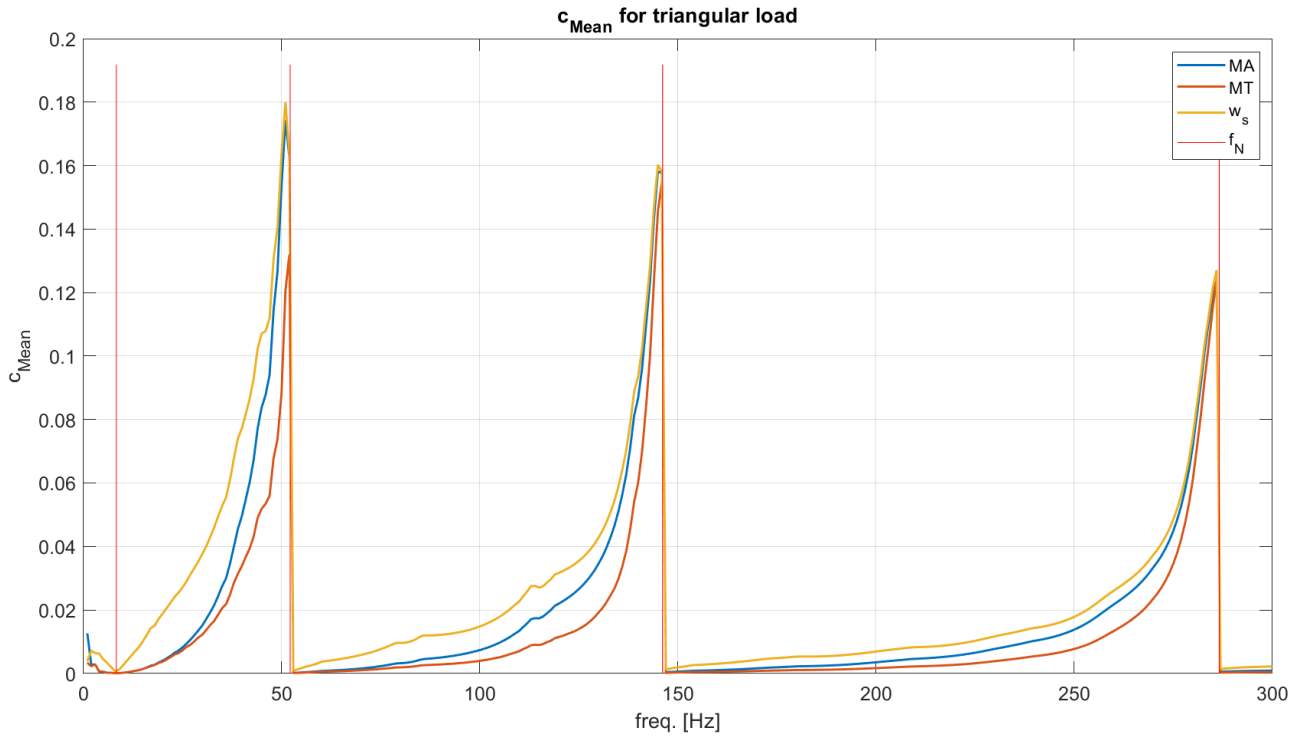

*Figure 2.45: c_{Mean} as a function of load's frequency for the **triangular load**.*

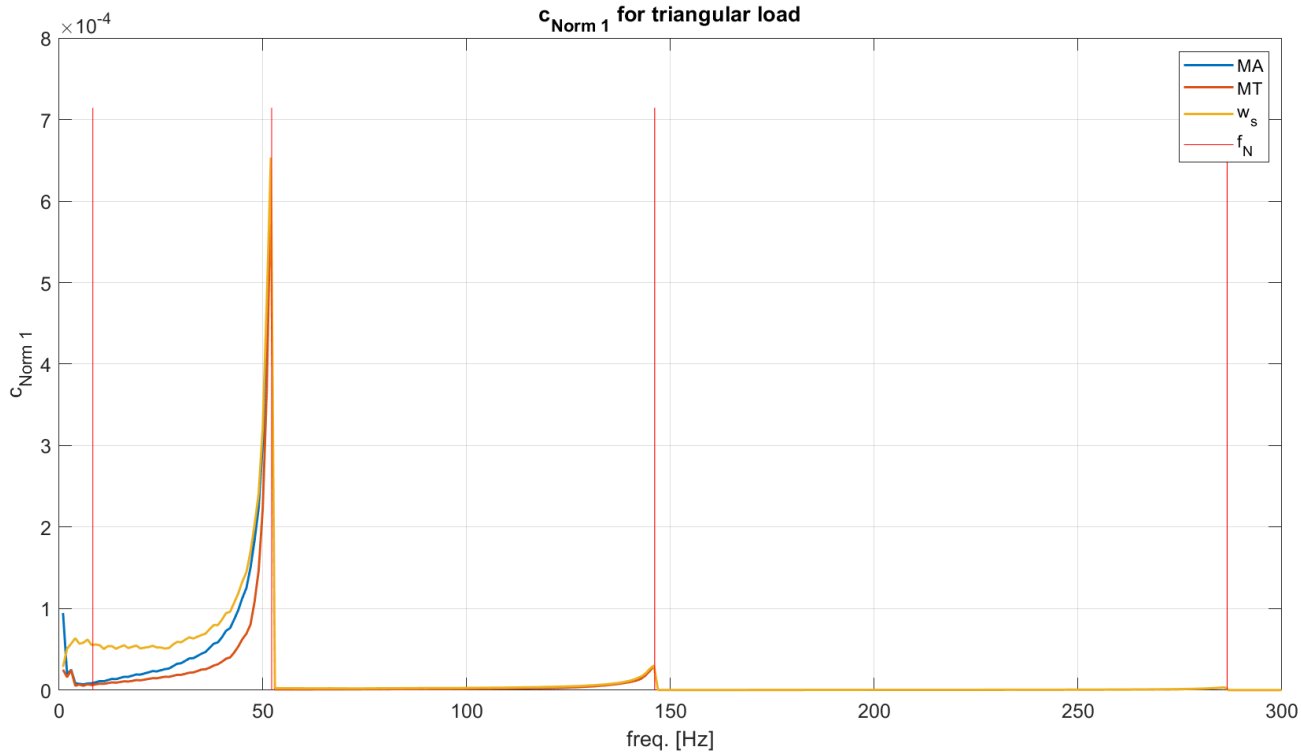

*Figure 2.46: $c_{Norm\,1}$ as a function of load's frequency for the **triangular load**.*

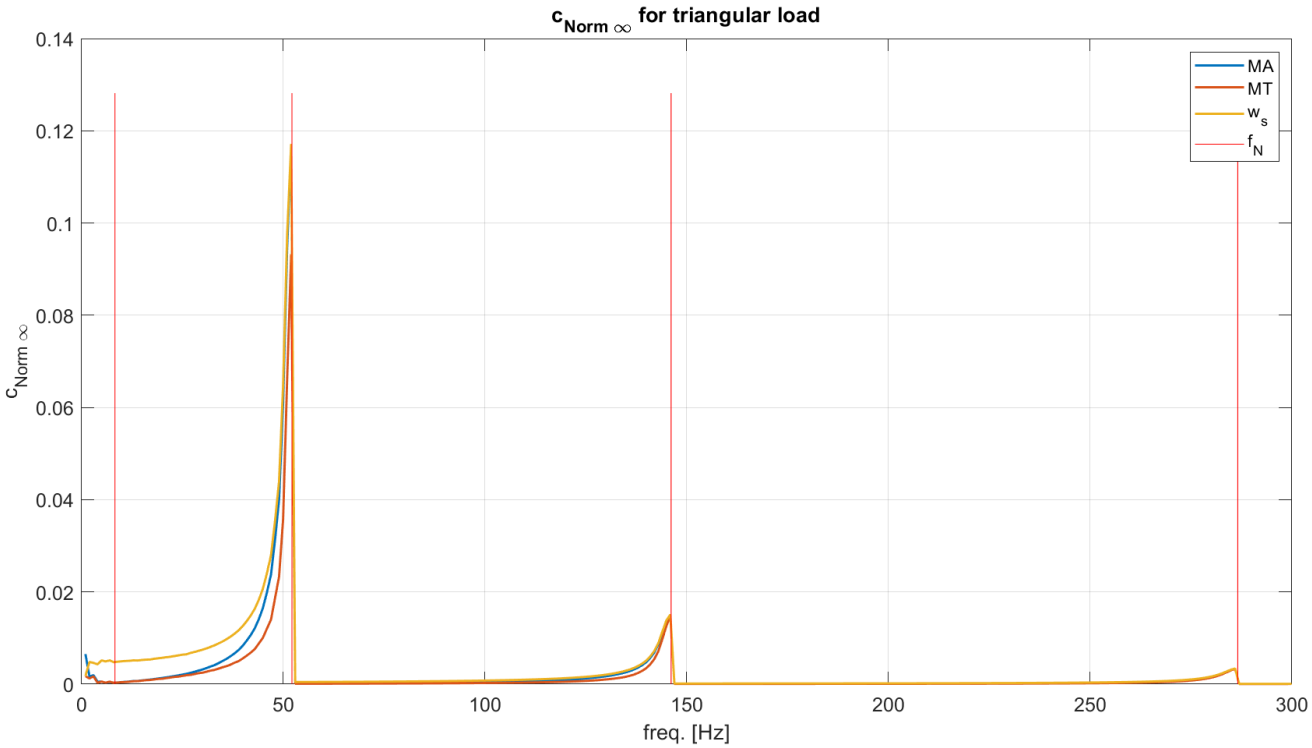

*Figures 2.47: $c_{Norm\,\infty}$ as a function of load's frequency for the **triangular load**.*

When approaching the next modal frequency from the left side, all the methods behave similarly and experience a rapid increase in the coefficients. This is because the MD response is mainly governed by the following mode that is not included in the computations of the MT and MA solutions. In fact, the algorithm only considers modes with a frequency lower than the applied load's frequency. Thus, in these circumstances, the primary mode contributing to the overall response is not accounted for, leading to maximum errors as large as the maximum real displacement of the beam. However, the presence of a pseudo-mode in the MT method reduces these mispredictions, leading often to less pronounced peaks.

It has been observed that the defined coefficients are always slightly larger for the MA method than for the MT method, for each frequency considered, indicating the overall better accuracy of the MT method over the MA method. Anyway, both methods enhance the results obtained by only considering the retained modes (w_s solution)

Furthermore, as more modes are retained (i.e. at higher load's frequency), the local peaks decrease near the following modal frequencies. However, the peaks of $c_{Norm\,1}$ And $c_{Norm\,\infty}$ decrease more rapidly than for c_{MAX} and c_{Mean}. Overall, the results obtained by $c_{Norm\,1}$ And $c_{Norm\,\infty}$ are in good agreement with those obtained by c_{MAX} and c_{Mean}.

The next figures provide an example of a load's frequency that is slightly lower than the frequency of the second mode, which is not retained by the considered approach. Figures 3.48, 3.49, and 3.50 study in a practical way the peaks mentioned before. Demonstrating once again the superiority of the MT method over the MA method since it always better approximates the MD results due to its capacity of considering dynamic amplifications, neglected in the MA method. However, the MT method has more difficulties for the concentrated force case.

It is reminded that the second modal frequency is $f_{N,2} = 52.20\ Hz$.

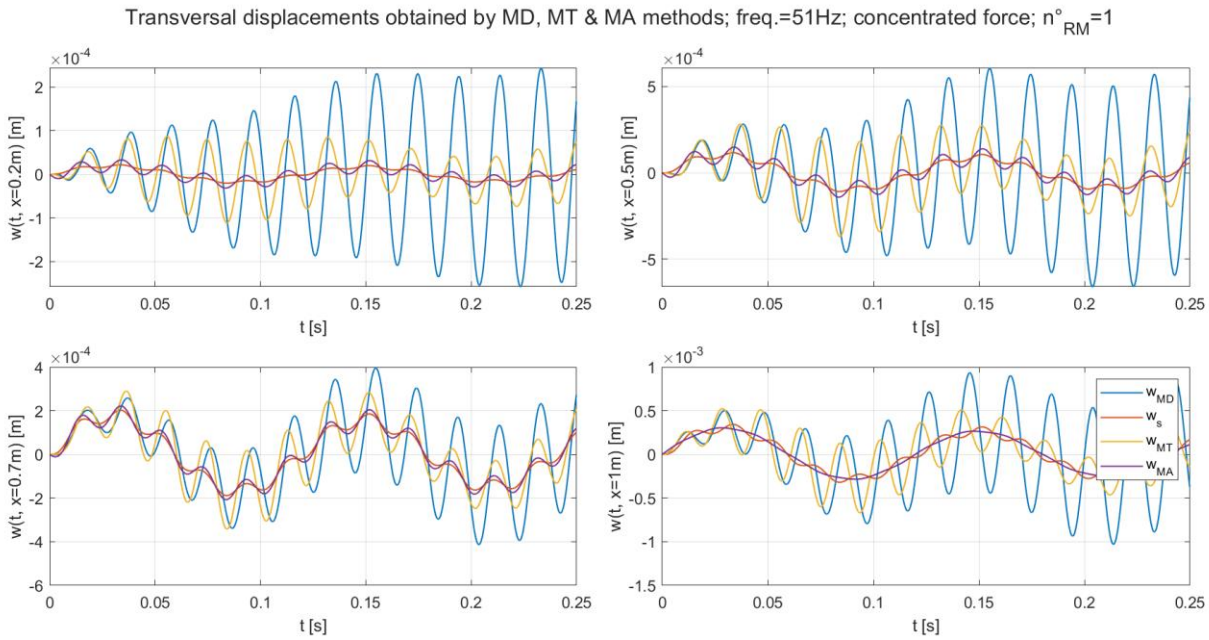

*Figure 2.48: Deviations of the MT and MA methods from the MD method for the **concentrated force** oscillating at 51 Hz.*

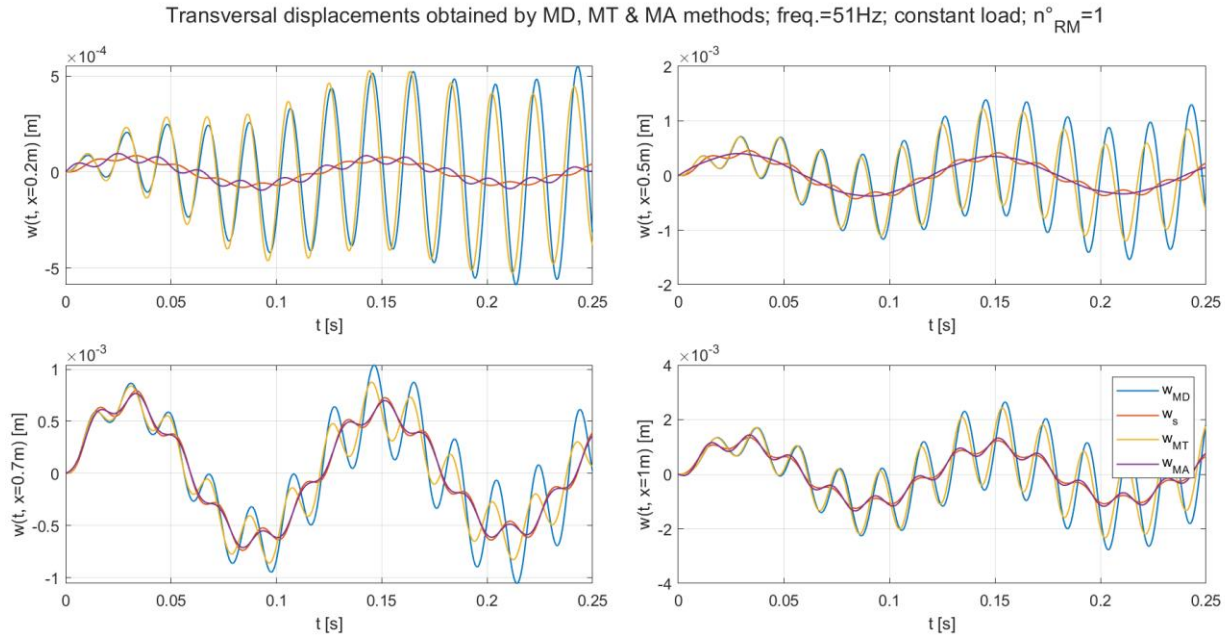

*Figure 2.49: Deviations of the MT and MA methods from the MD method for the **constant load** oscillating at 51 Hz.*

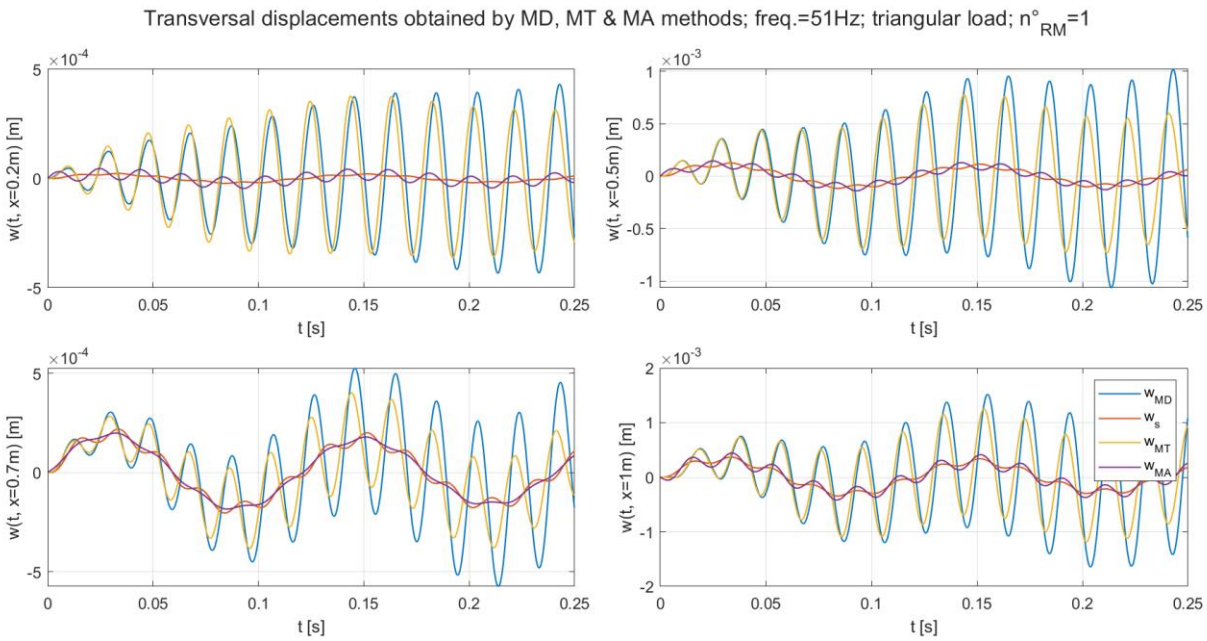

*Figure 2.50: Deviations of the MT and MA methods from the MD method for the **triangular** load oscillating at 51 Hz.*

2.4.3. Result enhancement approaches

In this and in the next paragraphs, the approach used in paragraph 2.4.1 will be referred to as **approach 'zero'**. To enhance the accuracy of the approach 0, two defined techniques are employed:

-The **first approach** involves averaging two contiguous modal frequencies to introduce an additional mode as the load's frequency exceeds the averaged frequency. The green lines in the images of the next paragraph indicate where the extra mode is introduced. This approach significantly reduces the errors and prevents them from reaching extreme peaks. The results obtained are reported in **paragraph 2.4.4**.

-The **second approach**, whose results are reported in the relative **paragraph 2.4.5**, involves categorically considering an additional mode compared to approach 0. If only one mode was retained for a given frequency in approach 0, the current approach now considers two frequencies. If before was $n_{RM,approach0} = 2$, now $n_{RM,approach2} = 3$, and so on. Implementing this strategy further improves the results and reduces errors but requires a higher computational cost compared to approaches 0 and 1.

2.4.4. Approach 1 results

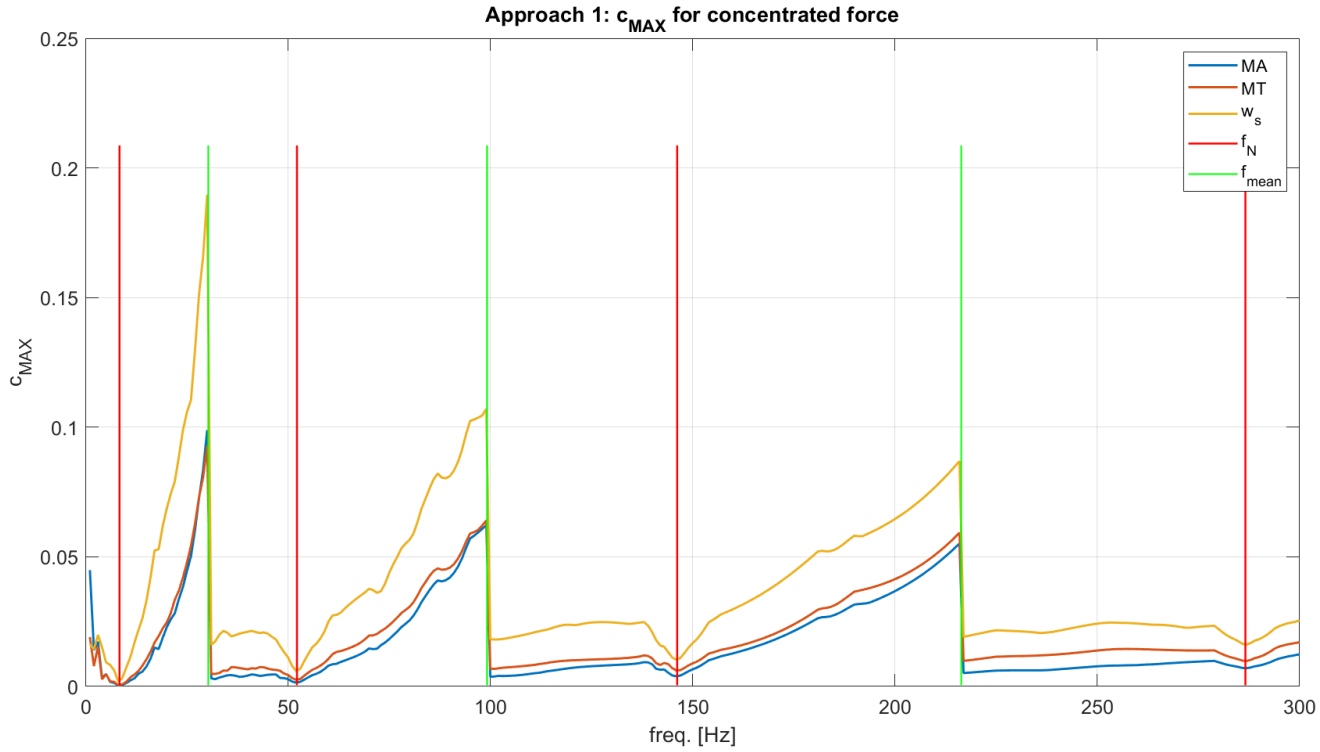

*Figure 2.51: **Approach 1**: c_{MAX} as a function of force's frequency for the **concentrated force**.*

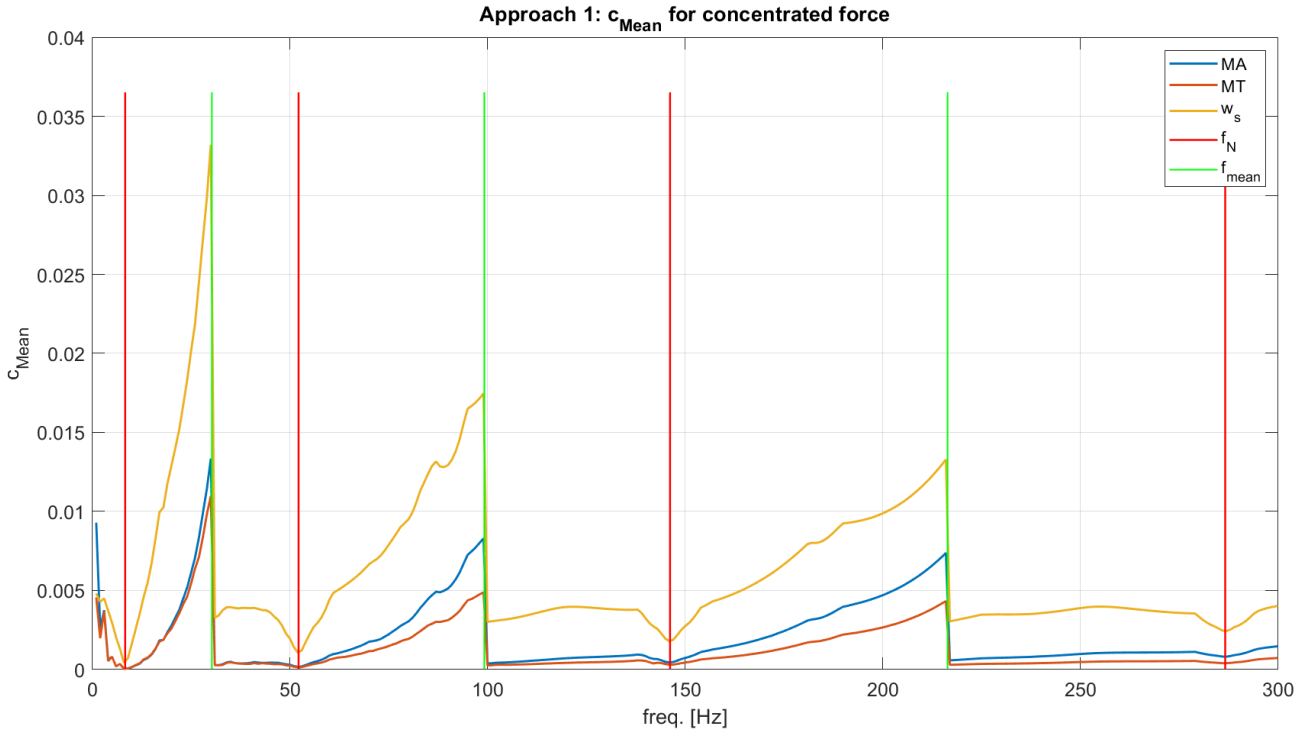

*Figure 2.52: **Approach 1**: c_{Mean} as a function of force's frequency for the **concentrated force**.*

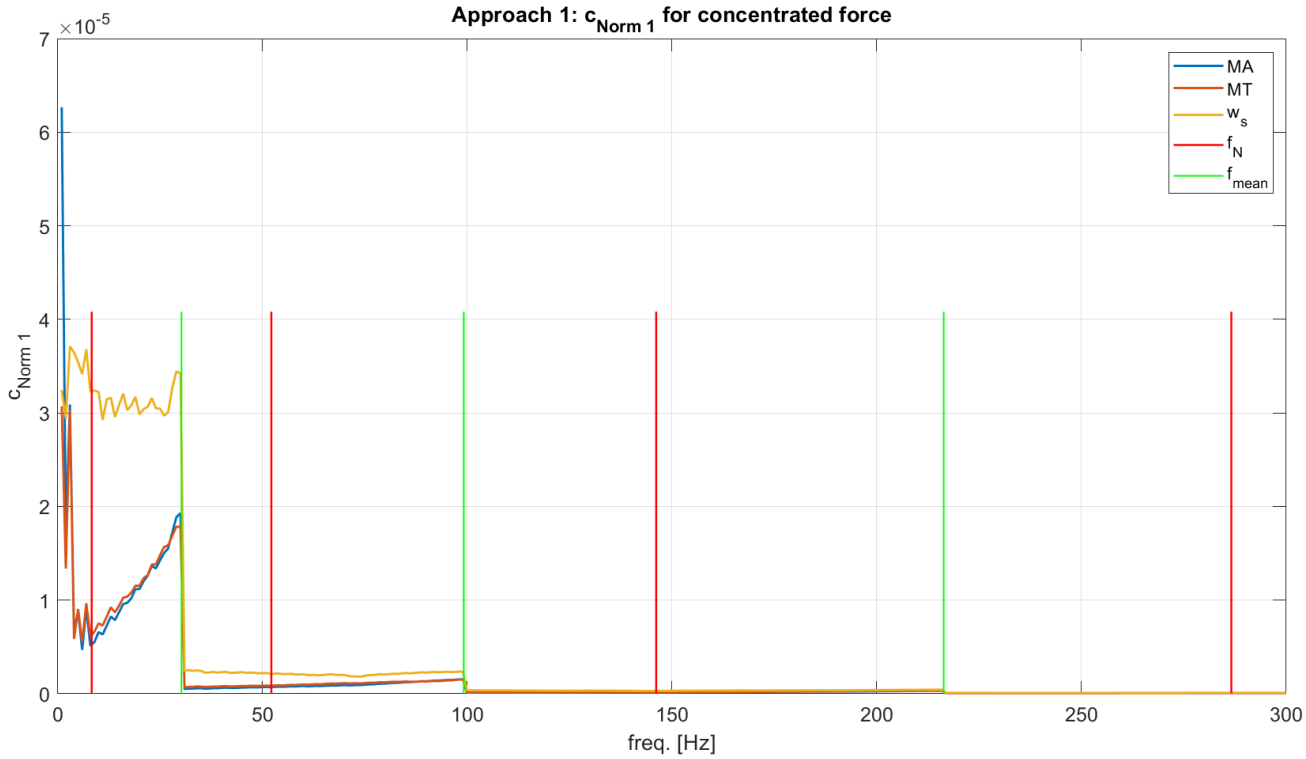

*Figure 2.53: **Approach 1**: $c_{Norm\ 1}$ as a function of force's frequency for the **concentrated force**.*

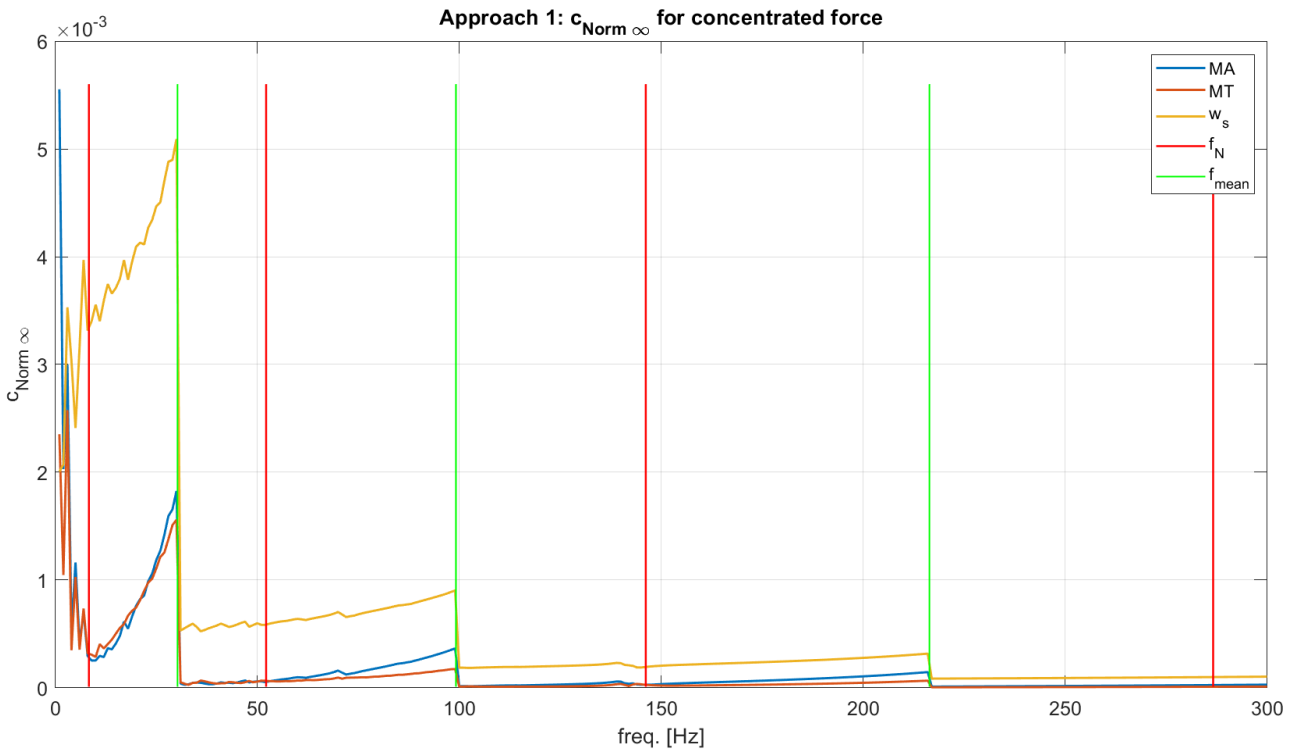

*Figures 2.54: **Approach 1**: $c_{Norm\ \infty}$ as a function of force's frequency for the **concentrated force**.*

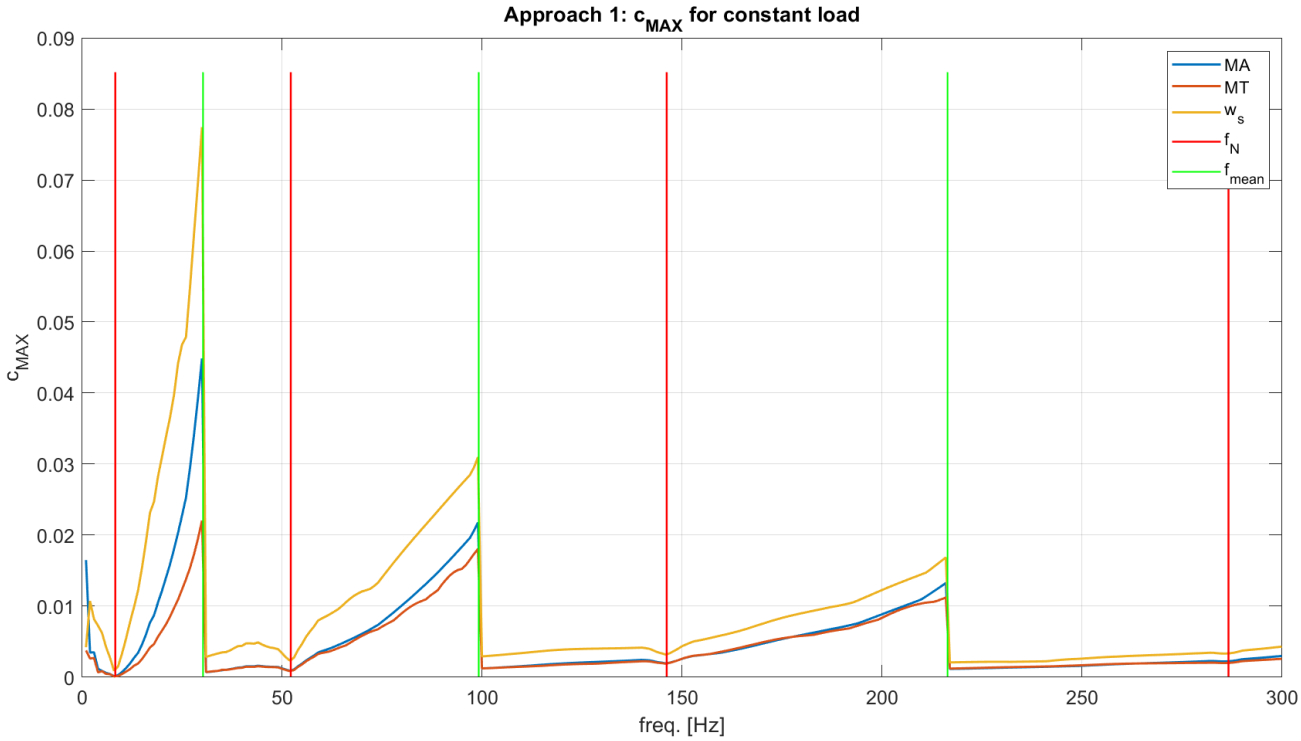

*Figure 2.55: **Approach 1**: c_{MAX} as a function of load's frequency for the **constant load**.*

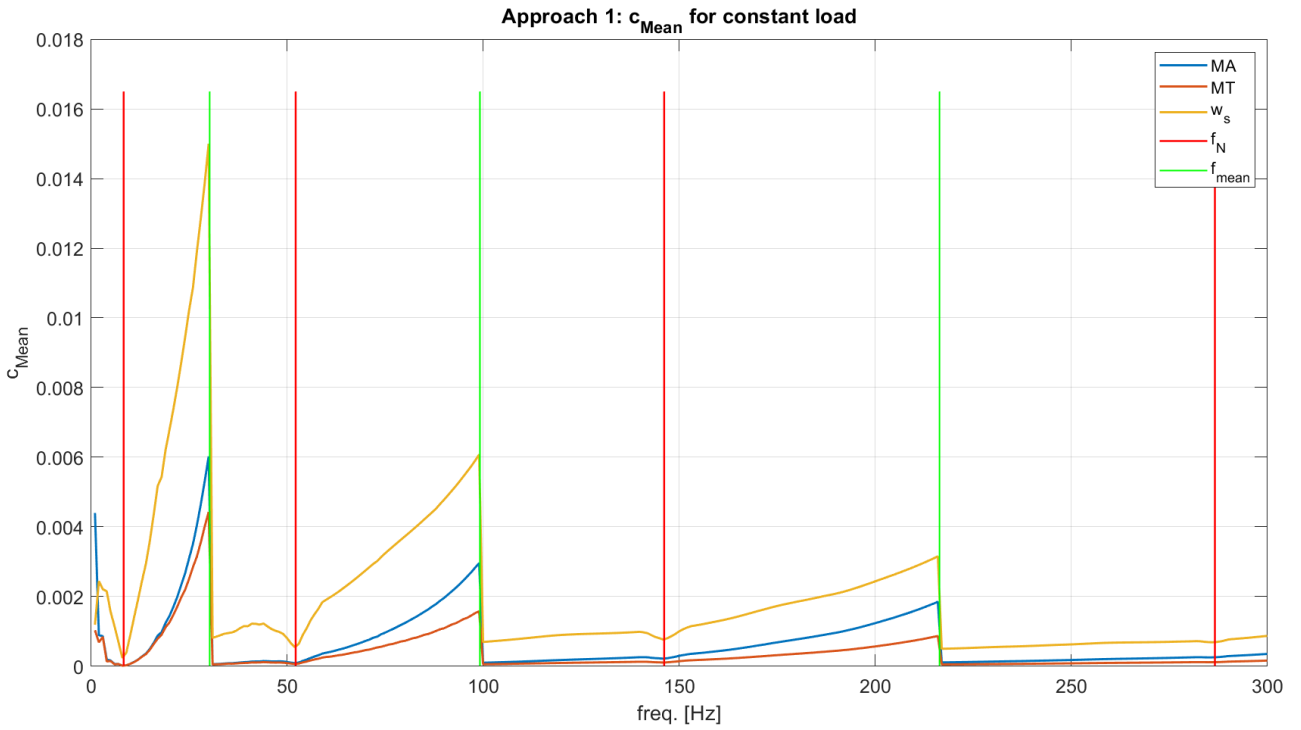

*Figure 2.56: **Approach 1**: c_{Mean} as a function of load's frequency for the **constant load**.*

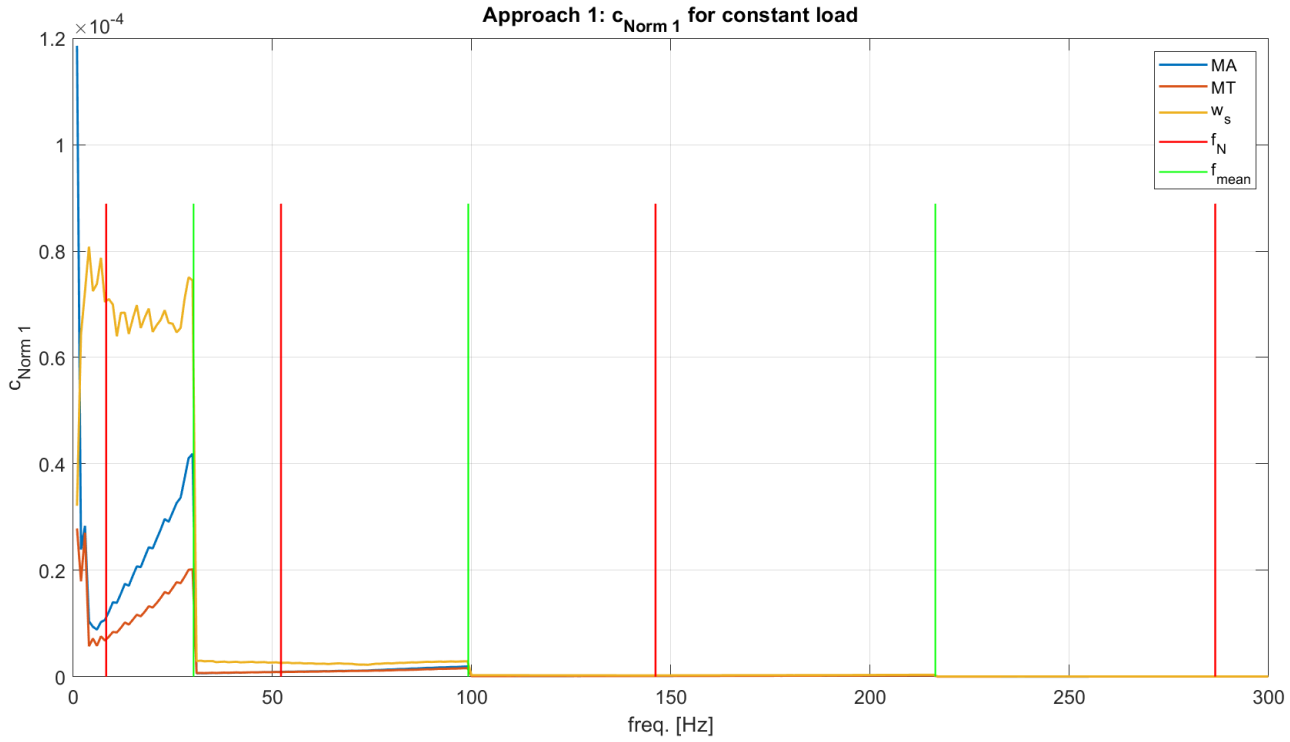

*Figure 2.57: **Approach 1**: $c_{Norm\ 1}$ as a function of load's frequency for the **constant load**.*

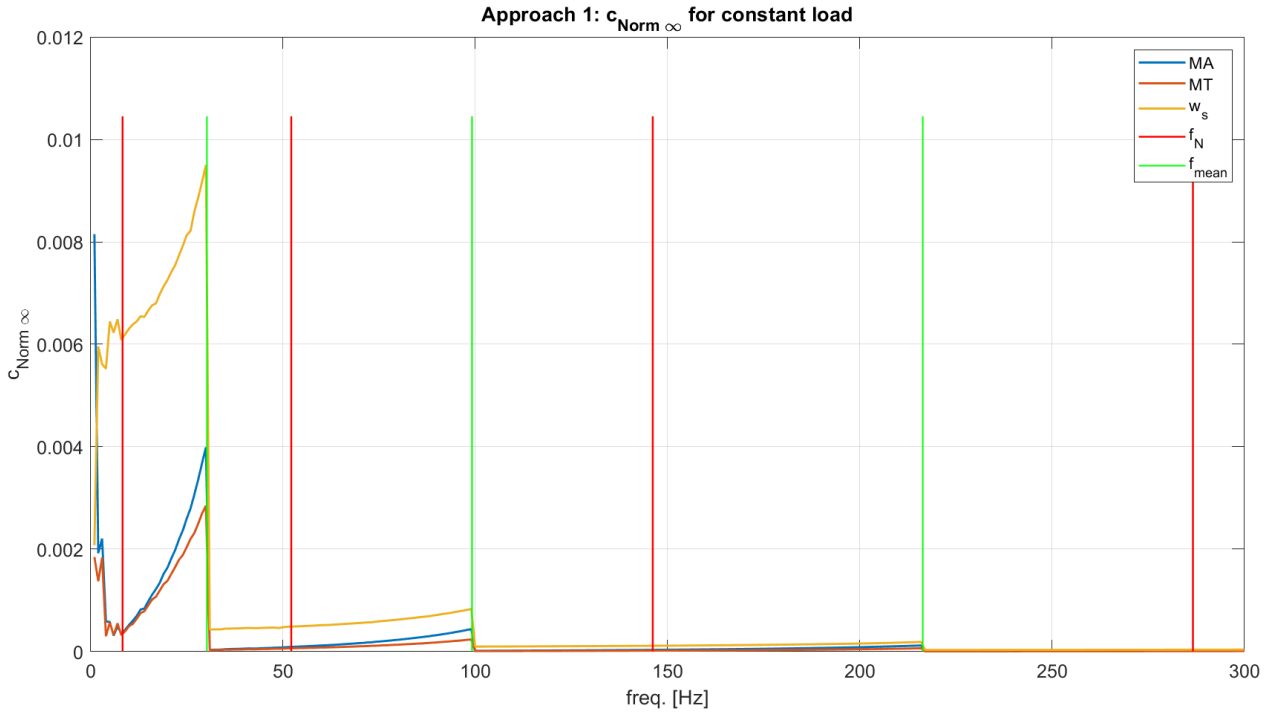

*Figures 2.58: **Approach 1**: $c_{Norm\ \infty}$ as a function of load's frequency for the **constant load**.*

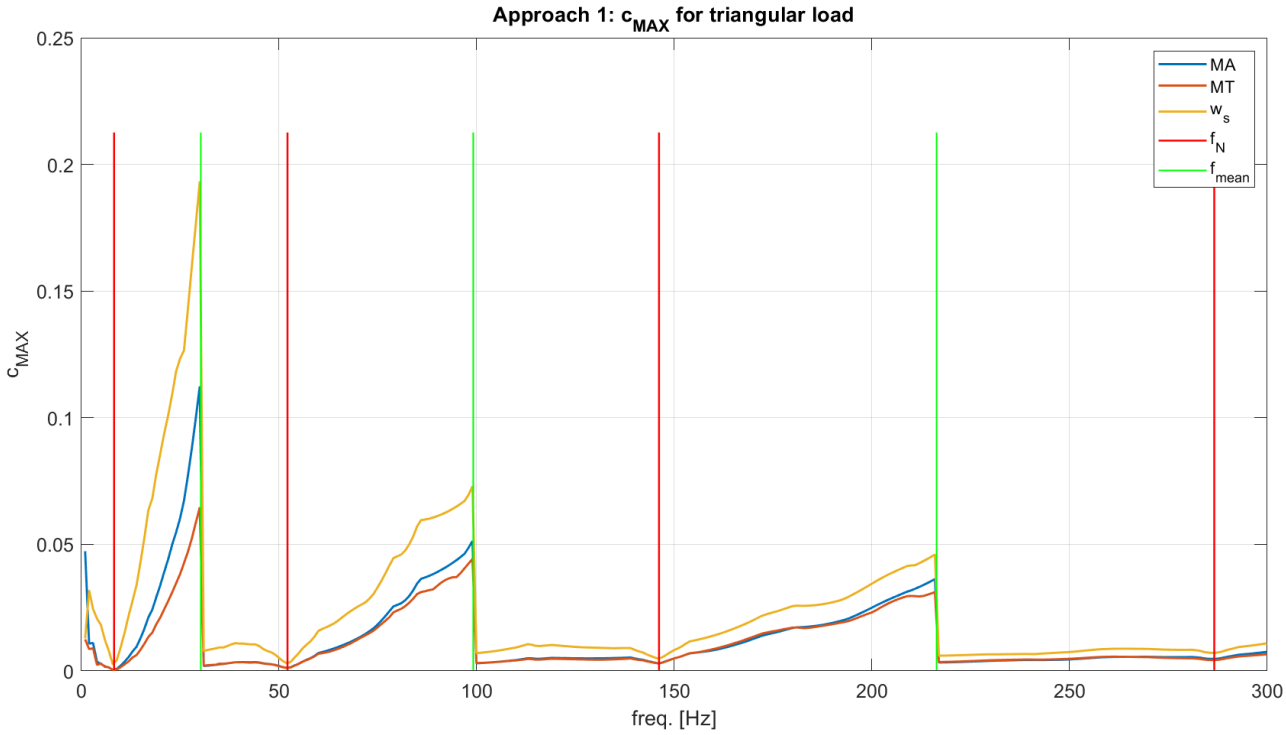

*Figure 2.59: **Approach 1**: c_{MAX} as a function of load's frequency for the **triangular load**.*

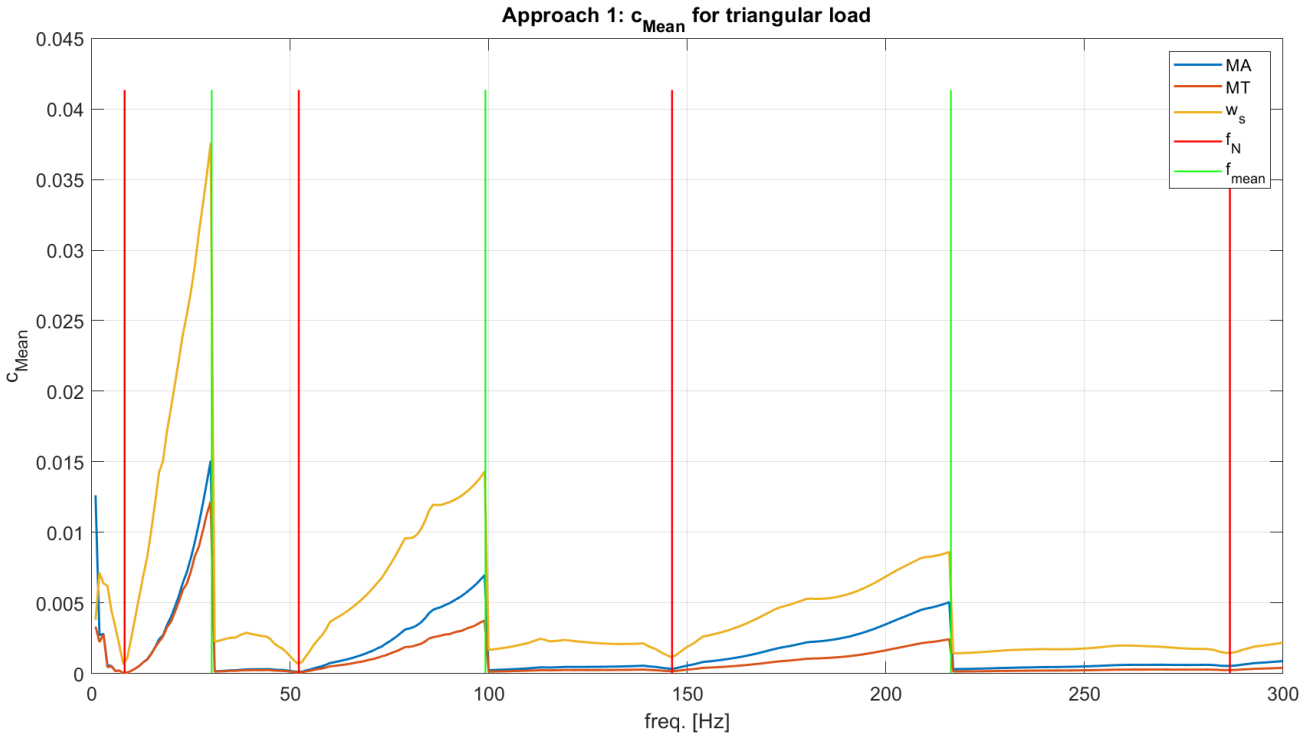

*Figure 2.60: **Approach 1**: c_{Mean} as a function of load's frequency for the **triangular load**.*

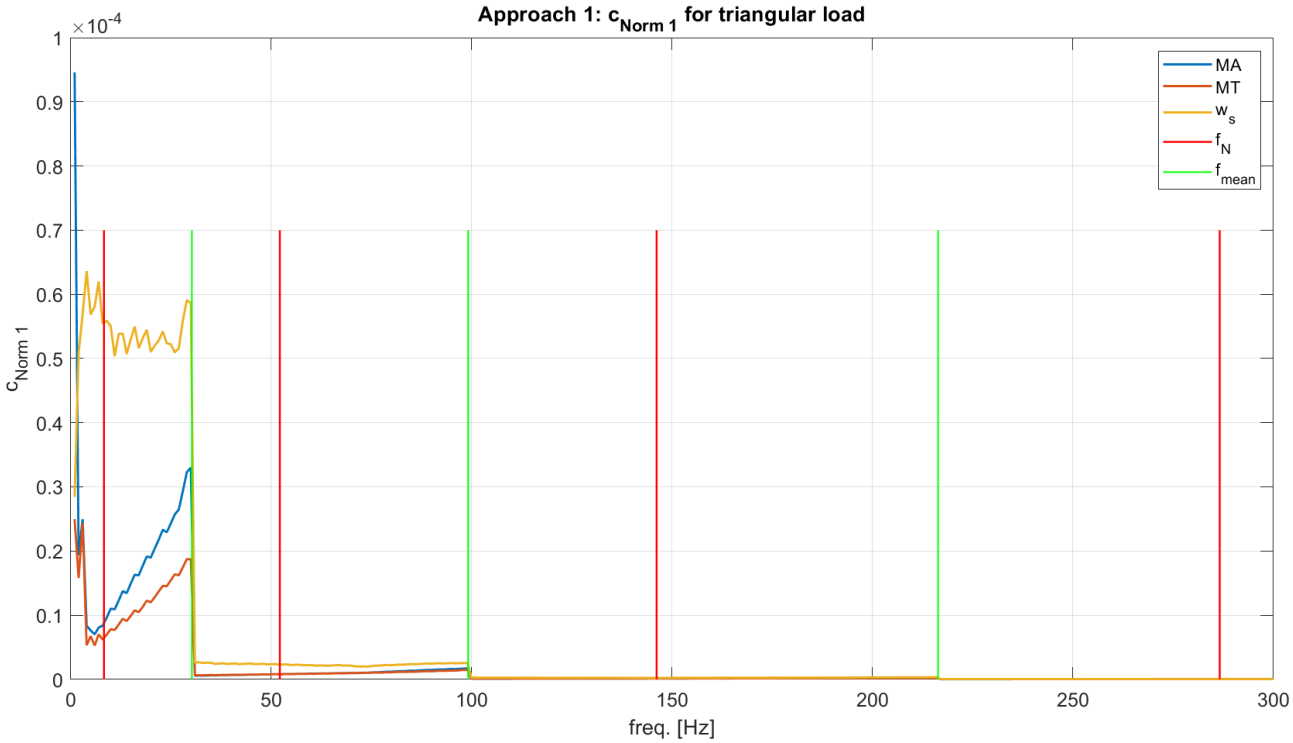

*Figure 2.61: **Approach 1**: $c_{Norm\ 1}$ as a function of load's frequency for the **triangular load**.*

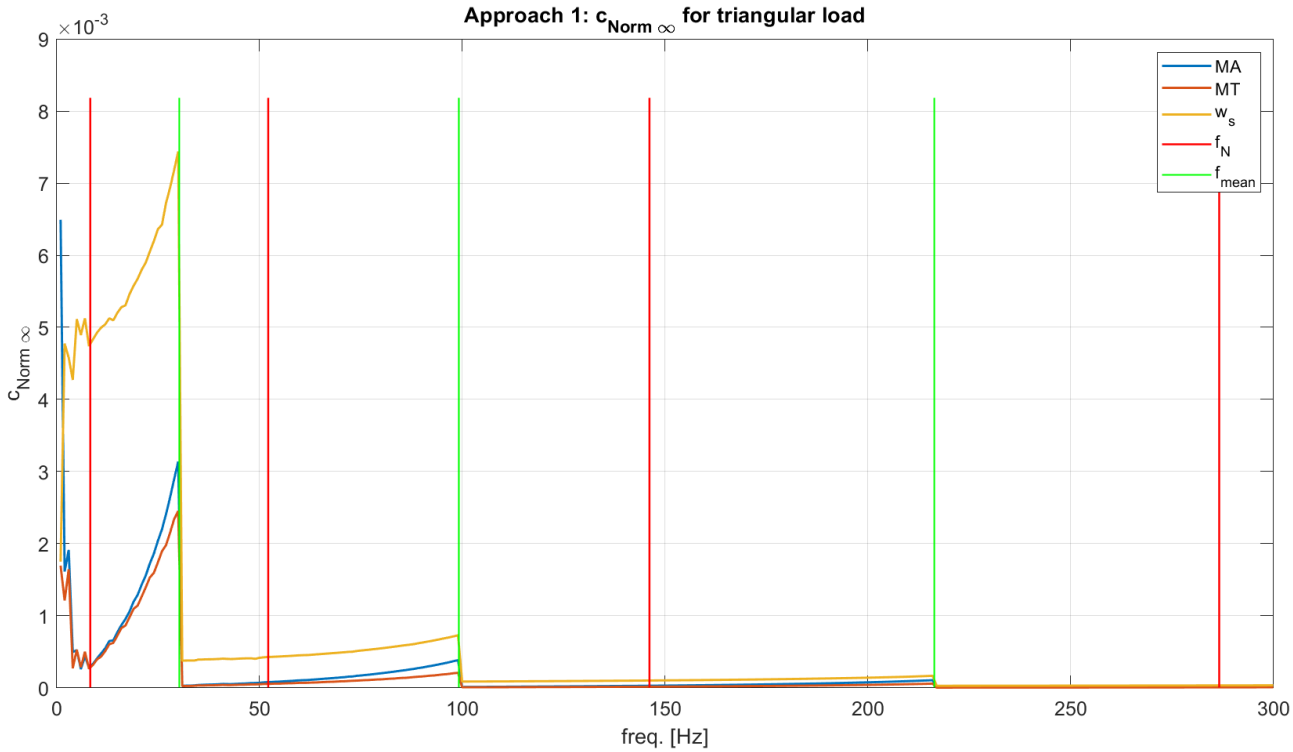

*Figure 2.62: **Approach 1**: $c_{Norm\ \infty}$ as a function of load's frequency for the **triangular load**.*

2.4.5. Approach 2 results

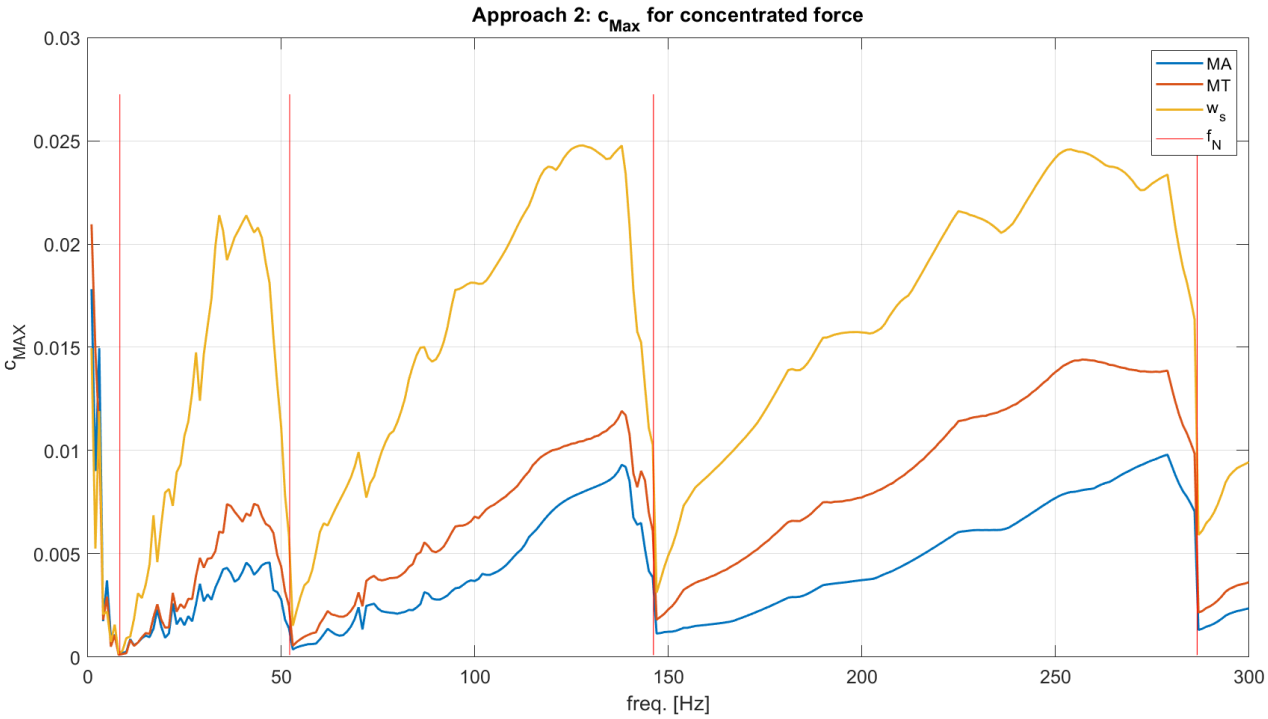

*Figure 2.63: **Approach 2**: c_{MAX} as a function of force's frequency for the **concentrated force.***

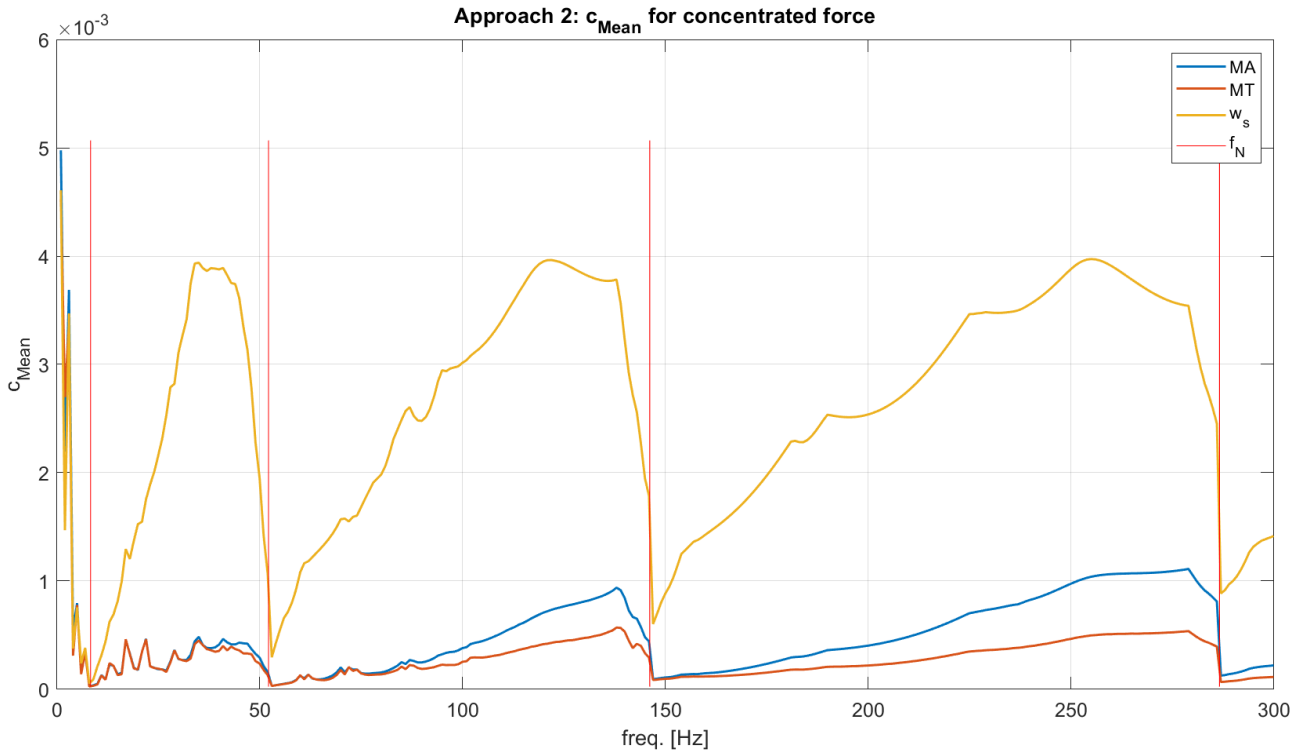

*Figure 2.64: **Approach 2**: c_{Mean} as a function of force's frequency for the **concentrated force.***

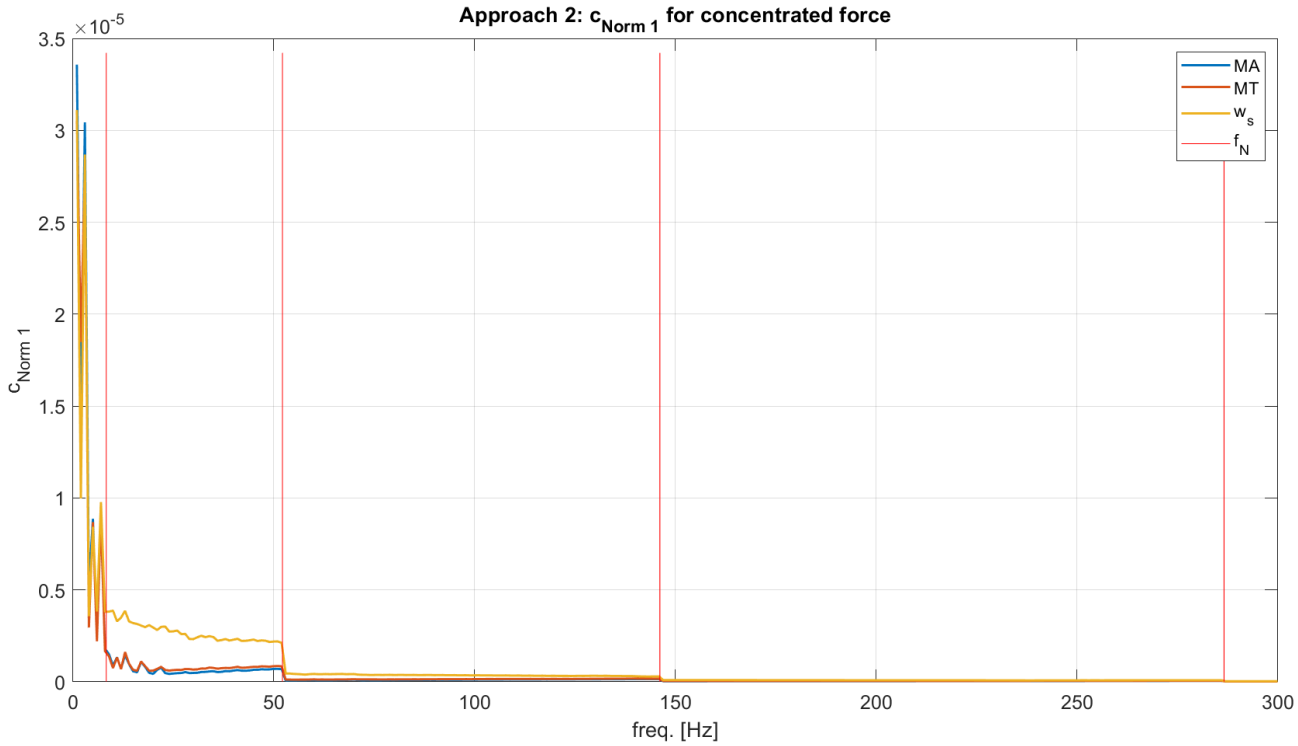

*Figure 2.65: **Approach 2**: $c_{Norm\ 1}$ as a function of force's frequency for the **concentrated force.***

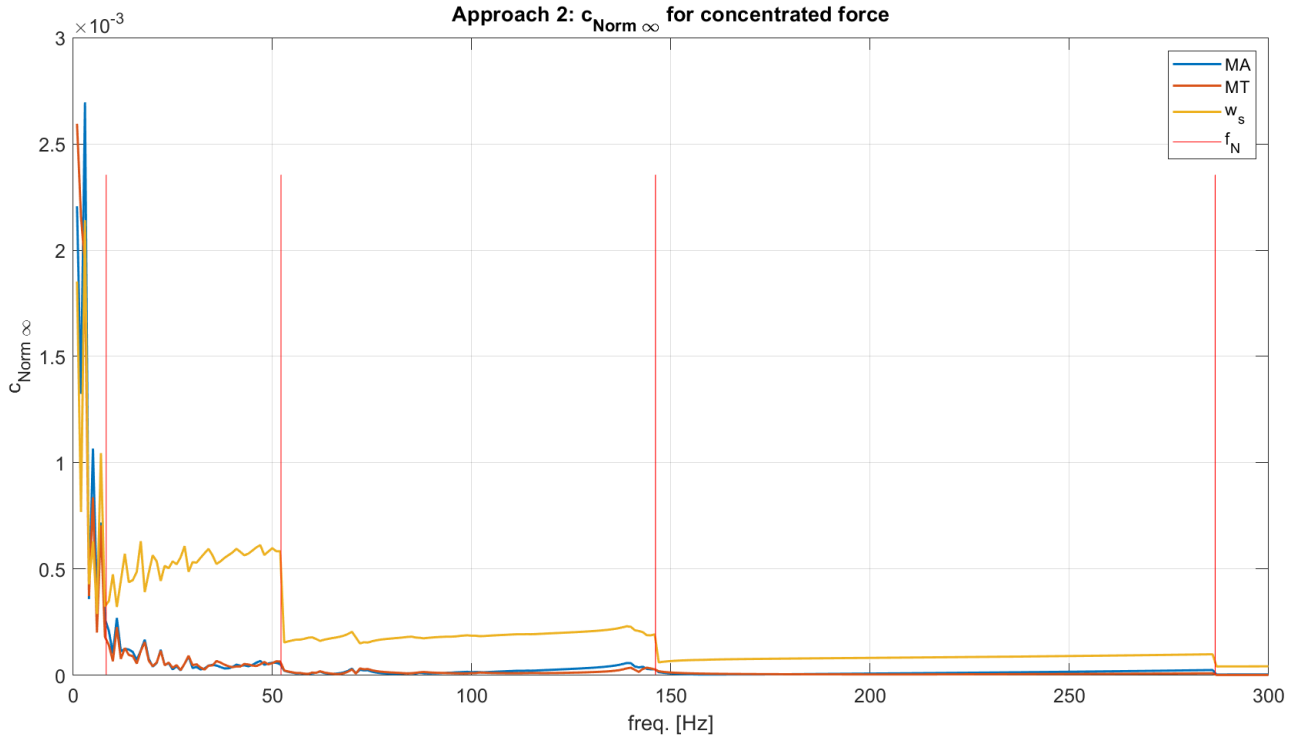

*Figure 2.66: **Approach 2**: $c_{Norm\ \infty}$ as a function of force's frequency for the **concentrated force.***

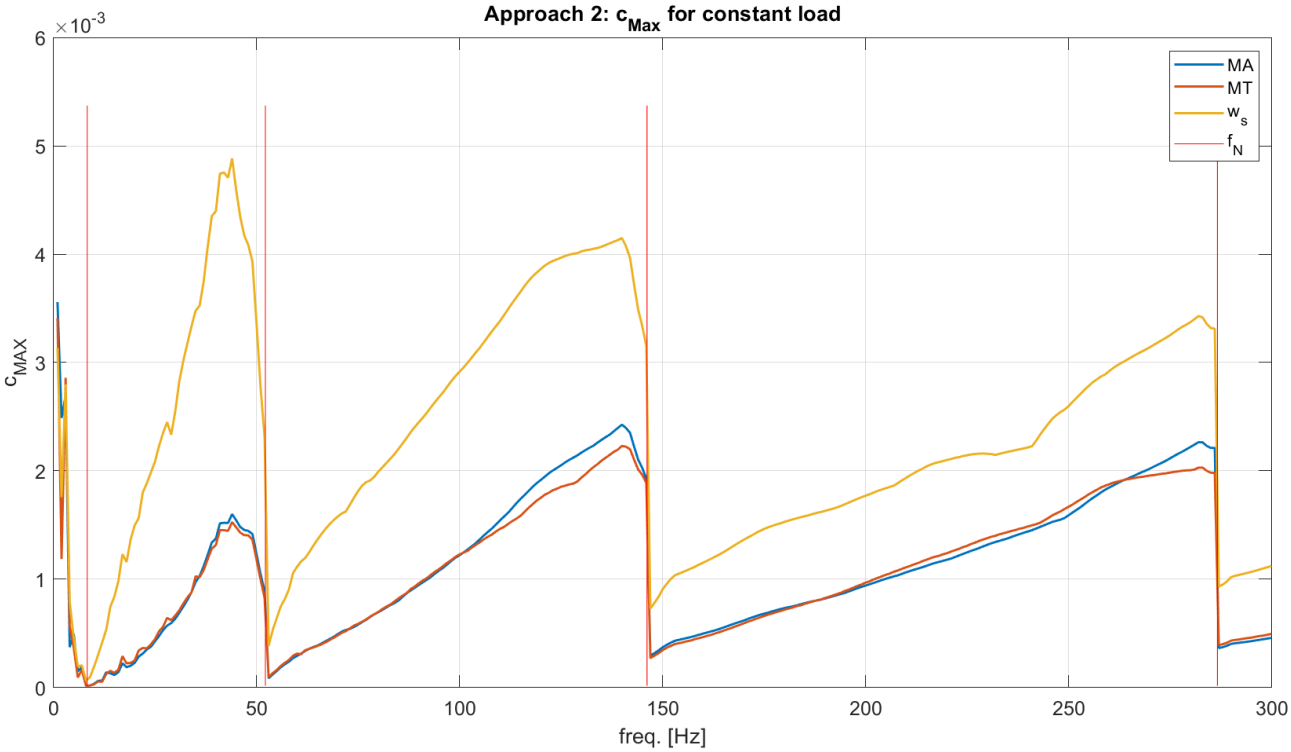

*Figure 2.67: **Approach 2**: c_{MAX} as a function of load's frequency for the **constant load.***

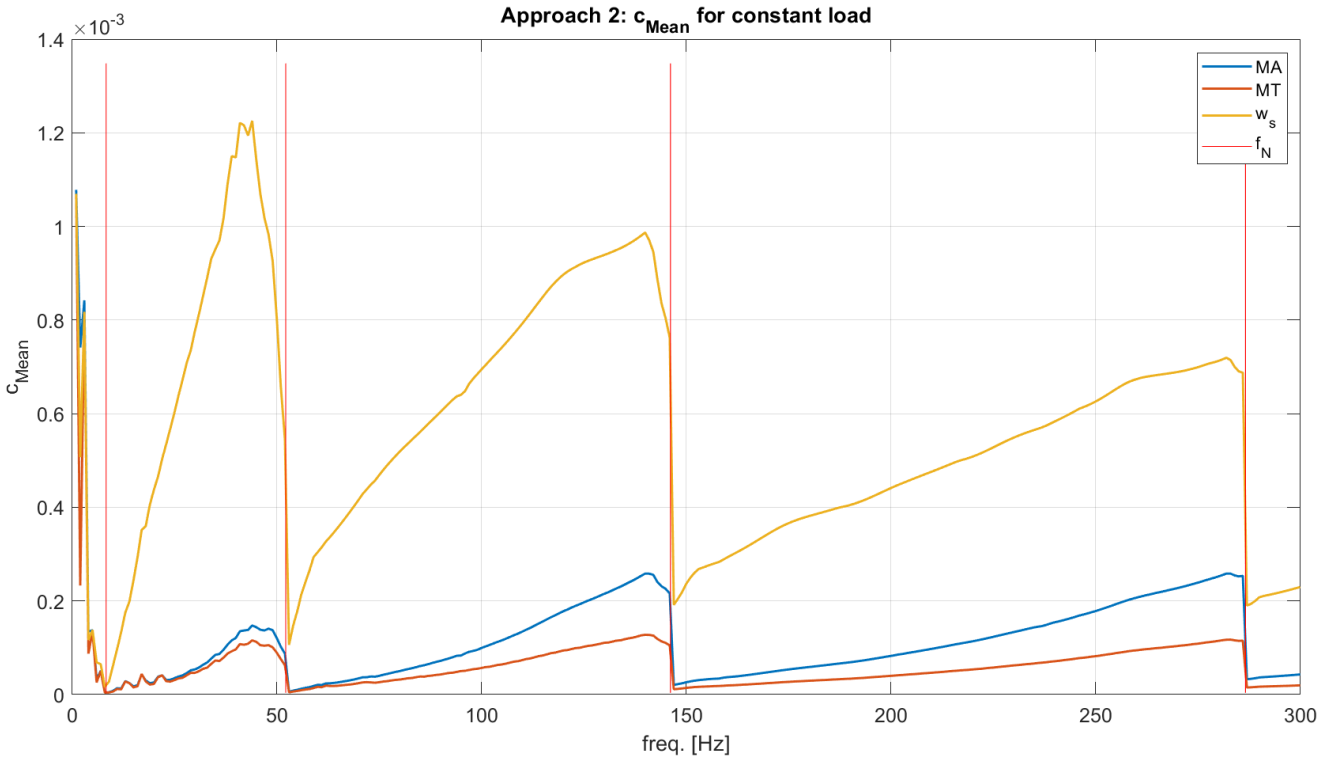

*Figure 2.68: **Approach 2**: c_{Mean} as a function of load's frequency for the **constant load.***

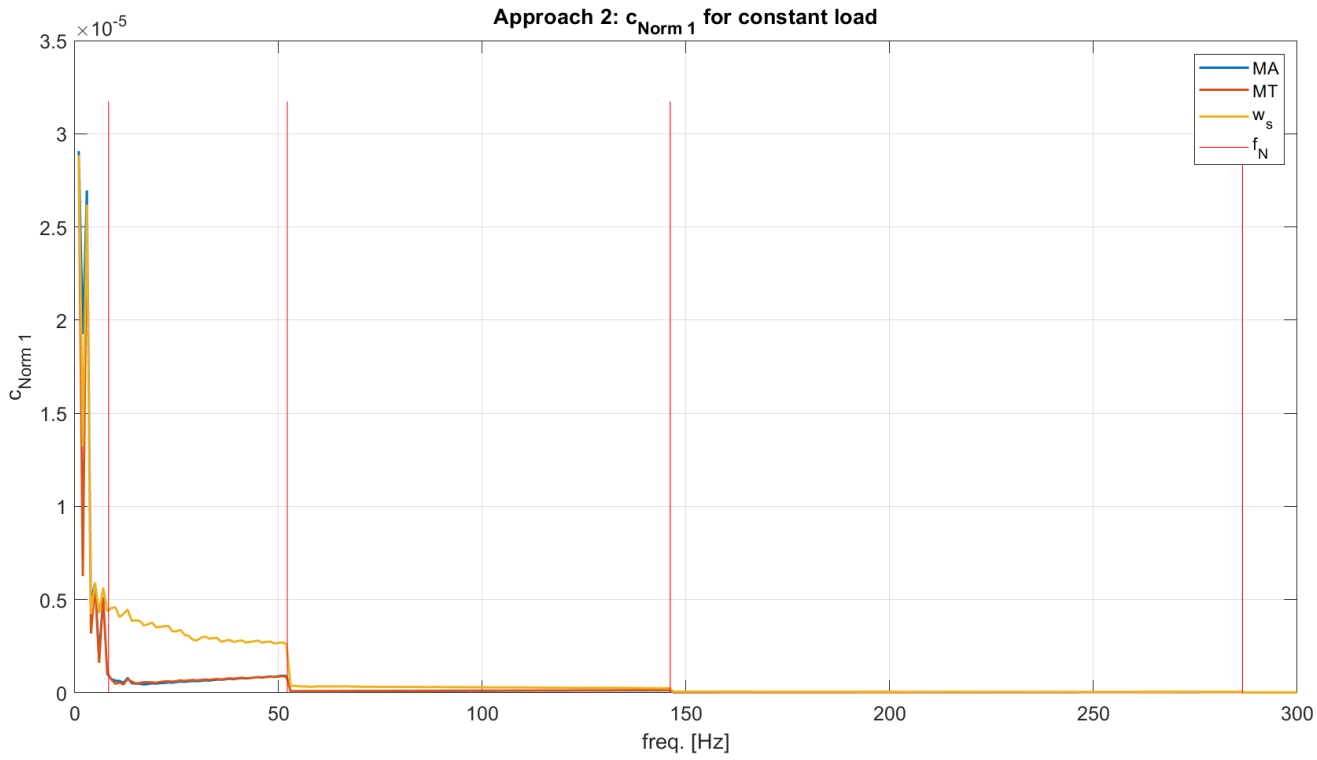

*Figure 2.69: **Approach 2**: $c_{Norm\ 1}$ as a function of load's frequency for the **constant load.***

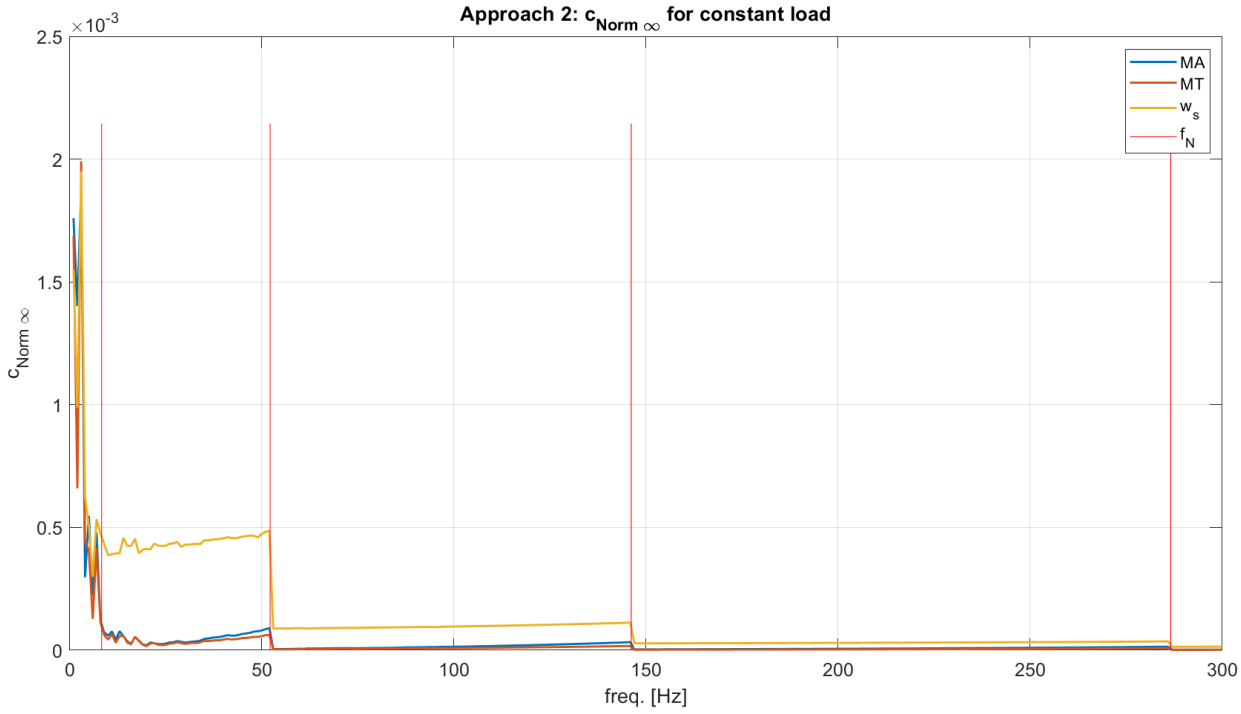

*Figure 2.70: **Approach 2**: $c_{Norm\ \infty}$ as a function of load's frequency for the **constant load.***

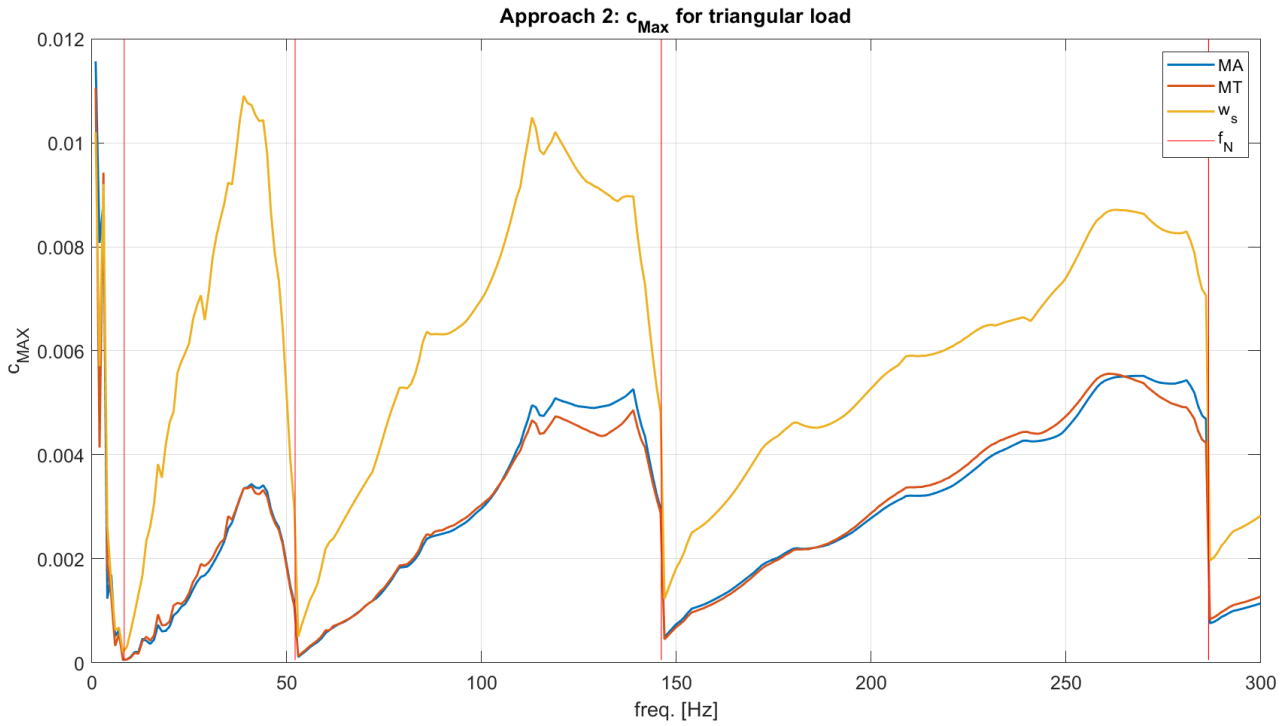

Figure 2.71: ***Approach 2****: c_{MAX} as a function of load's frequency for the* ***triangular load.***

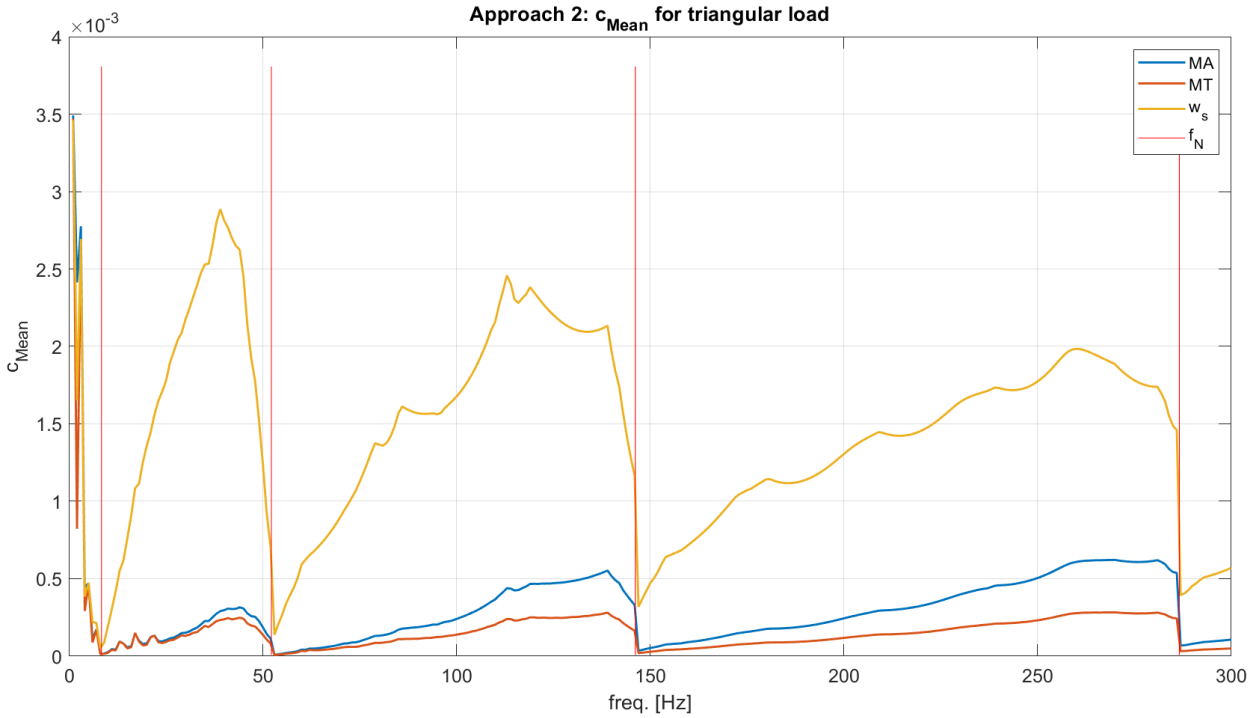

Figure 2.72: ***Approach 2****: c_{Mean} as a function of load's frequency for the* ***triangular load.***

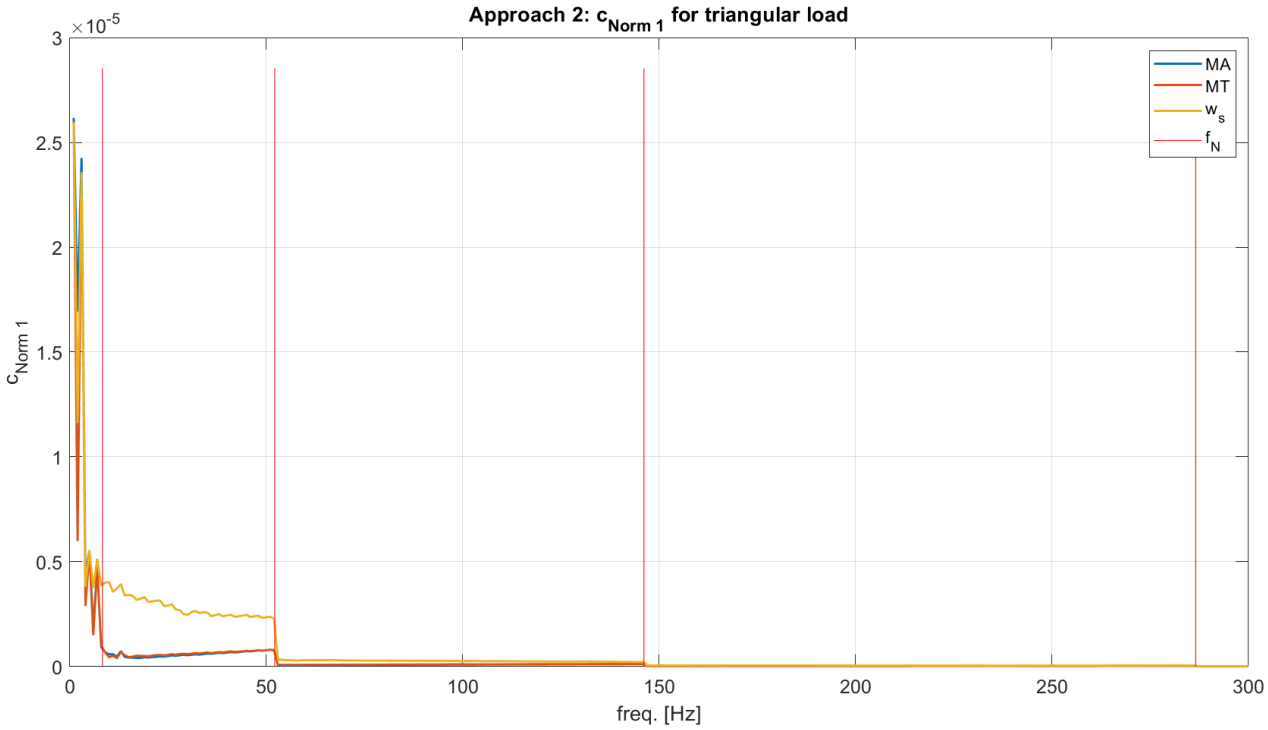

*Figure 2.73: **Approach 2**: $c_{Norm\ 1}$ as a function of load's frequency for the **triangular load.***

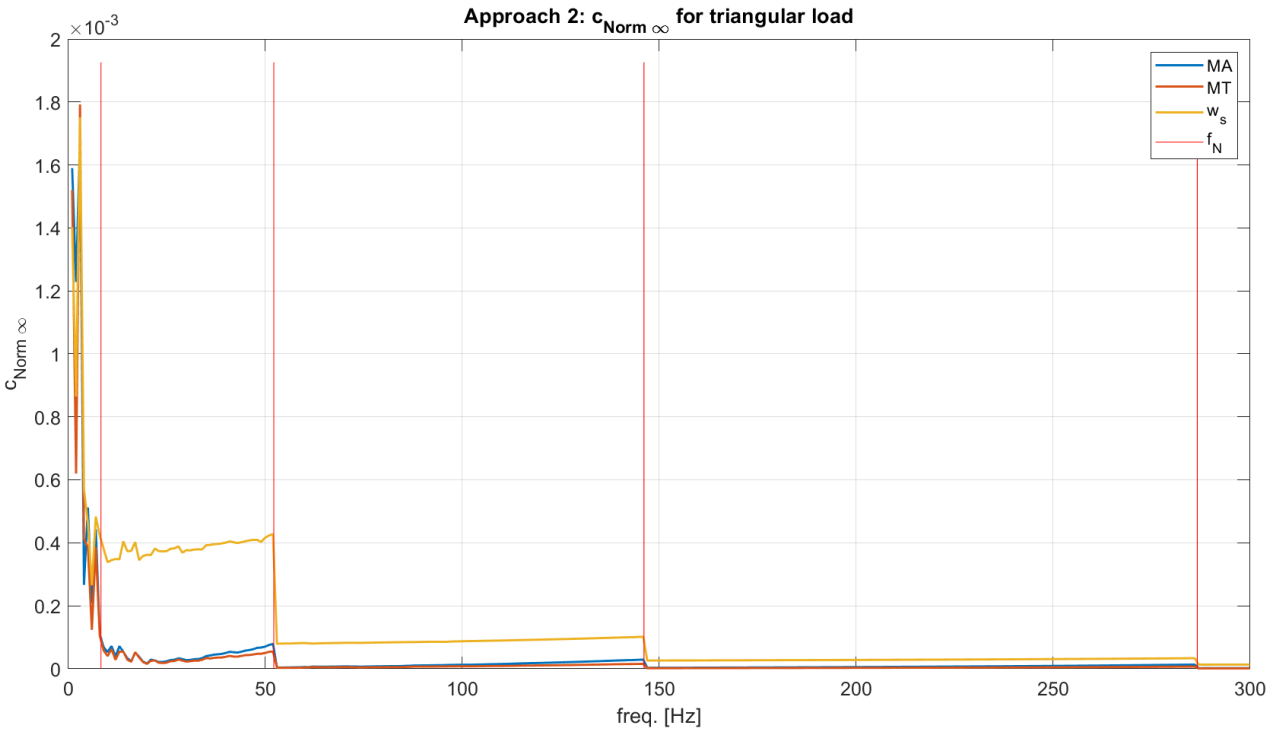

*Figure 2.74: **Approach 2**: $c_{Norm\ \infty}$ as a function of load's frequency for the **triangular load.***

2.4.6. Approach 0 and Approach 1 comparison

In this paragraph, the two defined approaches '0' and '1' are compared. In Figures 2.75-2.86 pedicle "1" indicates the lately defined Approach 1, while pedicle "0" indicates the results obtained using Approach 0.

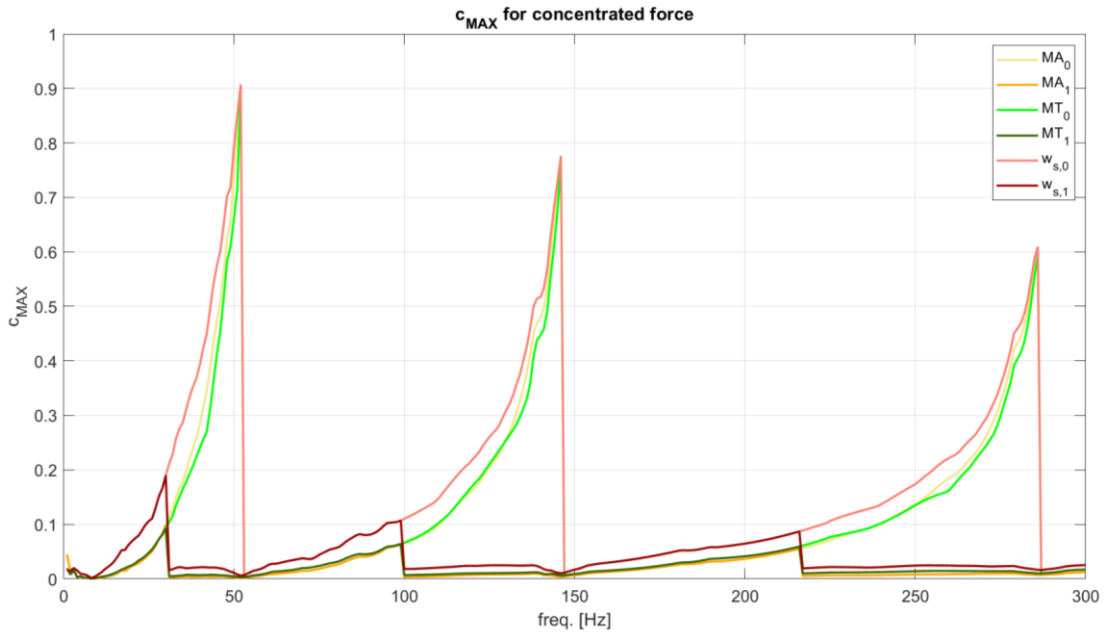

*Figure 2.75: Comparison of c_{MAX} for **approach 0** (pedicle '0') and **approach 1** (pedicle '1') for the **concentrated force** as a function of force's frequency.*

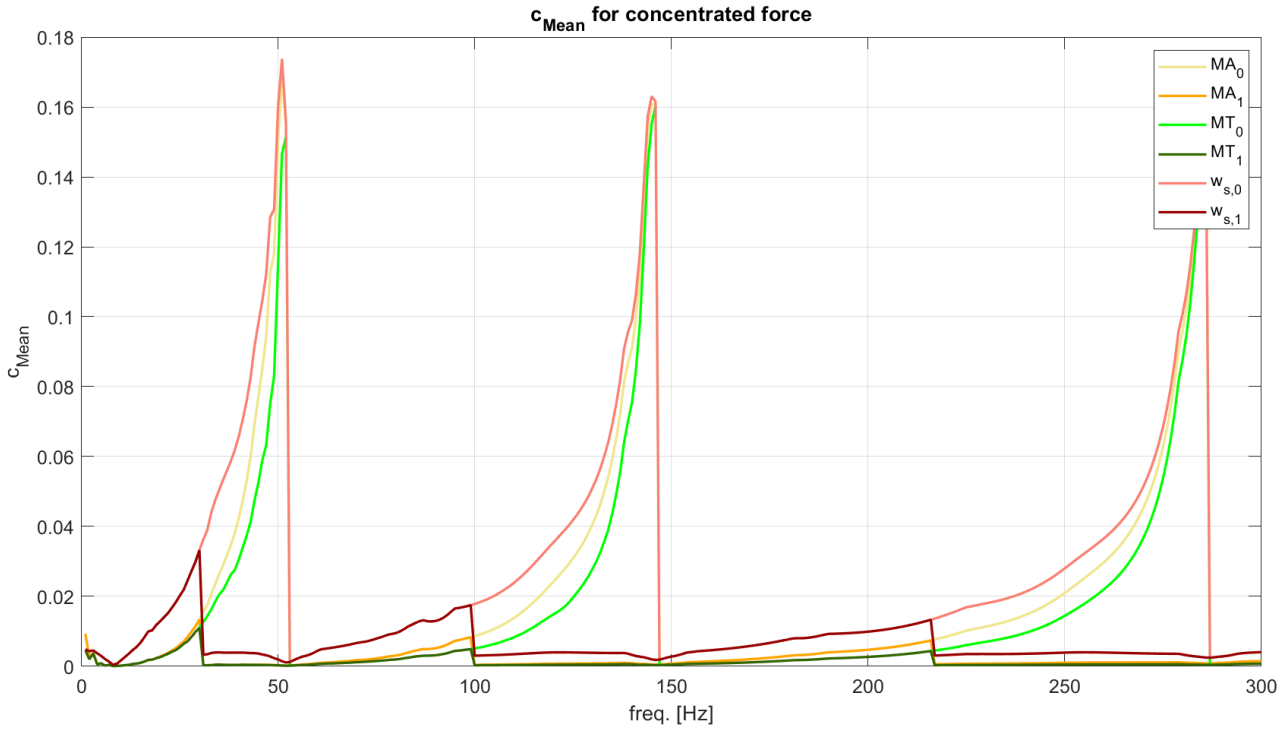

*Figure 2.76: Comparison of c_{Mean} for **approach 0** (pedicle '0') and **approach 1** (pedicle '1') for the **concentrated force** as a function of force's frequency.*

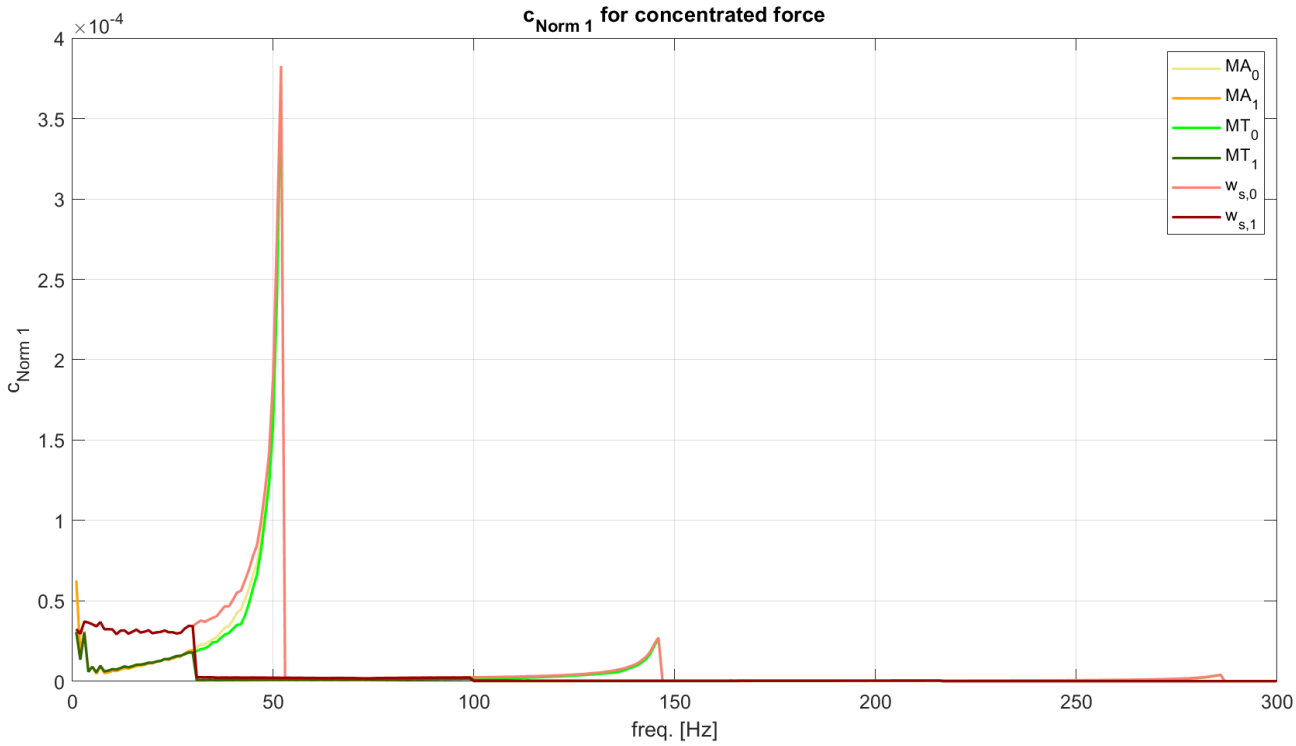

*Figure 2.77: Comparison of $c_{Norm\ 1}$ for **approach 0** (pedicle '0') and **approach 1** (pedicle '1') for the **concentrated force** as a function of force's frequency.*

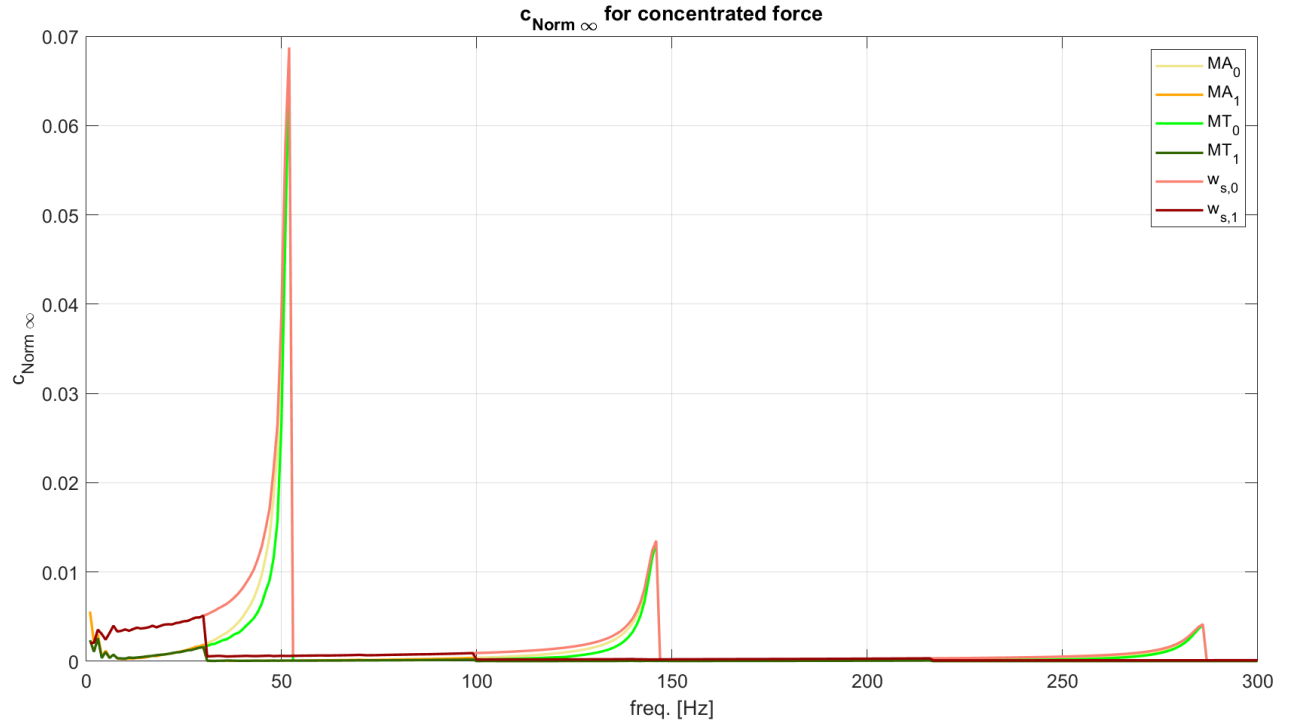

*Figure 2.78: Comparison of $c_{Norm\ \infty}$ for **approach 0** (pedicle '0') and **approach 1** (pedicle '1') for the **concentrated force** as a function of force's frequency.*

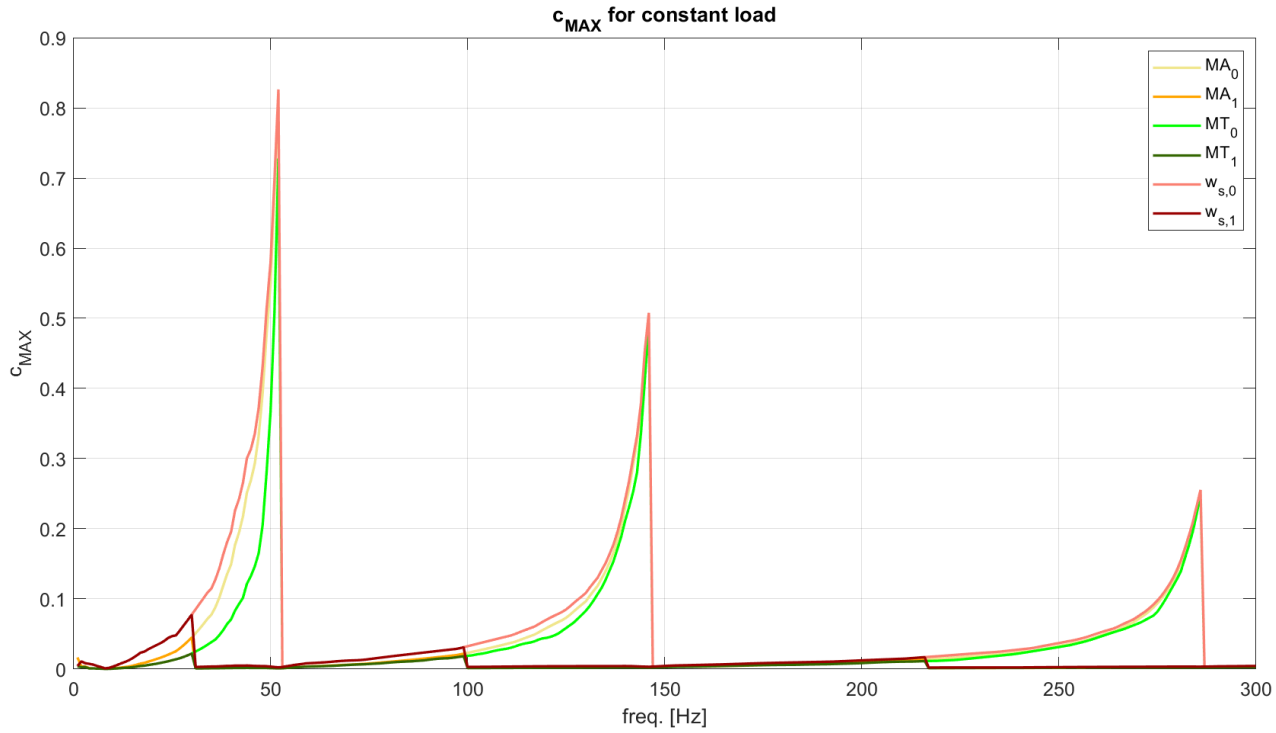

*Figure 2.79: Comparison of c_{MAX} for **approach 0** (pedicle '0') and **approach 1** (pedicle '1') for the **constant load** as a function of load's frequency.*

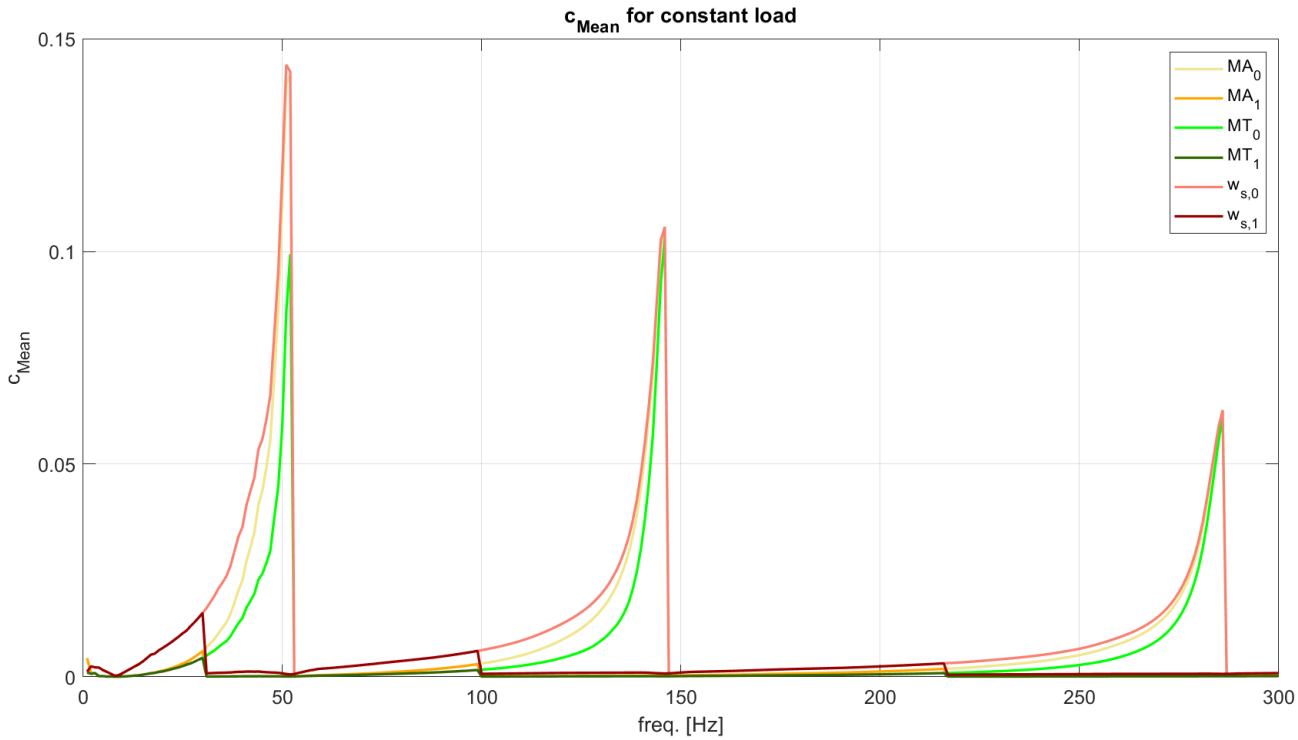

*Figure 2.80: Comparison of c_{Mean} for **approach 0** (pedicle '0') and **approach 1** (pedicle '1') for the **constant load** as a function of load's frequency.*

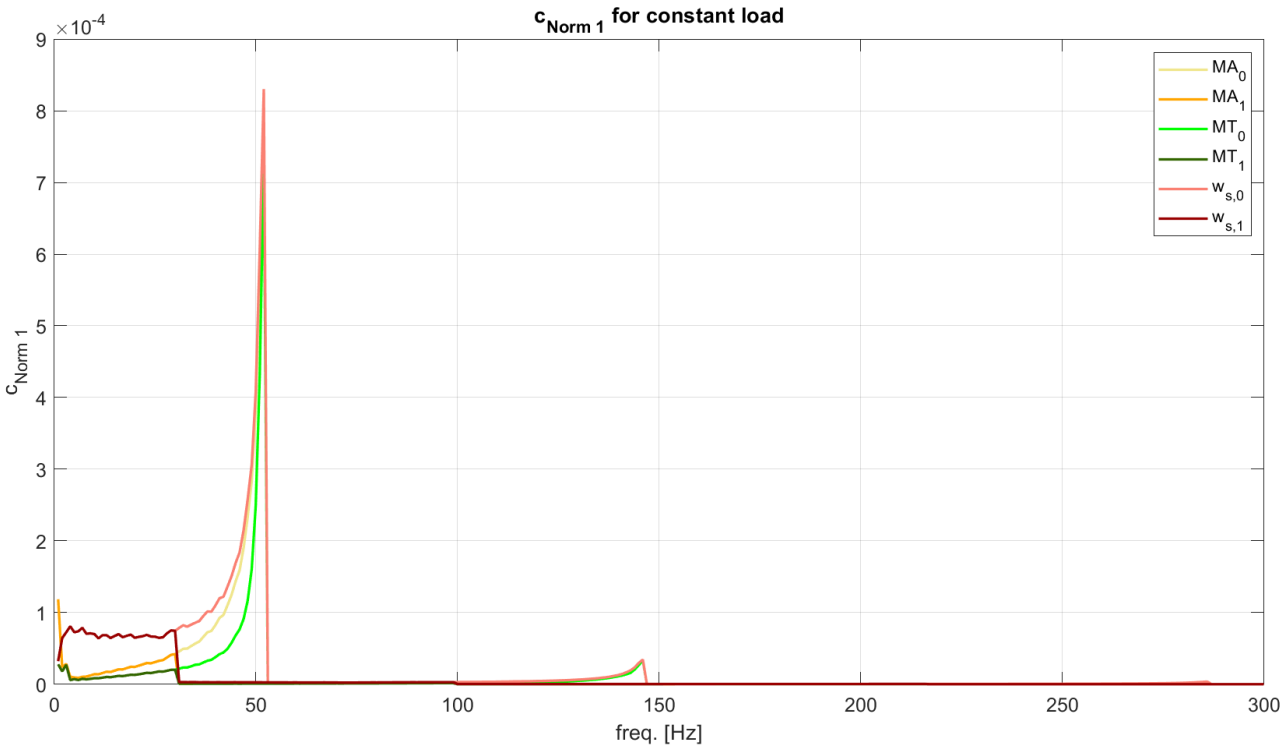

*Figure 2.81: Comparison of $c_{Norm\ 1}$ for **approach 0** (pedicle '0') and **approach 1** (pedicle '1') for the **constant load** as a function of load's frequency.*

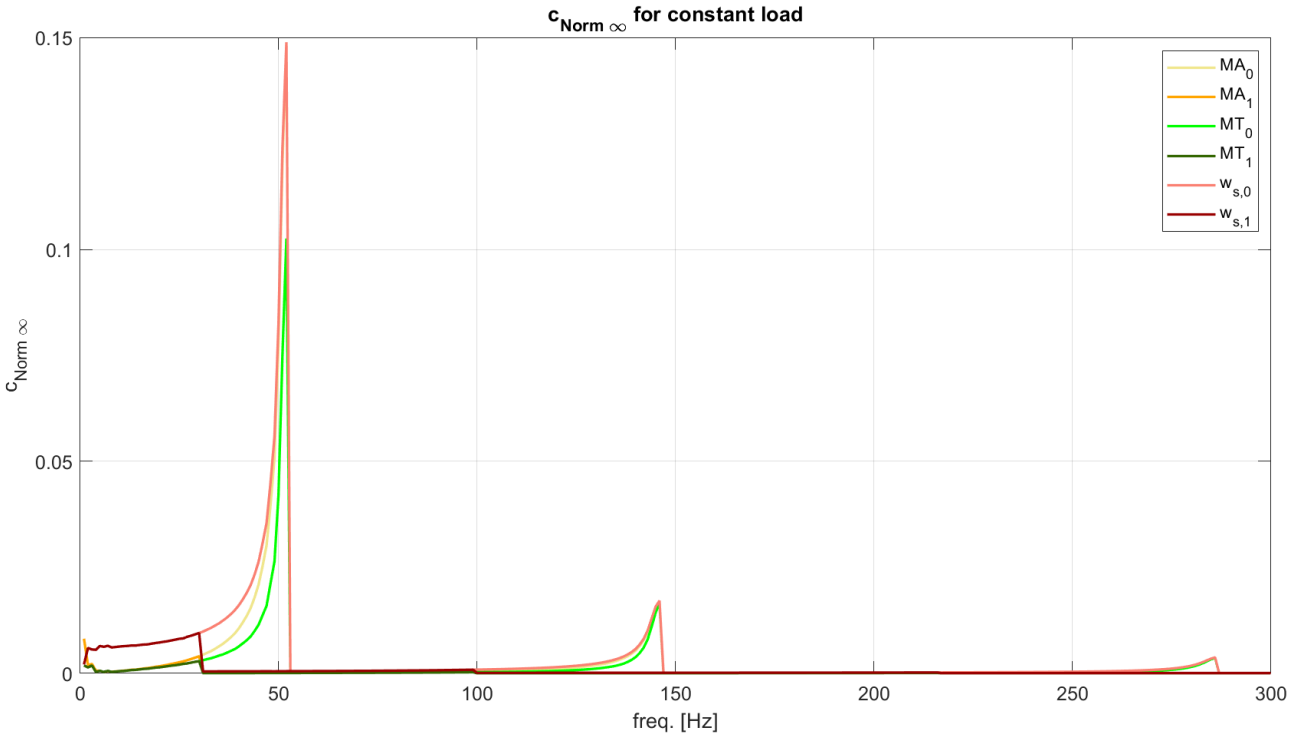

*Figure 2.82: Comparison of $c_{Norm\ \infty}$ for **approach 0** (pedicle '0') and **approach 1** (pedicle '1') for the **constant load** as a function of load's frequency.*

*Figure 2.83: Comparison of c_{MAX} for **approach 0** (pedicle '0') and **approach 1** (pedicle '1') for the **triangular load** as a function of load's frequency.*

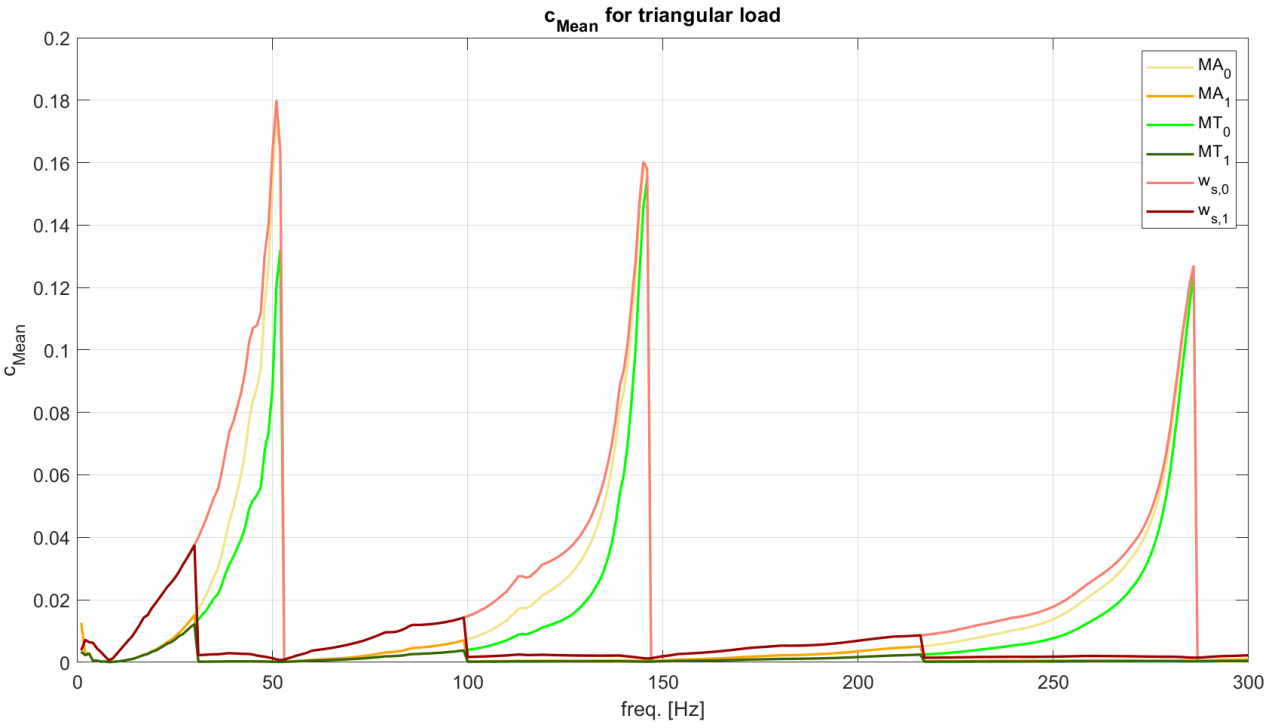

*Figure 2.84: Comparison of c_{Mean} for **approach 0** (pedicle '0') and **approach 1** (pedicle '1') for the **triangular load** as a function of load's frequency.*

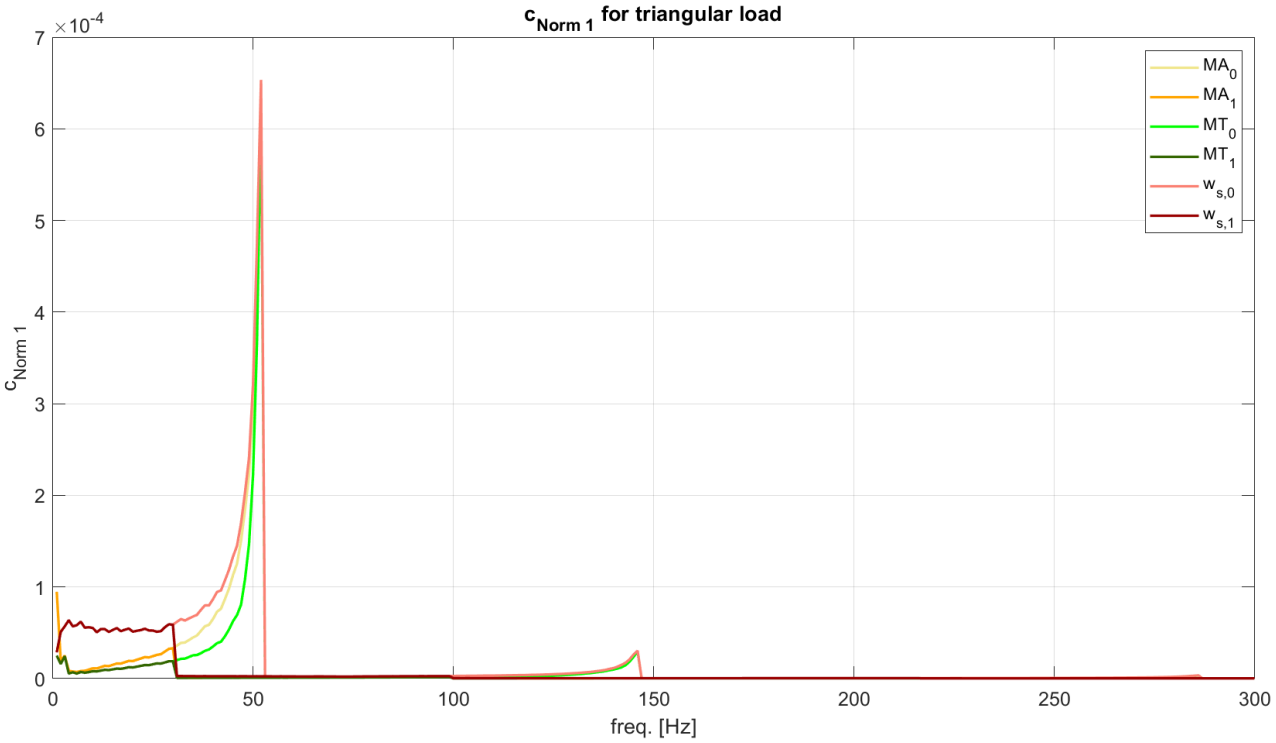

*Figure 2.85: Comparison of $c_{Norm\ 1}$ for **approach 0** (pedicle '0') and **approach 1** (pedicle '1') for the **triangular load** as a function of load's frequency.*

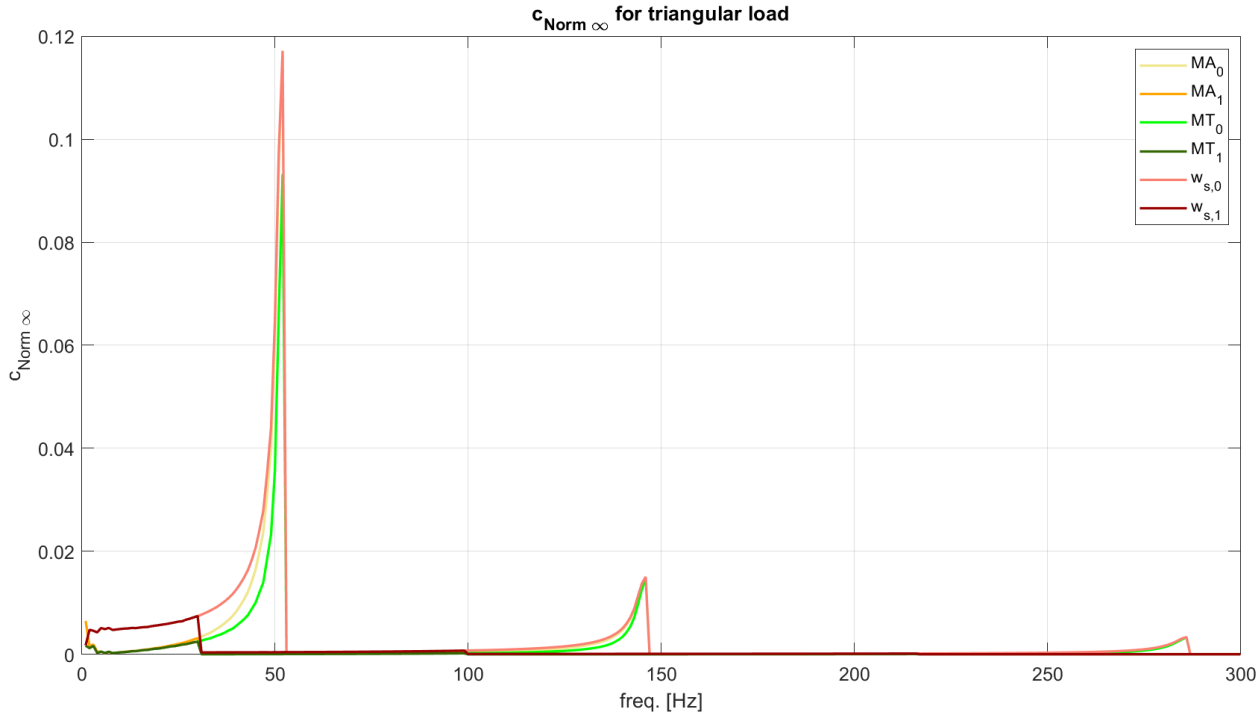

*Figure 2.86: Comparison of $c_{Norm\ \infty}$ for **approach 0** (pedicle '0') and **approach 1** (pedicle '1') for the **triangular load** as a function of load's frequency.*

2.4.7. Conclusions

Approach 2 provides the best overall enhancements but is also the most expensive, computationally. On the other hand, approach 1 yields significant benefits only when the next modal shape is added. Introducing another mode strategically could offer advantages, as it does not necessarily need to be introduced at the averaged frequency. For example, it could be introduced at one-third of the distance between two contiguous modal frequencies, however, this depends on the chosen enhancement criterion.

The enhancement criterion could aim to improve outputs when one or more performance coefficients reach a certain threshold value, or when the impact of the improvement would be more beneficial compared to the solution without residual vectors (w_s). For instance, approach 0 does not provide strategic benefits since it introduces another mode where the error of MT or MA is practically the same of the error obtained with w_s. In contrast, approach 1 introduces another mode where the errors of MT and MA methods are approximately half of the error of w_s. Therefore, an enhancement threshold could be implemented to improve the solution when the error of the residual vector method chosen exceeds a certain portion of the error obtained without any residual vector, making its use still meaningful.

Clearly, the enhancement criterion could consist of a combination of the criteria mentioned above: analytical studies on different systems and loading conditions could be made in order to determine how many modes to retain to offer the best possible solution at the lowest computational cost, however, this implies also the precise definition of the criterions necessary for the suggested optimization.

The problem arises when the spatial portion of the applied load is no longer simple or linear as in the presented cases, the approaches discussed may fail due to the excitation of modal shapes having frequencies well above the maximum frequency content of the load. An example of this is reported in the next paragraph.

2.5. Considering a particular force

Let's consider a Global force structured as:

$$F_w^{(G)} = \{\, 0{,}0,\ \ -\mathbf{700},\ 0,\ \ 0{,}0,\ \ 0{,}0,\ \ \mathbf{140},0,\ \ 0{,}0,\ \ -\mathbf{45},0,\ \ -1.7{,}0,\ \ -\mathbf{8},\ 0,\ \ 0{,}0,\ \ \mathbf{7.1},\ 0\,\}^T\ [N, N\cdot m, \dots]$$

In the equation above are paired the solicitations applied on each DOF (concentrated forces and moments, respectively). The values of the force $F_w^{(G)}$ were chosen so that the static associated was purposely similar to one of the beam's modal shapes, in order to excite it.

The static displacement results and the reference modal shape are reported in Figure 2.87:

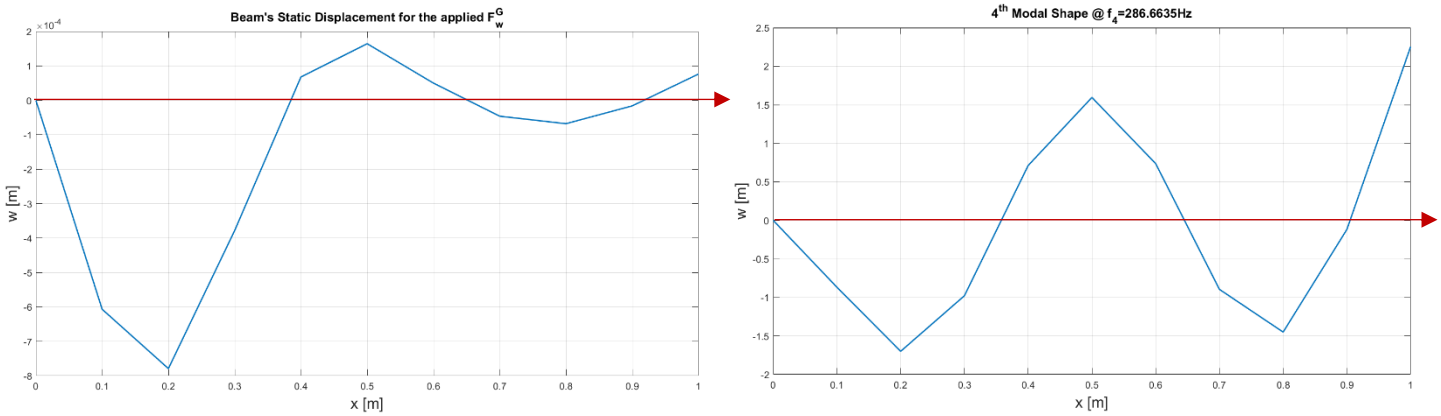

Figure 2.87: Comparison between the beam's static displacement for the applied $F_w^{(G)}$ and the 4^{th} modal shape.

The performance coefficients defined in paragraph 2.4.1 are reported in Figures 2.88-2.91 for the specified spatial force at different frequencies for approaches 0 and 1. The chosen frequency span for the analyses is $f = 0 - 600\ Hz$.

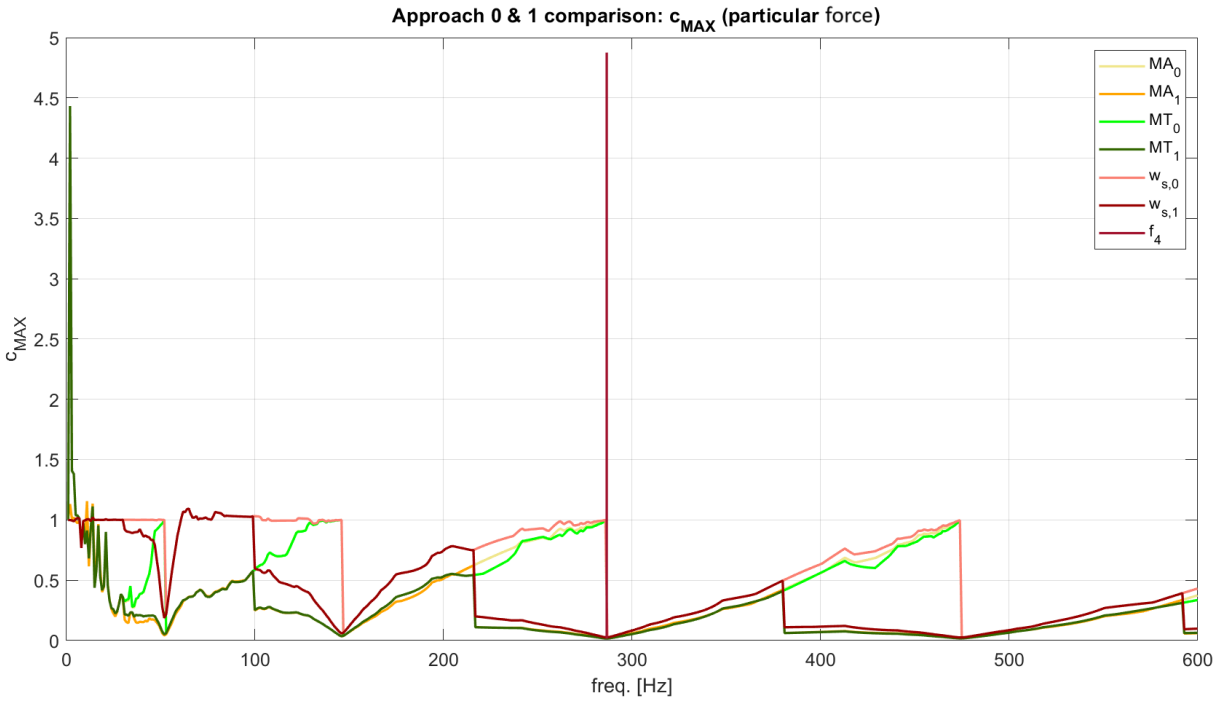

*Figure 2.88: Comparison of c_{MAX} for **approach 0** (pedicle '0') and **approach 1** (pedicle '1') for the **particular force** as a function of force's frequency.*

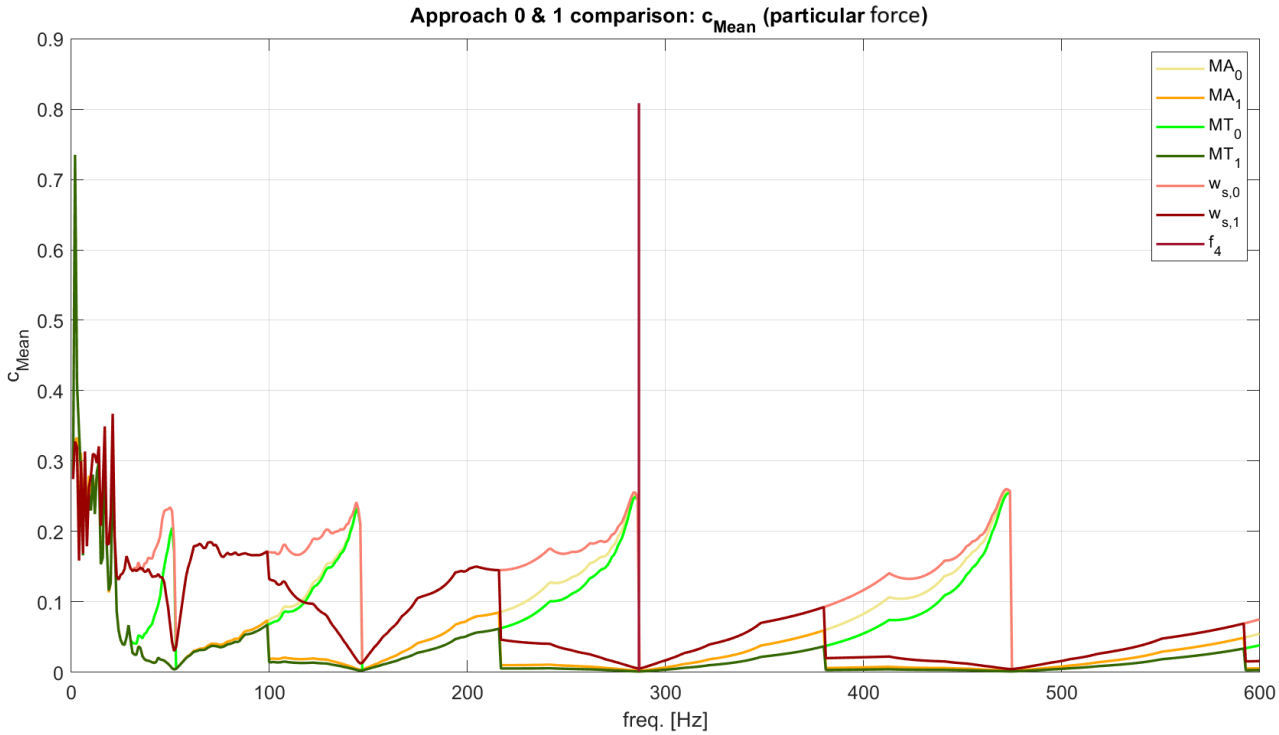

*Figure 2.89: Comparison of c_{Mean} for **approach 0** (pedicle '0') and **approach 1** (pedicle '1') for the **particular force** as a function of force's frequency.*

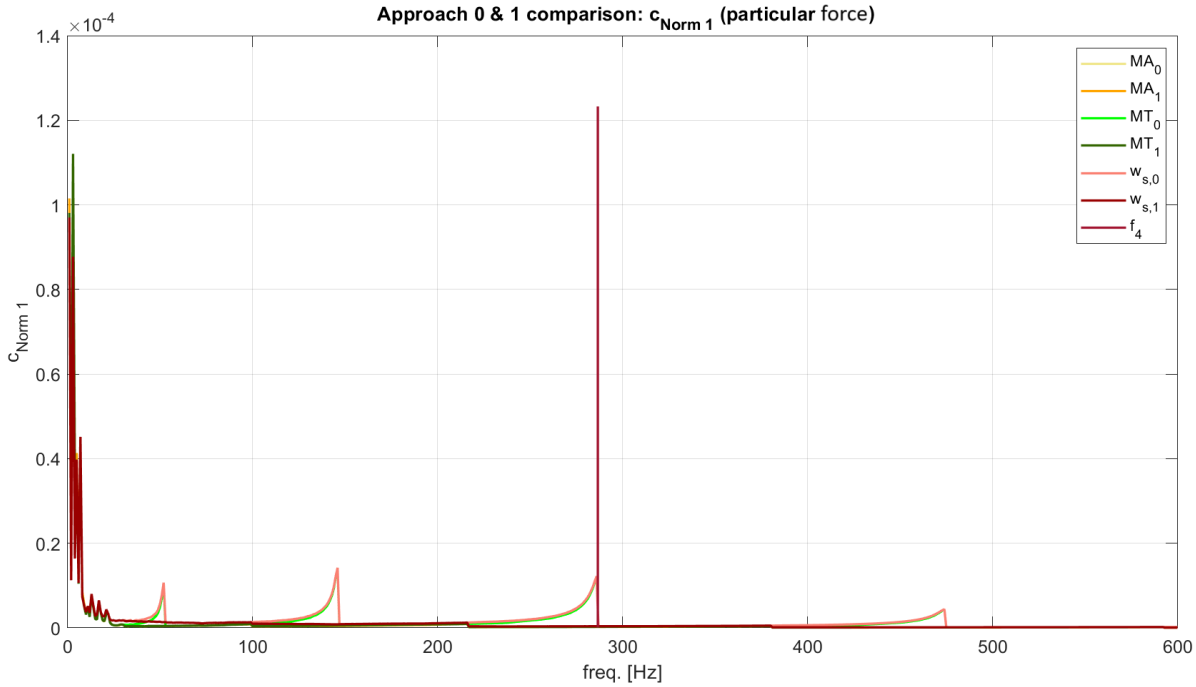

*Figure 2.90: Comparison of $c_{Norm\ 1}$ for **approach 0** (pedicle '0') and **approach 1** (pedicle '1') for the **particular force** as a function of force's frequency.*

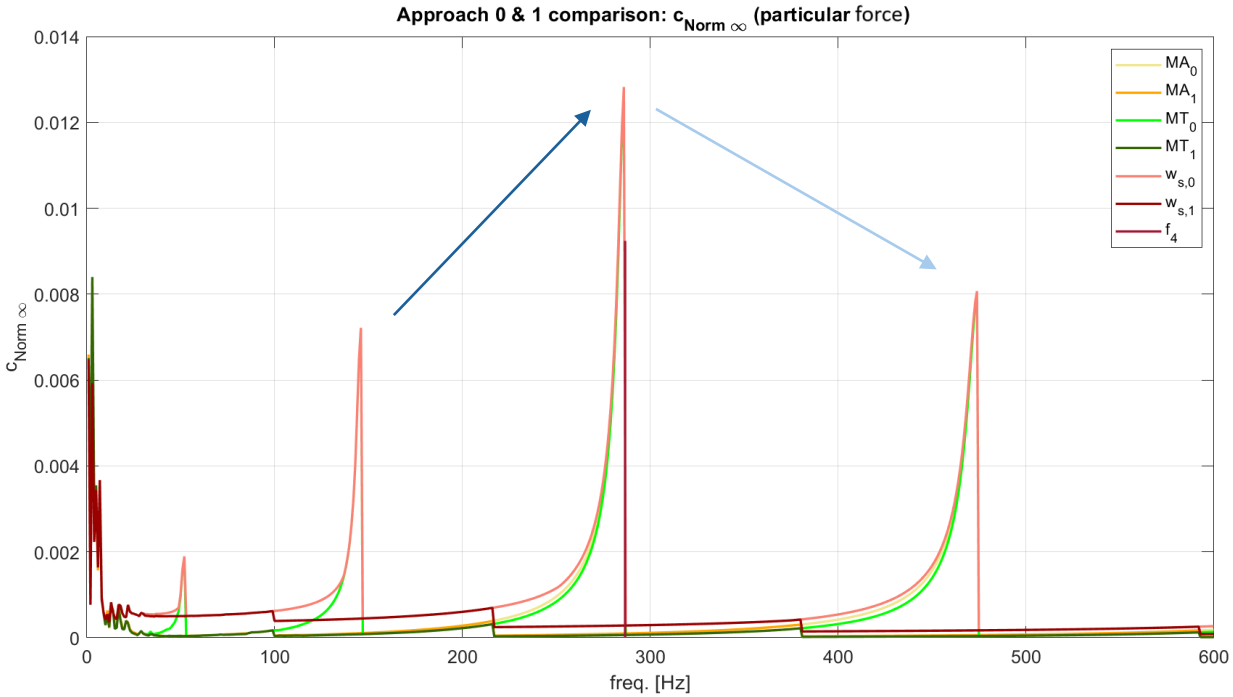

Figures 2.91: Comparison of $\boldsymbol{c_{Norm\,\infty}}$ *for* ***approach 0*** *(pedicle '0') and* ***approach 1*** *(pedicle '1') for the* ***particular force*** *as a function of force's frequency.*

In the reported simulations the errors were analysed before and after the fourth mode retention. It is important to note that the errors are very large for the MT method when only the first mode is retained and the frequency is really low. All the coefficients oscillate until the second mode is reached. For $n_{RM} < 4$, c_{MAX} rapidly increases until its peak level of 1, however, this increment is less evident for the MA and MT methods. The main difference with the simulations reported in paragraph 2.4 is that c_{MAX} here increases similarly to a logarithmic-like function instead of an exponential-like one, however, upon retaining the fourth mode, it increases linearly. c_{Mean} also experiences a slight decrease of the slope after the 4th modal shape retention and, before its retention, has values higher than those relative to the cases analysed in the previous paragraphs. c_{Mean} is generally higher for the MA method than for the MT method.

It is also observed that at the resonance frequency, the dynamic displacements were relatively well characterized (for MT and MA methods in particular). Furthermore, it can be hypothesized that when one or more retained modes vaguely match the static displacement result associated to the spatial force, a general improvement of the solution can be observed. In the simulations is evident that the MT method gives the best results at higher frequencies and both methods globally improve the results obtained by not using any residual vector (w_s), however at lower frequencies, the error obtained by the MT method is the largest due to the incorrect representation of the displacement of the beam in the range $x = 0 - 0.4\,m$.

$c_{Norm\,1}$ And $c_{Norm\,\infty}$ peaks increase until the 4^{th} mode is retained, then they start to decrease. For the latter this is more evident. However, their trend is similar, indicating a generally better response reconstruction after the 4th mode retention from both time and spatial domain perspectives.

Overall, approach 1 provides here a substantial enhancement of the solution for MA and MT methods. While the effects of approach 1 are less evident on the w_s coefficients due to their rapid increase. For instance, for approach 1 the peaks of c_{MAX} and c_{Mean} improve by up to 70% relatively to those obtained using approach 0 for MT and MA methods, while the enhancements are still not sufficient to well represent the w_s solution at each force's frequency, giving marginal benefits only on the frequency domain portion where a further

mode is retained and after the 4th mode retention. Differently from the results obtained in paragraph 2.4 where the effects of approach 1 were always evident on w_s.

In conclusion, for each case analysed, approaches 1 and 2 denote the capabilities of the MT and MA methods of improving the w_s solution, with MT being slightly better than the MA method, in every aspect and circumstance, except for really low numbers of retained modes, where the peaks of c_{MAX} and c_{Mean} can reach values 4 times higher than for MA and w_s.

3. Study of an aircraft wing section using the Residual Vectors methods already available in Nastran

3.1. Structural Model

The main goal of this chapter is to study the differences between the methods that use the concept of residual vectors already implemented in MSC Patran/Nastran. The model used in these analyses is a wing section with a NACA 2414 airfoil composed of 4 ribs and 3 spars, predominantly made of multilayer composites.

The geometry of the model and composite's orientation are reported in Figure 3.1, while material properties and the composite stacking sequences are reported in Tables 3.1 and 3.2, respectively.

Material:	Tooray – TCA T700S-12K-50C/#2510 Plain Weave Fabric $E_{11} = 55\ GPa$ $E_{22} = 55\ GPa$ $\nu_{12} = 0.04$ $G_{12} = 4.3\ GPa$ $G_{13} = 1\ GPa$ Ply thickness: $t = 0.00021\ m$

Table 3.1: Material properties.

Airfoil base shell:	$[0/+30/90\ /-30/0]_{(10s)}$
Stiffening shell, ribs and spars:	$[0/(45)_2/90]_{(10s)}$

Table 3.2: ply stacking sequences for the composites. The pedicle 's' implies symmetry.

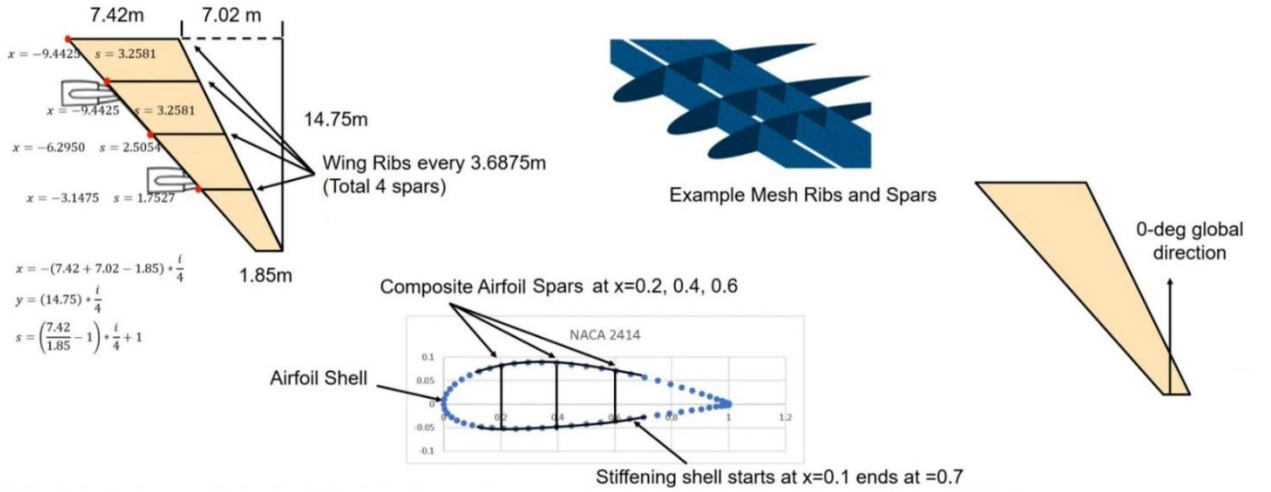

Figures 3.1: Wing geometry and features.

3.2. Model Creation

The model main geometric points were defined in Matlab, distinguishing those belonging to the skin, the stiffening, and the spars' cores, then, they were added separately in MSC Patran as a starting point for the model creation. An impulse lasting 0.1 seconds was applied to the structure, it was deliberately chosen to only involve the first 4 modal frequencies. The cut-off frequency of the impulse is 28 Hz, defined as the frequency at which its Fourier Transform absolute value reaches 1/100 of the peak value. The third and fourth modal frequencies of the model are approximately 15 and 35 Hz indeed. It is important to note that skin panels near the trailing edge were removed due to their association with local deformation modal shapes, which were several and pervasive.

It was decided to remove this part instead of adding further reinforcements such as stringers or ribs in the proximity of the skin panels which constituted the trailing edge. The constraint used in the model is a full-fixity applied to the first rib at $x = 0\ m$, while, for the first simulation, the impulse was exclusively applied to node no. 2772, which belongs to the fourth rib. The obtained mesh is composed of 2167 nodes.

Loading, constraints, finite element mesh, and the first 5 modal shapes are shown in the following figures. The modal frequencies were also compared to the frequencies obtained by the study reported in Reference [*9*] to ensure the validity of the current modal shapes, 2 extracts are reported in Figures 3.13 and 3.14.

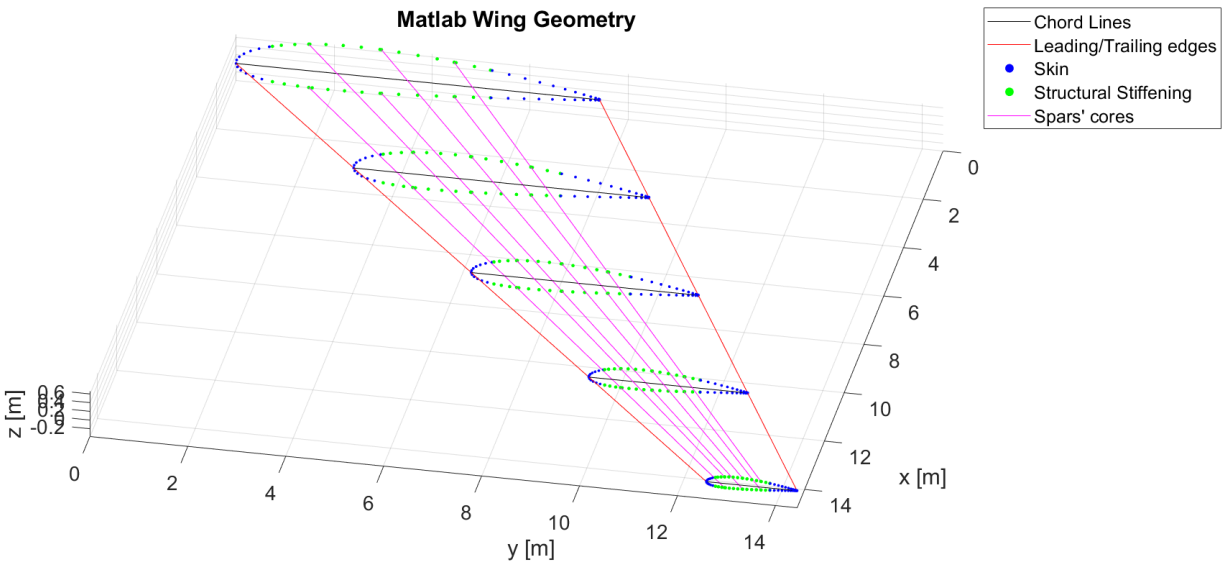

Figure 3.2: Geometric points reconstruction in Matlab. They are subsequently imported in MSC Patran to create in order: lines, surfaces, constraints, material properties associated to the geometry and finally the mesh.

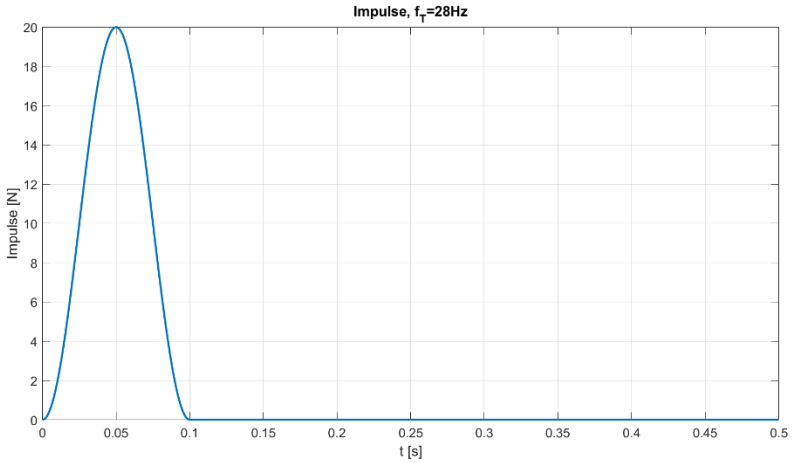

Figure 3.3: Impulse applied on the structure; $f_{T,1} = 28\ Hz$.

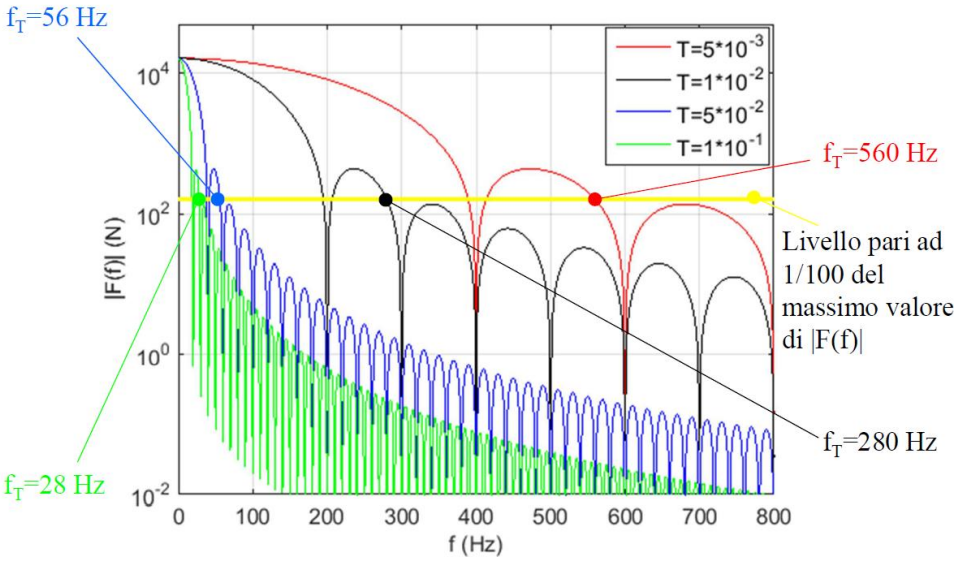

*Figure 3.4: Fourier Transform and cut frequencies for different impulses, the **lime-green** and **blu** impulses will be used in the first and second simulations, respectively presented in paragraphs 3.5 and 3.6. (extracted from Ref.* [*10*]*)*

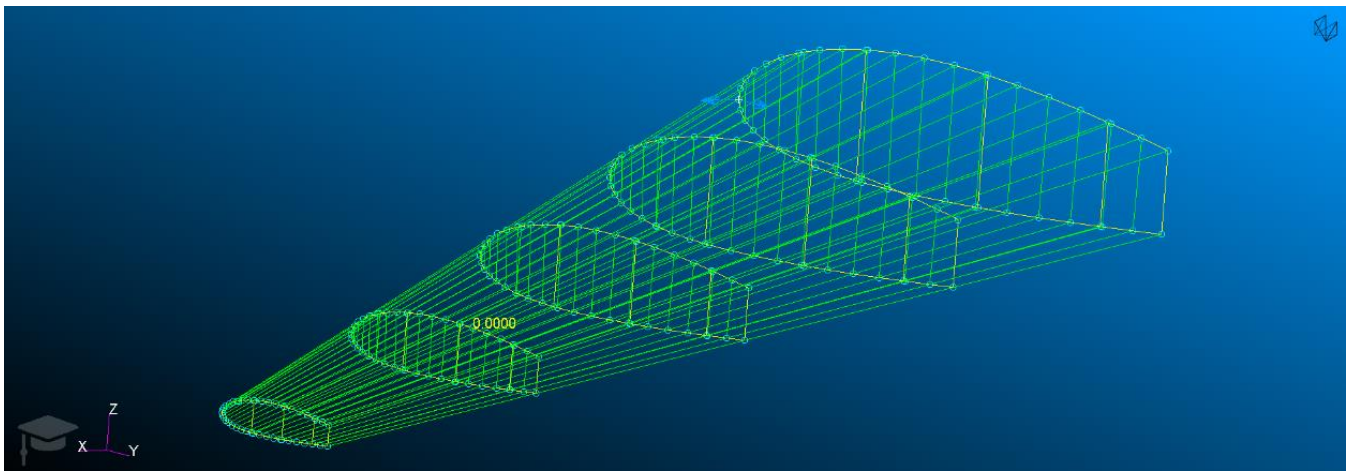

Figure 3.5: Model's geometry created in MSC Patran.

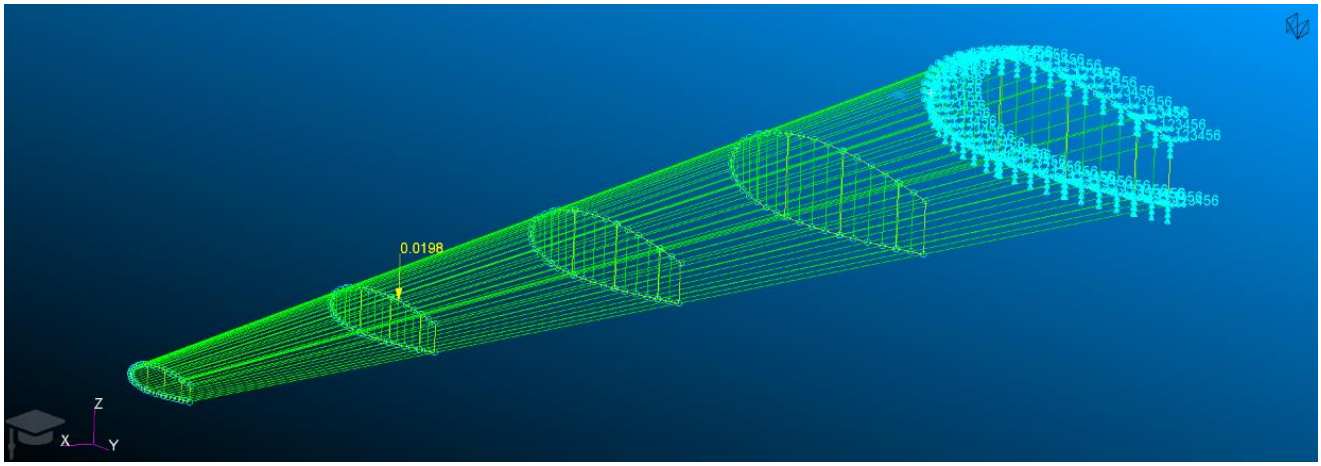

Figure 3.6: Constraints (Perfect Joint) and force applied to the model's geometry [force displayed at $t = 0.001\ s$].

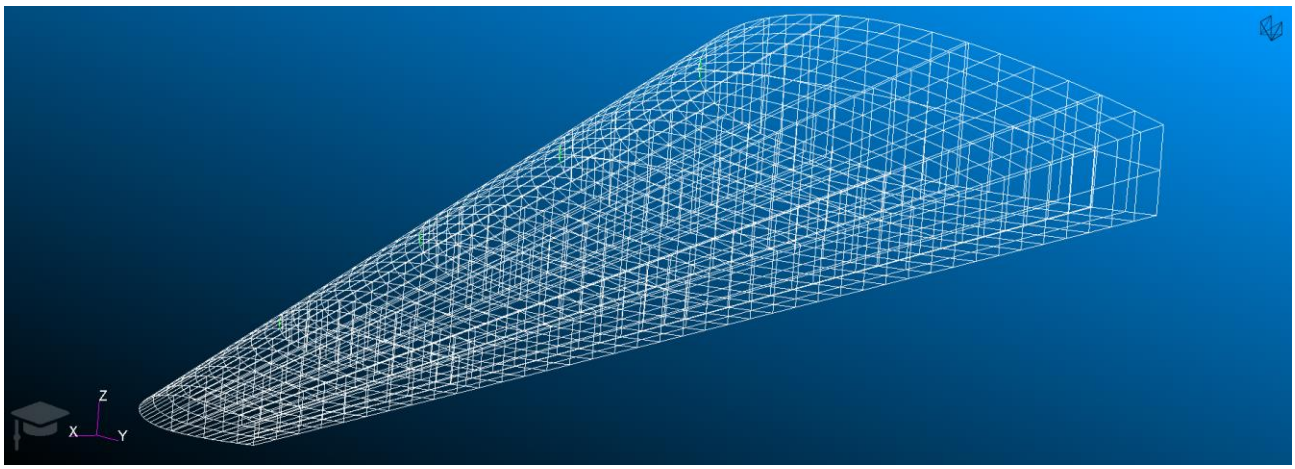

*Figure 3.7: Final structure's finite element mesh with **2167 nodes**.*

3.3. Modal Analysis

Figures 3.8-3.12 report the first 5 modal shapes used in both simulations, which are presented in paragraphs 3.5 and 3.6.

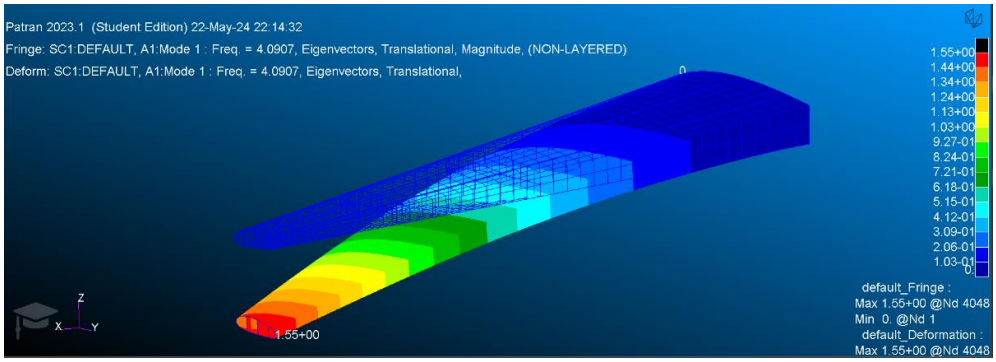

*Figure 3.8: Model's **first** modal shape at $f_1 = 4.091\ Hz$.*

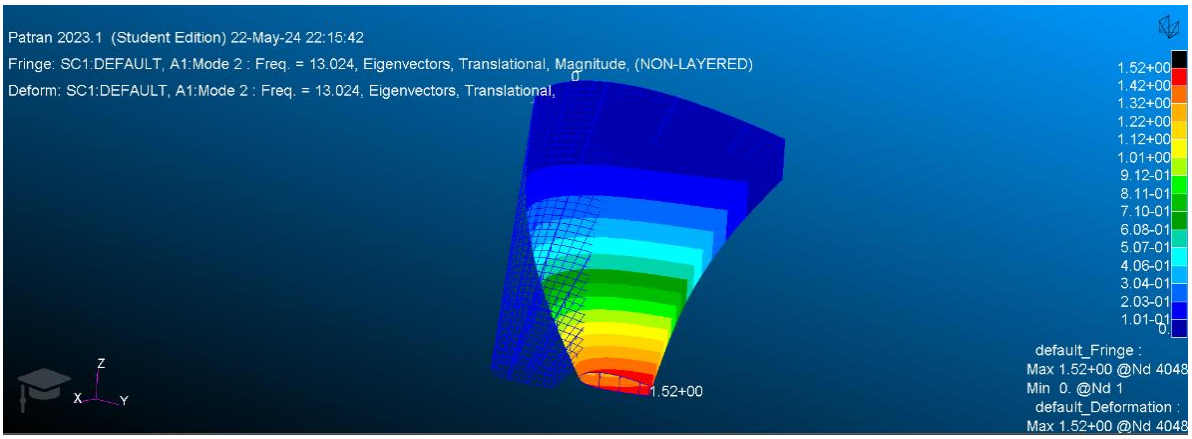

*Figure 3.9: Model's **second** modal shape at $f_2 = 13.024\ Hz$.*

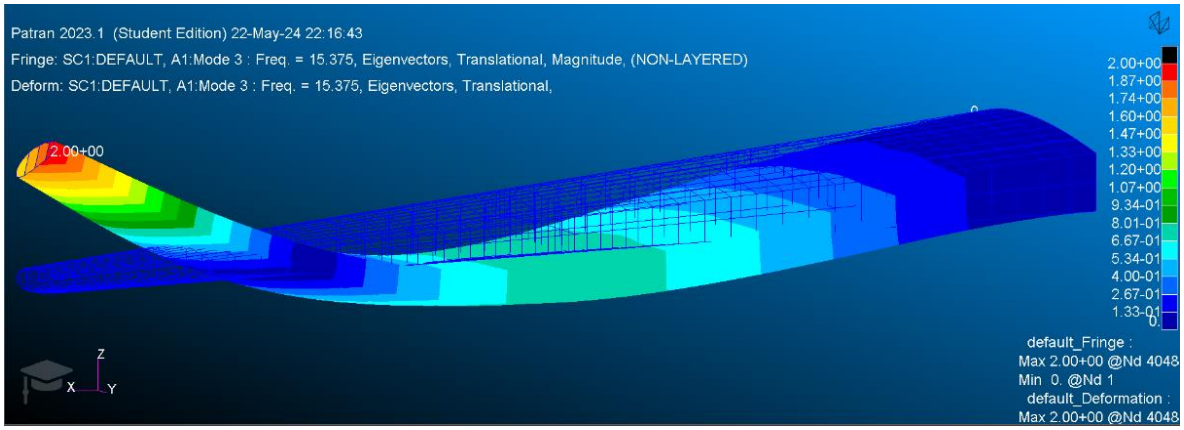

*Figure 3.10: Model's **third** modal shape at $f_3 = 15.375\ Hz$.*

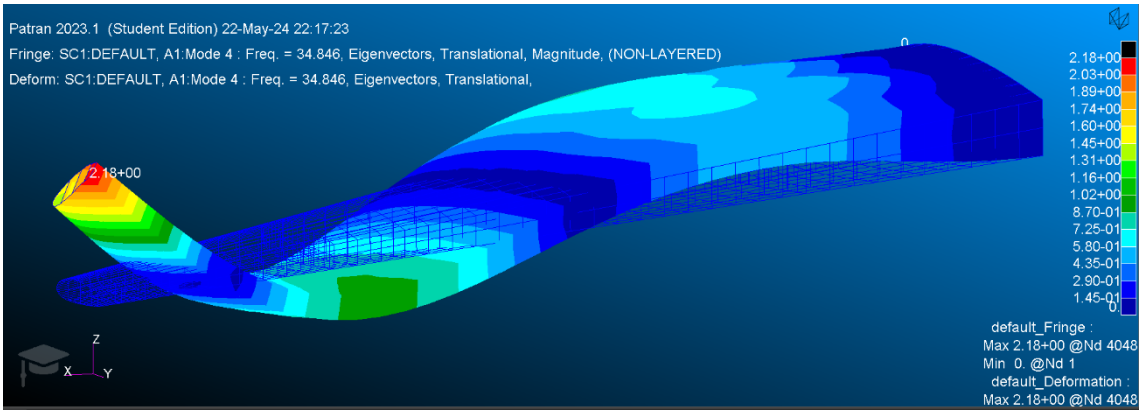

*Figure 3.11: Model's **fourth** modal shape at $f_4 = 34.846\ Hz$.*

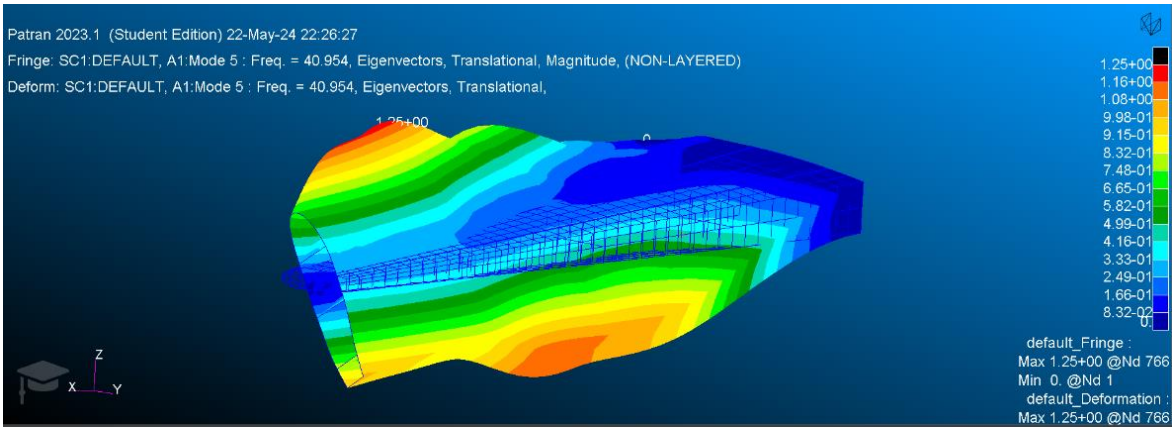

*Figure 3.12: Model's **fifth** modal shape (torsional) at $f_5 = 40.954\ Hz$.*

Here are reported 2 extracts from Ref. [*9*], which define typical modal frequency ranges for aeronautical wings.

First modal analysis (natural frequencies) of the wing including engine and the wig-let is carried out using ANSYS ver 15. It is decided to obtain the natural frequencies between 0-300 Hz so that it can be simulated with the engine operating frequencies for resonance analysis. We obtained 60 frequencies (modes) in the range 0-300 Hz. Typically, modal analysis of the fifth mode *f*=13Hz is shown in the Fig.3. To indicate all the modal frequencies, a plot of the maximum amplitude vs. modal frequencies is shown in the Fig.4

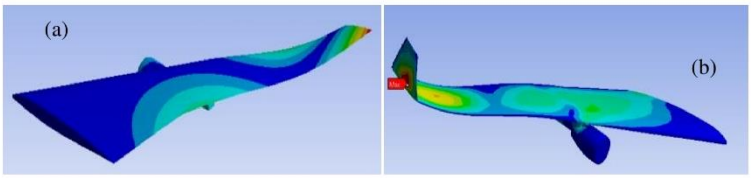

Fig.3 Typically (a) modal analysis (b) von Mises stress distribution of the fifth mode *f*=13Hz

*Figure 3.13: Example of typical modal frequencies for an aeronautical wing (**extract 1** from Ref. [9]).*

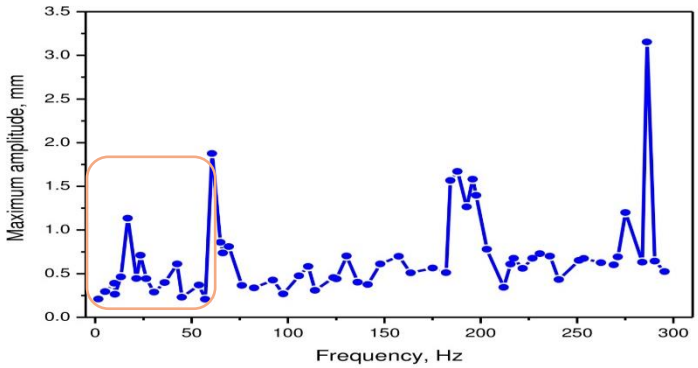

Fig.4. Maximum amplitude vs. modal frequencies

*Figure 3.14: Typical modal frequencies for a wing (**extract 2** from Ref. [9]). The orange box denotes the presence of multiple modes in the first 50 Hz, validating the modal frequency values obtained for the current analysis.*

3.4. RESVEC function configurations

3.4.1. The RESVEC function

Different configurations of the MSC Nastran RESVEC function were evaluated for the defined problem at different numbers of retained modes. The main goal was to compare the two methods implemented in MSC Nastran: The Modal Truncation Augmentation method, which was already analysed in previous chapters, and the 'Inertia Relief-based' method, which is arbitrarily named so by the author of the thesis based on the MSC Nastran's manual definitions (Figure 3.15). The method name will be shortened to Inertia Relief (IR) from now on, not to be confused with homonym method, which is used to study non-constrained structures, however the 2 methods may share a common logic [*11*]. It consists in applying 6 accelerations (3 translational and 3 rotational) to the structure and then obtain the associated distributed loadings: for each of them it is calculated the MT vector associated. In Patran, these methods are used simultaneously by default by the RESVEC function to optimize the calculation of the dynamic response. The results will show that this approach is the most effective but requires the highest computational cost.

However, it is difficult to determine which of the two methods mentioned is better because it depends on the perspective and the dynamic forces applied to the system. The following paragraphs attempt to shed light on this problem by analyzing and comparing the methods IR, MT, IR+MT (RESVEC = YES configuration), and the solution without any Residual Vectors implementation (RESVEC = NO configuration). All the Residual Vectors were allowed to dynamically respond to the defined loading and were calculated based on the user-defined viscous damping (which was set to 3% of the critical viscous damping coefficient). In the Patran manual, no further information could be found on the meaning of RVDOFi (Figure 3.15), which could be connected to the super element definition (not used in the presented simulations). Anyway, as reported in Figure 3.16, it seems to be irrelevant for the analysis purposes.

3.4.2. RESVEC configurations

The different commands used for the different methods mentioned in paragraph 3.4.1 are reported below and an extract from the MSC Nastran's manual, regarding the function RESVEC, is reported in Figure 3.15:

For no residual vector calculation: **RESVEC = NO**
For the standard Patran residual vector calculation: **RESVEC = YES**
For the calculation of the residual vectors based on inertial relief only: **RESVEC(INRLOD,NOAPPL,NOADJLOD,NORVDOF,DAMPLOD,DYNRSP) = YES**
For the calculation of the residual vectors using the Modal Truncation Augmentation method only: **RESVEC(NOINRL,APPLOD,NOADJLOD,NORVDOF,DAMPLOD,DYNRSP) = YES**

Table 3.3: RESVEC configurations used in paragraph 3.5 and 3.6.

RESVEC Controls Residual Vectors

Specifies options for and calculation of residual vectors.

Format:

$$\text{RESVEC}\left[\left(\begin{bmatrix}\text{INRLOD}\\ \text{NOINRL}\end{bmatrix},\begin{bmatrix}\text{APPLOD}\\ \text{NOAPPL}\end{bmatrix},\begin{bmatrix}\text{ADJLOD}\\ \text{NOADJLOD}\end{bmatrix}\begin{bmatrix}\text{RVDOF}\\ \text{NORVDO}\end{bmatrix},\begin{bmatrix}\text{DAMPLOD}\\ \text{NODAMP}\end{bmatrix},\begin{bmatrix}\text{DYNRSP}\\ \text{NODYNRSP}\end{bmatrix}\right)\right] = \begin{Bmatrix}\text{SYSTEM/NOSYSTEM}\\ \text{COMPONENT/NOCOMPONENT}\\ \text{BOTH or YES}\\ \text{NO}\end{Bmatrix}$$

Examples:

```
RESVEC=SYSTEM
RESVEC(NOINRL)=COMPONENT
RESVEC=NO
```

Describer	Meaning
INRLOD/ NOINRL	Controls calculation of residual vectors based on inertia relief (Default = INRLOD).
APPLOD/ NOAPPL	Controls calculation of residual vectors based on applied loads (Default = APPLOD).
ADJLOD/ NOADJLOD	Controls calculation of residual vectors based on adjoint load vectors (SOL 200 only; Default = ADJLOD).
RVDOF/ NORVDOF	Controls calculation of residual vectors based on RVDOFi entries (Default = RVDOF).
DAMPLOD/ NODAMP	Controls calculation of residual vectors based on viscous damping (Default = DAMPLOD).
DYNRSP/ NODYNRSP	Controls whether the residual vectors will be allowed to respond dynamically in the modal transient or frequency response solution. See Remark 5. (Default = DYNRSP).
SYSTEM/ NOSYSTEM	Controls calculation of residual vectors for system (a-set) modes. For NOSYSTEM, describers inside the parentheses are ignored. See Remark 2. for default.
COMPONENT/ NOCOMPONENT	Controls calculation of residual vectors for component (superelement or o-set) modes. For NOCOMPONENT, describers inside the parentheses are ignored. See Remark 2. for default.

Figure 3.15: MSC Patran/Nastran manual on Residual Vectors function 'RESVEC'. (Ref. [12]*).*

```
n° Modal Shapes Retained = 2


RESVEC = YES

       3       3      9.343122E+03      9.665983E+01      1.538389E+01      1.000000E+00      9.343122E+03
       4       4      5.734279E+04      2.394635E+02      3.811181E+01      1.000000E+00      5.734279E+04
       5       5      7.235208E+04      2.689834E+02      4.281004E+01      1.000000E+00      7.235208E+04
       6       6      8.140323E+04      2.853125E+02      4.540890E+01      1.000000E+00      8.140323E+04
       7       7      1.876809E+05      4.332215E+02      6.894935E+01      1.000000E+00      1.876809E+05
       8       8      2.803132E+05      5.294462E+02      8.426397E+01      1.000000E+00      2.803132E+05
       9       9      3.287679E+05      5.733829E+02      9.125672E+01      1.000000E+00      3.287679E+05


RESVEC(INRLOD,APPLOD,ADJLOD,NORVDOF,DAMPLOD,DYNRSP) = YES

       3       3      9.343122E+03      9.665983E+01      1.538389E+01      1.000000E+00      9.343122E+03
       4       4      5.734279E+04      2.394635E+02      3.811181E+01      1.000000E+00      5.734279E+04
       5       5      7.235208E+04      2.689834E+02      4.281004E+01      1.000000E+00      7.235208E+04
       6       6      8.140323E+04      2.853125E+02      4.540890E+01      1.000000E+00      8.140323E+04
       7       7      1.876809E+05      4.332215E+02      6.894935E+01      1.000000E+00      1.876809E+05
       8       8      2.803132E+05      5.294462E+02      8.426397E+01      1.000000E+00      2.803132E+05
       9       9      3.287679E+05      5.733829E+02      9.125672E+01      1.000000E+00      3.287679E+05
```

Figure 3.16: RVDOF/NORVDOF subfunction comparison at the same $n°_{RM}$. The subfunction is the only change between the 2 RESVEC configurations.

Results denote no difference between the modal frequencies or modal shapes obtained enabling or disabling the RVDOF subfunction.

3.5. Analyses (transversal force)

3.5.1. RESVEC configurations applied to the wing model

The RESVEC configurations defined were used to study the wing section model under an impulsive force, the study was reiterated at different numbers of retained modes. In figures 3.17-3.27 are reported the total displacement in absolute value and the transversal displacement of the node n° 2772 (node where the impulse is applied) for different numbers of retained modes ($n°_{RM}$).

Displacements indicate that for $n°_{RM} = 1$ and $n°_{RM} = 2$ there is not a considerable difference, while at higher $n°_{RM}$ the total and transversal displacements start to pack together.

Furthermore, from the mentioned images, it can be observed that the MT method seems to better approximate the 'RESVEC = YES' solution at each number of retained modes for the current study, In fact, it seems to outperform the IR method for what concerns displacements accuracy. However, the 'IR' method could be more practical for preliminary studies though because it allows the calculation of 6 additional modal shapes without defining any loading case.

Anyway, these results must be contextualized, subsequent analysis (paragraph 3.6) will show that the MT and IR methods are both valid depending on the studied case. It is anticipated the IR method performs better when $n°_{RM}$ is very low and the spatial loading is complex but it generally necessitates a higher computational cost, which makes it, in this case, less convenient than directly calculating the solution using more original eigenvectors and applying the MT method instead.

Furthermore, it will be shown that the MT method aids in a better convergence to the ideal solution, which is not assured by the IR method and the 'RESVEC = NO' configuration. The 'RESVEC = YES' solution seems to be good independently from the $n°_{RM}$.

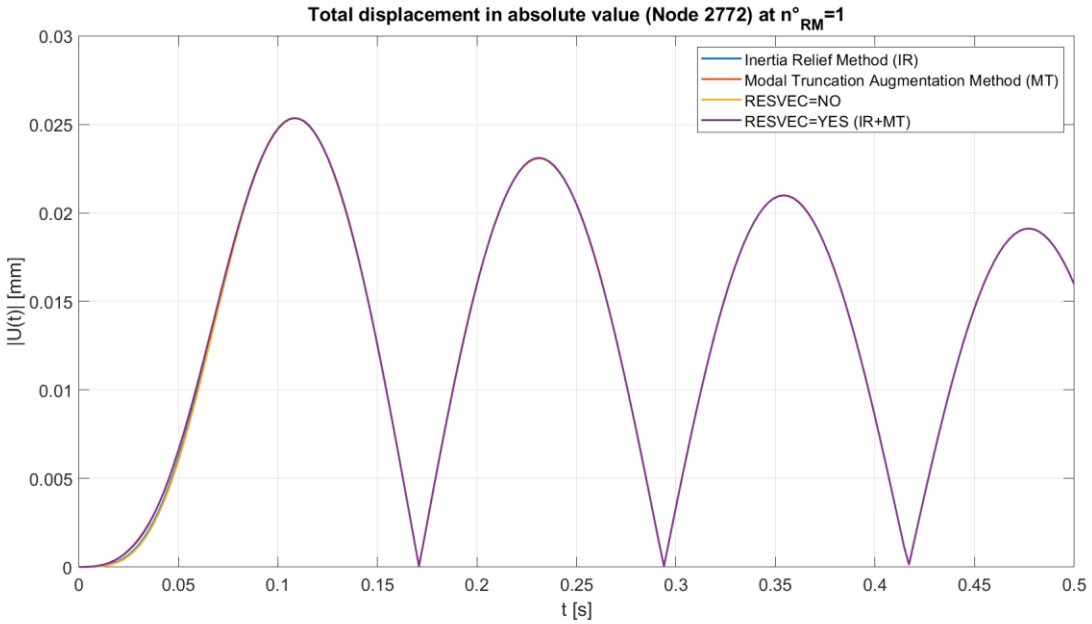

*Figure 3.17: Total displacement in absolute value for the central node **2772** at **1** retained mode.*

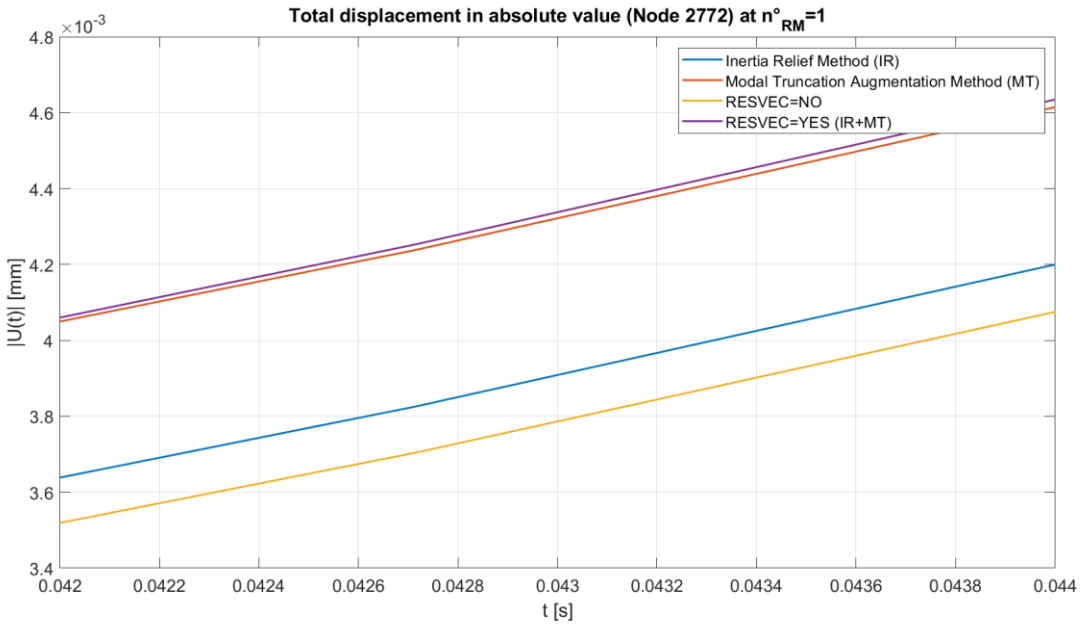

*Figure 3.18: Total displacement in absolute value for the central node **2772** at **1** retained-mode. (Zoomed).*

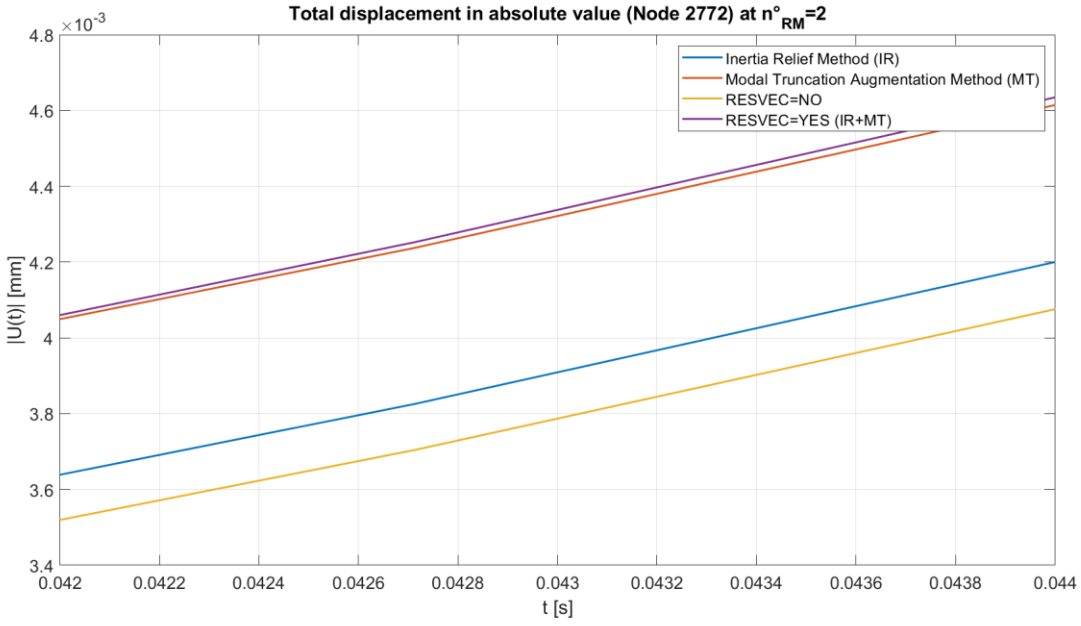

*Figure 3.19: Total displacement in absolute value for the central node **2772** at **2** retained modes. (Zoomed). No evident differences with the previous case where the number of retained modes $n°_{RM}$ was set to 1.*

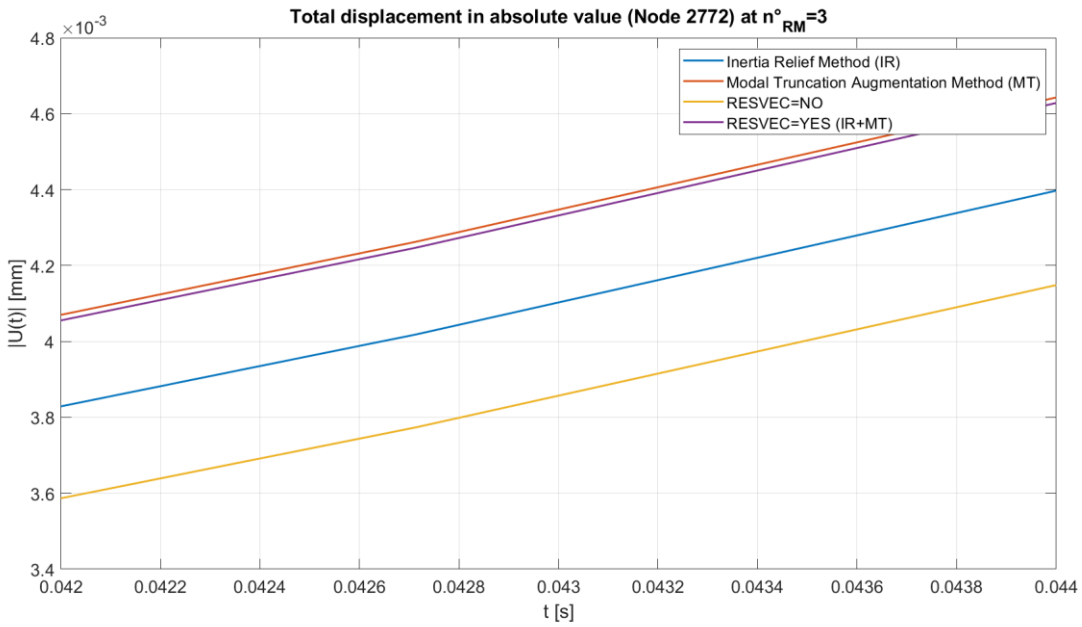

*Figure 3.20: Total displacement in absolute value for the central node **2772** at **3** retained modes. (Zoomed).*

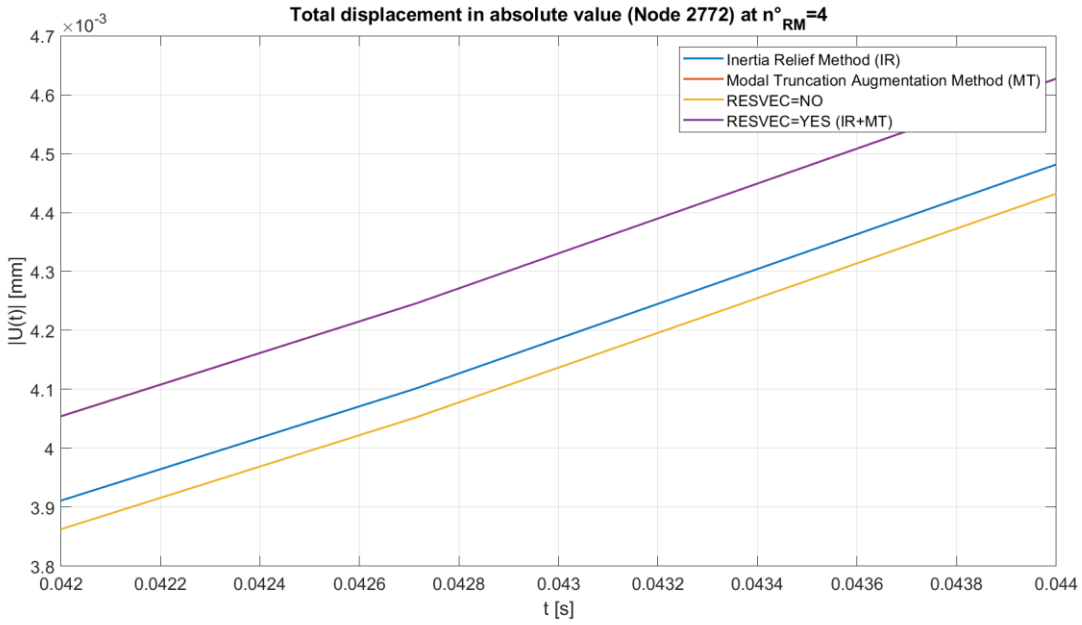

*Figure 3.21: Total displacement in absolute value for the central node **2772** at **4** retained modes. (Zoomed).*

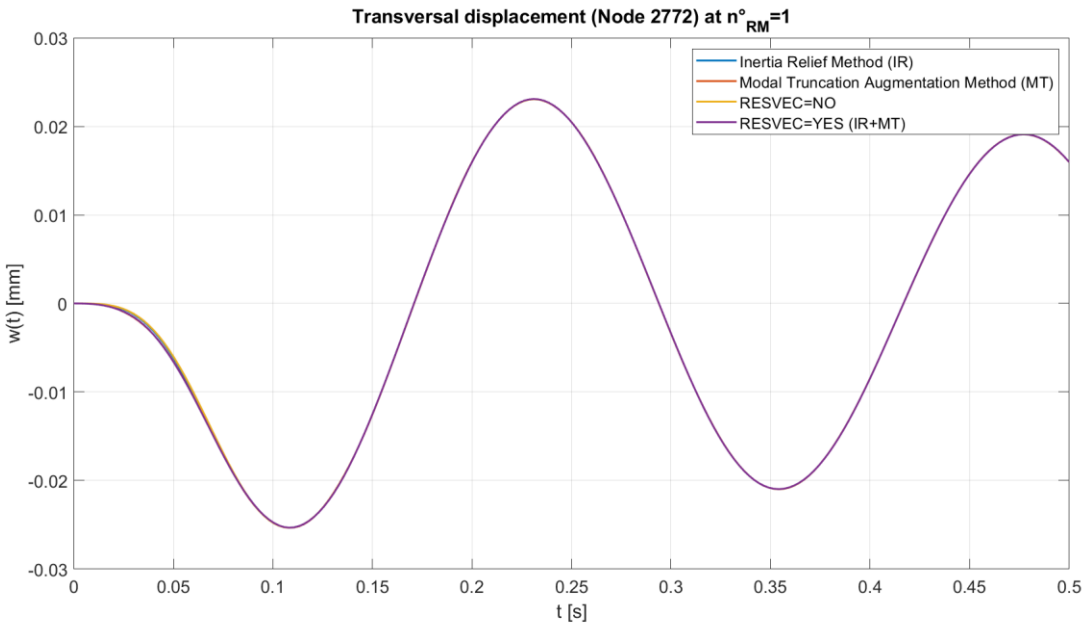

*Figure 3.22: Transversal displacement for the central node **2772** at **1** retained mode.*

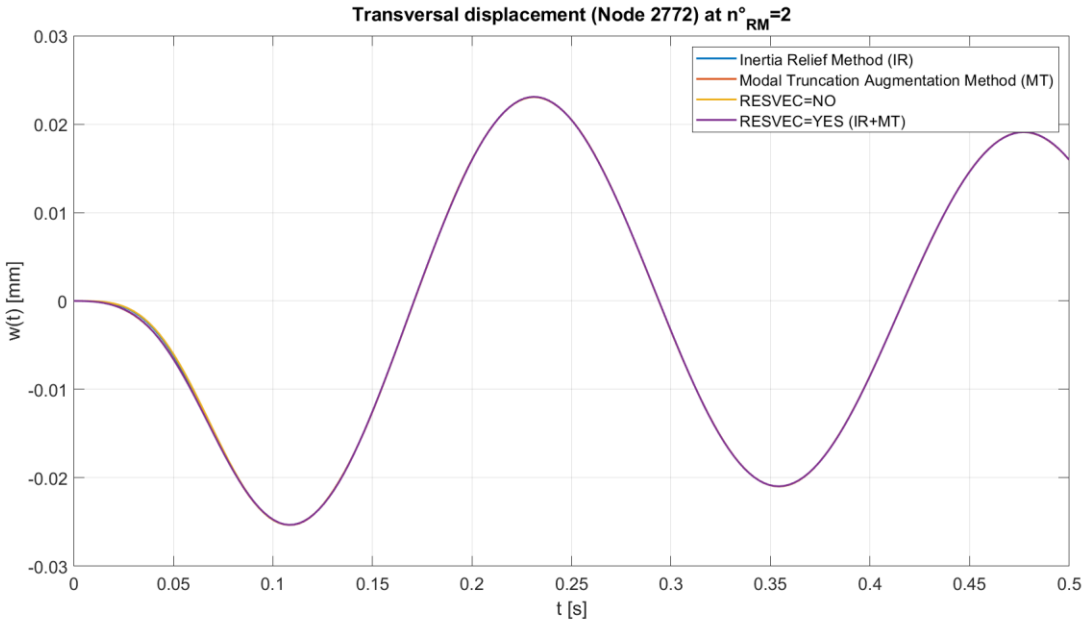

*Figure 3.23: Transversal displacement for the central node **2772** at **2** retained modes.*

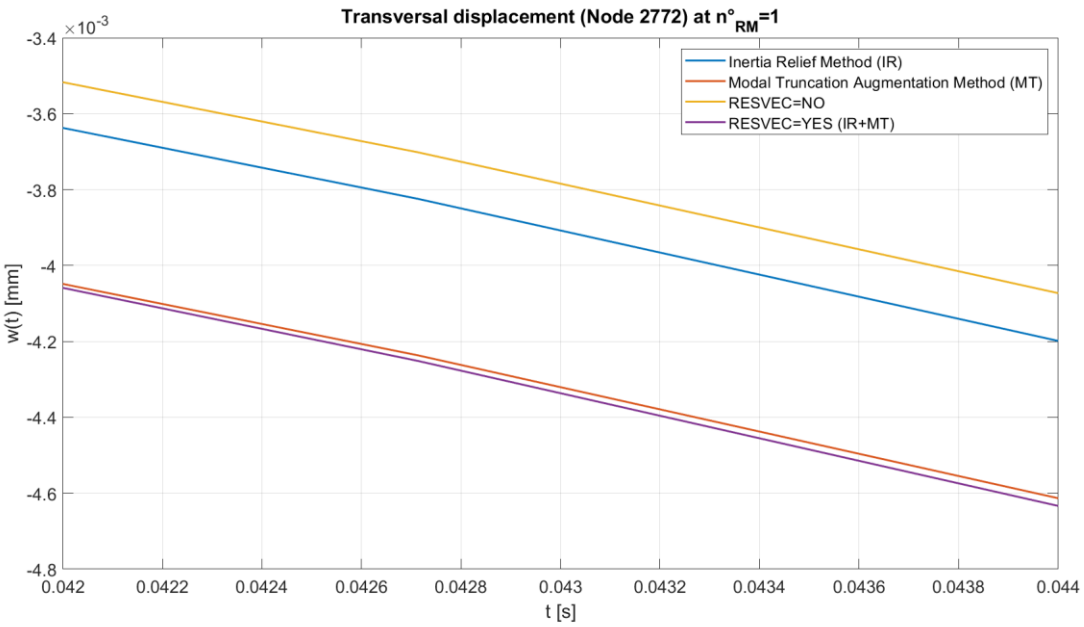

*Figure 3.24: Transversal displacement for the central node **2772** at **1** retained mode. (Zoomed).*

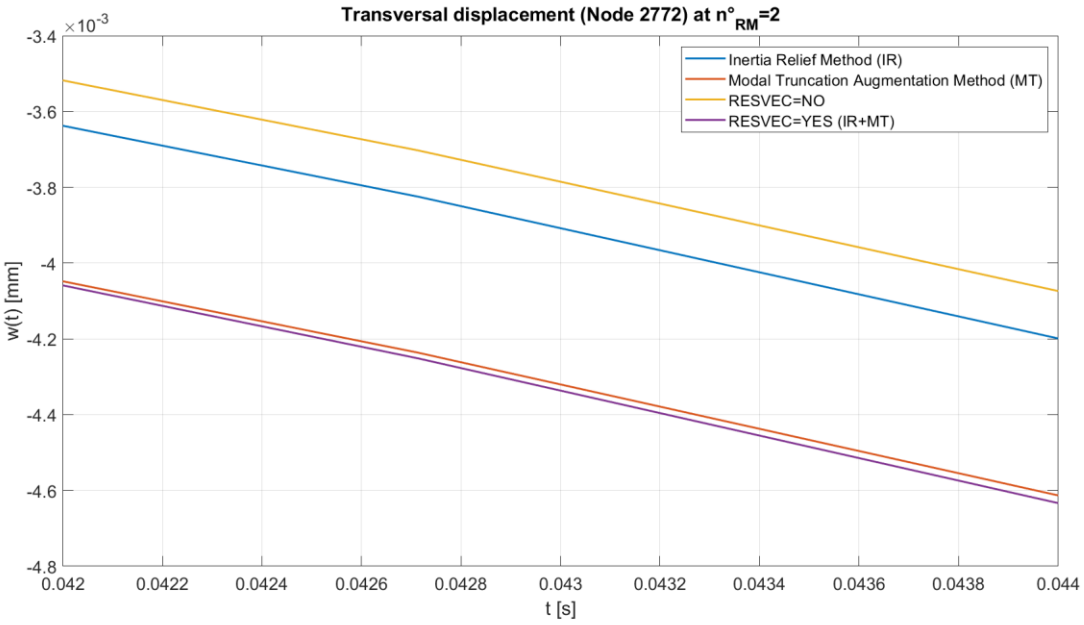

*Figure 3.25: Transversal displacement for the central node **2772** at **2** retained modes. (Zoomed). No evident differences with the previous case where $n°_{RM} = 1$.*

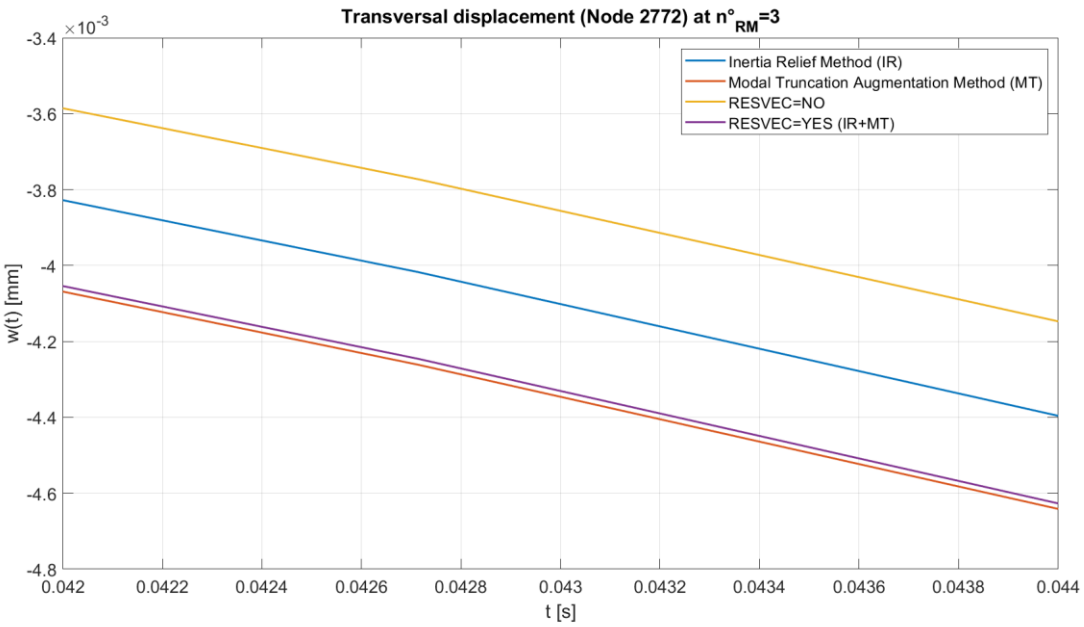

*Figure 3.26: Transversal displacement for the central node **2772** at **3** retained modes. (Zoomed).*

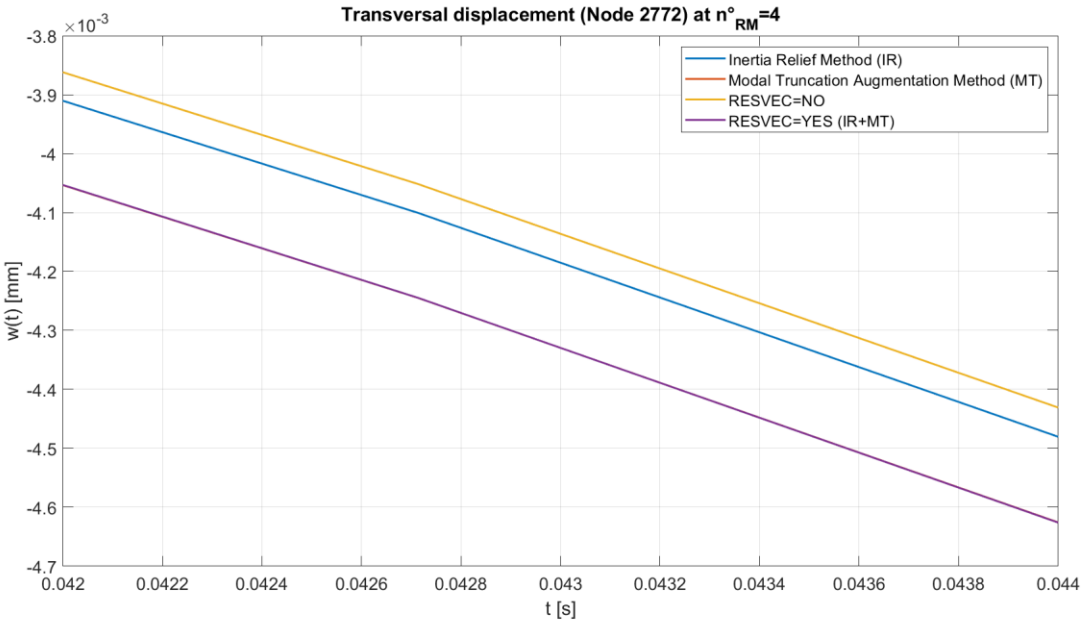

*Figure 3.27: Transversal displacement for the central node **2772** at **4** retained modes. (Zoomed).*

3.5.2. Performance coefficients definition and results

To globally compare the methods, the solution found consists of subtracting an ideal solution (pedicle 'Master') from the specified method's solutions. The ideal solution is the full dynamic response of the system obtained using $n°_{RM} = 300$ and the "RESVEC = YES" configuration.

The global displacements were imported in Matlab and were 3D Matrices of 2167x3x200 (2167 Nodes x $[T_1\ T_2\ T_3]$ x 200 Time Steps, T here stays for translation), except for the calculation of k_{min}, which was performed on selected nodes (these are reported in Figure 3.28, and the resultant matrix in this case has dimensions of 762x3x200). The defined coefficients are:

- Global ∂U_G maximum value, normalized with $U_{Master,max}$ ($\boldsymbol{k_{MAX}}$).
- Global ∂U_G mean value, normalized with $U_{Master,max}$ ($\boldsymbol{k_{Mean}}$).
- Global ∂U_G minimum value, normalized with $U_{Master,max}$ ($\boldsymbol{k_{min}}$).
- Norm 1, defined as the maximum DOF sum of each $\partial \mathrm{U}_{DOF,i}$ among all the time steps ($\boldsymbol{k_{Norm\ 1}}$).
- Norm ∞, defined as the maximum of the time sum of each $\partial U_{DOF,i}(t)$ among all the DOFs ($\boldsymbol{k_{Norm\ \infty}}$).

Practically, to calculate the norm 1 is necessary to sum at each time step all the differences from the Master solution of each DOF, then it is chosen the maximum among all the time steps. While to calculate norm ∞, it is necessary to sum for each DOF all the differences across all the time steps, then it is chosen the maximum value among all the DOFs.

$\boldsymbol{U_{ij} = \sqrt{u_{ij}^2 + v_{ij}^2 + w_{ij}^2}}$ and $\boldsymbol{\partial}$ refers to the difference between the calculated and the ideal solution (U_{Master}). $\boldsymbol{\partial U_G}$ is defined as:

$$\boldsymbol{\partial U_{G,ij} = \left|U_{method,ij} - U_{Master,ij}\right| = \left|\sqrt{u_{method,ij}^2 + v_{method,ij}^2 + w_{method,ij}^2} - \sqrt{u_{Master,ij}^2 + v_{Master,ij}^2 + w_{Master,ij}^2}\right|}$$

In Figures 3.29-3.33 are reported the just defined coefficients for different RESVEC configurations as a function of $n°_{RM}$. Figure 3.34 and Figure 3.35 show the total dynamic displacements in absolute value for a more peripheral node (node 308). Demonstrating that in some cases, hypothetically when the displacement variations are sudden, the IR method manages to better represent those variations, since it has more frequency-wise instruments (6 modal shapes) than the MT method (1 modal shape) for the analysed case.

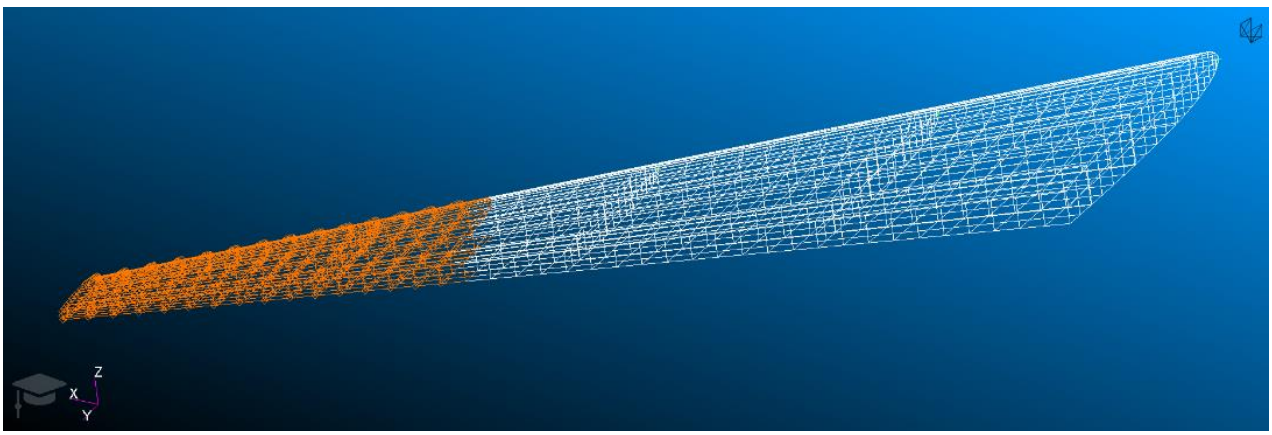

Figure 3.28: Nodes included in the evaluation of k_{min}.

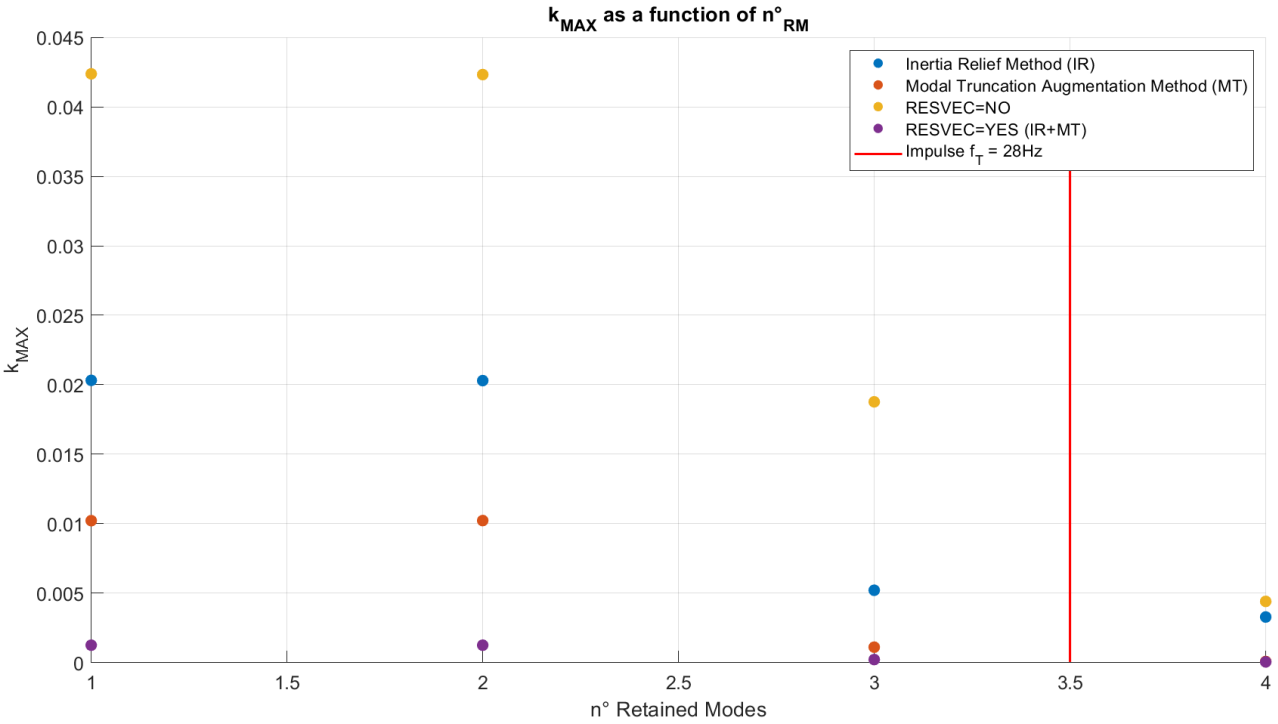

Figure 3.29: $\boldsymbol{k_{MAX}}$ as a function of $n°_{RM}$. There are minor differences between the cases where $n°_{RM} = 1$ and $n°_{RM} = 2$, this is valid for each defined coefficient.

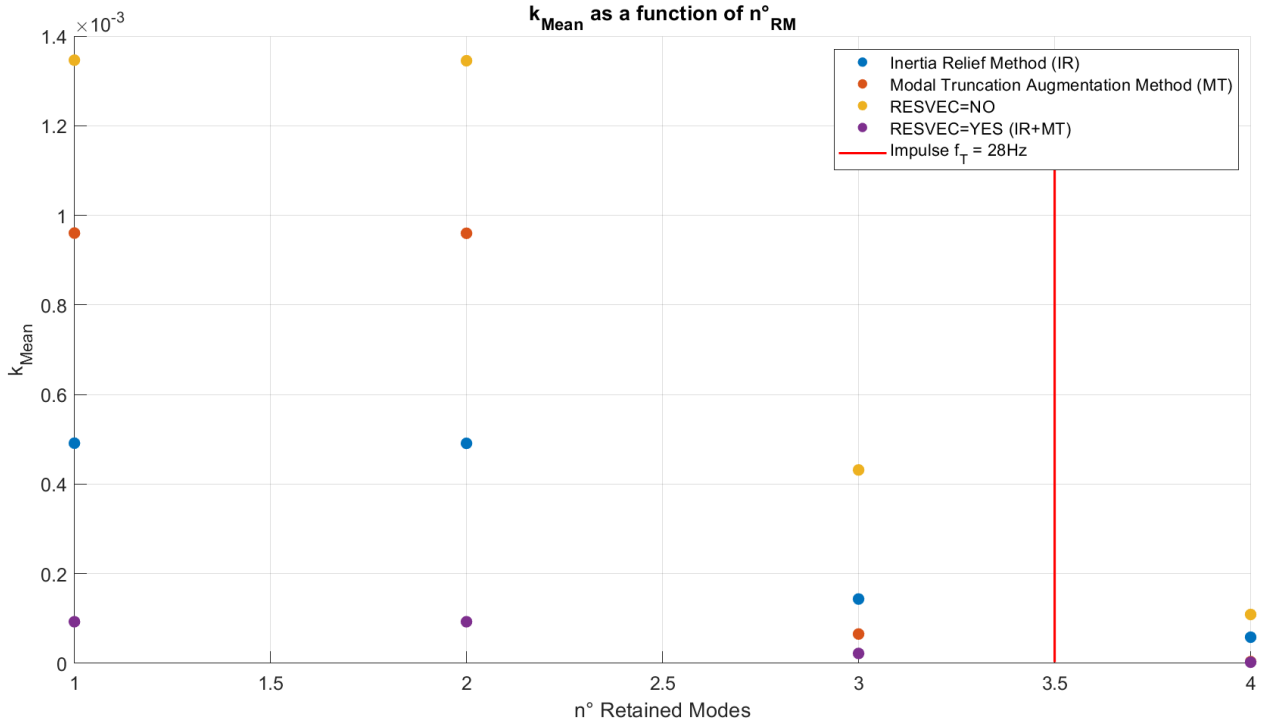

Figure 3.30: $\boldsymbol{k_{Mean}}$ as a function of $n°_{RM}$.

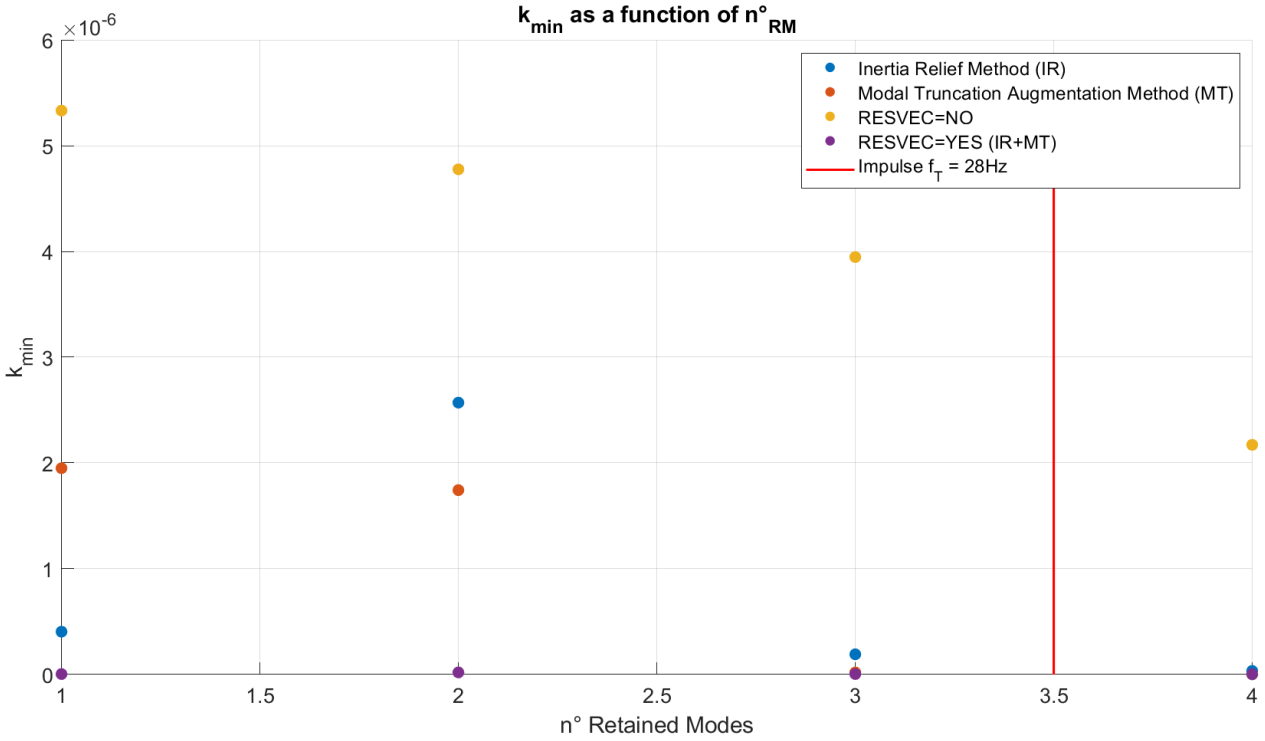

Figure 3.31: k_{min} as a function of $n°_{RM}$. No evident pattern can be deduced from this coefficient.

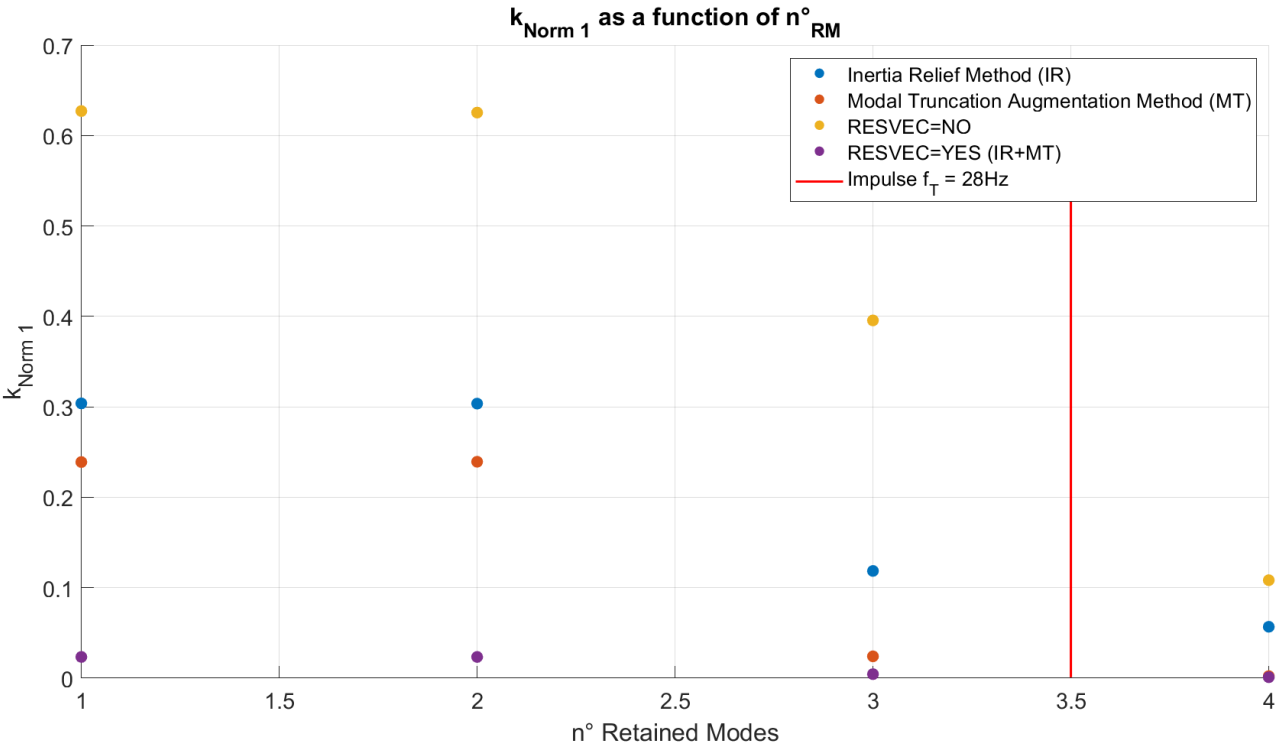

Figure 3.32: $k_{Norm\ 1}$ as a function of $n°_{RM}$.

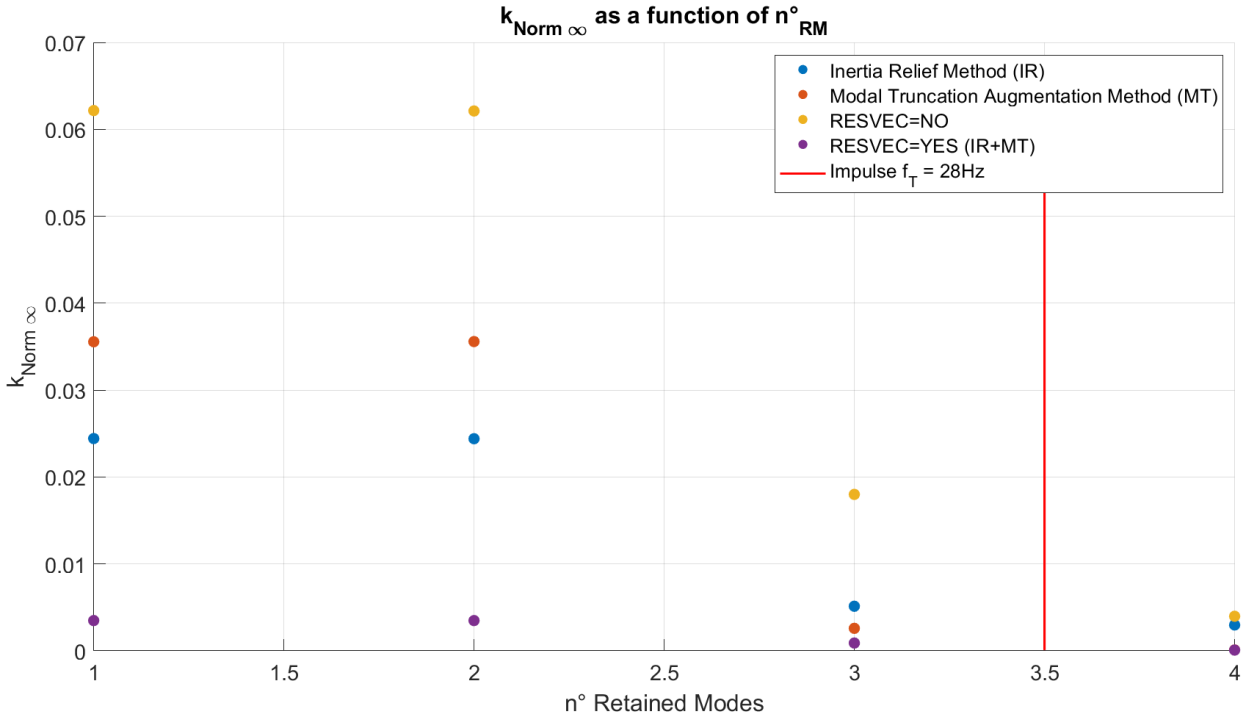

Figure 3.33: $\boldsymbol{k_{Norm\,\infty}}$ as a function of $n°_{RM}$.

Overall, in the analysed case, the impulse mainly solicits the first modal shape, letting in conclusion each method described at each $n°_{RM}$ to represent sufficiently well the solution ($k_{MAX} \leq 4.5\%$ of $U_{Master,MAX}$ for the "RESVEC = NO" method).

However, at really low $n°_{RM}$, k_{MAX} and k_{Mean} (Figure 3.29 and 3.30) show that while the IR method is characterized by the largest deviations from the ideal solution, it is closer to it on average. $k_{Norm\,1}$ and $k_{Norm\,\infty}$ (Figures 3.32 and 3.33) are coherent with the results obtained by k_{MAX} and k_{Mean}, furthermore indicating that the MT method could have a better spatial representation while the IR method a better temporal representation of the global solution at a higher computational cost. However, these differences disappear as the $n°_{RM}$ increases in favor of the MT method.

Anyway, the comparison between the MT, the IR and the 'RESVEC = YES' methods is here unequal because the number of the pseudo-eigenvectors calculated for the MT method directly depends on the number of differentiated dynamic loadings applied (which is 1 in this example), while the IR method calculates 6 eigenvectors independently from the applied dynamic loads and the 'RESVEC = YES' method calculate the same eigenvectors calculated by both IR and MT methods (7 for this example). The combination of the two methods is the more versatile and assures the best representation of the solution at each $n°_{RM}$, but for a higher computational cost indeed.

Furthermore, at $n°_{RM} \geq 3$ the MT method consistently outperforms the IR method in every defined coefficient, which is not insignificant since it gives an overall better solution representation relying only on 4 total modal shapes, instead of the 9 total modal shapes used by the IR method.

This also means that the MT method better converges to the solution solving less than half of the differential equations solved by the IR method. Furthermore, at $n°_{RM} = 3$, it is more convenient to use the MT method than the 'RESVEC = NO' method with $n°_{RM} = 4$, confirming the best convergence (at parity of total solved differential equations) around all the presented methods. For higher $n°_{RM}$ the "RESVEC = YES" solution has

only marginal benefits over the MT solution, at an expensive computational cost. This will be further investigated in paragraph 3.6.

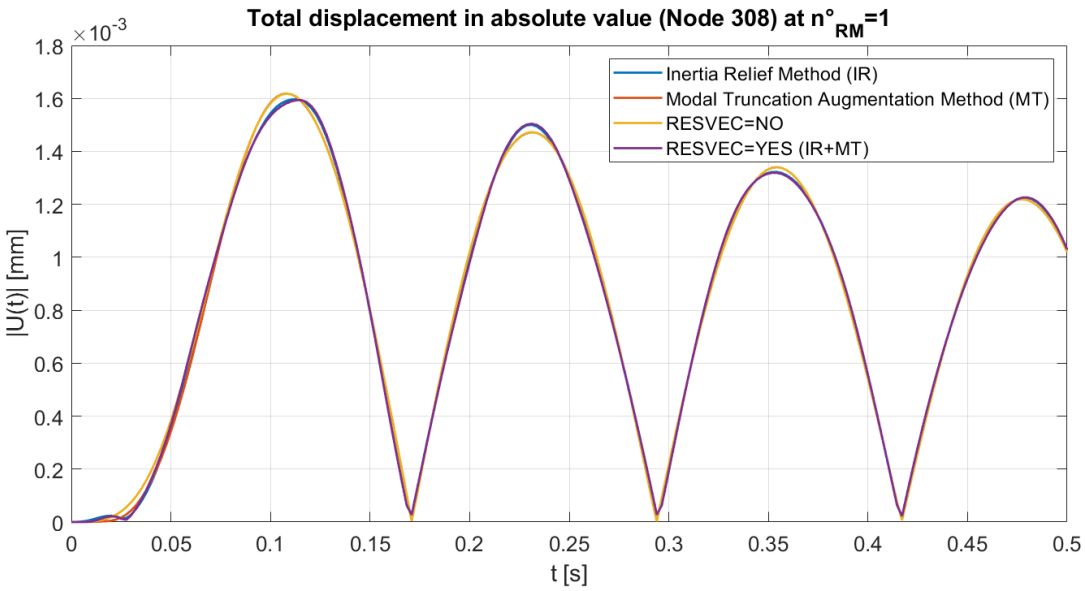

*Figure 3.34: Total displacement in absolute value for the peripheral node **308** (near the wing's trailing edge) at **1** retained mode.*

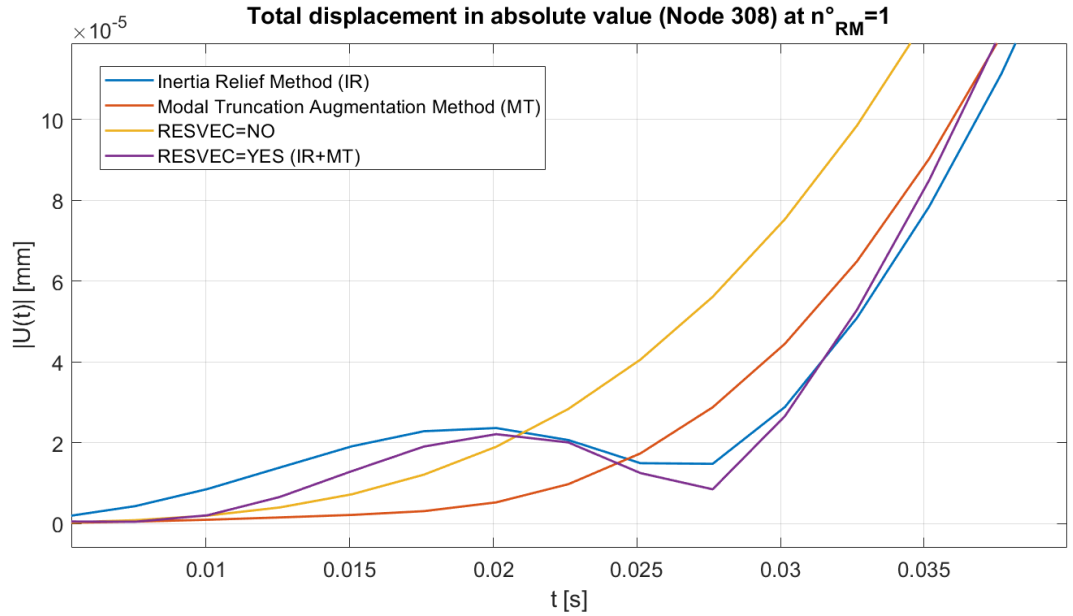

*Figure 3.35: Total displacement in absolute value for the peripheral node **308** (near the wing's trailing edge) at **1** retained mode (zoomed).*

3.6. Analysis (Torsional load)

3.6.1. Loading applied on the wing model and results

In order to excite the fifth modal shape of the model (torsional one) and observe the response of the described methods at the $n°_{RM}$ variation, a torsional couple of forces was applied to the system as indicated in Figure 3.36. The impulse chosen for the time component of the forces has a cut frequency of $f_{T,2}$=56 Hz, which is sufficient to excite the mentioned modal shape (Figure 3.12, $f_5 = 40.954\ Hz$). The coefficients used are the same as those introduced in paragraph 3.5.2.

The results indicate that the Modal Truncation Augmentation (MT) method performs the worst at low $n°_{RM}$, while even the solution without residual vectors outperforms it, and the Inertia Relief (IR) method is the second best, after the 'RESVEC = YES' configuration. This can be explained by observing the displacements at node 308 (node 308 is reported in Figure 3.36), reported in paragraph 3.6.4: the MT method emulates the correct solution but is out of phase sync due to the limited eigenvector matrix characterizing the system, resulting in the largest deviation from the correct solution. Paradoxically, the solution reported by not including any residual vectors is in a certain way more accurate since it cannot go out of phase as for the MT method, this is also related to the fact that the MT vectors' frequencies do not necessarily approximate the non-retained modes' frequencies (valid also for the IR method).

Analyzing the videos of the full structural displacements it can be observed that the IR and MT methods seem to correctly emulate the 'RESVEC = YES' solution at $n°_{RM} = 1$, while the no residual vectors method performs the worst from this perspective since it cannot represent any torsion of the structure as for the other 2 methods, but instead oscillates up and down. The modal shapes obtained using the IR and MT methods at $n°_{RM} = 1$ are shown in paragraph 3.6.3: even though the single MT vector seems to accurately account for the modally non-represented load, it is not sufficient to reconstruct the full system response. In contrast, the IR method has a larger pool of residuals, making it more capable of representing the full displacements at lower $n°_{RM}$ because of its reactivity from the time domain perspective. After $n°_{RM} > 3$, the MT method consistently outperforms the IR method. It is also worth noting that after the inclusion of the fifth (torsional) modal shape, even the solution without any residual vectors tends towards the correct result, but along with the IR method, as reported in Figures 3.38 and 3.42, it cannot fully converge to the ideal solution.

In conclusion, at lower $n°_{RM}$ the MT method gives a good representation of the solution at a lower computational cost for simple applied forces which excite only few and transversal modal shapes (as reported for the first simulation in paragraph 3.5), and outperforms the IR method for what concerns k_{MAX} and $k_{Norm\ 1}$, which instead is more accurate, at very low $n°_{RM}$, for k_{Mean} and $k_{Norm\ \infty}$ for any spatial load and in every defined coefficient for particular spatial loads. The fact that the MT method consistently outperforms the IR method at higher $n°_{RM}$ is due to its capability to calculate the residuals directly from the modally non-represented portion of the load, trying to solve the dynamic displacements as a function of the applied loading case and not a priori as for the IR method.

However, the combined use of MT and IR methods generally ensures the best results at each $n°_{RM}$ and for each applied dynamic force, helping to maintain the error exceptionally low in any presented case. At higher $n°_{RM}$ it should be better to use only the MT method, while the 'RESVEC = YES' solution would be the best at really low $n°_{RM}$, although it would be better to add some modes and again to use the MT method. For instance, starting from $n°_{RM} = 3$ the differences between the MT and the "RESVEC = YES" solution are really marginal for a big difference in the computational cost.

Overall, the results do not give a precise indication why the MT and IR methods are both implemented and used simultaneously. It is hypothesized that the MT method is the best choice when are retained all the modes which sufficiently span the frequency content of the load, while the combined use of the IR and MT methods is preferable otherwise. Other studies should be made in order to understand why MSC Nastran's algorithm adopts both methods by default and at which point one method is preferable over the other.

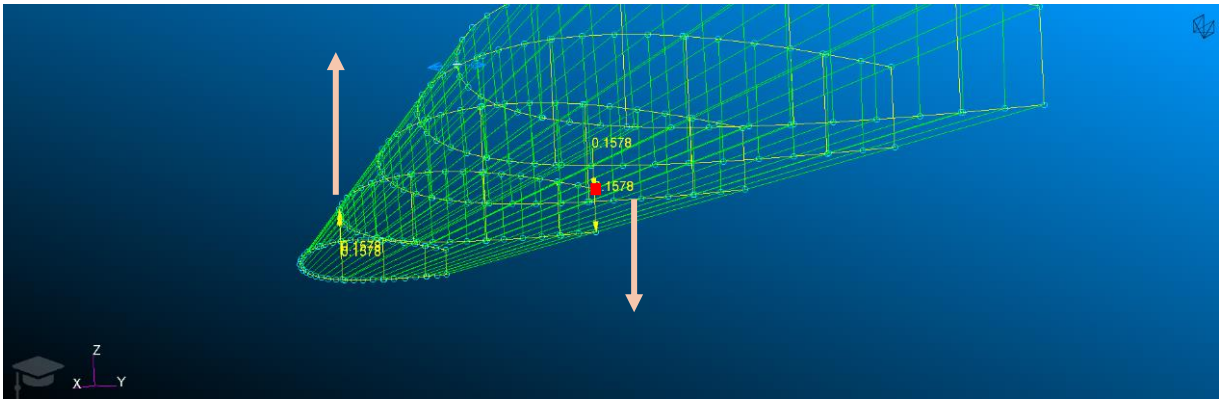

Figure 3.36: Forces applied to model's geometry (displayed at $t = 0.001\ s$). In red is reported the node 308.

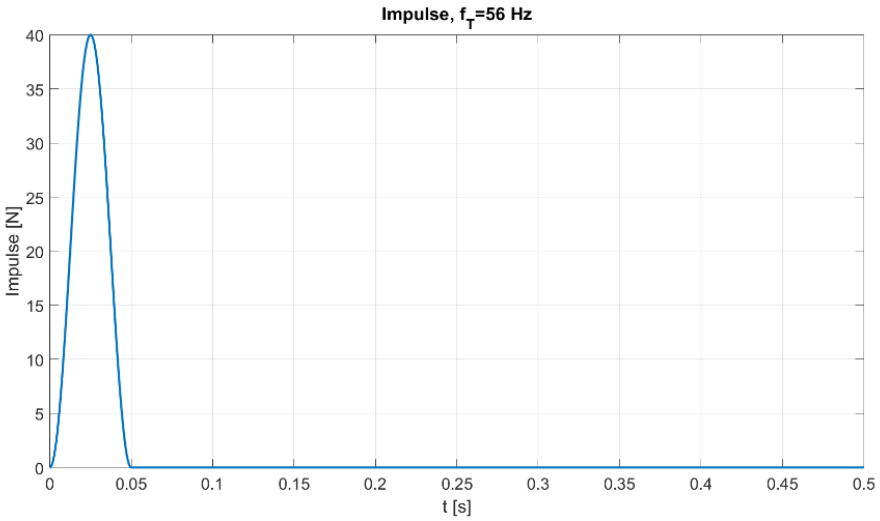

Figure 3.37: Impulse applied on the structure; $f_{T,2} = 56\ Hz$.

3.6.2. Performance coefficients results

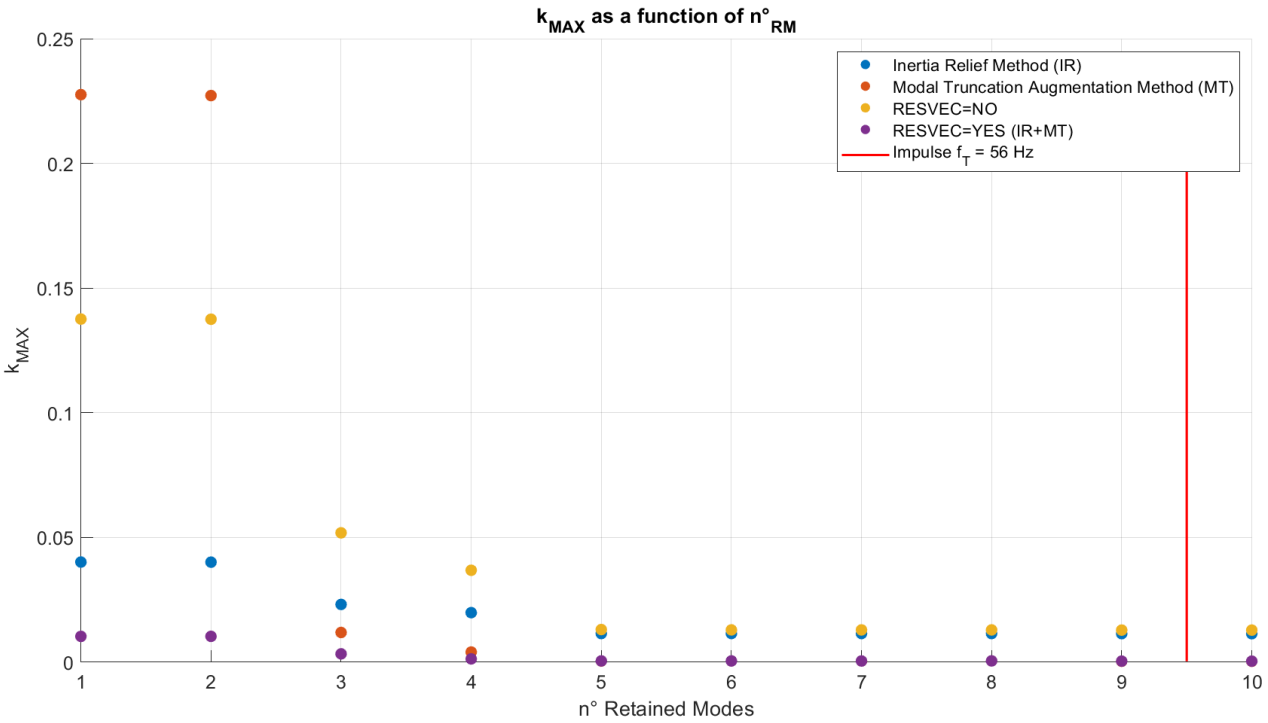

Figure 3.38: k_{MAX} as a function of $n°_{RM}$.

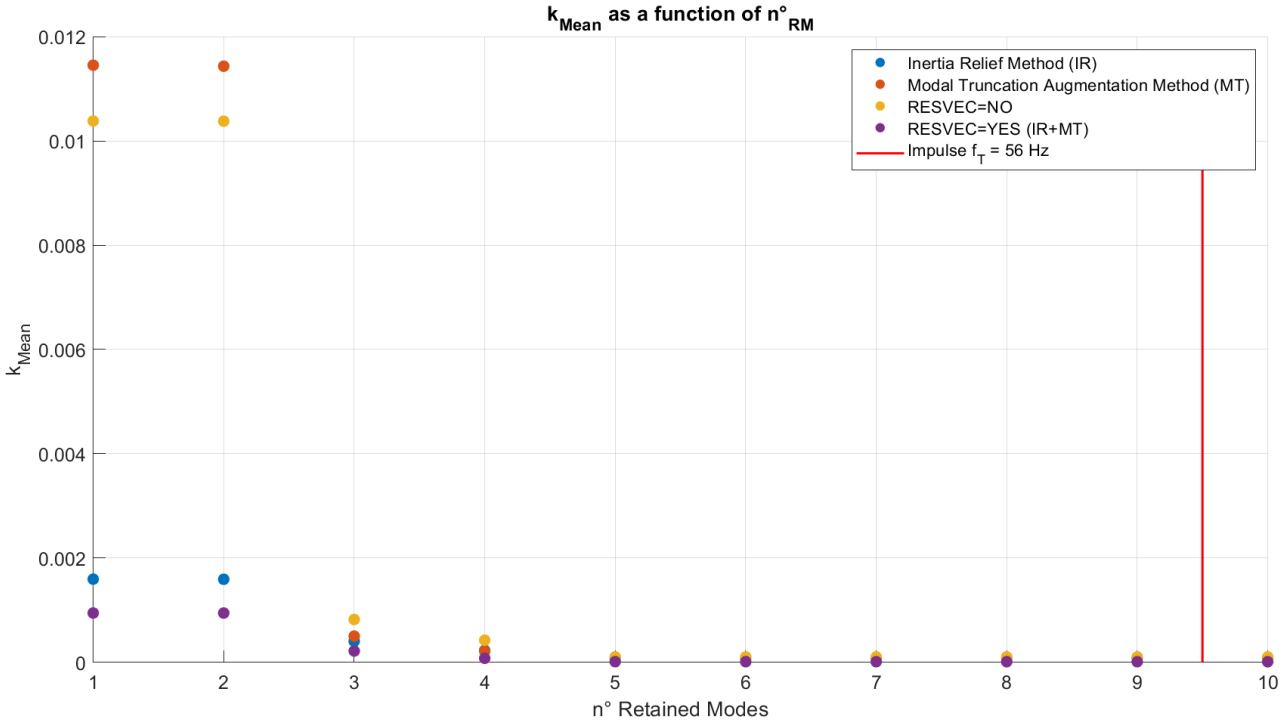

Figure 3.39: k_{Mean} as a function of $n°_{RM}$.

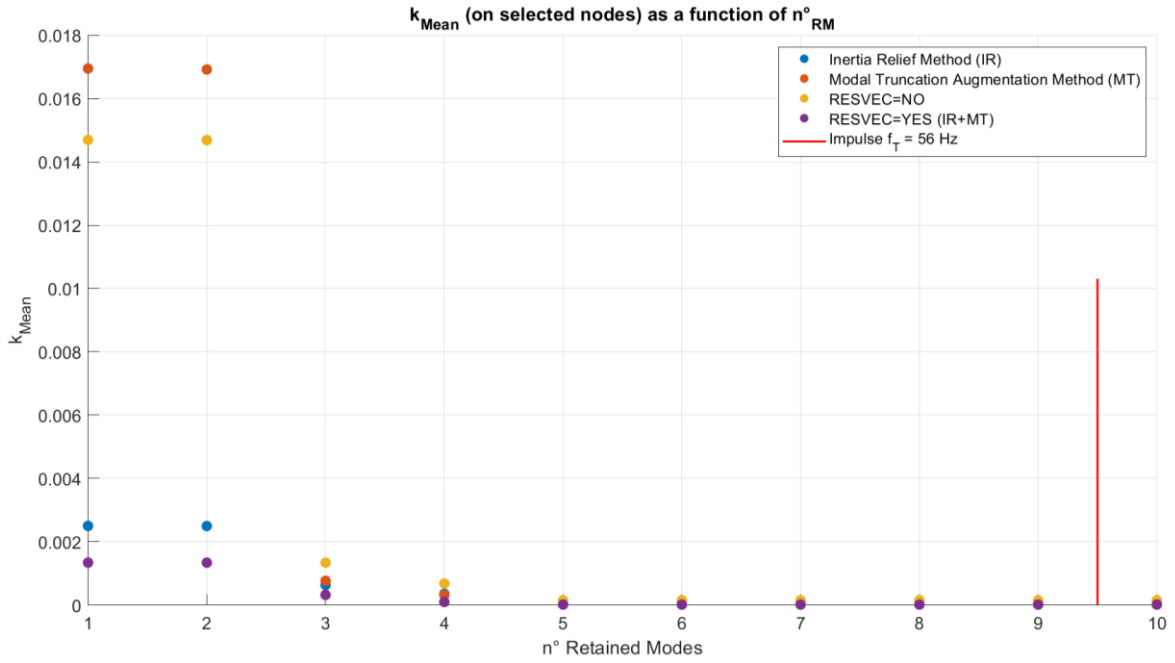

Figure 3.40: $\boldsymbol{k_{Mean}}$ as a function of $n°_{RM}$ (on selected nodes, they are reported in Figure 3.28).

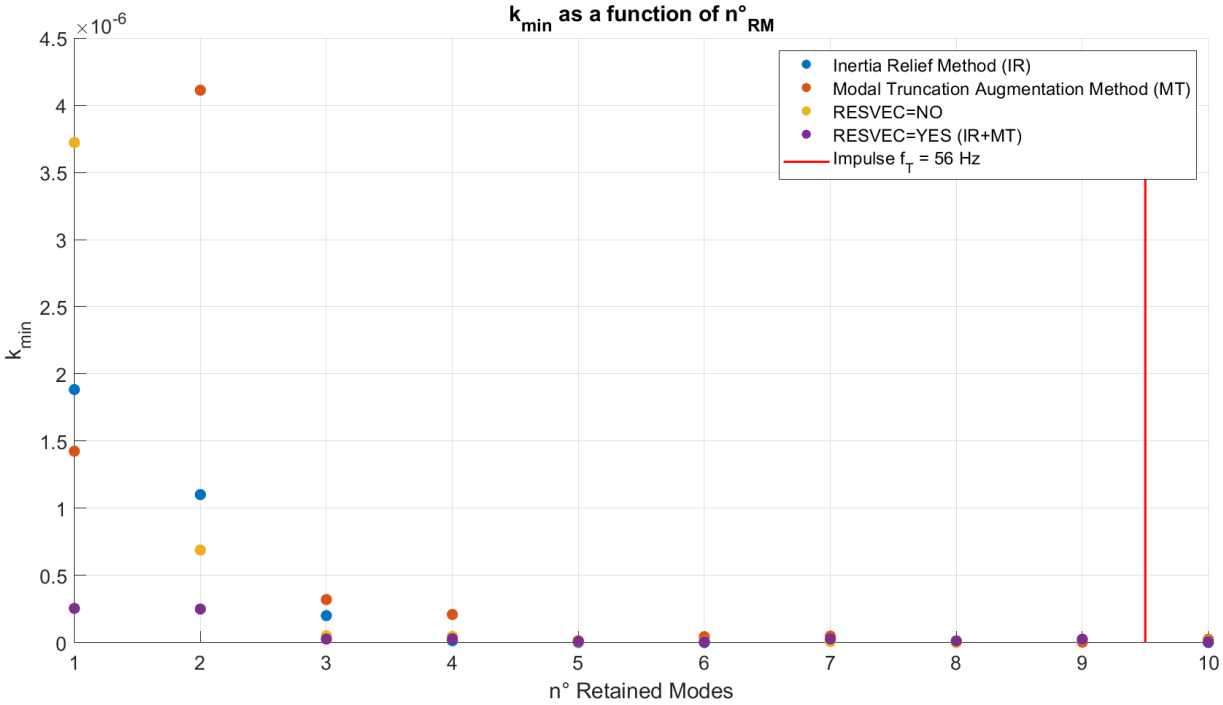

Figure 3.41: $\boldsymbol{k_{min}}$ as a function of $n°_{RM}$. No evident pattern can be deduced from this coefficient.

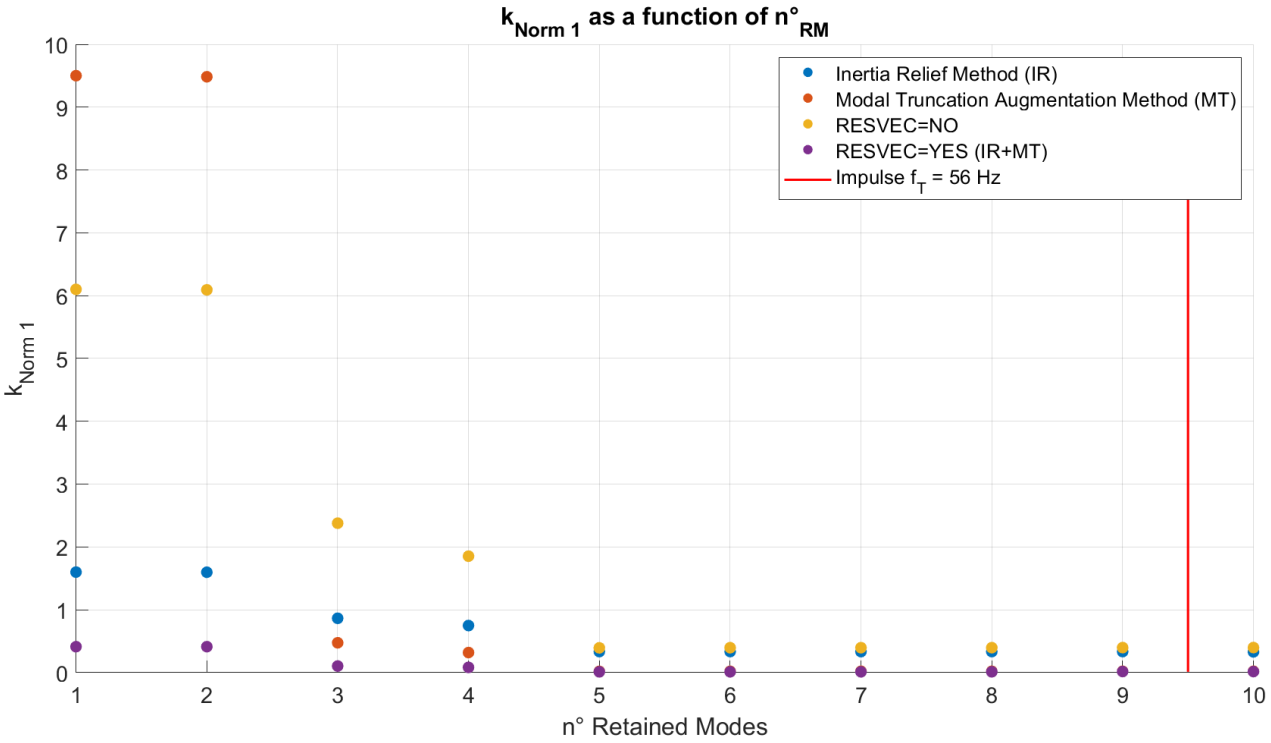

Figure 3.42: $k_{Norm\ 1}$ as a function of $n°_{RM}$.

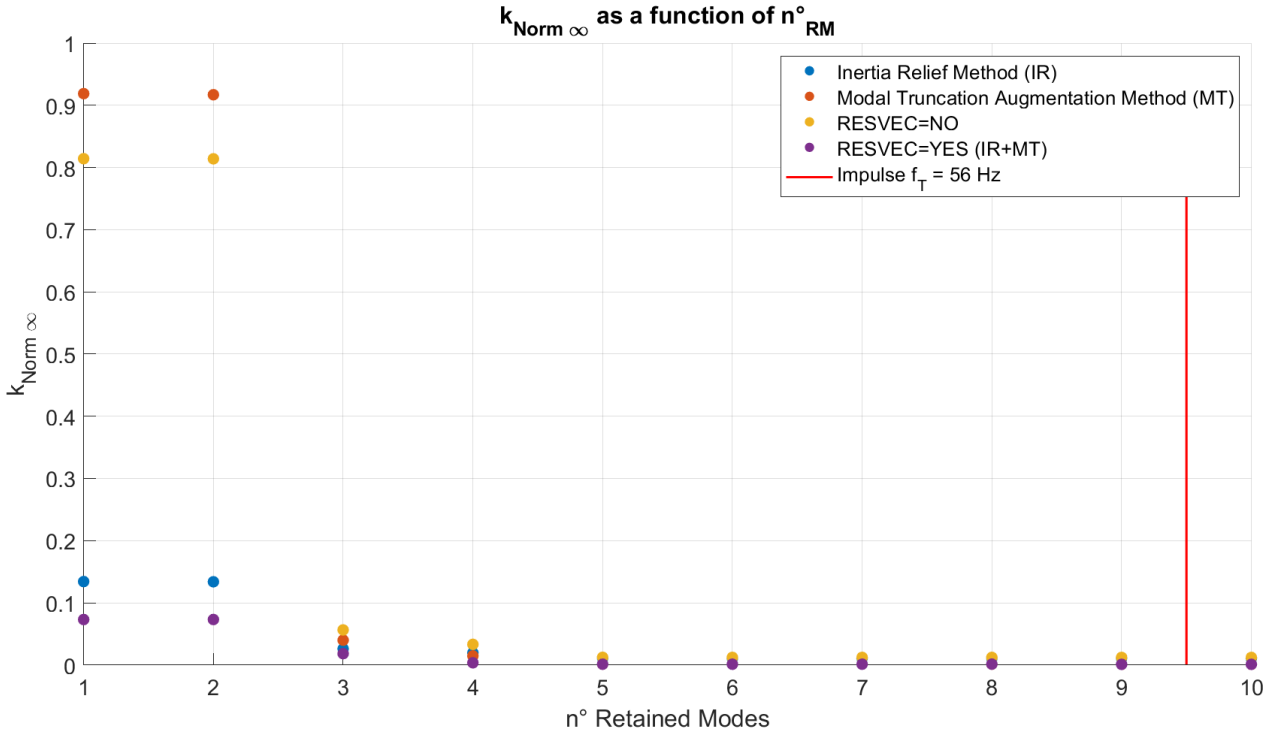

Figure 3.43: $k_{Norm\ \infty}$ as a function of the $n°_{RM}$.

3.6.3. MT and IR methods' pseudo-modal shapes

Here are presented the IR and MT method's pseudo modal shapes which are capable of responding to the defined torsional load case. They are all calculated at $n°_{RM} = 1$.

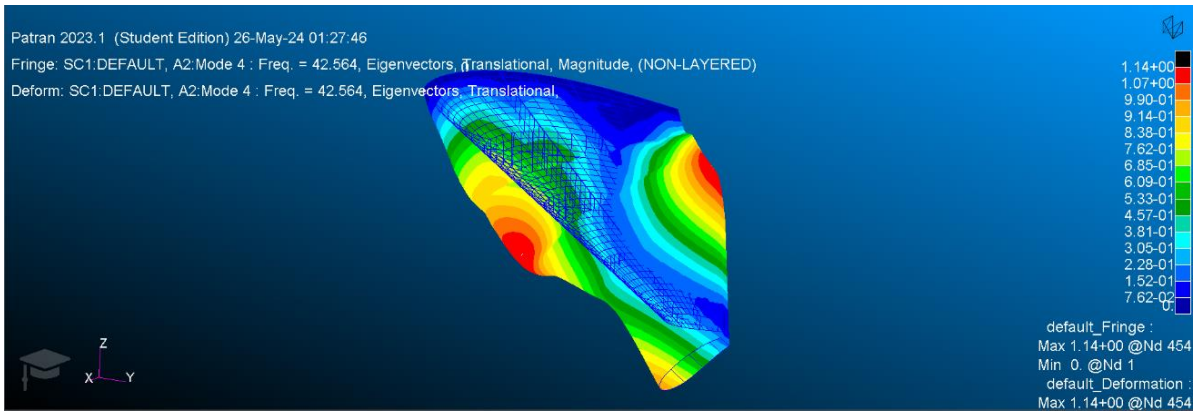

*Figure 3.44: Augmented (fourth) Modal Shape for the **Inertia Relief** method; $f_4 = 42.56\ Hz$.*

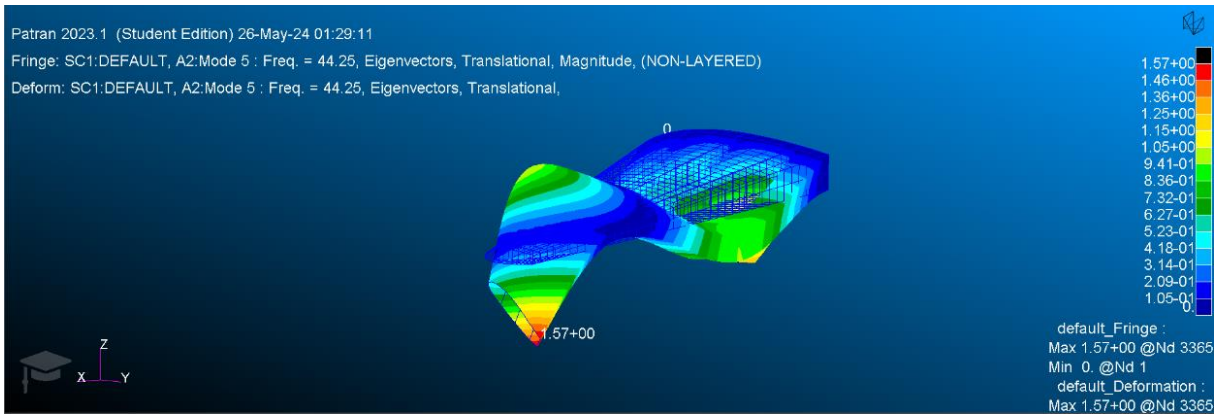

*Figure 3.45: Augmented (fifth) Modal Shape for the **Inertia Relief** method; $f_5 = 44.25\ Hz$.*

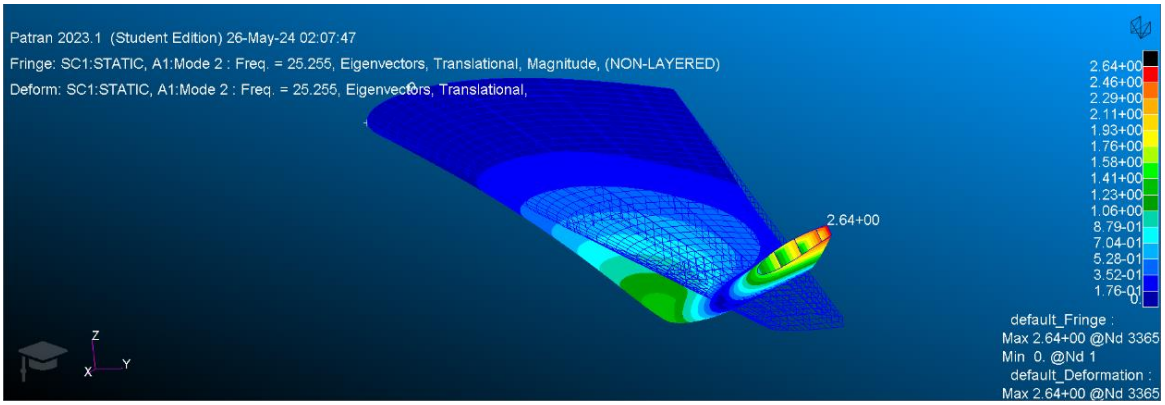

*Figure 3.46: Augmented (second) Modal Shape for **Modal Truncation Augmentation** method. $f_2 = 25.26\ Hz$.*

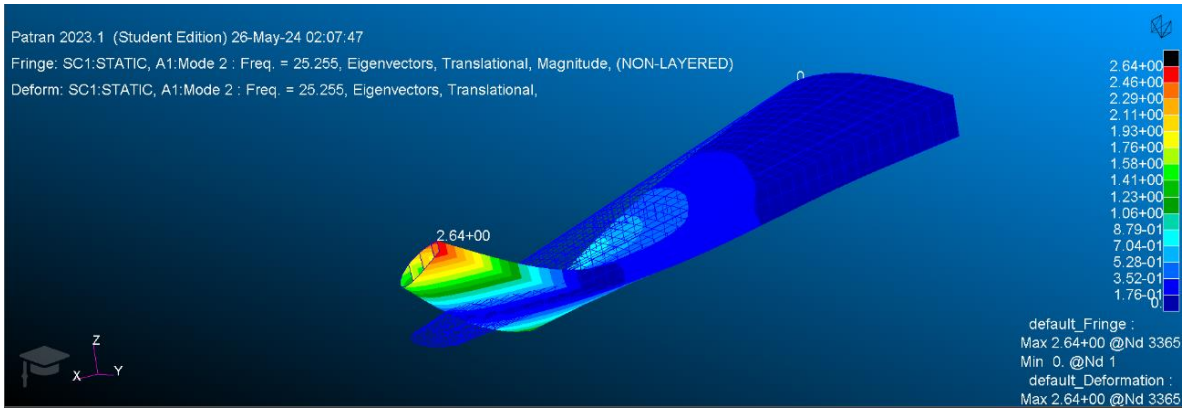

*Figure 3.47: Augmented (second) Modal Shape for **Modal Truncation Augmentation** method. $f_2 = 25.26\ Hz$ (**Different view**).*

3.6.4. Displacement results

In this last paragraph are reported total displacements in absolute value ($|U| = \sqrt{u^2 + v^2 + w^2}$) and transversal displacements (w) for the peripheral node 308 (represented in Figure 3.36). Figures 3.48, 3.49, 3.53, and 3.54 give a visual representation of why the coefficients associated to the MT method have such high values at low $n°_{RM}$, which exceed even those obtained for the 'RESVEC = NO' configuration. While Figure 3.50 and 3.55 report the convergence of the MT method to the 'RESVEC = YES' solution, starting from $n°_{RM} = 3$.

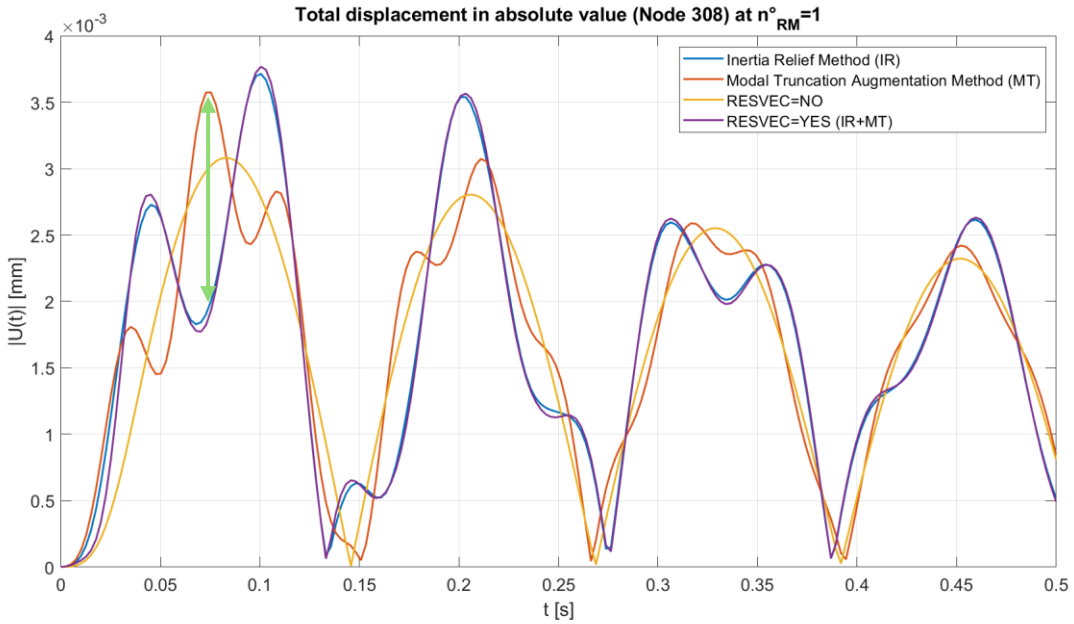

*Figure 3.48: Total displacement in absolute value for the peripheral node **308** (near the wing's trailing edge) at **1** retained mode. The light-green arrow indicates the solution difference between the MT method and the "RESVEC = YES" method.*

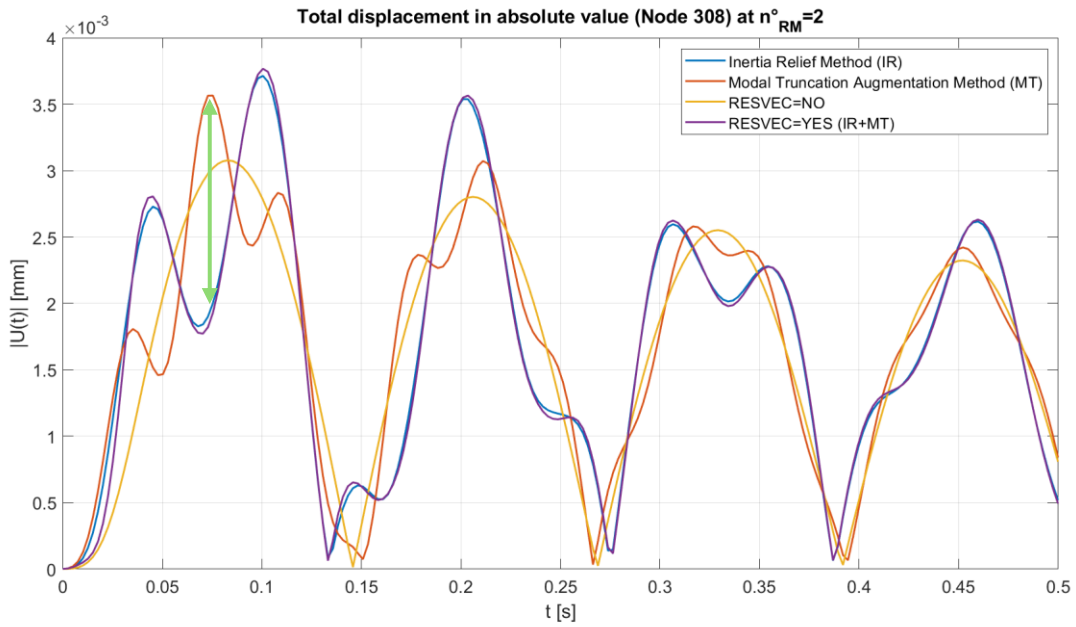

Figure 3.49: T*otal displacement in absolute value for the peripheral node **308** (near the wing's trailing edge) at **2** retained modes. Small differences between the cases where $n°_{RM} = 1$ and $n°_{RM} = 2$. The light-green arrow indicates the solution difference between the MT method and the "RESVEC = YES" method.*

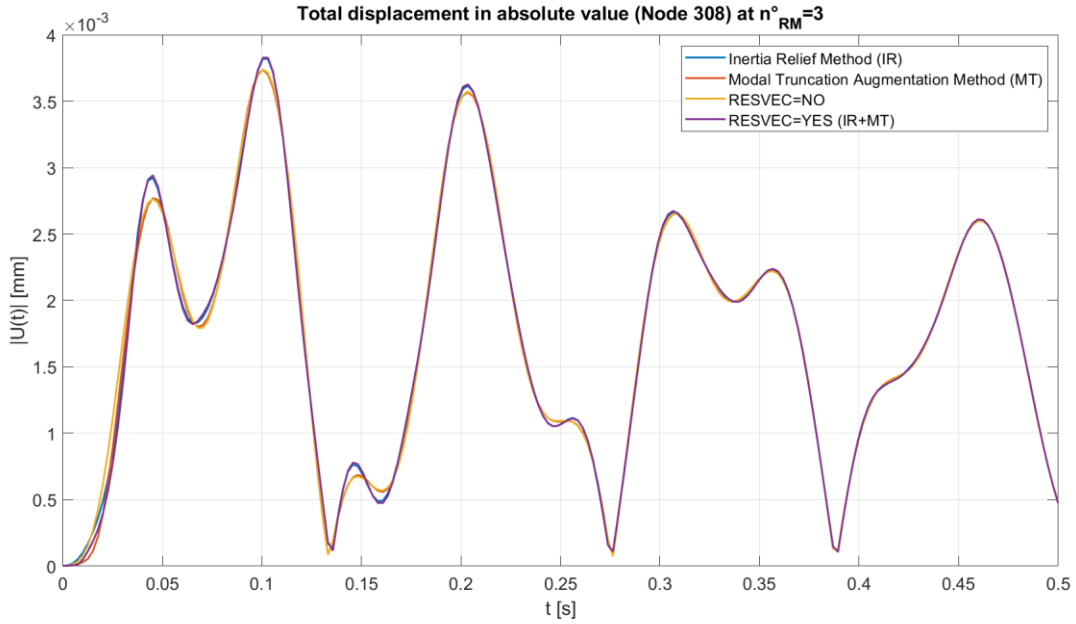

*Figure 3.50: Total displacement in absolute value for the peripheral node **308** (near the wing's trailing edge) at **3** retained modes.*

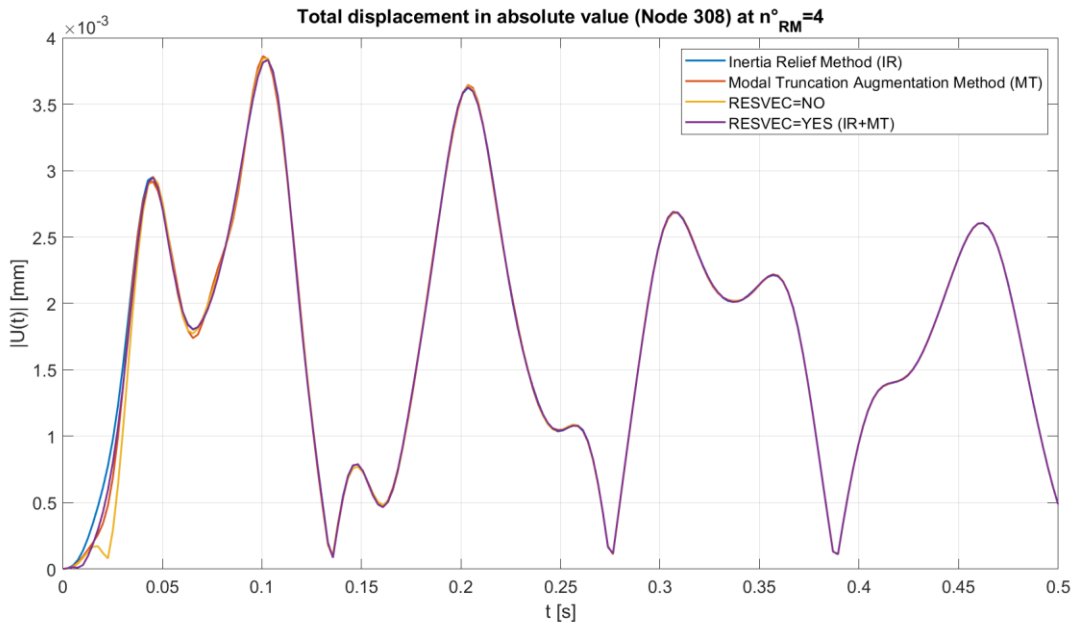

*Figure 3.51: Total displacement in absolute value for the peripheral node **308** (near the wing's trailing edge) at **4** retained modes.*

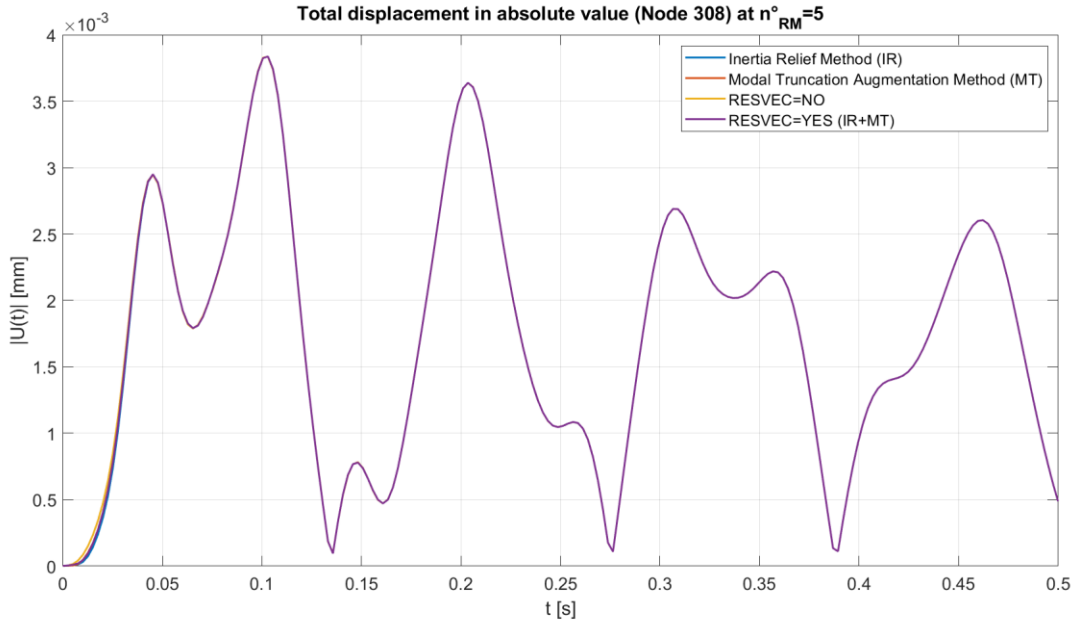

*Figure 3.52: Total displacement in absolute value for the peripheral node **308** (near the wing's trailing edge) at **5** retained modes.*

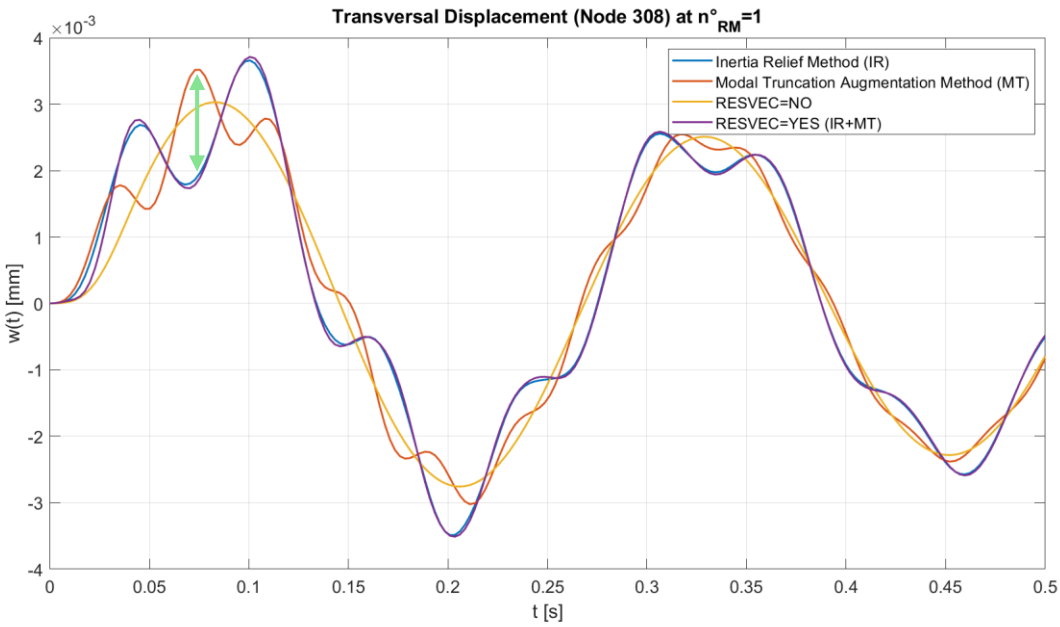

*Figure 3.53: Transversal displacement for the peripheral node **308** (near the wing's trailing edge) at **1** retained mode. The light-green arrow indicates the solution difference between the MT method and the "RESVEC = YES" method.*

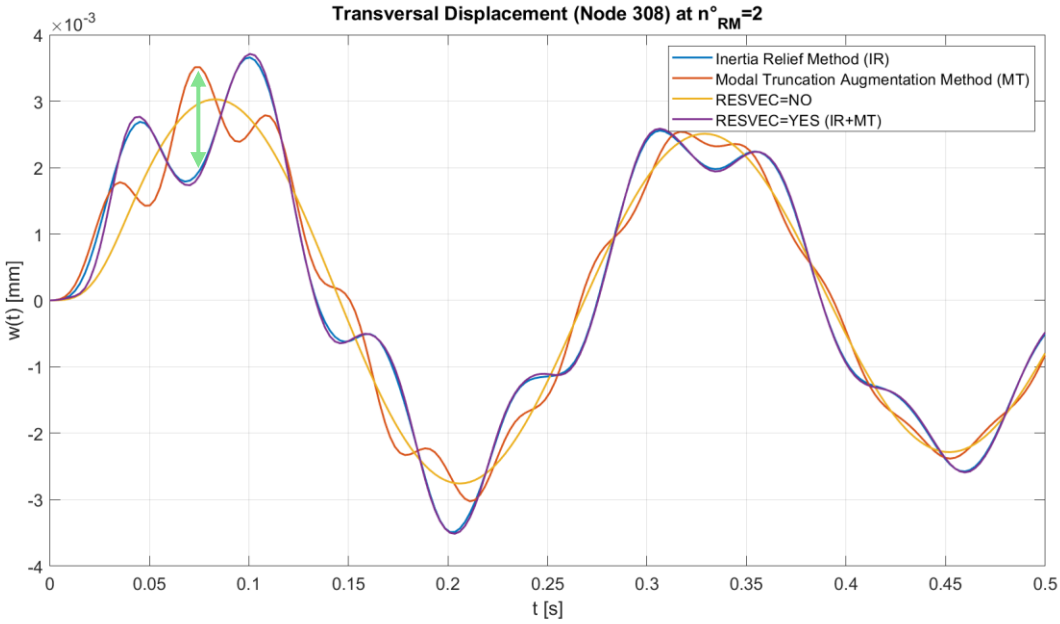

*Figure 3.54: Transversal displacement for the peripheral node **308** (near the wing's trailing edge) at **2** retained modes. Small differences between the cases where $n°_{RM} = 1$ and $n°_{RM} = 2$. The light-green arrow indicates the solution difference between the MT method and the "RESVEC = YES" method.*

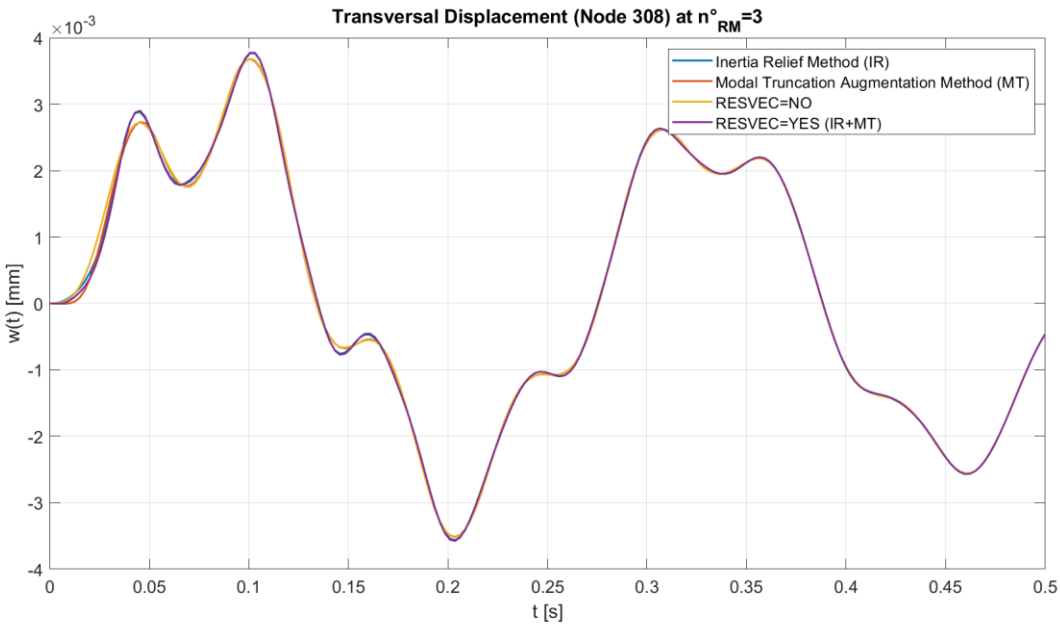

*Figure 3.55: Transversal displacement for the peripheral node **308** (near the wing's trailing edge) at **3** retained modes.*

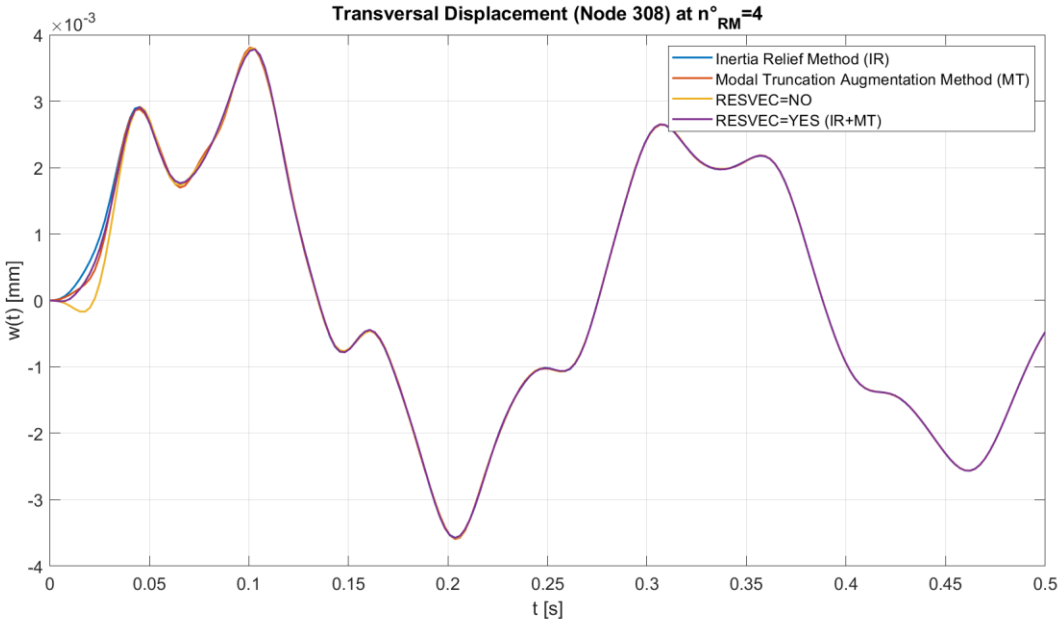

*Figure 3.56: Transversal displacement for the peripheral node **308** (near the wing's trailing edge) at **4** retained modes.*

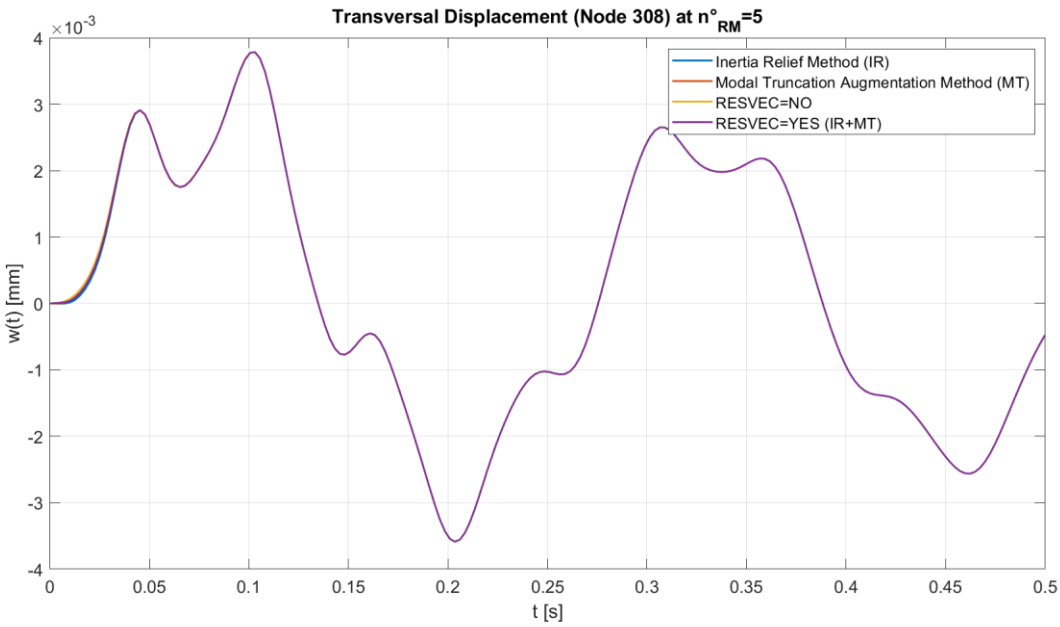

*Figure 3.57: Transversal displacement for the peripheral node **308** (near the wing's trailing edge) at **5** retained modes.*

4. Conclusions

Table 4.1 presents the advantages and disadvantages deduced from the analyses performed on the studied methods. All the methods were evaluated based on solution accuracy and their computational cost, except for the Mode Acceleration (MA) method, which is outdated and not used in modern structural dynamic response algorithms.

Overall, the Modal Truncation Augmentation (MT) method seem to provide the best balance between computational cost and solution accuracy. In the MSC Nastran algorithm, it is used simultaneously with the Inertia Relief-based (IR) method by default for the dynamic response calculation. Its use provides only marginal benefits at higher numbers of retained modes ($n°_{RM}$). However, it can enhance the solution accuracy at lower $n°_{RM}$ at a relatively high computational cost.

For instance, the results do not give a precise indication why the MT and IR methods are both implemented and used simultaneously. It is hypothesized that the MT method gives better results if compared to the IR method when are retained all the modes which sufficiently span the frequency content of the load, while the combined use of IR and MT methods is preferable otherwise. Other studies are necessary to understand why MSC Nastran's algorithm adopts both methods by default and at which point one method is preferable over the other.

Method	***pros***	***cons***
Mode Displacement	*Allows to obtain the complete dynamic response for small systems.*	*Computationally expensive for large systems.*
No residual vectors	*Useful for simple applied loads which mainly excite the first modal shapes of the structure. However, the MA, MT and IR methods can significantly enhance its solution.*	*Extremely expensive to ensure the solution convergence since it does not account for the modally non-represented loads/forces. At parity of $n°_{RM}$ there are often better alternatives.*
Mode Acceleration	*Can enhance the results obtained by not including any residual vector.*	***Outdated**, there are better alternatives since it does not include any dynamic amplification relatively to the modally non-represented loads.*
Modal Truncation Augmentation	*Best convergence at the $n°_{RM}$ increase. Best trade-off between computational cost and solution approximation. Calculation of the pseudo-modal shapes based on the applied loads/forces.*	*Large solution mispredictions when are retained only few modes and are applied complex loadings which excite modal shapes with higher frequencies. Its computational cost is directly related to the number of differentiated applied loads.*
Inertia Relief-based (MSC Nastran algorithm)	*Possibility of calculating pseudo modal shapes without defining any loading case, useful for preliminary structural analyses. (**Possible**) better solution approximation than for the MT method when the retained modes' frequencies do not sufficiently span the frequency content of the loads/forces.*	*Worse solution convergence than for the MT method at the $n°_{RM}$ increase at a higher computational cost. When is useful (at low $n°_{RM}$) there are probably better options at parity of computational cost, for example, to add more modal shapes and use the MT method instead. However, this **might** depend on the load's frequency content.*
"RESVEC = YES" (MSC Nastran algorithm)	*It has been observed empirically that this method assures the best solution approximation at each $n°_{RM}$. (**Possible**) best choice when the retained modes' frequencies do not sufficiently cover the load's frequencies.*	*High cost for marginal benefits respect to the MT method at the $n°_{RM}$ increase. For this reason, it might be better to add more modal shapes and use the MT method instead. However, this **might** depend on the load's frequency content.*

*Table 4.1: Advantages and disadvantages of the analysed methods. (**Possible**) and '**might**' refer to the hypothesis discussed above.*

References

[1] Li, Li, and Yujin Hu. "Generalized mode acceleration and modal truncation augmentation methods for the harmonic response analysis of nonviscously damped systems." *Mechanical Systems and Signal Processing* 52 (2015): 46-59.

[2] Dickens, J. M., J. M. Nakagawa, and M. J. Wittbrodt. "A critique of mode acceleration and modal truncation augmentation methods for modal response analysis." Computers & structures 62.6 (1997): 985-998.

[3] Dickens, J. M., and K. V. Pool. "Modal truncation vectors and periodic time domain analysis applied to a cyclic symmetry structure." Computers & structures 45.4 (1992): 685-696.

[*4*] Soriano, H. L., and F. Venâncio Filho. "On the modal acceleration method in structural dynamics. Mode truncation and static correction." *Computers & structures* 29.5 (1988): 777-782.

[5] Rixen, Daniel. "Generalized mode acceleration methods and modal truncation augmentation." *19th AIAA Applied Aerodynamics Conference*. 2001.

[*6*] Wilson, Edward L., Ming-Wu Yuan, and John M. Dickens. "Dynamic analysis by direct superposition of Ritz vectors." Earthquake Engineering & Structural Dynamics 10.6 (1982): 813-821.

[*7*] Gherlone, M., "*Elementi finiti mono-dimensionali: la trave (Eulero-Bernoulli)*", master's course: "*Dinamica delle Strutture aerospaziali*", Academic Year 2022/2023, Politecnico di Torino.

[*8*] https://simulatemore.mscsoftware.com/simacademy-residual-vectors-in-modal-solutions-msc-nastran-video/

[*9*] Basutkar, Akhil, Kunal Baruah, and Shashidhar K. Kudari. "Frequency Analysis of Aircraft Wing Using FEM." *Recent Trends in Mechanical Engineering: Select Proceedings of ICIME 2019*. Springer Singapore, 2020.

[10] Gherlone, M., "*Analisi FEM della risposta dinamica di un pannello irrigidito a carichi di impatto*", master's course: "*Dinamica delle Strutture aerospaziali*", Academic Year 2022/2023, Politecnico di Torino.

[*11*] *https://2022.help.altair.com/2022/inspire/en_us/topics/inspire/tutorials/tut_inertia_c.htm#:~:text=Inertia%20relief%20is%20a%20numerical,mass%20of%20the%20total%20aircraft*.

[12] *https://help-be.hexagonmi.com/bundle/MSC_Nastran_2021_Reference_Guide/raw/resource/enus/MSC_Nastran_2021_Reference_Guide.pdf*